Mechanical behaviour of steel lined pipes under monotonic and cyclic bending

THE UNIVERSITY *of* EDINBURGH
Institute for Infrastructure
and Environment

Ilias Gavriilidis

This dissertation is submitted for the degree of
Doctor of Philosophy

August 2021

To my grandparents Dimitra and Ilias...

Declaration

I hereby declare that except where specific reference is made to the work of others, the contents of this dissertation are original and have not been submitted in whole or in part for consideration for any other degree or qualification in this, or any other university. This dissertation is my own work and contains nothing which is the outcome of work done in collaboration with others, except as specified. Some of the work has been presented in the following publications:

Journal papers, peer reviewed conference papers and extended abstracts:

- Gavriilidis, I., and Karamanos, S. A., 2021. "Structural response of steel lined pipes under cyclic bending". *International Journal of Solids and Structures, Accepted.*
- Gavriilidis, I., and Karamanos, S. A., 2021. "Liner wrinkling in offshore steel lined pipes during reeling installation". *Thin-Walled Structures*, **166**, p. 108114.
- Gavriilidis, I., and Karamanos, S. A., 2020. "Effect of manufacturing process on lined pipe bending response". *Journal of Offshore Mechanics and Arctic Engineering*, **142**(5), p. 051801.
- Gavriilidis, I., and Karamanos, S. A., 2019. "Influence of lined pipe fabrication on liner wrinkling". *Proceedings of the ASME 2019 38th International Conference on Ocean, Offshore and Arctic Engineering*. American Society of Mechanical Engineers, Glasgow, Scotland, UK, June 9 - 14, V05BT04A021, OMAE2019-95743.
- Gavriilidis, I., and Karamanos, S. A., 2019. "Bending and buckling of internally-pressurized steel lined pipes". *Ocean Engineering*, **171**, pp. 540 - 553.

Ilias Gavriilidis
August 2021

Acknowledgements

First of all, I would like to express my gratitude to my supervisor Spyros A. Karamanos for giving me the opportunity to conduct my PhD research at The University of Edinburgh. Professor Karamanos guided and supported me constantly not only throughout my doctoral research, but also during my undergraduate studies in Greece. I would also like to thank The University of Edinburgh for funding my work and providing all the necessary equipment (hardware and software licences) I needed for my research.

In addition, I would like to thank Dr. Daniel Vasilikis, working now as a Rigid Pipelines Development Engineer for TechnipFMC, Aberdeen, Scotland, UK for providing the experimental data I used for my PhD research and for his valuable help and comments at the beginning of my project. Furthermore, I would like to thank my friend Kostis for his assistance in cyclic modelling issues, my friends Nikos and Vasilis for proofreading early drafts of my thesis providing me very helpful comments, and Dr. Antonis Giannopoulos and Dr. Stefanos Aldo Papanicolopulos for their valuable help and suggestions during the post-viva corrections period.

Furthermore, I am very grateful to my brother Dimitris for his continuous help throughout all these years and especially during the first days in Edinburgh, while the constant support of my family, Manthos, Angeliki, Dimitris, Ilias, and Dimitra, during my undergraduate studies and since I left Greece is much acknowledged. In addition, I would like to thank my friend Giannis for his advice and significant help after my graduation in Volos. The support of Zeynep, Vasilis, Yorgos, George, Zoe and Niki, which are friends that I met here in Edinburgh, is much appreciated and I would also like to thank them for the pleasant memories we shared over the last years. Finally, I would like to thank the examiners of my PhD thesis Dr. Francisca Martinez-Hergueta and Dr. Adam Jan Sadowski, for their valuable comments and suggestions.

Abstract

Steel pipelines that transfer hydrocarbons may be exposed to several corrosive elements. In order to ensure the structural integrity of the pipeline against corrosion, double-walled pipes are produced, containing a thick-walled low-carbon steel (“outer pipe”) providing strength, and a thin layer (“liner pipe”) from a corrosion resistant alloy (CRA) material, which is fitted inside the outer pipe, resulting in a cost effective solution instead of producing pipelines from stainless steel or nickel alloy.

First, the structural response of double-walled pipes, also called “lined pipes”, under monotonic bending is investigated. In the first stage, two types of lined pipes are examined, with and without mechanical bonding between liner and outer pipe referred to as tight-fit pipe (TFP) and snug-fit pipe (SFP), respectively. It is shown that, upon applying monotonic bending, the liner pipe gradually detaches from the outer pipe, forming a uniform wrinkling at the compression zone leading to localized buckling with further increase of the curvature. Subsequently, the bending response of lined pipes under low or moderate levels of internal pressure is investigated, showcasing its beneficial effect on the bending performance of lined pipes. Furthermore, the influence of initial geometric imperfections on liner pipe buckling is examined, showing the imperfection sensitivity of internally pressurized and non-pressurized bi-metallic (double-walled) pipes.

Additionally, the effects of manufacturing process on the structural performance of mechanically lined pipes are investigated. Alternative manufacturing processes are considered, associated with either purely hydraulic or thermo-hydraulic expansion of the pipes. A three-dimensional model is developed, which simulates the manufacturing process in the first stage of the analysis, and subsequently, proceeds in the bending analysis of the lined pipe. This integrated two-stage approach constitutes an important contribution of this research to existing knowledge. Thermo-hydraulically expanded lined pipes are examined, with special emphasis on the case of partially heated liners, and reverse plastic loading in the liner pipe wall has been detected during depressurization. Furthermore, the numerical results show that the thermo-mechanical process results in higher mechanical bonding between the two pipes compared with the purely mechanical process, and that this bonding is significantly influenced by the liner pipe temperature level. It is also concluded that the value of initial gap between the two pipes before fabrication has a rather small effect on the value of liner buckling curvature. Numerical results on imperfection sensitivity are reported for different manufacturing processes, and the beneficial effect of internal pressure on liner bending response is verified.

Furthermore, the structural performance of a lined pipe under cyclic bending is investigated, motivated by offshore reeling installation. Five bending cycles are considered, representing the two installation cycles and three additional cycles of a failure/repair scenario. The loading cycles impose a bending curvature range corresponding to the strains developed during a typical reeling installation process. Different loading patterns are considered and their effect on liner performance is investigated. The results show that the application of reverse (negative) curvature during the loading cycles, representing the straightener, has a significant influence on the wrinkle size of the liner developed at the two critical generators and its rate of increase, compared with cyclic bending patterns with non-negative curvature. Numerical results on imperfection sensitivity are obtained, considering two types of imperfection of the liner pipe. In addition, the structural performance of liners with different thickness is examined, and the results show that there exists a minimum value of wall thickness, above which the liner does not exhibit local buckling at the end of the cyclic loading history. The beneficial effect of internal pressure on liner cyclic response is also verified, especially for thin-walled liners, preventing the development of wrinkles. The effect of manufacturing process is also examined, showing the superior structural performance of partially heated lined pipes, with respect to fully heated lined pipes, and to lined pipes manufactured by purely mechanical process.

Moreover, a three-dimensional numerical model of a mechanically bonded lined pipe is also developed, simulating its structural response during the reeling installation method. An installation failure/repair scenario is considered with five winding/unwinding cycles, accounting for the straightening process. The cyclic deformation of a lined pipe is presented, monitoring ovalization, local curvature and liner detachment from the outer pipe during reeling. The influence of pipe contact with the reel and the effects of back tension on the structural response of the lined pipe are examined. The results indicate a residual curvature of the pipeline at the end of unspooling. Applying different levels of back tension, the local curvature on the pipe decreases, affecting the detachment of the liner pipe from the outer pipe. Numerical results on imperfection sensitivity demonstrate the significant influence of geometric imperfections on liner buckling. Comparison of the present results with those from a pure bending model shows that a lower liner detachment rate is predicted by the present model. Furthermore, the reeling performance of thicker liners is examined, showing the gradual reduction of liner detachment with increasing wall thickness. Finally, the reeling process in the presence of moderate levels of internal pressure is simulated, verifying its beneficial effect on structural performance, preventing local buckling.

Table of contents

List of figures

List of tables

Symbols

$1/R_{\theta 0}$	Local hoop curvature of the liner pipe at maximum compression ($\theta = 0$) under monotonic bending
α_{ij}	Back stress tensor components
α_l	Thermal expansion coefficient of the liner pipe
α_o	Thermal expansion coefficient of the outer pipe
β	Material constant of Ziegler's kinematic hardening rule
χ	$(L-z)/\sqrt{D_{m,l}t_l}$; Dimensionless length parameter
Δ	Detachment of the liner pipe from the outer pipe, normalised by t_l
Δ_0	Initial imperfection amplitude of the liner pipe, normalised by t_l
Δ_{cr}	Normalised detachment of the liner pipe at κ_{cr}
δ_{ij}	Kronecker delta
Δ_r	Residual imperfection amplitude of the liner pipe after the manufacturing process, normalised by t_l
$\dot{\lambda}$	Plastic multiplier
$\dot{\mu}$	Material parameter depending on equivalent plastic strain; Ziegler's kinematic hardening rule
ε	$= \varepsilon^e + \varepsilon^p$; Total strain
ε^e	Elastic strain
ε_{ij}^e	Elastic strain tensor components
ε^p	Plastic strain

ε_{ij}^{p}	Plastic strain tensor components
ε_b	$= D_o/(2R_{reel}+D_o)$; Global bending strain
ε_{cr}	$= D_o/2\rho_{cr}$; Global bending strain at κ_{cr}
$\varepsilon_{h,M}$	Mechanical hoop strain of the liner pipe
$\varepsilon_{h,Tot}$	$= \varepsilon_{h,T}+\varepsilon_{h,M}$
ε_{ij}	$= \varepsilon_{ij}^{e}+\varepsilon_{ij}^{p}$; Total strain tensor components
$\varepsilon_{min,max}$	Minimum and maximum strain of a stress-controlled cyclic response
ε_n	Lüders strain, corresponding to the end of plastic plateau
$\varepsilon_{o,n}$	Strain of the outer pipe material at the end of plastic plateau
ε_p	Equivalent or accumulated plastic strain
ε_r	$= (\varepsilon_{max}+\varepsilon_{min})/2$; Average strain
$\varepsilon_{y,o}$	Yield strain of the outer pipe, corresponding to plastic plateau initiation
γ^q	$q = 1,...,M$; Rate of decrease of hardening of Chaboche's non-linear kinematic hardening rule
κ	$= k_r/k_o$; Normalised curvature
κ_{cr}	Curvature value where the liner pipe buckles locally
κ_{res}	Residual normalised curvature
λ_c	$= \pi\sqrt{R_{m,l}t_l}/[12(1-\nu^2)]^{1/4}$; Half-wavelength of a circular shell under uniform compression, considering elastic material
ν	Poisson's ratio
Ω	Plastic potential
ω	Rotation angle of the reel
ϕ	Applied rotation at lined pipe's cross-section
ρ_{cr}	Radius of curvature of the pipe neutral axis at κ_{cr}
σ	Stress

$\sigma_{\theta 0}$	Hoop stress of the liner pipe at maximum compression ($\theta = 0$) under monotonic bending
σ_{θ}	Hoop stress
σ_{ij}	Cauchy stress tensor components
$\sigma_{pr,l}$	Proportional limit of the liner pipe
σ_{res}	Residual hoop compressive stress of the liner pipe after the manufacturing process of the lined pipe
σ_{UTS}	Ultimate tensile stress
σ_{x0}	Axial stress of the liner pipe at maximum compression ($\theta = 0$) under monotonic bending
σ_{x}	Axial stress
$\sigma_{y,l}$	Yield stress of the liner pipe at 0.2% residual plastic strain
$\sigma_{y,o,n}$	Stress of the outer pipe material at the end of plastic plateau
$\sigma_{y,o}$	Yield stress of the outer pipe
σ_{y}	Uniaxial yield stress
θ	Angle around the circumference of the cross-section
ζ_{l}	$= (D_{m,l,h} - D_{m,l,v})/D_{m,l}$; Ovalization of the liner pipe cross-section
ζ_{o}	$= (D_{m,o,h} - D_{m,o,v})/(D_{m,o,h} + D_{m,o,v})$; Ovalization of the outer pipe cross-section
b	Material constant defining the rate of hardening
b_i	$i = 1, ..., 6$; Fitting parameter
c	Material constant of Prager's linear kinematic hardening rule
C^q	$q = 1, ..., M$; Hardening moduli of Chaboche's non-linear kinematic hardening rule
C_{ijkl}	Fourth order elasticity tensor components
D_l	Outside diameter of the liner pipe

$D_{m,l,h}$	Deformed horizontal mean diameter of the liner pipe
$D_{m,l,v}$	Deformed vertical mean diameter of the liner pipe
$D_{m,l}$	$= D_l - t_l$; Mean diameter of the liner pipe
$D_{m,o,h}$	Deformed horizontal mean diameter of the outer pipe
$D_{m,o,v}$	Deformed vertical mean diameter of the outer pipe
$D_{m,o}$	$= D_o - t_o$; Mean diameter of the outer pipe
D_o	Outside diameter of the outer pipe
E	Young's modulus
E_l	Young's modulus of the liner pipe
$E_{o,h,p}$	$= (\sigma_{y,o,n} - \sigma_{y,o})/(\varepsilon_{y,o,n} - \varepsilon_{y,o})$; Tangent modulus of the plastic plasteau of the outer pipe material
$E_{o,h,s}$	Initial tangent modulus after the end of the plastic plateau of the outer pipe material
E_o	Young's modulus of the outer pipe
F	Yield function
F_p	$= P_{in}\pi(D_l - 2t_l)^2/4$; Capped-end axial force due to internal pressure
G	Shear modulus
g_0	Initial radial gap between the liner and the outer pipe, normalised by t_l
g_r	Residual radial gap at the end of the manufacturing process, normalised by t_l
$h_{o,p}$	$= E_{o,h,p}/E_o$; Normalised tangent modulus of the outer pipe material
$h_{o,s}$	$= E_{o,h,s}/E_o$; Normalised initial tangent modulus of the outer pipe material
h_w	Wrinkle height of the liner pipe
I_1, I_2, I_3	Invariants
$IMP - i$	$i = 1, 2$; Types of liner pipe geometric imperfections
J_2, J_3	Invariants of the deviatoric stress tensor

K	Bulk modulus
k	Hardening parameter corresponding to the yield surface size
k_o	$= t_o/D_{m,o}^2$
k_r	$= \phi/L$; Curvature
L	Length of the lined pipe segment
$l_1, l_2, ..., l_m$	m material constants
L_{hw}	Half-wavelength
l_{hw}	$= L_{hw}/\sqrt{D_{m,l}t_l}$; Normalised half-wavelength
m	$= M_{Total}/M_o$; Normalised bending moment of the lined pipe
M_l	Bending moment of the liner pipe
m_l	$= M_l/M_o$; Normalised bending moment of the lined pipe
M_{Total}	Bending moment of the lined pipe
n	Ramberg-Osgood fitting parameter
N_{ij}	Unit vector, normal to the yield surface
n_o	$= (\varepsilon_{o,n} - \varepsilon_{y,o})/\varepsilon_{y,o}$; Dimensionless length of the plastic plasteau of the outer pipe material
p	$= P_{in}/P_{y,l}$; Normalised internal pressure
P_{in}	Internal pressure
$P_{y,l}$	$= 2\sigma_{y,l}t_l/D_{m,l}$; Yield pressure of the liner pipe
$P_{y,o}$	$= 2\sigma_{y,o}t_o/D_{m,o}$; Yield pressure of the outer pipe
Q	Material constant defining the saturated value of hardening
$R_{aligner}$	Radius of aligner
R_l	$= D_l/2$
R_{reel}	Radius of reel
RPL	Reverse plastic loading

s_{ij}	$= \sigma_{ij} - (I_1/3)\delta_{ij}$; Deviatoric stress tensor components
$SEG-i$	$i = A, B, C, D$; Lined pipe segments
SFP	Snug-fit pipe
T_i	Initial temperature
$t_{l,i}$	$i = A, B, C, D, E, F$; Different wall thickness values of the liner pipe
T_l	Temperature of the liner pipe
t_l	Wall thickness of the liner pipe
T_o	Temperature of the outer pipe
t_o	Wall thickness of the outer pipe
T_p	$= \sigma_{y,o}\pi D_{m,o}t_o$; Yield tension of the outer pipe
TFP	Tight-fit pipe
$TFP\ FH$	Tight-fit pipe fully heated
$TFP\ PH$	Tight-fit pipe partially heated
z	Direction along the lined pipe in three-dimensional space

Chapter 1

Introduction

Onshore and offshore pipelines constitute a common and reliable means of transporting a variety of fluids, such as hydrocarbons, chemicals or water. Over the last decades, the interest in offshore pipelines transporting hydrocarbons has increased significantly, continuously creating new challenges for pipeline installations exceeding the two thousand meters of water depth.

1.1 S-lay and J-lay installation methods

Two common offshore installation methods are S-lay and J-lay, referring to the shape of the pipeline from sea level to the seabed during installation, as shown in Figure 1.1. In the case of S-lay method, the line pipe segments are stored on the vessel, welded, inspected and coated offshore, and installed gradually, while the vessel moves. The pipeline is held by the tensioners and it is bent over the stinger before enters the sea water. In general, the pipeline is installed empty, considering a relatively small angle at which the pipeline leaves the stinger, reducing the required applied tension and the corresponding cross-sectional ovality of the pipe (Dyau and Kyriakides, 1992; Kyriakides *et al.*, 1994). Under these loading conditions, the pipeline is deformed elastically during the installation. For deep-water applications, the applied tension increases, while a much longer stinger is required to reduce the horizontal tensile force. The combination of high tension and stinger curvature deforms plastically the pipeline, while it is bent on the stinger. (Yun *et al.*, 2004). Therefore, S-lay is more suitable installation method in swallow and intermediate depth water up to one thousand meters (Kyriakides and Corona, 2007)and pipes with diameters up to thirty inches.

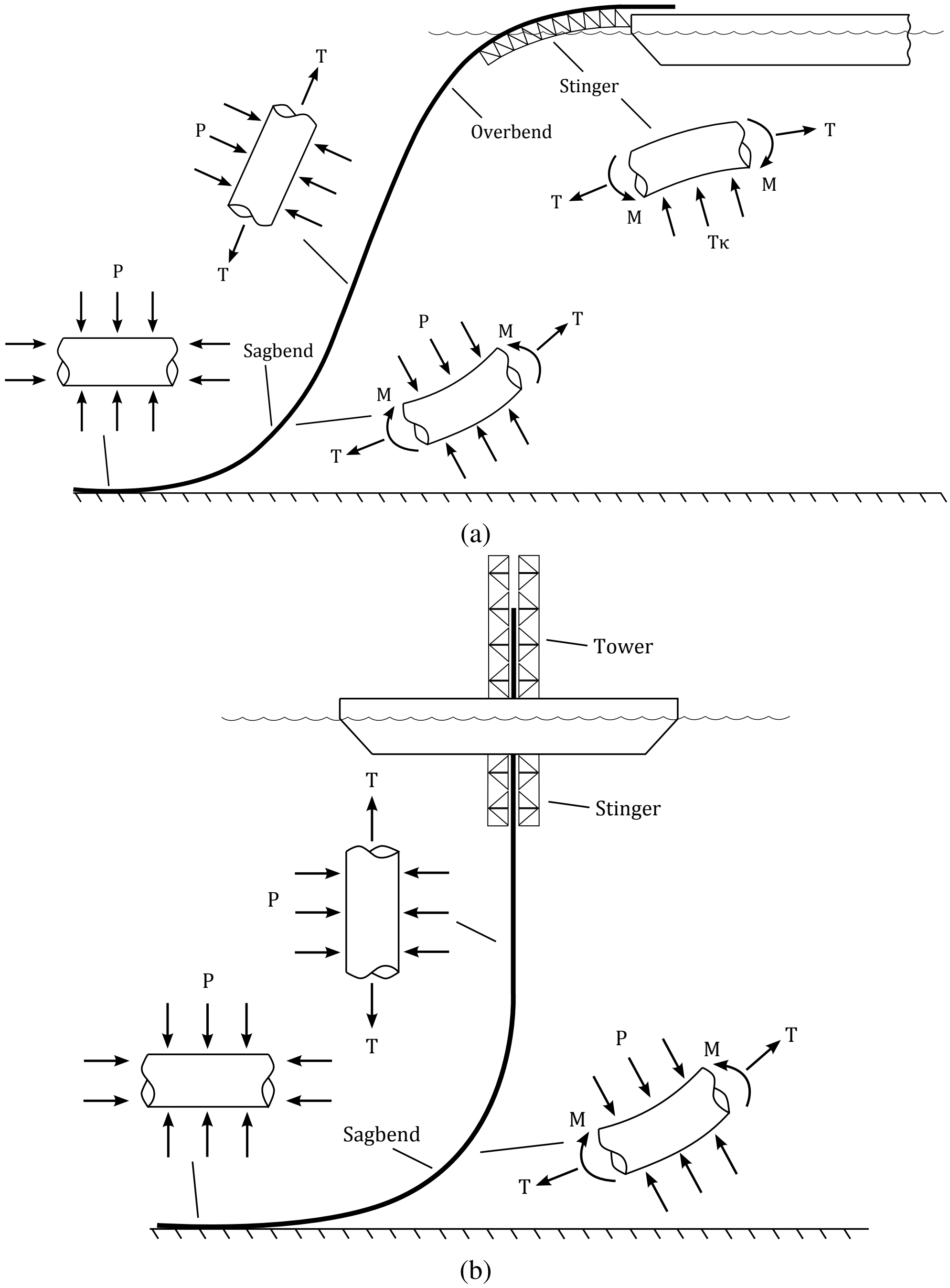

Figure 1.1 Schematic representation of (a) S-lay and (b) J-lay pipeline installation and associated loading conditions.

The J-lay is more suitable installation method for deeper water. In J-lay, the pipeline leaves the vessel from a nearly vertical position, as shown in Figure 1.1b. During this method, pre-welded pipe segments are raised into the tower, where they are welded to the free end of the pipeline, the welds are inspected, coated and then lowered the vessel gradually moves. Initially, the pipeline is under axial tension, while once the pipeline leaves the vessel, external pressure gradually increases with increasing the water depth. Approaching the seabed, the pipeline is subjected to combined loading under tension, bending and external pressure. Therefore, the pipe reaches its maximum deformation at sagbend. This method is capable of installing pipelines in water depths that exceed three thousand meters, due to the shorter suspended pipeline length resulting in reduced required lay tension. Both methods are presented in more detail in the book by Kyriakides and Corona (2007).

1.2 Bending of pipelines

During the deep-water installation with S-lay or J-lay, the pipeline is subjected to severe bending, so that significant stresses and strains are developed in the pipeline wall, associated with cross-sectional ovalisation. At the sagbend region, near the seabed, where the bending load is combined with tension and external pressure, the pipeline may buckle or “collapse”, as commonly mentioned (Kyriakides and Corona, 2007). Significant research has been conducted and several tools have been developed to describe the mechanical behaviour of single-walled pipes under combined loading conditions.

Bending of a thin-walled cylinder results in cross-sectional ovalisation, which also leads to loss of bending stiffness in the form of limit point instability, as shown in Figure 1.2. This phenomenon is called “ovalisation instability”. Brazier (1927) investigated the non-linear bending response of initially straight thin-walled pipes, resulting in a trigonometric solution for the cross-sectional displacement and a quadratic expression for the ovalisation, with respect the applied curvature. More specifically, the ultimate bending moment and the corresponding curvature were expressed as:

$$M_{Br} = 0.987 \frac{ERt^2}{\sqrt{1-\nu^2}} \quad \text{and} \quad k_{Br} = 0.471 \frac{t}{R^2\sqrt{1-\nu^2}} \tag{1.1}$$

where E is the Young’s modulus, t is the wall thickness, R is the radius of the cylinder, and ν is the Poisson’s ratio. Aside to ovalisation of initially straight tubes, von Karman (1911) investigated the ovalisation of elastic initially curved tubes, considering inextensional cross-section and negleting non-linear terms. A linear relationship was provided between the cross-sectional ovalisation and the applied curvature, as a function of geometric parameters. Additional work has been conducted by several researchers (Gross, 1953; Gross and Ford, 1953; Pardue and Vigness, 1951), developing design formulae for flexibility and stress concentrations and accounting for the effect of pressure. Furthermore, Reissner (1959) investigated ovalisation instability of initially straight and initially curved pipes, using non-linear ring kinematics and accounting for the effect of pressure, while Reissner (1961) examined the ovalisation instability of initially straight pipes, considering two independent variables; the rotation of the cross-section reference line and a stress function. Additionally, a non-linear formulation for the ovalisation instability of tubes under bending has been investigated by Axelrad (1961, 1962), based on an non-linear flexible shell theory. Initially straight and initially bent tubes were considered, accounting also the effect of pressure. More recently, Karamanos (2002) presented a detailed numerical study, investigating instabilities of long thin-walled elastic tubes. Both initially straight and initially bent tubes were analysed under in-plane bending, while it has been shown that the interaction between ovalisation instability and bifurcation instability depends on the value and the sign of the initial tube curvature.

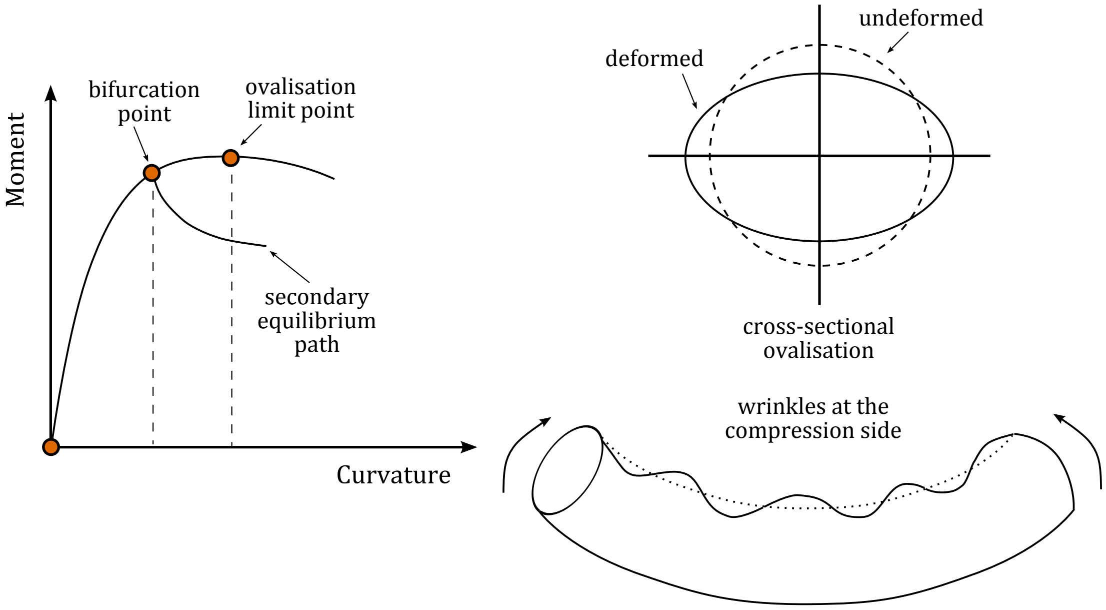

Figure 1.2 Schematic representation of ovalisation and bifurcation instability.

Bifurcation instability of tubes subjected to bending is a phenomenon more pronounced in long cylinders, free of boundary conditions. During bending, axial stresses increase at the compression side. At a certain stage of deformation, bifurcation instability (buckling) occurs forming longitudinal short-wave “wrinkles”, as shown in Figure 1.2; this usually happens before reaching the limit point, which corresponds to ovalisation instability. Therefore, two different formulations can be employed to analyse those two instabilities. Considering a cross-sectional ovalisation analysis, which can be also assumed as a generalised plane strain problem, buckling phenomena are excluded, leading to a maximum moment due to ovalisation. On the other hand, assuming three-dimensional analysis, a secondary equilibrium path is followed, before the limit point is reached in the ovalisation equilibrium path.

Bifurcation instability was investigated in an early stage by Brazier (1927). Seide and Weingarten (1961) attempted to predict the bending buckling of thin-walled elastic cylinders, concluding that the buckling moment of a cylinder under bending corresponds to a nominal stress similar to the buckling stress of a cylinder with the same radius under uniform compression. However, the formulation did not account for cross-sectional ovalisation of the tube on the post-buckling state. Therefore, this analysis can be used for short tubes with restrained ends, while it predicts unrealistic buckling moments for long tubes free to ovalise. Following the previous formulation, Axelrad (1965) introduced the so-called "local buckling hypothesis", considering the effects of the ovalised pre-buckling configuration of the tube. Axelrad (1965) assumed that buckling is determined by stress and strain inside the zone of the initial buckle. According to this assumption, buckling will occur when the maximum compressive stress reaches the uniform compressive critical value for a circular tube of radius equal to the local radius of the ovalised shell at the critical point. This point usually corresponds to the most extreme fiber of the compressive zone of the tube. Furthermore, Stephens *et al.* (1975) examined bifurcation instabilities of initially straight tubes, considering a non-linear shell analysis. Bifurcation moments were reported assuming a pre-buckling ovalisation of the tube, while the effect of pressure and the boundary conditions were also examined. It was shown that in case of bending of unpressurised long tubes, buckling occurs before the limi point is reached. This was also observed by Fabian (1977), investigating the buckling behaviour of elastic thin-walled initially straight tubes under the combination of bending and external pressure.

The bending response of relatively thick-walled elasto-plastic steel tubes, motivated by offshore pipeline applications, has been reported by Kyriakides and Shaw (1982), using analytical cross-sectional models based on an inextensional non-linear theory (Brush and Almroth, 1975), while the effect of external pressure has been also investigated. Subsequently, Shaw and Kyriakides (1985) and Corona and Kyriakides (1988) proposed an improved formulation, relaxing the inextensionality condition and allowing for large changes of hoop curvature. A numerical verification of those analytical results has been reported by Karamanos and Tassoulas (1991). It has been shown though that such a cross-sectional analysis may not lead to representative bending results of steel tubes, considering diameter-over-thickness ratio (D/t) higher than about forty five. In this case, the tube exhibits wall wrinkles leading to local buckling, before reaching the ovalisation limit moment, as shown in the work by Ju and Kyriakides (1992). Therefore, a three-dimensional analysis is required to model this structural response. Additional experimental and numerical work has been conducted by (Karamanos and Tassoulas, 1996*a*,*b*; Netto and Estefen, 1994), examining the structural response of tubes under monotonic bending and external pressure, while (Limam *et al.*, 2010) examined the effect of internal pressure accounting for operational conditions. Furthermore, experimental and analytical study of the response of pipelines under combined external pressure, bending and tension loads has been presented by Kyriakides *et al.* (1989), accounting for loads during the offshore installation, as shown in Figure 1.1. These tools can be used to ensure structural stability of thick-walled pipes and are summarised in the book by Kyriakides and Corona (2007).

More specifically, Kyriakides and Corona (2007) presented in detail the mechanics of inelastic bending of thick-walled steel tubes and the associated limit states. Shaw and Kyriakides (1985) expressed the formulation of inelastic pure bending, adopting more general kinematics than the one presented by Ades (1957) and Gellin (1980). Furthermore, Kyriakides and Corona (2007) extended further the formulation including more general initial geometric imperfections and wall thickness variations, while factors that also influence the limit state, such as yield anisotropy and residual stress fields, were also presented. Considering the combined loading conditions, that the pipeline is subjected during the deep-water installation, Kyriakides and Corona (2007) presented in detail the mechanics of inelastic bending of steel tubes in the presence of external pressure or under axial tension and the associated limit states. Several of the limit states, included in the aforementioned book by Kyriakides and Corona (2007), are also addressed in offshore pipeline design standards, such as API RP 1111 (1999); BS 8010-2:2004 (2004); DNV-OS-F101 (2013); ISO 13623 (2000), providing simplified design formulae.

More recently, extensive numerical work has been conducted on the structural stability of thin-walled elastic cylinders. Rotter *et al.* (2014) presented detailed numerical results on the effect of cylinder length on the non-linear elastic buckling under bending loading, considering both clamped ends. Furthermore, Fajuyitan and Sadowski (2018) examined the effect of geometric imperfections, accounting for linear buckling eigenmode, cross-sectional ovalisation and local defect due to welding, while Xu *et al.* (2017) presented numerical results on the bending response of cylinders with elliptical cross-sectional shape. Sadowski and Rotter (2013) investigated the non-linear plastic buckling behaviour of thick-walled tubes under bending, using different numerical modelling approaches. Several diameter over thickness ratios have been examined using either solid continuum finite elements or shell finite elements, showing the computational efficiency and the reasonable results considering shell elements. Wang *et al.* (2018) examined the influence of cross-sectional ovalisation under bending in the inelastic range, showing negligible influence on moment resistance decrease of thick-walled tubes. Furthermore, a detailed experimental and numerical work, presenting the four-point bending response of spiral-welded steel tubes, has been reported by van Es *et al.* (2016); Vasilikis *et al.* (2016). Tubes with several diameter over thickness ratios have been considered, while the influence of material properties, geometric imperfections and residual stress on local buckling has been reported. In a subsequent paper, Papadaki *et al.* (2018) investigated the influence of internal pressure during bending of spiral-welded steel pipes, while the stress-strain state of a spiral-welded pipe has been applied as initial condition on the pressurised numerical model, and Chatzopoulou *et al.* (2019) simulated the spiral-forming process accurately, and examined the influence of the pipeline fabrication process on the bending response under internal and external pressure.

1.3 Reeling installation process

The main deficiency of these two methods (S-lay and J-lay) refers to welding process. More specifically, welding and inspection should be performed on the lay barge. On the other hand, “reeling” installation method has been recognized as an efficient method for installing steel pipelines of diameter up to sixteen inches (Kyriakides and Corona, 2007). The major advantages of this method are the high production and laying rates, and the high quality of welding and inspection conditions which are conducted onshore. Reeling also consists an efficient installation method for swallow and deep waters.

However, in this method, the pipeline is subjected to two severe plastic bending cycles, as shown schematically in Figure 1.3a, while the bending strains are in well into the plastic range ($\sim 2\%$). First, the pipe line girth welds are performed onshore, forming a several kilometers long pipeline, followed by winding onto a large drum on the reeling vessel (⓪→①). Once the installation location is reached, the pipeline is unwound (①→②) as the vessel moves, with the corresponding configuration of the Figure 1.3b. Subsequently, the pipe is bent around the aligner (②→③), followed by pipe straightening and its reverse bending to eliminate the residual curvature due to plastic bending on the reel and aligner (③→④). In the final stage of reeling, the pipe is straightened, leaves the vessel and enters the water (④→⑤). However, in case where a serious defect is detected, the installation process is stopped so that the pipe is repaired. In this case, the pipe line is spooled and unspooled again passing through the aligner, reel and the straightener adding three bending cycles until the pipeline leaves the vessel. The installation speed of this process (up to two knots) and the onshore fabrication of the long pipeline segment provides significant time and cost reduction, compared with S-lay or J-lay method.

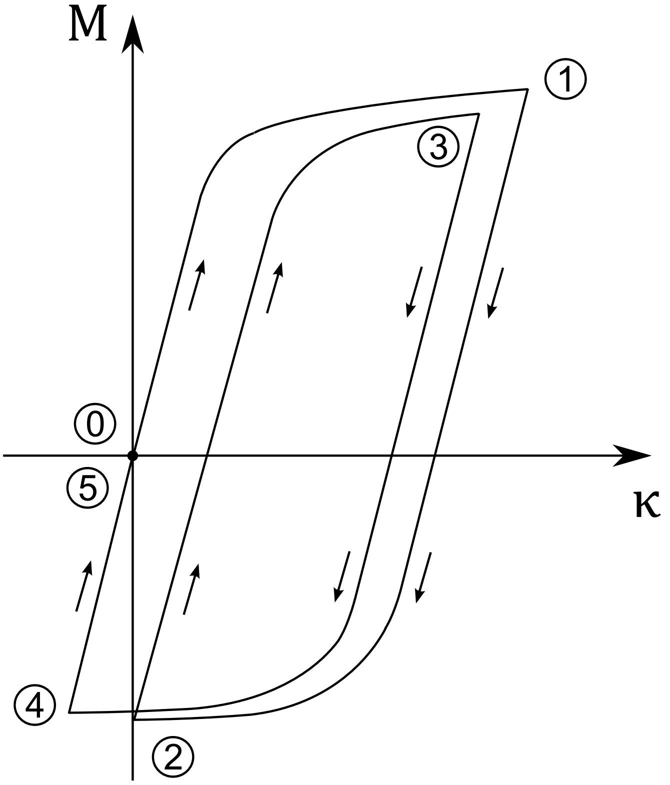

(a)

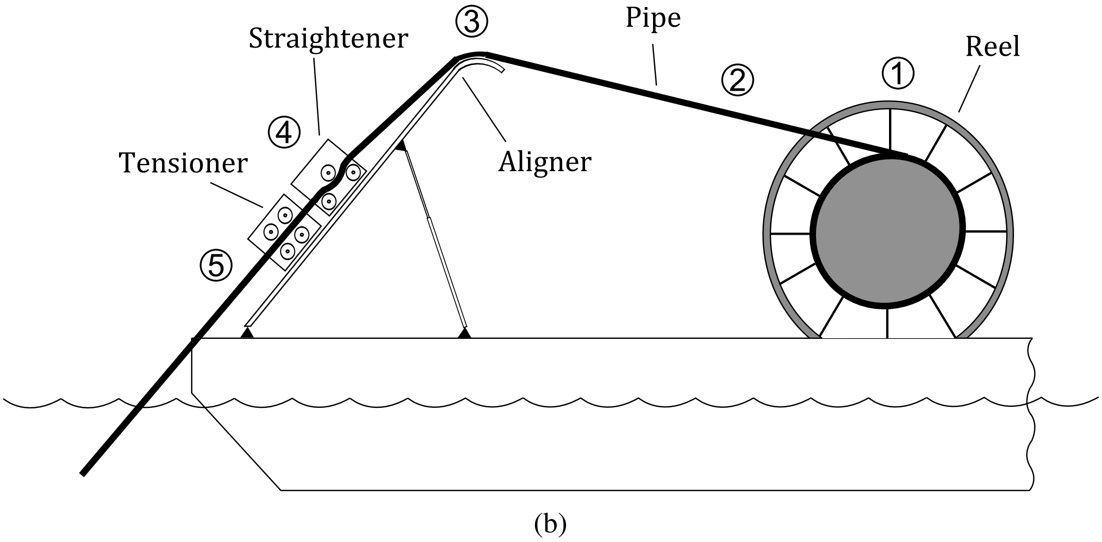

(b)

Figure 1.3 Schematic representation of (a) moment-curvature diagram during the reeling process, (b) a reeling pipeline vessel, showing the location of different stages of bending.

The influence of cyclic plastic deformation during reeling on the collapse pressure of single-walled pipes has been investigated in previous theoretical and experimental works (Estefen, 1999; Nagata and Tsuru, 2016; Pasqualino and Neves, 2010; Pasqualino *et al.*, 2004), and identified the importance of reeling-induced ovalisation of the cross-section on the ultimate strength of the pipe. Martinez and Brown (2005) and Karjadi *et al.* (2015) examined the change of pipe properties due to reeling-induced plastic deformations, through experimental tests and numerical analyses, and reported a dependence of the value of calculated ovalisation of the pipe, on the plasticity model considered. Furthermore, Brown *et al.* (2004) presented a method calculating the minimum reelable wall thickness of a pipe, considering also the mismatch of adjacent pipe ends, causing significant localised deformation, while the effect of reel on the different limit states (burst, collapse, fracture) of pipeline design has been examined by Manouchehri *et al.* (2008).

In addition, the effect of reeling installation on pipe material properties, such as microhardness and toughness, has also been investigated by Meiwes *et al.* (2014*a*,*b*); Shitamoto and Hisamune (2013); Shitamoto *et al.* (2014), using full-scale and small-scale experiments, while Tsuru *et al.* (2016) presented experimental tests supported by numerical simulations. Marines-Garcia *et al.* (2016) also examined the sour strength of pipes after small scale and full scale reeling compared with as-received pipes. Subsequently, fatigue qualification tests have been presented by Gray *et al.* (2009), while the fatigue performance, due to the presence of welding defects, and the fatigue crack growth rate behaviour of welded pipes in air and sour environment, have been examined by Netto *et al.* (2008*a*,*b*) and Thodla *et al.* (2015*a*,*b*), respectively.

Furthermore, the reeling influence on pressure collapse of a pipe has been reported in a recent work by Liu and Kyriakides (2016), while the effect of geometric and material properties of the pipe and reeling parameters on the reeling performance of a pipeline have been examined by Liu *et al.* (2015) and Liu and Kyriakides (2017). More specifically, Liu *et al.* (2015) investigated the structural response of pipelines exhibiting Lüders banding during reeling; this is a material instability associated with unpinning of dislocations from nitrogen and carbon atmospheres (Cottrell and Bilby, 1949; Hall, 1970), continuing the work conducted by Hallai and Kyriakides (2011*a*,*b*) on the monotonic bending of steel tubes. Moreover, small-scale experiments (Focke *et al.*, 2006; Kyriakides, 2017) and recent numerical simulation works (Chatzopoulou *et al.*, 2016*a*; Liu *et al.*, 2017) have reported the evolution of mechanical properties and cross-sectional ovalisation during reeling and compared the collapse pressure of reeled with unreeled pipelines.

1.4 Double-walled (bi-metallic) pipes

In many cases, hydrocarbon mixtures are conveyed in high pressure, temperature and may also contain several corrosive ingredients, such as hydrogen sulphide (H_2S) or hydrogen chloride (HCl), carbon dioxide (CO_2) and water (H_2O), which result in pipeline corrosion, causing failure with significant environmental and economical impact. In order to ensure the structural integrity of the pipeline against corrosion, bi-metallic pipes are produced, containing a thick-walled low-alloy carbon steel (“outer pipe”) providing strength, and a thin layer (“liner pipe”) from a corrosion resistant alloy (CRA) material, which is fitted inside the outer pipe, resulting in a cost effective solution instead of producing pipelines from stainless steel or nickel alloy. A bi-metallic pipe could be either metallurgically bonded (also called “clad pipe”), as described by several manufacturers (Chakravarti, 2004; Osborn and Worringer, 1999; Satoh *et al.*, 1996; Schulz *et al.*, 1999) patenting alternative methods to produce clad pipes, or mechanically bonded (referred to as “lined pipe”), where the liner pipe is in hoop compression due to confinement by the outer pipe (also called “gripping force” between both pipes). In this work, the research is conducted considering lined pipes which is shown in Figure 1.4, while in the following paragraphs different manufacturing processes of lined pipes are presented.

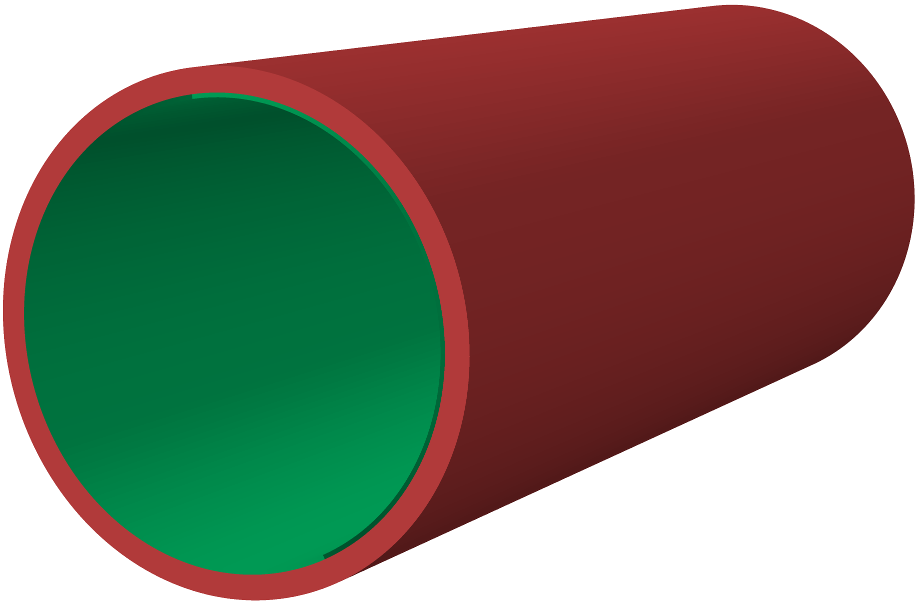

Figure 1.4 Visualization of a lined pipe.

1.4.1 Mechanically lined pipes

Lined pipes can be fabricated by a purely mechanical manufacturing process (Yoshida *et al.*, 1981), or by a thermo-mechanical process, called “TFP” (tight-fit pipe), as explained in detail by De Koning *et al.* (2004). The former method results in hoop compression of the liner and mechanical bonding of the two pipes, whereas in the latter method, bonding of the lined bi-metallic pipe depends on the amount of expansion of the two pipes. Experimental work, investigating the corrosion resistance and sustainability between metallurgically and mechanically bonded pipes in sour environment, was conducted by Chen and Petersen (1991) indicating deterioration of the corrosion performance of the metallurgically bonded pipes due to heat treatment. Additional experimental results are published on the corrosive performance of thermo-hydraulically expanded lined pipes, for different liner pipe materials, in a period of exposure (Kane *et al.*, 1991).

The manufacturing process of hydraulically expanded lined pipes has also been simulated analytically (Dezhi *et al.*, 2014; Guo *et al.*, 2017; Liu *et al.*, 2004; Wang *et al.*, 2005; Xuesheng *et al.*, 2004). In these works, the problem was solved as two-dimensional, assuming for simplicity (a) hydraulic expansion of both pipes up to a final elastic deformation in the outer pipe, (b) elastic perfect-plastic liner material, and (c) a relatively small-initial radial gap of both pipes in order to achieve mechanical bonding after the depressurization. These analyses result in analytical expressions of the contact pressure of both pipes after the manufacturing process, with respect to the applied internal pressure. However, in such a manufacturing process, a residual radial gap has been reported by industrial suppliers in the lined pipe after the depressurization, in contrast with previous publications (Sriskandarajah *et al.*, 2013*a*,*b*) referring to mechanical bonding of elastically expanded lined pipes. In addition, the effect of different temperature level of the lined pipe, due to the operational conditions, on contact pressure of lined steel pipes was investigated by Zeng *et al.* (2014). Furthermore, analytical expressions for the diameter change and the hoop stress in the liner, at the end of each step of the thermo-hydraulic manufacturing process, have been presented by Focke *et al.* (2004) assuming plane strain conditions with bi-linear stress-strain response of the liner pipe, and have been compared with numerical results.

1.4.2 Structural response of lined pipes

Extensive experimental work has been conducted by Focke (2007) presenting the initiation of detachment of the liner pipe from the outer pipe, leading to liner wrinkling and cross-section ovalisation of the pipe under monotonically increasing bending conditions, while the outer pipe is still structurally stable. These wrinkles are an impediment to the internal flow, might block pipeline pigging equipment, and could lead to fatigue cracks because of local stress concentrations under repeated loading (Dama *et al.*, 2007). Numerical results on liner wrinkling under axial compression have been reported by Hilberink *et al.* (2010*a*,*b*), while Hilberink *et al.* (2011) and Hilberink (2011) investigated the influence of friction and mechanical bonding of lined pipes, comparing also the results with experimental data from four-point bending tests. Furthermore, Montague *et al.* (2010) and Wilmot and Montague (2011) presented experiments on bending of heated lined pipes, while a detailed numerical study on the mechanical behaviour of a lined pipe under monotonic bending has been presented by Vasilikis (2012); Vasilikis and Karamanos (2012, 2013). This study identified two sequential bifurcation stages associated with liner wrinkling, and examined the effect of several geometric and material parameters. In those publications, the manufacturing process is considered by applying an initial compressive hoop stress on the model to simulate with a simpler manner the residual stresses induced by the manufacturing process and result on the final mechanical bonding. This assumption does takes into account the effects of the manufacturing process on the material properties and the corresponding severe plastic deformation of the liner pipe in an indirect manner, which is addressed in detail in the present work.

Further numerical analyses on monotonic bending of lined pipes have been reported by Yuan and Kyriakides (2014*a*, 2015), accounting for weld discontinuities on the structural integrity. In those works, the manufacturing process was simulated using a separate axisymmetric model, while the obtained stress-strain state of each pipe is averaged through its thickness and is inserted as initial condition in the bending finite element model. In addition, Tkaczyk and Pepin (2014) proposed analytical expressions for calculating the minimum wall thickness of the liner pipe to prevent local buckling. A practical method of delaying liner wrinkling and buckling is the application of relatively high levels internal pressure during reeling, proposed in a series of relevant patents (Endal *et al.*, 2012; Howard and Hoss, 2016; Mair *et al.*, 2013). The internal pressure corresponds to 30 *bar* (3 *MPa*), which is approximately equal to 50% of the plastic pressure of the liner pipe.

The beneficial effect of internal pressure on monotonic bending has also been noticed in the works by Yuan and Kyriakides (2014*a*, 2015). The bending response of a lined pipe in the presence of internal pressure was investigated systematically in the present work, and the results indicated that low or moderate levels of pressure, up to 10% of the plastic pressure of the liner pipe, are capable of preventing liner pipe detachment from the outer pipe and the formation of local buckling. More recently, Yuan and Kyriakides (2020) reported numerical results on the gradual spooling process of a lined pipe on a curved rigid surface, and the effect of different manufacturing processes (purely mechanical and thermo-mechanical) on monotonic bending response of a lined pipe is examined in the current research.

The above studies focused on monotonic bending of lined pipes. On the other hand, the cyclic response of lined pipes has received much less attention. Cyclic experiments on lined pipes have been reported by Tkaczyk *et al.* (2011), and presented the progressive liner detachment from the outer pipe over the cycles. In addition, Sriskandarajah *et al.* (2013*b*); Toguyeni and Banse (2012); Toguyeni *et al.* (2013) presented experimental results on the cyclic response of a lined pipe in the presence of high levels of relatively internal pressure (50% of the plastic pressure of the liner pipe), presenting its beneficial effect on liner wrinkling. However, despite the above works a thorough investigation on the cyclic performance of a lined pipe, monitoring the development and evolution of liner wrinkling at each cycle, including the influence of geometric, material and loading parameters, and the effect of moderate levels of internal pressure, is an open research issue.

1.5 Cyclic bending of tubes

Previous publications have demonstrated that cyclic loading of a single-wall pipe, within the safe range determined by monotonic loading conditions, causes the accumulation of plastic deformation, and this may result in local buckling failure. More specifically, Shaw and Kyriakides (1985) presented a formulation of a long tube cycled in pure bending into the plastic range, predicting the growth of ovalisation over the cycles, employing different non-linear hardening plasticity models. Pan *et al.* (1998) presented an apparatus for measuring experimentally the cross-sectional ovality and curvature of tubes, under cyclic bending tests. Experimental results have been presented by Corona and Kyriakides (1991), showing the effect of cyclic plastic bending on cross-sectional ovalisation accumulation of tubes, leading to local buckling. Different cyclic loading histories have been examined, such as curvature symmetric bending, bending about a mean curvature value, and moment-controlled bending about a moment mean value, while the strong influence of external pressure on increasing the accumulation of ovalisation has also been shown. More recently, Elchalakani *et al.* (2004) performed cyclic inelastic experimental tests of cold-formed circular hollow sections (CHS), simulating different amplitude earthquake-type oscillations, establishing slenderness design limits. Experimental and numerical work, investigating axial cyclic compression in the plastic range of tubes, has been conducted by Jiao and Kyriakides (2009, 2010), showing axisymmetric wrinkling of the tube, leading to limit load instability and collapse, while axial cyclic compression of tubed under internal pressure has been investigated by Jiao and Kyriakides (2011*a*,*b*)

Finally, Chang and Pan (2009); Sadowski *et al.* (2020); Varelis and Karamanos (2014) presented experimental and numerical results on the degradation and buckling of circular tubes under cyclic plastic bending, while Zeinoddini *et al.* (2016) proposed a closed-form analytical solution for strain ratcheting of tubes subjected to cyclic inelastic bending. It has also been shown that, under cyclic loading conditions, small geometric imperfections in the pipe wall may grow, leading to local buckling after a number of loading cycles (Jiao and Kyriakides, 2009; Varelis and Karamanos, 2014). It is expected that such a behaviour may also occur in the case of lined pipes under cyclic bending, and that the existence of small imperfections in the liner may have a significant role on cyclic structural performance. For this reason, a pure cyclic bending model is developed in the present work, in order to conduct a more detailed investigation, and a more complex numerical model of reeling installation is considered for more accurate predictions.

1.6 Offshore applications of single-walled and double-walled pipelines

In the present section, several offshore applications of single-walled and double walled pipelines are presented, considering the works discussed in the previous sections on monotonic and cyclic bending of circular tubes. *Medgaz* is a single-walled pipeline project, which transfers natural gas from Algeria to Spain. It was discussed since 1980s and it was completed in 2009 crossing the Mediterranean Sea. The pipeline has been installed in water depths exceeding two thousand meters, while its offshore part is two hundred kilometers length. Another pipeline from the same decade is *Trans-Mediterranean*, joining Tunisia to Sicily and then to mainland Italy. *Blue stream* is also single-walled pipeline, which was constructed in 2003. The pipeline was installed at similar water depth, such as *Medgaz*; it has length more than seven hundred kilometers, and it was the deepest offshore pipeline at time of construction. In addition, the pipeline was installed with the J-lay method, considering the water depth. More recent offshore pipelines projects are the *South Stream* and *Galsi* pipelines. *South Stream* was designed for 2250 water depth with length equal to 1480 kilometers, which was considered the most demanding offshore project to date. Furthermore, *Galsi* pipeline was designed for higher water depth, reaching 2850 meters, pushing further the limit and reaching ultra-deep water depths. A more detailed description of the aforementioned projects has been reported by Kyriakides and Corona (2007), including additional offshore applications of single-walled pipelines, such as *Mardi Gras*, *Independence Trail* and *Jansz & Gorgon* projects.

Furthermore, several offshore applications, where the pipeline was installed using the reeling method, are Na Kika (Kopp *et al.*, 2004), Marlin (Lecomte *et al.*, 2002), Devils Tower (Menier, 2003), Matterhorn (Kavanagh *et al.*, 2004) and K2 (Campbell *et al.*, 2006). Finally, a technologically important project, considering double-walled pipes, is the Guará-Lula NE project in Brazil (Mair, 2012). Mechanically bonded lined pipe steel catenary risers were installed in ultra-deep waters by the reel-lay method.

1.7 Motivation & objectives

During the last years, significant research has been published about the mechanical behaviour of bi-material lined pipes under monotonic bending conditions. Detachment between liner and outer pipe was observed at the compressed side of the structure during bending. Increasing the applied curvature, a first uniform wrinkling of the liner was observed, which occurs at a critical curvature; the liner detaches abruptly after that critical value. Subsequently, increasing further the curvature, a second type of wrinkling occurs, which results in local buckling of the liner. It should be noted that the liner pipe buckles locally in low curvature levels, while the thick-walled outer pipe is still structurally stable. Therefore, local buckling of the liner pipe is considered as a limit state and it is assumed as the performance limit. The presence of a local buckle in the liner pipe may be a threat for structural integrity. Under continuation of pipeline operation, fatigue cracks may appear because of local concentrations of stresses under operational thermo-mechanical loads, leading to corrosion of the outer pipe, resulting in reducing its burst capacity and increasing the possibility of an accident with significant environmental and financial impact. In addition, several studies examined the structural response of a lined pipe in the presence of high levels of internal pressure, showing its beneficial role. On the other hand, a thorough study on the bending response of lined pipes, under relatively low levels of internal pressure, is an open issue, as an attempt to create a cost effective and safe structure. Furthermore, a lot of studies have presented analytical or numerical results about the manufacturing process of lined pipes, considering several assumptions. For this reason, a complete numerical analysis, considering different manufacturing processes provided by industrial suppliers, is necessary, adopting the appropriate material definition, in order to examine how the fabrication process affects the mechanical bonding and the monotonic or cyclic bending response of lined pipes. Finally, single-walled pipeline behaviour during reeling has been extensively investigated. However, the structural response of lined pipes under reeling (cyclic loading) conditions is still an open issue.

The objectives of this doctoral work are listed below:

- Simulate the monotonic bending of lined pipes, under low levels of internal pressure (compared with high pressure levels used in the industry), developing numerical models verified with previously published numerical and experimental results. A liner performance criterion should be established to examine the influence of internal pressure on liner buckling, and the results are compared with the response of non-pressurized lined pipes.

- Simulate different fabrication processes of lined pipes, and investigate their influence on the mechanical bonding of the pipes and liner buckling response under bending.
- Analyse lined pipes under reverse and cyclic loading, accounting for the Bauschinger effect and the plastic strain accumulation on liner wrinkling, and investigate the influence of different parameters, such as different bending strain values, liner pipe wall thickness, and the application of moderate internal pressure level on liner pipe buckling response.
- Develop a full-scale three-dimensional reeling model to investigate the response of a lined pipe in reeling conditions (i.e. contact with reel, back tension force), accounting for internal pressure, liner wall thickness, initial geometric imperfections, to result in reelable lined pipes.

1.8 Outline of thesis

This thesis is divided into five chapters, in addition to the current introductory chapter, while a brief description of each chapter is outlined below:

- **Chapter 2:** Brief review of metal plasticity models
  A brief description of metal plasticity theory fundamentals and the corresponding constitutive models are discussed. The mathematical formulation of an associative plasticity model, considering a von Mises yield surface and different hardening rules, such as isotropic, kinematic and combined, is presented.
- **Chapter 3:** Bending of internally pressurized steel lined pipes
  A three-dimensional model is developed simulating the structural response of non-pressurized snug-fit and tight- fit lined pipes, under monotonically increasing bending. A “failure” or “buckling” criterion is also defined. Ovalisation and buckling analyses are performed, examining the effect of moderate levels of internal pressure during bending, on the liner detachment, in order to prevent local buckling. The bending response is compared with the non-pressurized case using the buckling criterion.

- **Chapter 4:** Influence of manufacturing process on lined pipe monotonic bending
  Different lined pipe fabrication methods are analysed, including purely hydraulic and thermo-hydraulic manufacturing processes, presenting their influence on the mechanical bonding between the outer and the liner pipe. The effect of different manufacturing processes on liner pipe buckling under monotonic bending is investigated, presenting the significance of the plastic deformation in the liner pipe on the structural response.

- **Chapter 5:** Cyclic bending of steel lined pipes
  The mechanical behaviour of mechanically bonded lined pipes is examined under cyclic loading, applying bending conditions motivated by reeling. Using a numerical model, accounting for the manufacturing process in the first part of the analysis and the cyclic performance in the second part, the structural response and the evolution of the liner pipe detachment is monitored. The influence of various parameters, such as different applied curvature ranges, initial imperfections, application of internal pressure and alternative fabrication processes, is investigated.

- **Chapter 6:** Reeling of lined pipes and its influence on liner buckling
  A large-scale three-dimensional numerical model is developed, simulating the structural response of lined pipes during spooling-unspooling on a rigid surface (reel), under the application of back tension force. The effect of contact with the reel, and the application of back tension on cross-sectional ovality and liner pipe buckling is investigated. The influence of pipeline straightening, performed by a three point bending, on liner pipe buckling is examined. A sensitivity analysis of several parameters of the numerical model, such as different reel sizes, geometric imperfections, back tension levels, application of internal pressure, and liner pipe wall thickness values, is investigated.

- **Chapter 7:** Summary, conclusions and recommendations
  In the final chapter, a summary of the research conducted in this work and key findings highlighting the novelty are presented, while some additional perspectives for future work are discussed.

Chapter 2

Brief review of metal plasticity models

2.1 Chapter outline

The present chapter describes briefly the fundamentals of metal plasticity theory and the corresponding constitutive models to be employed in the following chapters. The elasto-plastic response of a material can be described by an initial yield condition, specifying the state of stress for which plastic flow occurs, a flow rule to connect the plastic strain increment with the stress and stress increment, and a hardening rule specifying the change of the yield condition in the course of plastic flow. The chapter presents the mathematical formulation of an associative model, considering also a von Mises yield surface. The isotropic, kinematic and combined hardening rules are discussed, identifying their description in the three-dimensional stress space. For an in depth treatment of plasticity theory for metals and the relevant constitutive models, the reader is referred to the following textbooks Chen and Han (1988); Khan and Huang (1995); Lubliner (2008); Voyiadjis and Yaghoobi (2019). Furthermore, the book by de Souza Neto *et al.* (2011) constitutes an important tool for fundamental and advanced knowledge. Initially, the book presents tensor analysis, continuum mechanics of solids, and the finite element method in solid mechanics, providing basic knowledge to the reader. The book also includes fundamentals of plasticity theory, advanced plasticity models and their computational implementation, while it expands further to large strain theory. Finally, the review article in metal plasticity reported by Chaboche (2008) could be useful, presenting in detail constitutive equations of cyclic plasticity and viscoplasticity. These models were also summarised in the book by Lemaitre and Chaboche (1994).

2.2 Strain additive decomposition

The elasto-plastic behaviour of a metal component during a uniaxial experiment is presented schematically in Figure 2.1. Initially, the material deforms elastically and linearly for the stress up to the initiation of yield at σ_y (point A), while the stress-strain curve slope of this linear part is equal to the elastic modulus E. Increasing further the stress, the slope of the stress-strain curve changes to the elasto-plastic tangent modulus E_T (point B), which is often a much smaller value ($E_T \ll E$).

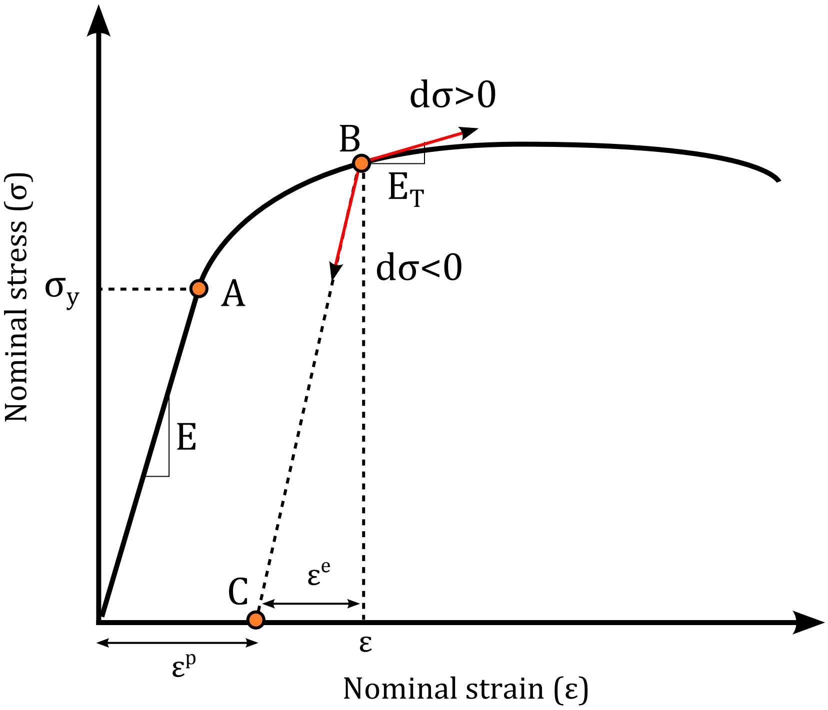

Figure 2.1 Elasto-plastic behaviour of metal component during uniaxial experiment.

During the unloading process (from point B to C), the material follows a path with slope equal to the elastic modulus E. Once the load is removed, the material does not return to its initial state and a residual deformation or plastic strain (ε^p) is observed. The total strain, as shown in Figure 2.1, can be additively decomposed to the elastic part and the plastic part, as follows:

$$\varepsilon = \varepsilon^e + \varepsilon^p \tag{2.1}$$

Assuming the linear elastic relation between the stress and strain (Hooke's law) for the uniaxial experiment in Figure 2.1, the following expression is obtained:

$$\sigma = E\varepsilon^e = E\left(\varepsilon - \varepsilon^p\right) \tag{2.2}$$

The additive decomposition of the total strain can be generalised to the three-dimensional state of strain as follows:

$$\varepsilon_{ij} = \varepsilon_{ij}^{e} + \varepsilon_{ij}^{p} \tag{2.3}$$

where ε_{ij}, ε_{ij}^{e} and ε_{ij}^{p} are the Cartesian components of the total, elastic and plastic strain tensors, respectively, while the equation 2.3 can be described in a rate form, as follows:

$$\dot{\varepsilon}_{ij} = \dot{\varepsilon}_{ij}^{e} + \dot{\varepsilon}_{ij}^{p} \tag{2.4}$$

Furthermore, the uniaxial elastic relationship of the stress and strain, expressed by equation 2.2, can be described in the general three-dimensional case by the following expression where the Einstein convention is followed for repeated indices:

$$\sigma_{ij} = C_{ijkl}\varepsilon_{kl}^{e} = C_{ijkl}\left(\varepsilon_{kl} - \varepsilon_{kl}^{p}\right) \tag{2.5}$$

where C_{ijkl} is the fourth order elasticity tensor components, which for the case of isotropic elastic material are given by the following expression:

$$C_{ijkl} = G\left(\delta_{ik}\delta_{jl} + \delta_{il}\delta_{jk}\right) + \left(K - \frac{2}{3}G\right)\delta_{ij}\delta_{kl} \tag{2.6}$$

and K, G are the bulk and shear modulus, while δ_{ij} is the Kronecker delta.

2.3 Yield criterion

A yield criterion is necessary to determine the stress state of a material at which plasticity initiates. A yield function F can be described by the following expression:

$$F = F\left(\sigma_{ij}, l_1, l_2, ..., l_m\right) \tag{2.7}$$

where σ_{ij} is the Cauchy stress tensor and $l_1, l_2, ..., l_m$ are m material constants. The relationship $F\left(\sigma_{ij}, l_1, l_2, ..., l_m\right) = 0$ defines a yield surface or criterion in the stress space. The shape of the surface is usually convex and defines a subspace of stress states where the material behaves elastically, meaning that $F\left(\sigma_{ij}, l_1, l_2, ..., l_m\right) < 0$. Once the stress state reaches the yield surface, then the material behaves inelastically and the yield surface can translate in the stress space or change its shape, or both.

In case of isotropic materials, the yield surface can be described as a function of the invariants of the stress tensor, such as $F\left(I_1, I_2, I_3\right)$, while the invariants I_1, I_2, I_3 are independent of the coordinate axis rotation.

$$I_1 = \sigma_{kk} \tag{2.8}$$

$$I_2 = \frac{1}{2}\left(I_1^2 - \sigma_{ij}\sigma_{ji}\right) \tag{2.9}$$

$$I_3 = \frac{1}{3}\left(3I_1I_2 - I_1^2 + \sigma_{ij}\sigma_{jk}\sigma_{ki}\right) \tag{2.10}$$

Additionally, it has been demonstrated experimentally that the plastic deformation, in the case of metallic materials, is independent of hydrostatic pressure $\sigma_{kk}/3$ and depends only on the deviatoric stress tensor. Therefore, the yield surface for isotropic metals can be described by the invariants of the deviatoric stress tensor, as follows:

$$F = F\left(J_2, J_3\right) = 0 \tag{2.11}$$

where,

$$J_2 = \frac{1}{2}s_{ij}s_{ji} \tag{2.12}$$

$$J_3 = \frac{1}{3}s_{ij}s_{jk}s_{ki} \tag{2.13}$$

and $s_{ij} = \sigma_{ij} - (I_1/3)\delta_{ij}$ is the deviatoric stress tensor with δ_{ij} the Kronecker delta. Furthermore, a robust, simple and widely used yield surface, such as in the present study in Chapters 3, 4, 5 and 6, is the von Mises (1928) yield criterion, described mathematically by the following expression:

$$F\left(J_2, \sigma_y\right) = \sqrt{3J_2} - \sigma_y = 0 \tag{2.14}$$

where σ_y is the uniaxial yield stress. The von Mises yield surface is shown in principal three-dimensional stress space in Figure 2.2a. However, in case of a plane stress problem (i.e. $\sigma_3 = 0$), the von Mises yield surface becomes an ellipse, as shown in Figure 2.2b.

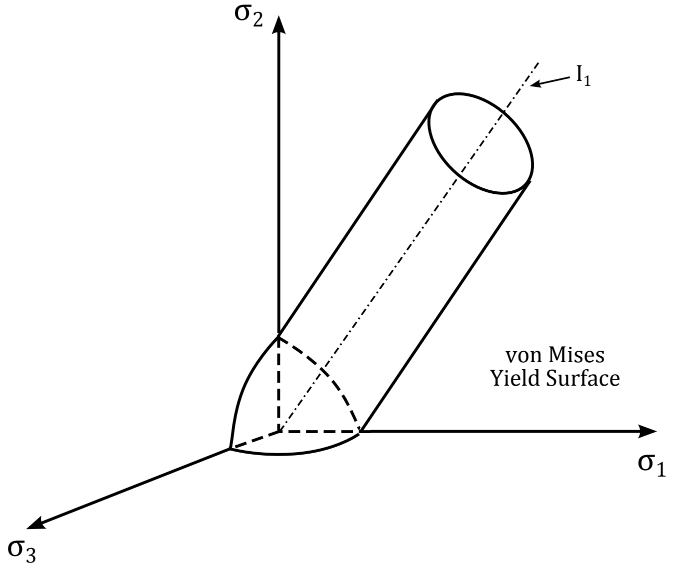

(a)

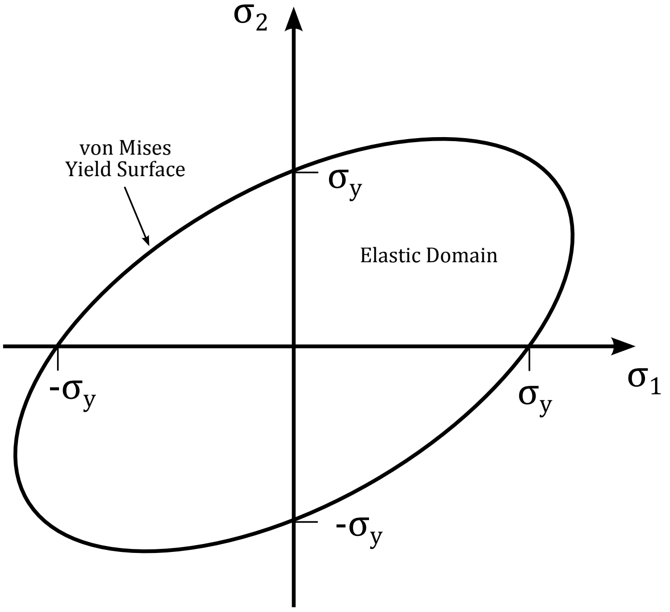

(b)

Figure 2.2 Schematic representation of the von Mises yield surface (a) in the three-dimensional principal stress space and (b) in a plane stress problem (i.e. $\sigma_3 = 0$).

2.4 Plastic flow rule

Assuming a function of plastic potential Ω, then the plastic strain increment can be written by the following expression:

$$\dot{\varepsilon}^p_{ij} = \dot{\lambda}\frac{\partial \Omega}{\partial \sigma_{ij}} \tag{2.15}$$

Equation 2.15 indicates that the plastic strain increment is parallel to the gradient to the yield surface $\left(\partial\Omega/\partial\sigma_{ij}\right)$ in the stress space, while $\dot{\lambda}$ is a positive scalar factor of proportionality, which is also called plastic multiplier and can be determined by the consistency condition ($\dot{F}=0$). Furthermore, the plastic potential function Ω is convex, non-negative and zero at the origin, while equation 2.15 indicates that the plastic strain increment tensor is normal to the surface $\Omega=0$.

In case the plastic potential function Ω coincides the yield surface F, then the model is called "associated". Associated plasticity models describe successfully the plastic deformation in metals and it is also adopted in the plasticity models used in the present study in Chapters 3, 4, 5 and 6. However, soils and granular materials exhibit a non-linear volume change during hardening, which can not be represented with associated plasticity models, therefore a non-associated flow rule is needed (Runesson and Mroz, 1989; Simo, 1987).

Consequently, the plastic strain increment tensor components in equation 2.15 can be described by the following expression, considering the associated flow rule:

$$\dot{\varepsilon}_{ij}^{p}=\dot{\lambda}\frac{\partial F}{\partial\sigma_{ij}} \tag{2.16}$$

The above equation 2.16 indicates that the direction of the plastic strain increment tensor is normal to the yield surface ($F=0$). This is also called as the normality hypothesis of plasticity and it is shown that it ensures the uniqueness of the solution of the boundary-value problem for an elasto-plastic material (Chen and Han, 1988).

2.5 Hardening rules

Upon reaching the yield stress of a material, further increase of stress is necessary when additional plastic deformation occurs, as shown in Figure 2.1 beyond point A. In case the material is unloaded in the inelastic range, it follows a linear path with slope equal to the Young's modulus E, resulting in a residual deformation. If the material is loaded again, then it follows the same linear path and it yields at the highest stress attained before the unloading begun. Due to the higher yield stress during the reloading, the material is considered "hardened" by the plastic deformation.

Hardening of a material can be translated as a change in the geometry and location of its yield surface in the three-dimensional stress space. In the following sections 2.5.2, 2.5.3 and 2.5.4, three widely-used hardening rules are presented in more detail.

2.5.1 Loading criteria

The yield surface can be defined as a function of the stress tensor σ_{ij}, the plastic strain tensor ε_{ij}^{p} and a hardening parameter k as shown in the following expression:

$$F\left(\sigma_{ij}, \varepsilon_{ij}^{p}, k\right) = 0 \tag{2.17}$$

where hardening parameter k is a function of the plastic strain tensor ε_{ij}^{p} and will de discussed further in the following sections. At this point, a unit tensor $\left(N_{ij}\right)$, which is normal to the yield surface, should be defined to establish the loading and unloading conditions. The vector $(N_{ij}$ is described by the following expression:

$$N_{ij} = \frac{\partial F / \partial \sigma_{ij}}{\sqrt{\dfrac{\partial F}{\partial \sigma_{ij}} \dfrac{\partial F}{\partial \sigma_{ij}}}} \tag{2.18}$$

A fundamental assumption of the elasto-plastic theory is that the stress function F should always be either (a) lower than zero, which means that the stress point is inside the yield surface and the material is elastic ($F < 0$), or (b) equal to zero, which means that the stress point is on the yield surface and the material deforms plastically ($F = 0$). However, if the stress point returns inside the yield surface, then the plastic deformation of the material stops and the deformation becomes elastic. It is important to note that the yield function can not obtain values greater than zero ($F > 0$); this scenario violates the “consistency” condition ($\dot{F} = 0$). The different loading cases could be described mathematically as follows:

- $F = 0$ and $N_{ij}\dot{\sigma}_{ij} > 0$ corresponds to plastic loading.
- $F = 0$ and $N_{ij}\dot{\sigma}_{ij} < 0$ corresponds to elastic unloading.
- $F = 0$ and $N_{ij}\dot{\sigma}_{ij} = 0$ describes a loading condition, which is neither loading nor unloading, and it is called neutral loading.
- $F < 0$ corresponds to elastic behaviour of the material for every $\dot{\sigma}_{ij}$.
- $F > 0$ is not valid. If the material deforms plastically $\left(F = 0,\ N_{ij}\dot{\sigma}_{ij} > 0\right)$, then its properties change accordingly to obtain $F = 0$ at the new stress point.

2.5.2 Isotropic hardening

The case of isotropic hardening corresponds to the simplest hardening model, where the yield surface expands with plastic deformation of the material, as shown schematically in Figure 2.3, without any distortion or translation of the surface in the stress space. For that case, the elastic domain expands uniformly in all directions during plastic flow, leading to increase of radius of the yield surface in three-dimensional space. Therefore, the yield criterion can be described by the following expression:

$$F\left(\sigma_{ij},k\right)=\frac{1}{2}\sigma_{ij}\sigma_{ij}-\frac{k^2\left(\varepsilon_p\right)}{3}=0 \tag{2.19}$$

where ε_p is the accumulated plastic strain or the von Mises effective plastic strain, which controls the hardening of the material and the corresponding expansion of the yield surface ($k\left(\varepsilon_p\right)$), and is described by the following expression:

$$\dot{\varepsilon}_p=\sqrt{\frac{2}{3}\dot{\varepsilon}_{ij}^p\dot{\varepsilon}_{ij}^p} \tag{2.20}$$

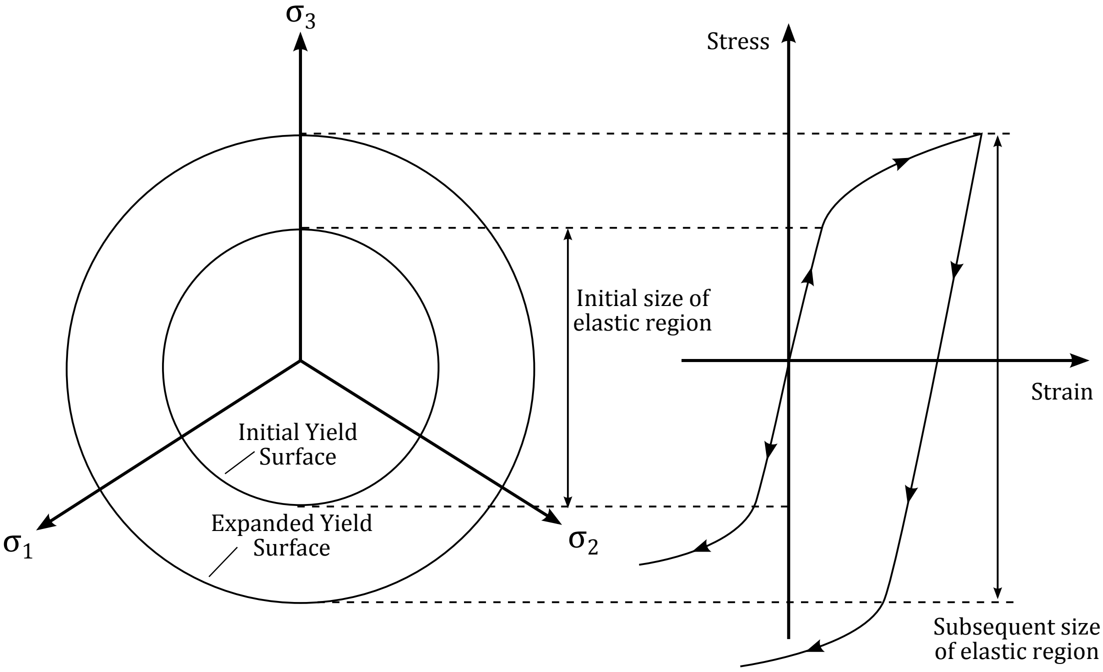

Figure 2.3 Schematic representation of the π-plane and stress-strain curve of a material during uniaxial cyclic loading, considering isotropic hardening.

2.5.3 Kinematic hardening

The kinematic hardening rule, described in the present section, represents a rigid body translation of the yield surface in stress space by shifting its reference point from the origin to another stress point, as shown in Figure 2.4. In some materials, the increase of yield stress and plastic deformation in the direction of applied load, leads to decrease of the yield stress on the opposite direction during reverse plastic loading.

This behaviour is commonly called “Bauschinger effect” and it can not be modelled using isotropic hardening, where the yield surface expands with plastic loading in both directions, as shown in Figure 2.3. In this case, the yield criterion can be described by the following expression:

$$F\left(\sigma_{ij},\alpha_{ij},k\right)=\frac{1}{2}\left(\sigma_{ij}-\alpha_{ij}\right)\left(\sigma_{ij}-\alpha_{ij}\right)-\frac{k^2}{3}=0 \tag{2.21}$$

where k is a constant material parameter and α_{ij} is the back stress tensor which defines the centre of yield surface during plastic deformation, as shown in Figure 2.4.

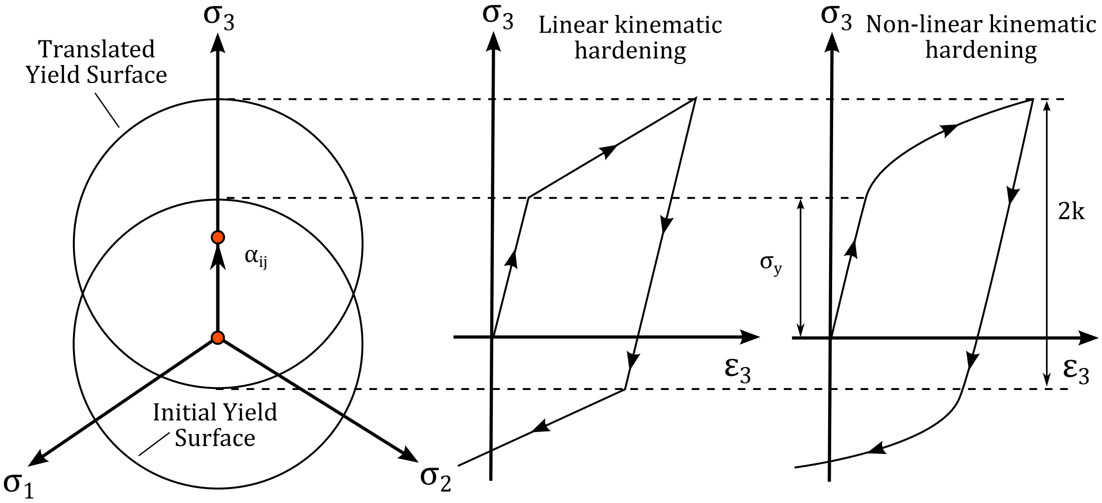

Figure 2.4 Schematic representation of the π-plane and stress-strain curve of a material during uniaxial cyclic loading, considering linear and non-linear kinematic hardening.

At this point, a relation between the back stress tensor α_{ij} and the plastic strain tensor ε_{ij}^{p} needs to be defined. A simple kinematic hardening rule has been introduced by Melan (1938), which is in fairly good agreement with the Bauschinger effect of those materials that present linear work-hardening. A similar proposal is reported by Ishlinskii (1954), considering a linear relation between the back stress α_{ij} and the plastic strain tensor ε_{ij}^{p}, and generalized by Prager (1955, 1956) establishing the term “kinematic hardening”, while the linear expression is defined as:

$$\dot{\alpha}_{ij}=c\dot{\varepsilon}_{ij}^{p} \tag{2.22}$$

where c is material constant. Over the years, several kinematic hardening models have been proposed (Backhaus, 1968; Lehmann, 1972), while Ziegler (1959) identified that the loading surface may be distorted in case where some stress components are zero. Therefore, the following modification of Prager’s kinematic hardening rule has been proposed:

$$\dot{\alpha}_{ij} = \dot{\mu}\left(\sigma_{ij} - \alpha_{ij}\right) \tag{2.23}$$

where $\dot{\mu}$ is a parameter that depends on the equivalent plastic strain by the following expression:

$$\dot{\mu} = \beta \dot{\varepsilon}_p \tag{2.24}$$

and β is a material constant.

The aforementioned kinematic hardening models may not be able to describe efficiently the cyclic response of metals, and therefore, various more advanced models have been developed. One of the most widely used model has been proposed by Chaboche (1986); Lemaitre and Chaboche (1994), which is an extension of the classical non-linear kinematic hardening rule introduced by Armstrong and Frederick (1966) , and is given by the following expression:

$$\dot{\alpha}_{ij} = \sum_{q=1}^{M} \dot{\alpha}_{ij}^{q},\ \dot{\alpha}_{ij}^{q} = \left(\frac{2}{3} C^{q} \dot{\varepsilon}_{ij}^{p} - \gamma^{q} \alpha_{ij}^{q} \dot{\varepsilon}_p\right) \tag{2.25}$$

where M is the number of back stresses considered, C is the hardening moduli and γ determines the rate of decrease of hardening with increasing plastic deformation.

2.5.4 Combined hardening

Besides the hardening rules described in the previous sections, a more general hardening rule can be assumed, which is a combination of isotropic and kinematic hardening rules. In this case, the yield surface is free to expand and translate in the stress space during plastic deformation. Therefore, the yield criterion, assuming a combined hardening rule, can be described by the following expression:

$$F\left(\sigma_{ij}, \alpha_{ij}, k\right) = \frac{1}{2}\left(\sigma_{ij} - \alpha_{ij}\right)\left(\sigma_{ij} - \alpha_{ij}\right) - \frac{k^2\left(\varepsilon_p\right)}{3} = 0 \tag{2.26}$$

In the above equation 2.26, the translation of the yield surface is governed by the back stress tensor α_{ij} expressed by an equation similar to 2.25, while the expansion of the surface by the term $k\left(\varepsilon_p\right)$, which is defined by the following expression:

$$k\left(\varepsilon_p\right) = \sigma_y + Q\left(1 - e^{-b\varepsilon_p}\right) \tag{2.27}$$

where Q and b are material parameters, defining the change of the yield surface size as the equivalent plastic strain accumulates. Therefore, both the Bauschinger effect and the cyclic hardening or softening of the material can be described, assuming combined hardening rule. Defining appropriately the Q material parameter value, cyclic hardening or softening can be achieved, describing adequately the cyclic response of stainless steel (Chaboche *et al.*, 1979) and low carbon steel (Chai and Laird, 1987) materials, respectively. A brief comment and additional references on cyclic hardening or softening of metals is also provided in the following section 2.6. It should be also noted that, other combined hardening rules can be assumed, such as accounting for distortion of the yield surface (Voyiadjis and Foroozesh, 1990), but their implementation is out of the scope of the present thesis.

2.6 Models for cyclic plasticity

Several cyclic plasticity constitutive models have been developed to simulate properly the mechanical behaviour of metallic components of structural and mechanical systems, subjected to severe cyclic loading conditions in the inelastic range. The earthquake response of structural steel components (Mahin *et al.*, 1980), the seismic or shutdown conditions of piping systems (Ravikiran *et al.*, 2015), and the severe cyclic plastic deformation of pipelines during offshore reeling installation (Manouchehri, 2012; Martinez and Brown, 2005) are typical examples of these loading conditions. The cyclic deformation into the inelastic range of the metal material could lead to excessive plastic strain accumulation, which might lead to damage of the microstructure of the material, crack initiation and potential failure of the structure.

2.6.1 Features of cyclic plasticity

The mechanical behaviour of metals under uniaxial cyclic loading has been examined extensively (Landgraf, 1970; Morrow, 1965), and their behaviour can be categorised into different groups based on several unique features, as follows. Depending on several factors of the material, such as the initial conditions, cyclic hardening or softening of the material has been shown. The phenomenon of cyclic hardening, which characterises stainless steel materials, and cyclic softening, which appears on low carbon steels, can be demonstrated in symmetric strain-controlled cyclic loading. In both cases, the hysteresis loop stabilises after a number of cycles. Furthermore, in case the strain cycles have an offset, then the hysteresis loop shifts its mean stress and tends to stabilise at zero mean stress, while this phenomenon is called cyclic relaxation. Furthermore, when a metallic component is subjected to non-symmetric stress-controlled cyclic loading, then progressive increase of strain occurs, which is referred to as “ratcheting”. This phenomenon is discussed in more detail in section 2.6.2.

Structural components made of low carbon steel materials are characterised by the presence of a plastic plateau, upon first yielding of the material. During reverse reverse plastic loading, the Bauschinger (1881) effect is present. This is an important feature of metallic materials, both stainless steel and carbon steel materials, which leads to plastic deformation of the material at a lower stress level than the initial yield. Based on the aforementioned features of metals in the inelastic region, it is necessary to develop reliable constitutive models to predict the structural response of steel components. An important work, accounting for the plastic plateau of metals upon first yielding and the Bauschinger effect during reverse plastic loading, has been reported by Ucak and Tsopelas (2011, 2012). Furthermore, Hu *et al.* (2018) proposed a plasticity model which is capable to describe the plastic plateau, the material cyclic softening or hardening, and the Bauschinger effect. This constitutive model was also calibrated with experimental tests (Hu *et al.*, 2016). In these cyclic plasticity models, the hardening modulus is defined indirectly, through the consistency condition, leading to coupling of the hardening modulus with the kinematic hardening rule. Therefore, these models are referred to as “coupled models”. A different approach could be adopted to describe the cyclic plasticity of metals, using the so-called “uncoupled models”. In this category, the definition of plastic modulus is defined directly through an appropriate function, so that the plastic modulus is influenced indirectly by the kinematic hardening rule. This is described in detail by Tseng and Lee (1983), accounting for the aforementioned features of metals under cyclic plastic loading.

2.6.2 Ratcheting of metals

When a metallic component is loaded under unsymmetrical stress-controlled cyclic loading, then a positive mean stress occurs.Therefore, the hysteresis loop never closes, leading to “creeping” of strain or ratcheting in the direction of the mean stress. Figure 2.5 presents schematically the stress-strain curve for an unsymmetrical stress-controlled loading and the corresponding increase of the maximum strain of each cycle. Therefore, the material softens with each cycle, leading to failure in a relatively small number of applied cycles.

Over the last decades, extensive experimental testing has been conducted (Chai and Laird, 1987; Lebey and Roche, 1979; Pilo *et al.*, 1979) on ratcheting under uniaxial or biaxial loading. For the biaxial loading case, two experiment types have been investigated. The first consists of symmetrical strain-controlled torsional cyclic loading of a thin-walled circular tube under a constant axial load. The interaction between the constant stresses and the cyclic shear stresses leads to ratcheting of the tube on the axial direction. The second type of experiment consists of a symmetrical strain-controlled torsional cyclic loading of a thin-walled circular tube under a constant internal pressure. In this case, the interaction of axial and hoop stresses lead to ratcheting of the tube on the circumferential direction increasing the tube diameter.

To model this mechanical behaviour, various constitutive models has been reported, predicting the ratcheting of materials, under stress-controlled cycles. Dafalias (1981); Ohno and Wang (1993*a*,*b*) proposed two surfaces models, considering a yield surface and a bounding surface, while Hassan (1994); Hassan *et al.* (1992); Hassan and Kyriakides (1992) modified the bounding surface, allowing for translation in the ratcheting direction. Moreover, constitutive models, considering the non-linear kinematic hardening rule proposed by Armstrong and Frederick (1966), have also been developed (Chaboche and Nouailhas, 1989*a*,*b*; Chaboche and Rousselier, 1983*a*,*b*) predicting both uniaxial and biaxial ratcheting.

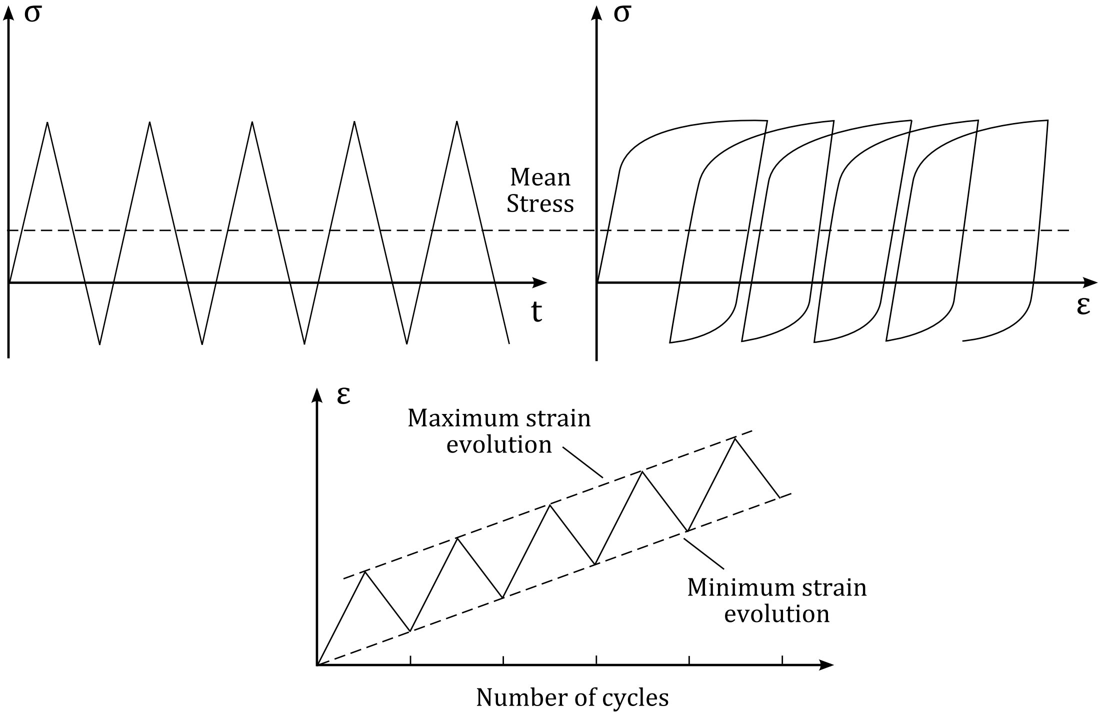

Figure 2.5 Schematic representation of ratcheting; unsymmetrical stress-controlled cyclic loading, leading to increasing maximum strain per cycle.

Chapter 3

Bending of internally pressurized steel lined pipes

3.1 Chapter outline

The work in the present chapter is motivated by reeling of lined pipes, and focuses on the structural behaviour of lined pipes subjected to monotonic bending in the presence of low and moderate levels of internal pressure. Advanced finite element tools are used to simulate thin-walled liner deformation, including wrinkling and post-buckling behaviour. Numerical results are presented for the "tight-fit" pipe (TFP), which account for the hoop compressive pre-stress due to the manufacturing process, and the "snug-fit" pipe (SFP), where no bonding pressure exists (zero compression on the liner). In this chapter, the manufacturing process is considered by applying an initial compressive hoop stress on the model to simulate with a simpler manner the residual stresses induced by the manufacturing process and result on the final mechanical bonding. This assumption does takes into account the effects of the manufacturing process on the material properties and the corresponding plastic deformation in the liner pipe. The results are presented for several levels of internal pressure and compared with corresponding results from non-pressurized pipes. An ovalisation analysis is conducted investigating the influence of internal pressure on lined pipe cross-section, while a three-dimensional analysis examined liner wrinkling and post-buckling behaviour for different internal pressure levels. In addition, a parametric study on the effect of initial wrinkles on the liner is conducted on both types of bonding and for pressurized and non-pressurized lined pipes, in an attempt to investigate the imperfection sensitivity of those bi-material pipes.

3.2 Material properties and numerical modelling

3.2.1 Lined pipe geometry and material properties

A lined pipe, typical for offshore applications, is considered, similar to a lined pipe examined by Focke (2007). It consists of a thick-walled outer pipe, made from X65 steel material and a stainless steel 316L liner pipe. The outside diameter (D_o) and thickness (t_o) of the outer pipe are 325 *mm* (12.79 *in*) and 14.3 *mm* (0.56 *in*) respectively, while the liner diameter (D_l) and thickness (t_l) are 296.4 *mm* (11.67 *in*) and 3 *mm* (0.12 in) respectively. The stress-strain curve of the outer pipe material, obtained from a uniaxial tensile test (Focke, 2007), is shown in Figure 3.1, with Young modulus $E_o = 210,000$ *MPa*, Poisson's ratio $\nu = 0.3$ and yield stress $\sigma_{y,o} = 566$ *MPa*. The corresponding stress-strain curve of the liner pipe material is also shown in Figure 3.1, with parameters $E_l = 193,000$ *MPa*, $\nu = 0.3$, proportional limit $\sigma_{pr,l} = 250$ *MPa* at 0.13% and yield stress $\sigma_{y,l} = 298$ *MPa* corresponding to 0.2% residual plastic strain. The stress-strain curves and the corresponding values used in the present study are chosen to validate the numerical model with previous studies (Vasilikis, 2012; Vasilikis and Karamanos, 2012).

Furthermore, the tensile response of the 316L stainless steel material of the liner pipe is represented through a power-law relationship to permit the reader to reproduce the stress-strain curve. A commonly used relationship is the three-parameter Ramberg and Osgood (1943) expression

$$\varepsilon = \frac{\sigma}{E}\left[1 + \frac{3}{7}\left(\frac{\sigma}{\sigma_y}\right)^{(n-1)}\right] \tag{3.1}$$

where E is the slope of the linearly elastic part of the curve, σ_y is the stress value at the intersection of the stress-strain curve and a line through the origin with slope equal to $0.7E$, while the value n can be obtained from the slope of the linear part of the plot of $\log(\varepsilon - \sigma/E)$ versus $\log(\sigma)$. The stress-strain fit procedure is explained in more detail in the book by Kyriakides and Corona (2007), while the fit parameters of the liner pipe for the present study are $E = 193,000$ *MPa*, $\sigma_y = 240$ *MPa* and $n = 8.5$.

The stress-strain curve of carbon steel materials is characterized by three distinct regions. The first corresponds to a linear elastic until a yield point is reached. Then, a plastic plateau is reached, where Lüders bands (Callister and Rethwisch, 2018; Hall, 1970) of plastic deformation develop, propagating through the specimen. Once the Lüders strain ε_n is reached, the carbon steel hardens; the stress rises with increasing the strain, up to a maximum value (ultimate tensile stress: σ_{UTS}), followed by necking of the specimen and fracture.

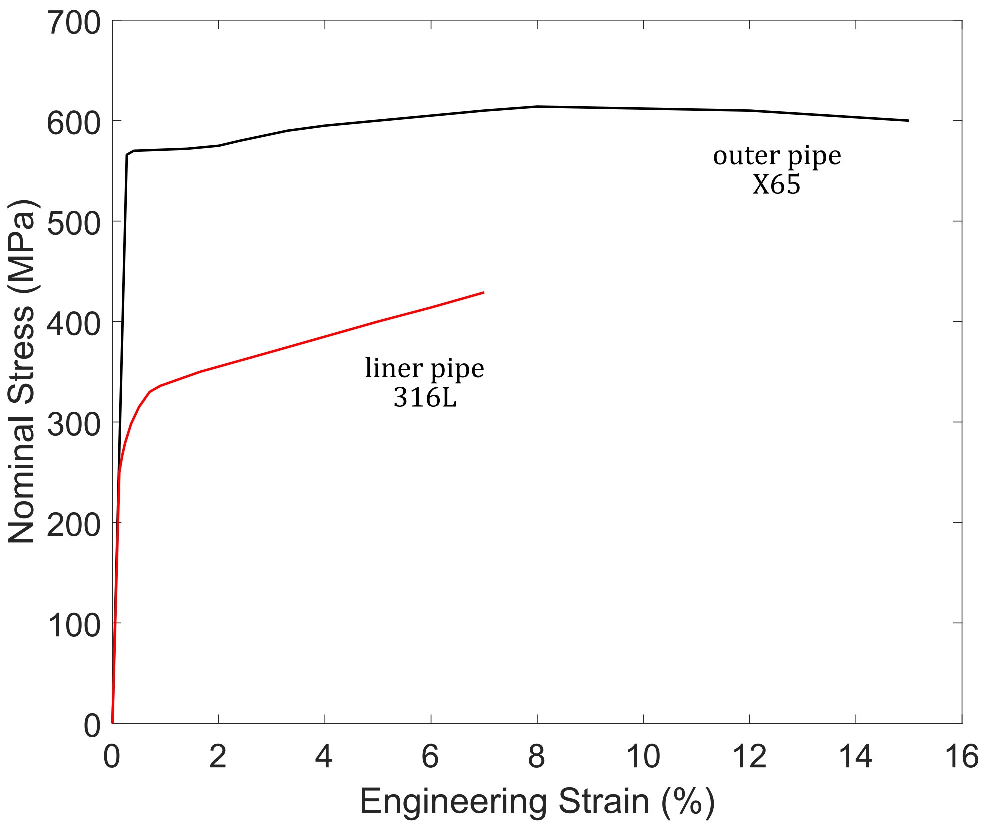

Figure 3.1 Stress-strain curves of outer and liner pipe (Focke, 2007).

Regarding the experimental curve of the X65 carbon steel material of the outer pipe (Focke, 2007), a curve fitting methodology is followed, as presented by Sadowski *et al.* (2015, 2017). First, the material deforms elastically up to the point where the plastic plateau begins at strain equal to $\varepsilon_{y,o} = \sigma_{y,o}/E_o$. In the following, a very low rigidity plastic plateau is shown until stress and strain values $\sigma_{y,o,n}$ and $\varepsilon_{o,n}$, respectively. The tangent modulus of the plastic plateau can be calculated by $E_{o,h,p} = (\sigma_{y,o,n} - \sigma_{y,o})/(\varepsilon_{y,o,n} - \varepsilon_{y,o})$, and the dimensionless length is defined by $n_o = (\varepsilon_{o,n} - \varepsilon_{y,o})/\varepsilon_{y,o}$. Finally, the hardening region of the carbon steel material is determined by least-squares curve fitting and it is given by the following 6^{th} order polynomial

$$\sigma = \sum_{i=0}^{6} b_i \left(\varepsilon - \varepsilon_{o,n}\right)^i \tag{3.2}$$

where $b_0 = \sigma_{y,o,n}$ corresponds to the stress value at the end of the plastic plateau and $b_1 = E_{o,h,s}$ is the initial tangent modulus of the true strain hardening after $\varepsilon_{o,n}$. Table 3.1 presents the fitting coefficients of expression 3.2 for the X65 carbon steel material at the hardening region, and the material parameters assuming an inclined plastic plateau.

Both hardening tangent moduli are presented in a normalised form by the nominal Young's modulus of the outer pipe (E_o), so that $h_{o,p} = E_{o,h,p}/E_o$ and $h_{o,s} = E_{o,h,s}/E_o$.

Table 3.1 Fitting parameters and material properties of the outer pipe X65 carbon steel.

X65 - Outer Pipe	
b_0	574.8
b_1	1542.5
b_2	$-3.631\ 10^4$
b_3	$4.8699\ 10^5$
b_4	$-4.4687\ 10^5$
b_5	$-4.0644\ 10^7$
b_6	$2.0827\ 10^8$
$\sigma_{y,o}$ (MPa)	566
$\sigma_{UTS,o}$ (MPa)	614
n_o	6.42
$h_{o,p}$ (%)	0.25
$h_{o,s}$ (%)	0.74

3.2.2 Finite Element Modelling

The mechanical behaviour of lined pipes subjected to bending is analysed numerically using non-linear finite element tools. The numerical simulations were conducted using general-purpose finite element software ABAQUS (Hibbitt *et al.*, 2016). The analysis considers non-linear geometry in the description of the liner and the outer pipe, whereas, the materials of the liner and the outer pipe are both considered elastic-plastic through a J_2 (von Mises, 1928) flow plasticity model with isotropic hardening, calibrated through uniaxial stress-strain curves from coupon tests, reported in previous publications (Focke, 2007; Vasilikis, 2012; Vasilikis and Karamanos, 2012).

The finite element model is three-dimensional, considering a lined pipe segment of appropriate length L. Based on symmetry of geometry and deformation with respect to the plane of bending, a symmetric model with respect to the y-z-plane is considered, as shown in Figure 3.2, analysing half of the pipe cross-section. In addition, x-y-plane symmetry of the model is assumed in the $z = 0$ plane allowing only for in-plane motion on the corresponding nodes. In the $z = L$ plane, a reference node is introduced. In this node, the rotation is applied (as shown in Figure 3.2), and the node is appropriately coupled with the corresponding nodes of the lined pipe cross-section, so that these nodes may slide on the rotated plane, allowing the lined pipe cross-section to ovalise freely during bending, representing a segment from an infinite pipeline. The reference node at $z = L$ is simply supported, so that it is free to move in the z-direction and rotate about the x-axis.

The liner pipe is modelled with four-node reduced-integration shell elements (S4R), whereas the outer pipe is modelled using twenty-node reduced-integration brick (solid) elements (C3D20R). Sadowski and Rotter (2013) reported a detailed study presenting the response of cylindrical tubes using shell elements with diameter over thickness ratio (D/t) equal to 100, which is similar to the liner pipe in the present study. On the other hand, in previous publications (Hilberink, 2011; Hilberink *et al.*, 2010*a*, 2011; Vasilikis and Karamanos, 2012; Yuan and Kyriakides, 2014*a*, 2020) brick elements were used to model the thick-walled outer pipe with a diameter over thickness ratio around twenty. This type of elements is preferred over shell elements; in the latter a contact pair that uses finite-sliding formulation, does not account for shell thickness and offset. Furthermore, results from this type of elements are in good agreement with experimental results reported by Focke (2007) and Hilberink (2011), as shown by Vasilikis (2012); Vasilikis and Karamanos (2012) and in section 3.3. The half cross-section of the outer pipe contains fifty elements, as shown in Figure 3.2, while one hundred elements are employed around the half-circumference of the liner (as shown in Figure 3.2). This number of elements was found adequate in order to achieve convergence and accuracy of the numerical results based on previous results (Vasilikis, 2012; Vasilikis and Karamanos, 2012; Yuan, 2015; Yuan and Kyriakides, 2014*a*).

A surface-to-surface interaction of the two pipes is also considered, with finite-sliding contact formulation, allowing for arbitrary separation, sliding and rotation between the surfaces. The effect of friction on separation and wrinkling of the liner pipe during bending has been investigated extensively by Hilberink (2011); Tkaczyk *et al.* (2011); Vasilikis (2012); Yuan (2015), and the numerical results have shown negligible influence on the response. Furthermore, zero friction between both pipes is considered in the present study, after a discussion with Kyriakides (2018), which is also assumed in previous works (Vasilikis and Karamanos, 2012, 2013; Yuan and Kyriakides, 2014*a*,*b*, 2015, 2020), providing very good results.

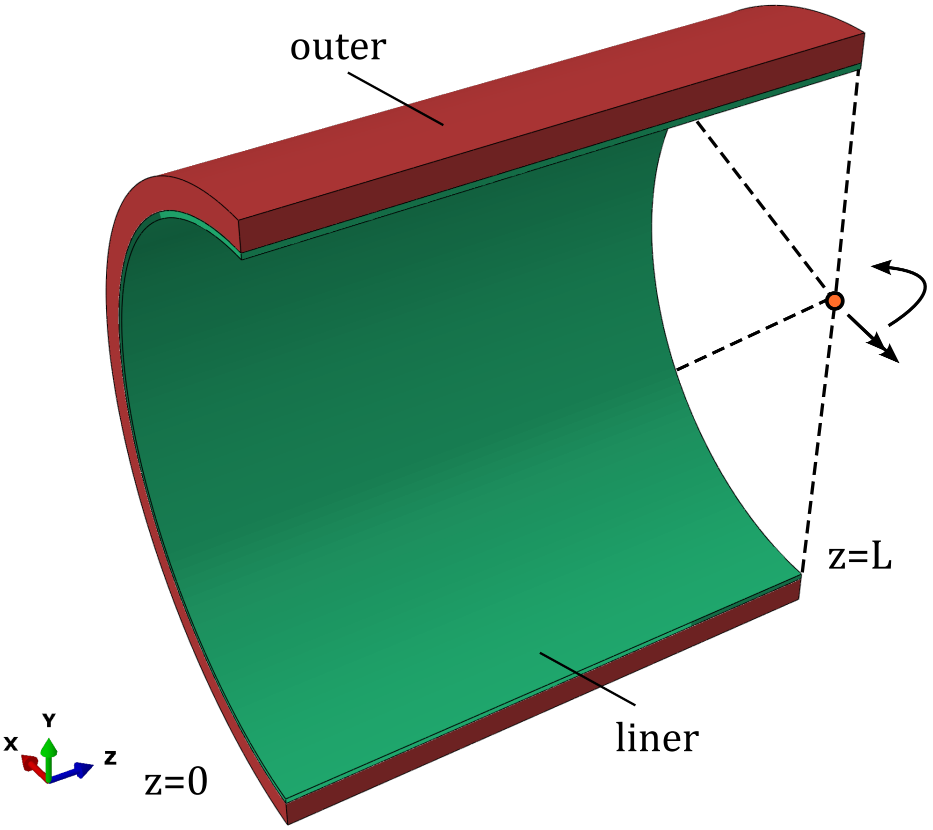

Figure 3.2 Three-dimensional finite element model of the lined pipe.

The length of the lined pipe model and the number of elements in each pipe depends on the type of simulation to be performed. In the case of ovalisation analysis, which is presented in section 3.4.1, a small length of the lined pipe shown in Figure 3.2 is assumed, equal to 3% of the outer diameter of the outer pipe. The model consists of four and two elements of liner and outer pipe respectively, in the longitudinal direction. Considering this small length segment, wall wrinkling phenomena are excluded, focusing on cross-section ovalisation and liner detachment. At this stage one may argue that the problem could also be modelled as a generalised plain strain case. However, assuming the present type of model, i.e. a very small length pseudo-three-dimensional model, the kinematic conditions required for an ovalisation analysis are satisfied. Furthermore, this type of modelling is chosen for convenience, because it is directly related to the three-dimensional model, which is used for the three-dimensional bending analysis, adjusting only the length of the model.

On the other hand, in order to simulate liner wrinkling, during bending loading, and the corresponding imperfection sensitivity, a longer model is necessary, which is presented in section 3.4.2. Introducing the dimensionless length parameter $\chi = (L-z)/\sqrt{D_{m,l}t_l}$ (where $D_{m,l} = D_l - t_l$ is the liner pipe mean diameter and z ranges from zero to L, shown in Figure 3.2), which represents the number of buckling waves of an elastic tube under uniform compression, the normalised lined pipe length is equal to $\chi = 10$. Initially, a two half-wavelength long model has been considered, following the approach presented by Vasilikis (2012); Vasilikis and Karamanos (2012). The half-wavelength of the liner pipe is not known a priori, therefore a series of analyses are necessary, as presented by Vasilikis and Karamanos (2012), so that the actual half-wavelength is the one corresponding to earliest bifurcation. This methodology has also been used by Houliara and Karamanos (2006, 2010) in analysing long elastic tubes. However, using this approach one may not account for buckle localization properly. Therefore, a longer lined pipe segment is assumed in the present study, while the numerical model is validated with experimental data, as shown later in section 3.3.

The number of elements in the model is mainly dictated by the need to describe accurately the buckling pattern of the liner pipe. Following the mesh density presented by Vasilikis (2012); Vasilikis and Karamanos (2012); Yuan (2015); Yuan and Kyriakides (2014*a*), the liner pipe model consists of eighteen elements at each half-wavelength λ_c in z-direction, where $\lambda_c = \pi\sqrt{R_{m,l}t_l}/[12(1-\nu^2)]^{1/4}$ ($R_{m,l} = R_l - t_l/2$ is the mean radius and t_l is the wall thickness of the liner pipe) is the half-wavelength of a circular cylindrical shell under uniform compression, assuming elastic material (Timoshenko and Gere, 1961). Using fewer elements per half-wavelength λ_c, it is shown that liner wrinkling and its evolution with the applied curvature, may not be very accurate. Using eighteen elements per λ_c or more, converged results are obtained, while the influence of coarser liner meshes on liner detachment is presented in section 3.3.2 . For the outer pipe, a coarser mesh is used consisting of six elements every half-wavelength λ_c in z-direction, because its deformation is not associated with local buckling patterns. The choice of the numerical model parameters results in good agreement with test data from the physical experiments conducted at Delft University of Technology and presented by Focke (2007) and Hilberink (2011), as shown in section 3.3. Furthermore, numerical analyses considering five, seven and nine integration points through the liner pipe wall thickness are conducted showing identical response. Therefore, five integration points are considered in the following analyses.

The mechanical bonding of the lined pipe is considered following the terminology used by Focke (2007). In the case of TF Pipes, an initial compressive hoop stress of magnitude 200 *MPa* (67.1% of the liner yield stress) is applied on the liner pipe, followed by an unloading step, resulting in residual compressive hoop stress σ_{res} for the liner pipe equal to 166 *MPa*. This is a simple and efficient procedure to account for the manufacturing process, also used by Vasilikis and Karamanos (2012). However, it does not account for the effects of manufacturing on the material properties of the liner, which is examined in a more accurate manner later in Chapter 4.

Finally, internal pressure P_{in} is applied, up to 10% of the liner pipe yield pressure ($P_{y,l} = 2\sigma_{y,l} t_l / D_{m,l}$, where $D_{m,l}$ is the mean diameter of the liner pipe), and the pressure load parameter $p = P_{in}/P_{y,l}$ is introduced. In this case, the maximum internal pressure level corresponds to 6 *bar*. A tensile force (F_p) is also applied on the reference node in the $z = L$ plane, which equals to the applied internal pressure times the internal cross-section of the liner ($F_p = P_{in}\pi(D_l - 2t_l)^2/4$) in order to simulate the force at the two capped ends due to the pressure. This force will be referred to as “capped-end force”, and remains constant during bending, following the orientation of reference node at $z = L$ (follower force).

3.3 Validation of the numerical model with experimental data

Experimental work has been conducted by Focke (2007) and Hilberink (2011), showing the gradual separation of the liner from the outer pipe under monotonic pure bending, which leads to liner wrinkling and eventually to local buckling 3.3. In the present section, numerical results for a TF Pipe are compared with corresponding experimental data and additional numerical presented by Vasilikis (2012). Furthermore, it is important to underline that modal buckling analysis may not be possible in the present problem due to its high non-linearity, mainly because of the contact between the two pipes, and the confinement that the outer pipe offers to the inner pipe. Therefore, the liner pipe separation from the outer pipe and the corresponding wave-length are compared with existing experimental and numerical data for validation of the present model.

The geometric and material properties of a TF Pipe, presented in section 3.2.1, are similar with the lined pipes OR-2, GR-1, GR-2 and WT-2 tested by Focke (2007), P01KA tested by Hilberink (2011) and Lined Pipe A examined by Vasilikis (2012). The residual liner hoop compression σ_{res}, due to manufacturing process, has been measured equal to 178 *MPa* for OR-2 lined pipe, 199 *MPa* for GR-1 and GR-2 pipes, 185 *MPa* for the P01KA lined pipe, and 166 *MPa* for the Lined Pipe A, which is comparable with the tested specimens and it is also considered in the present study. Moreover, the residual compression of the liner pipe for the WT-1 and WT-2 pipes has been measured equal to 53 *MPa*.

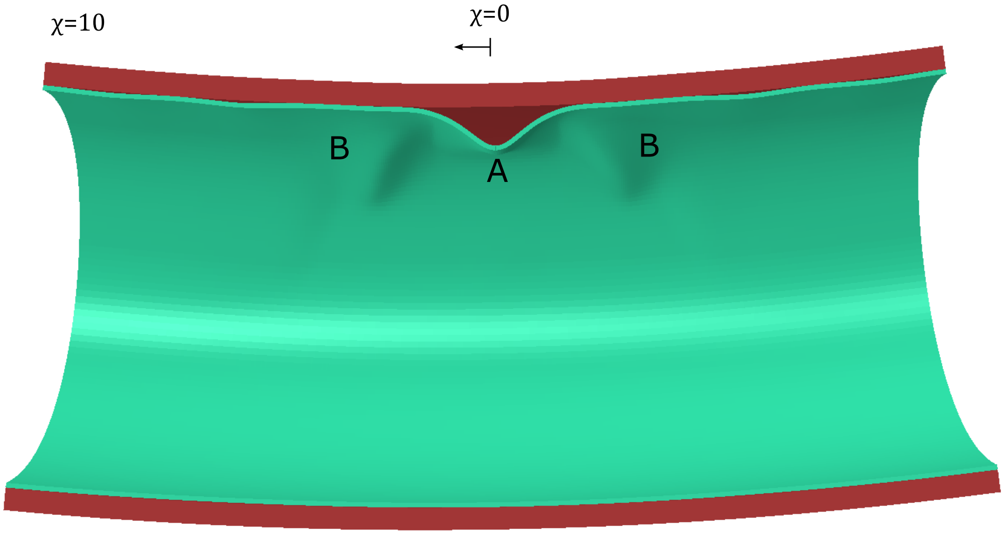

Figure 3.3 Liner pipe buckling shape at $\chi = 0$ location forming a main buckle (A) and four adjacent minor buckles (B) of liner pipe.

3.3.1 Wrinkle half-wavelength

The experimental wave-length of wrinkle (L_w), reported by Focke (2007); Hilberink (2011) and corresponding numerical result by Vasilikis (2012), is presented in Table 3.2, normalised by the value $\sqrt{D_{m,l}t_l}$ (Ju and Kyriakides, 1992; Kyriakides and Ju, 1992). The experimental wave-length L_w corresponds to the secondary buckling mode where a main buckle (A) is formed with four adjacent minor buckles (B), shown in Figure 3.3. Furthermore, the wave-length reported by the numerical analysis of Vasilikis (2012) and the one presented in the current study corresponds to the wrinkling wave-length of the first bifurcation mode. The half-wavelength of the numerical model presented in section 3.2.2 is in fairly good agreement with previous studies. The results also indicate that the level of hoop compression of the liner pipe, due to manufacturing process, does not affect the significantly the buckling wavelength. This observation is also mentioned by Hilberink (2011); Vasilikis (2012).

Table 3.2 Wavelength values of the present study compared with previous experimental and numerical results (Focke, 2007; Hilberink, 2011; Vasilikis, 2012).

Normalised length of wrinkle ($L_w/\sqrt{D_{m,l}t_l}$)	
OR-2 (Focke, 2007)	2.45
GR-1 (Focke, 2007)	3.03
GR-2 (Focke, 2007)	2.71
WT-1 (Focke, 2007)	2.92
WT-2 (Focke, 2007)	2.74
P01KA (Hilberink, 2011)	2.33
Lined Pipe A (Vasilikis, 2012)	2.90
Present Study	2.85

3.3.2 Evolution of liner pipe wrinkle height

Figure 3.4 presents the wrinkle height (h_w) of liner pipe in the case of snug-fit pipe, normalised by the liner thickness t_l, for different element sizes on the longitudinal direction. The evolution of wrinkle is monitored at the most compressed generator of the pipe, where the liner wrinkles and buckles locally as shown in Figure 3.3, with respect to normalised curvature ($\kappa = k_r/k_o$; $k_r = \phi/L$, where ϕ is the rotation applied on the reference node at $z = L$; $k_o = t_o/D_{m,o}^2$). It is shown that coarser liner mesh densities affect the liner detachment, leading to stiffer bending response, while using eighteen elements or more per λ_c similar results are obtained.

Figure 3.5 presents the wrinkle height of the liner pipe in case of TF Pipe, with respect to normalised curvature κ, compared with experimental data. Appropriate initial imperfection wrinkles are considered, so that after the unloading step, the residual wrinkle height before bending corresponds to the range of initial wrinkling measurements reported in specimen locations OR-2 W4, OR-2 W5, GR-2 W4, and GR-2 W5 (Focke, 2007). Figure 3.5 shows very good agreement between the evolution of the liner pipe wrinkle height obtained from the present numerical model and the experimental measurements.

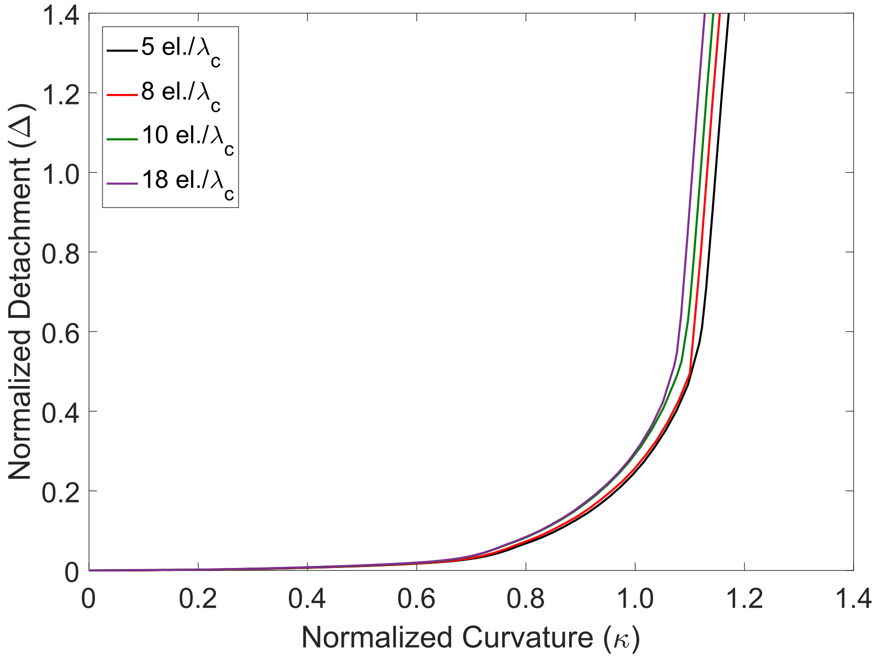

Figure 3.4 Normalised value of liner detachment of SF Pipe, considering different finite element sizes on the longitudinal direction, with respect to applied curvature.

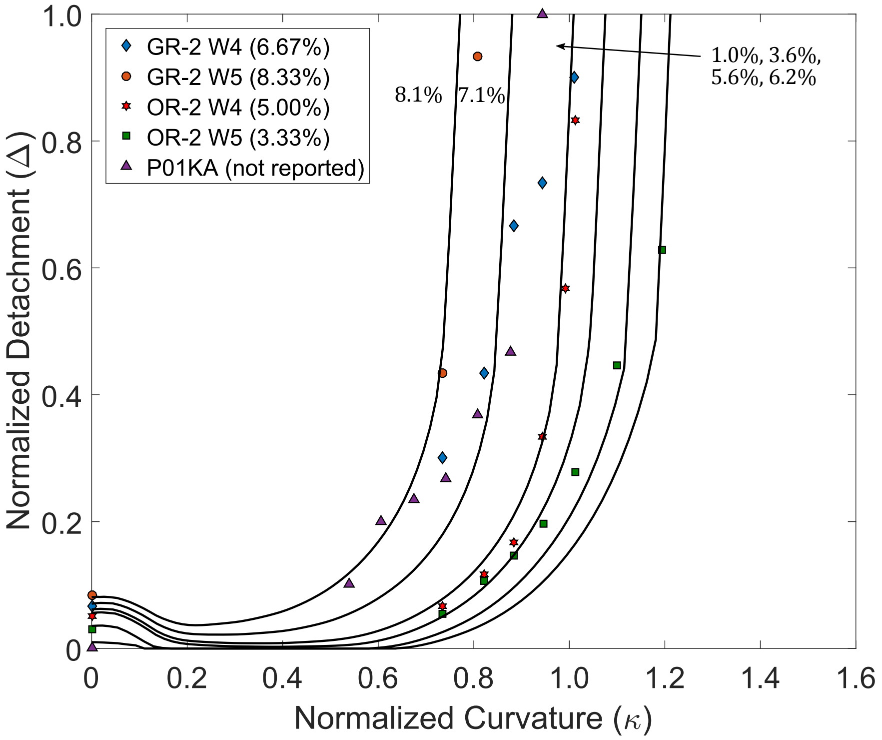

Figure 3.5 Normalised value of liner detachment of TF Pipe, for different values of initial imperfection, compared with experimental results (Focke, 2007; Hilberink, 2011).

3.4 Numerical results

In the following results, the curvature $\kappa = k_r/k_o$, where $k_r = \phi/L$ and ϕ is the rotation applied on the reference node at $z = L$, is normalised by the curvature-like parameter $k_o = t_o/D^2_{m,o}$ (Corona and Kyriakides, 1988) (where $D_{m,o}$ is the mean diameter of the outer pipe), so that $\kappa = k/k_l$; the bending moment of the lined pipe M is normalised by $M_o = \sigma_{y,o} t_o D^2_{m,o}$, so that $m = M_{Total}/M_o$; the detachment (Δ) of the liner pipe from the outer pipe is normalised by the liner thickness t_l at the most compressed generator of the pipe, as shown in Figure 3.6a. Furthermore, the ovalisation (ζ_l) of the liner pipe cross-section is defined as $\zeta_l = (D_{m,l,h} - D_{m,l,v})/D_{m,l}$, where $D_{m,l,h}$ and $D_{m,l,v}$ is the deformed horizontal and vertical mean diameter of the liner, while $D_{m,l}$ is the initial mean diameter of the liner pipe. The local hoop curvature ($1/R_{\theta 0}$), hoop stress ($\sigma_{\theta 0}$) and axial stress (σ_{x0}) in the liner pipe are also computed at $\theta = 0$ (as shown in Figure 3.6b), where maximum compression occurs. The value of local curvature at $\theta = 0$ is associated with local buckling resistance of the cylinder. Finally, the local hoop curvature of the liner due to ovalisation is normalised by $1/R_l$ and the longitudinal and hoop stresses on the liner are normalised by the yield stress of the liner $\sigma_{y,l}$.

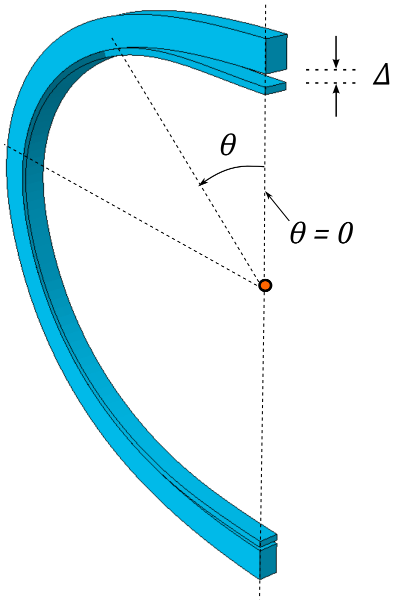

(a)

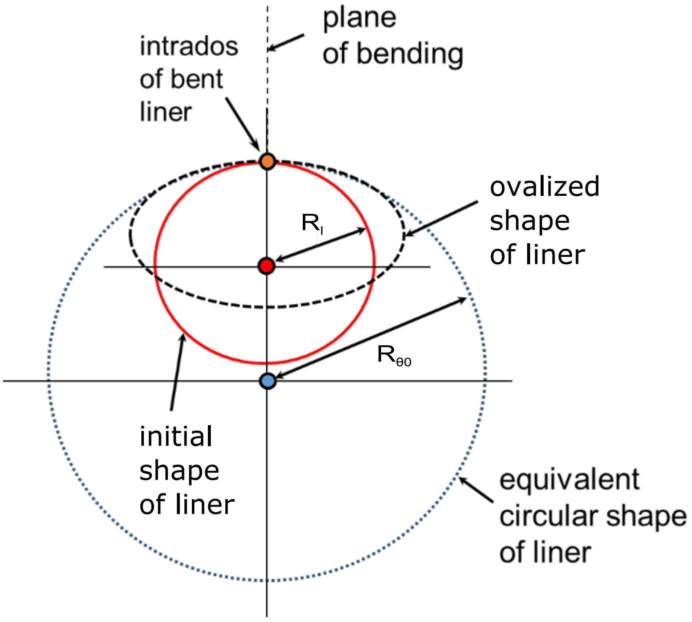

(b)

Figure 3.6 (a) Liner detachment and cross-section ovalisation. (b) Schematic representation of liner ovalisation and local radius of hoop curvature at the most compressed location ($\theta = 0$).

3.4.1 Ovalisation analysis

An ovalisation analysis is conducted first, in order to understand some key features of lined pipe mechanical behaviour during bending in the presence of different levels of internal pressure, using the numerical model shown in Figure 3.2 and explained in detail in section 3.2.2. The detachment of the liner pipe from the outer pipe (Figure 3.6a) is presented in Figure 3.7, for TF Pipes (Figure 3.7a) and SF Pipes (Figure 3.7b), at the most compressed location of the cross-section ($\theta = 0$) for different levels of internal pressure ranging from $p = 1\%$ to $p = 10\%$. An important observation refers to the reduction of detachment size (amplitude) as the internal pressure increases. More specifically, in the case of $p = 10\%$, the detachment is practically zero, even for high values of applied curvature ($\kappa = 4$). A rapid increase of liner pipe detachment is also observed at normalised curvature value around $\kappa = 3$. This is beyond the limit point, where the bending moment of the liner pipe reaches its maximum value (an issue presented in a later paragraph of the present section), indicating excessive cross-sectional ovalisation of the liner pipe. The limit point of the liner corresponds to normalised curvature value around $\kappa = 2.5$.

The evolution of ovalisation in SF and TF Pipes under bending for various levels of pressure is shown in Figure 3.8. The ovalisation of the cross-section is slightly reduced with increasing internal pressure for high values of curvature. Furthermore, the results show that there is no difference between the response of SF Pipes and TF Pipes, which has also been observed by Vasilikis and Karamanos (2012) for non-pressurized lined pipes. In addition, Figure 3.9 shows the influence of different pressure levels on local hoop curvature of the liner pipe at the most compressed location of the cross-section $\theta = 0$ (Figure 3.6b). The results indicate that as the pressure level increases, the liner is more round. Furthermore, no difference is observed between SF and TF Pipes in terms of detachment and local hoop curvature.

Figure 3.10 shows the influence of internal pressure on the evolution of average axial stress across the thickness at $\theta = 0$ on both SF and TF Pipe. This average stress is computed using Simpson integration (default ABAQUS integration scheme through shell elements thickness) over the wall thickness of the liner pipe. The abrupt drop of stress after a value of κ equal to about 3, is due to the severe cross-sectional ovalisation of lined pipe. Figures 3.11a and 3.11b also show the evolution of moment of the lined pipe and liner pipe for several levels of internal pressure, respectively. The results show that the applied moment decreases at normalised curvature κ values of about 3, which is also attributed to cross-sectional ovalisation, which is interrelated with the corresponding decrease of axial stress of the liner pipe at $\theta = 0$, shown in Figure 3.10.

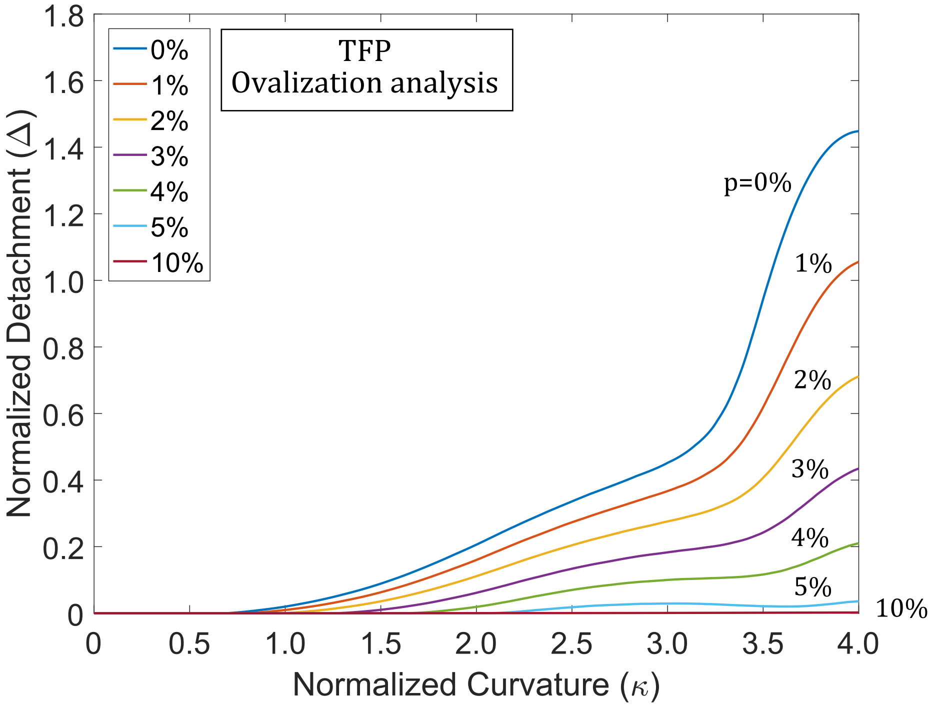

(a)

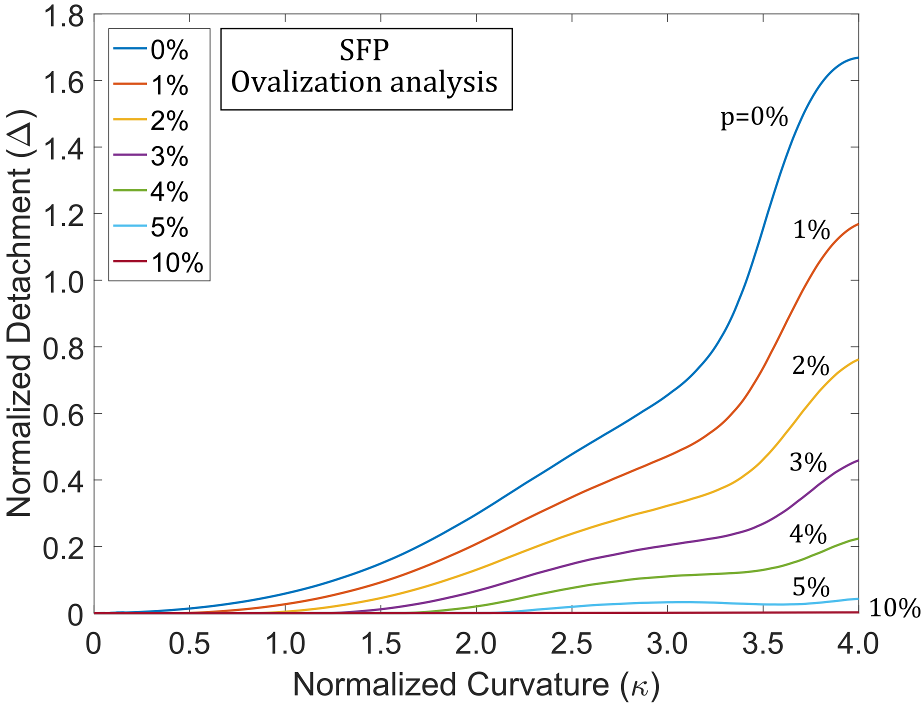

(b)

Figure 3.7 Detachment of liner from outer pipe for different levels of internal pressure (TF Pipe and SF Pipe); ovalisation analysis.

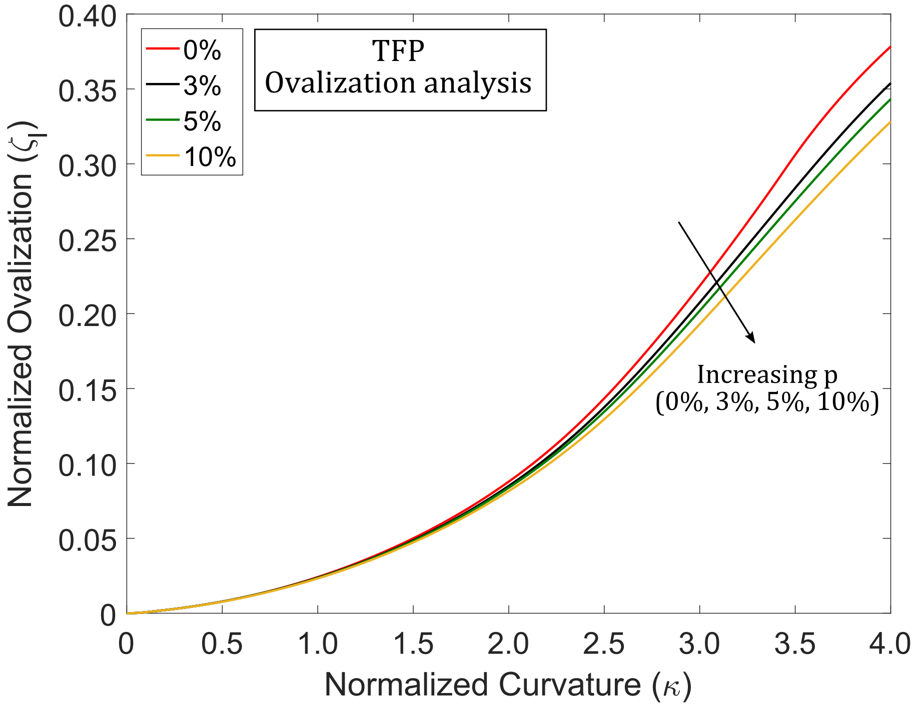

(a)

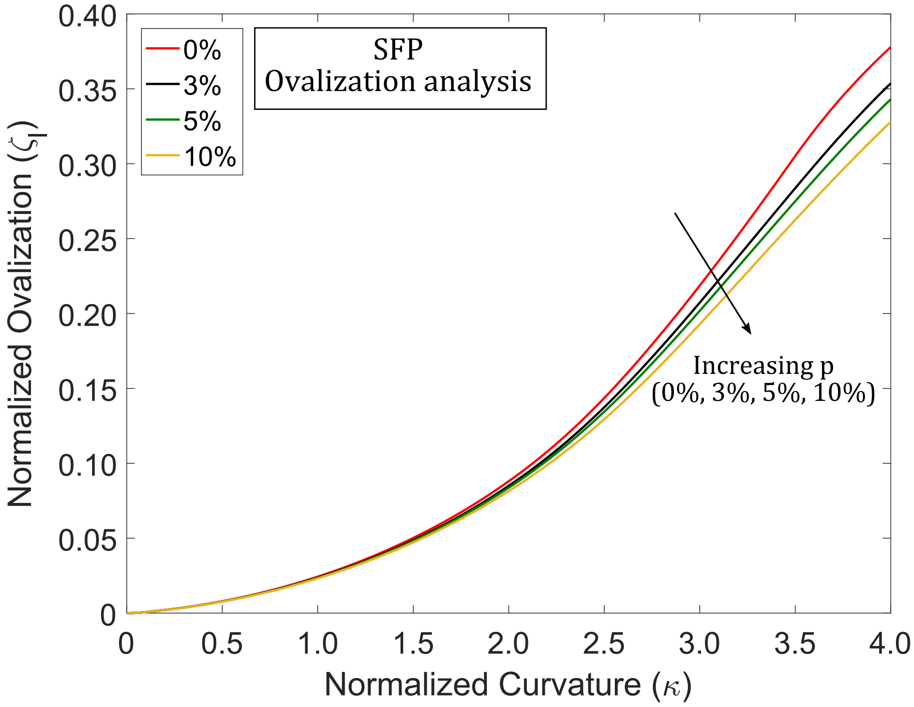

(b)

Figure 3.8 Increase of ovalisation of liner cross-section in terms of applied curvature for different levels of internal pressure for a (a) TF Pipe and (b) SF Pipe; ovalisation analysis.

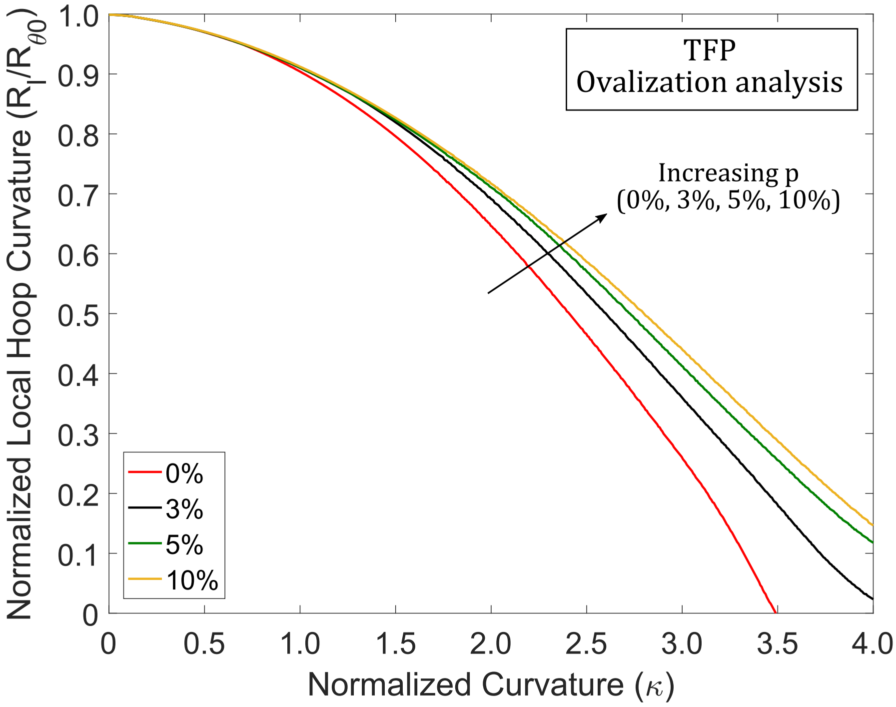

(a)

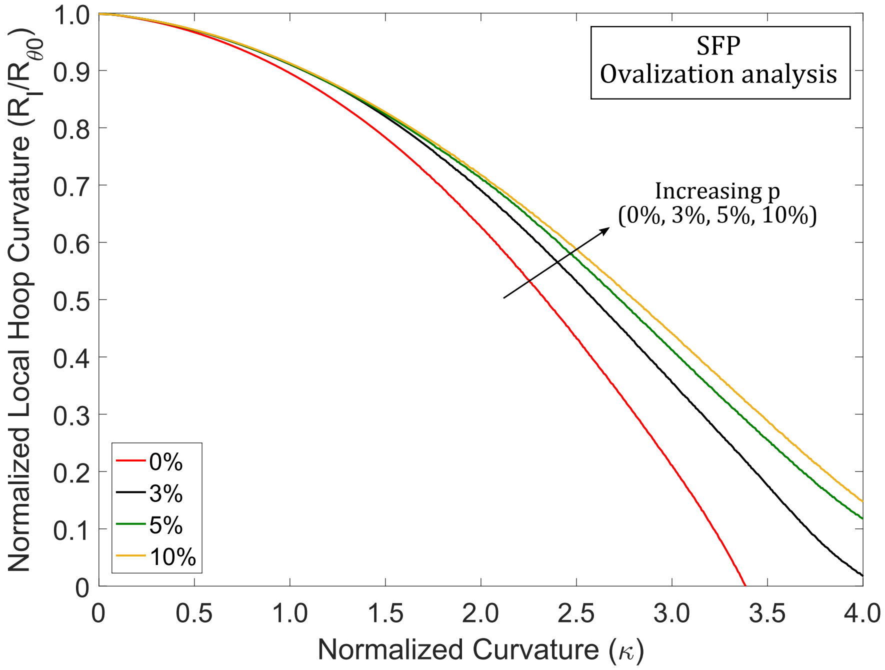

(b)

Figure 3.9 Evolution of local hoop curvature of liner at $\theta = 0$ in terms of applied curvature for different levels of internal pressure for a (a) TF Pipe and (b) SF Pipe; ovalisation analysis.

Furthermore, Figure 3.12 presents the distribution of axial stress across the wall thickness of the liner for different values of normalised curvature. For small values of κ the distribution is quasi-constant (as shown in Figure 3.12), despite the fact that the liner material is already in the inelastic region, whereas the distribution for larger values of κ is influenced by excessive cross-sectional ovalisation and local hoop bending. More specifically, hoop bending introduces hoop stresses that interact with longitudinal stresses due to inelastic material response through the von Mises (1928) yield criterion, which is presented schematically in Figure 2.2b and described by the following expression:

$$\sigma_y = \sqrt{\sigma_x^2 - \sigma_x \sigma_\theta + \sigma_\theta^2} \tag{3.3}$$

for a plane stress problem, such as in this case for the liner pipe.

Figure 3.13 depicts the variation of average axial stress through liner thickness with respect to the distance from the neutral axis around the cross-section (y/R_l), for different values of curvature. For high values of curvature, this is a variation reminiscent of the corresponding variation of stress observed in curved pipes (elbows), as described in detail by Karamanos (2016). Figure 3.14 presents the hoop stress at $\theta = 0$ of liner during bending for the TF Pipe. In those diagrams, the hoop stresses are compressive, but are shown positive for the sake of convenience. In this case, the liner is pre-stressed, due to the manufacturing process and initial hoop stress is 55% of yield stress. Upon applying curvature, the hoop compression of the liner pipe decreases, reaching a local low value around $\kappa = 0.7$, which corresponds to initiation of liner detachment, as shown in Figure 3.7a. Increasing further the applied curvature, the liner pipe tends to ovalise more than the outer pipe. Therefore, the outer pipe confines the increase of the horizontal diameter of the liner pipe, resulting in gradual increase of hoop compression.

In addition, there is no difference observed on the detachment and local hoop curvature between the response of SF and TF Pipes at $\theta = 0$, when increasing the level of internal pressure, even for high values of curvature, as indicated in Figures 3.15 and 3.16. The values of liner detachment of TFP and SFP in Figures 3.7a and 3.7b are larger than those of Figure 3.15 by two orders of magnitude, indicating the important influence of internal pressure on liner detachment. Furthermore, the normalised local hoop curvature $R_l/R_{\theta 0}$ increases by approximately 160%, for $p = 10\%$ (Figure 3.16) compared with non-pressurized pipes, for high values of curvature. In the case of non-pressurized pipes the local hoop curvature becomes zero at a curvature value around $\kappa = 3.5$, as shown in Figures 3.9 and 3.16, indicating that the liner has become flat at $\theta = 0$ location; beyond that stage, the local hoop curvature becomes negative, indicating that "inversion" of the liner pipe wall has occurred.

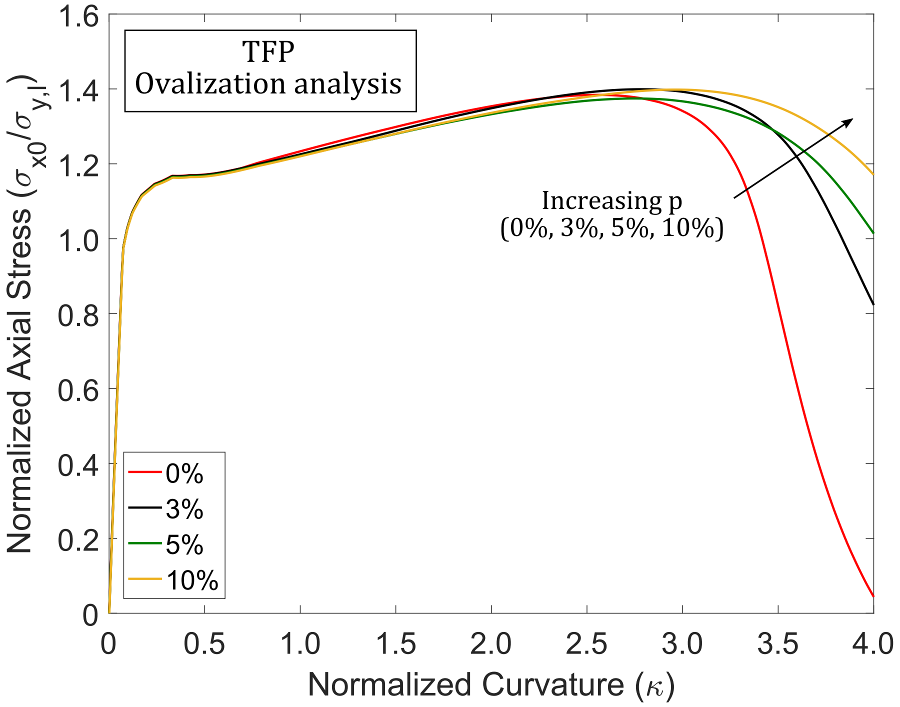

(a)

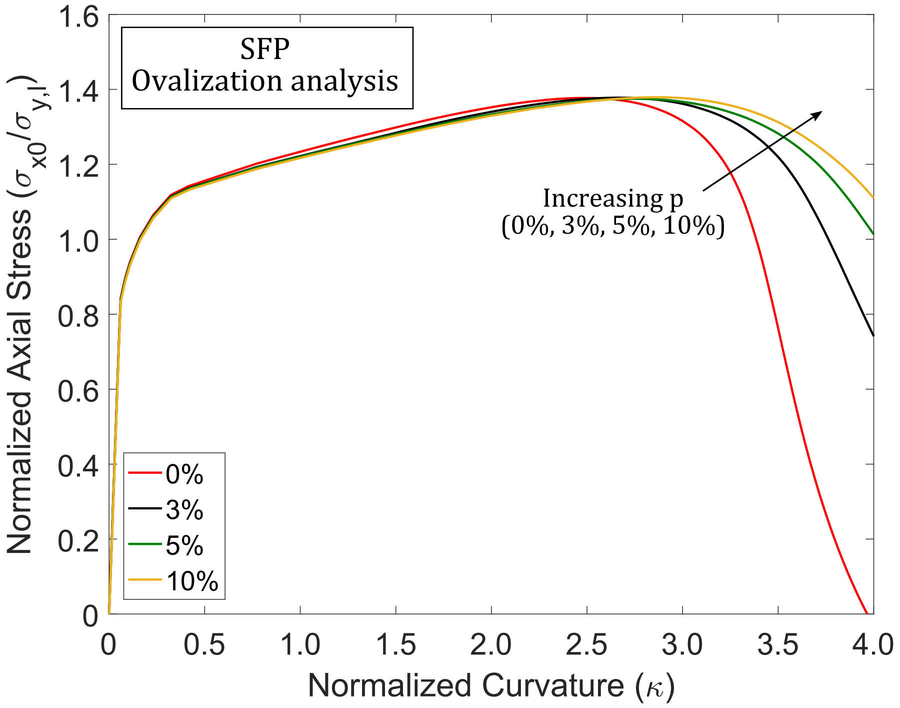

(b)

Figure 3.10 Evolution of average axial stress across the thickness of liner at $\theta = 0$ in terms of applied curvature for different levels of internal pressure for a (a) TF Pipe and (b) SF Pipe; ovalisation analysis.

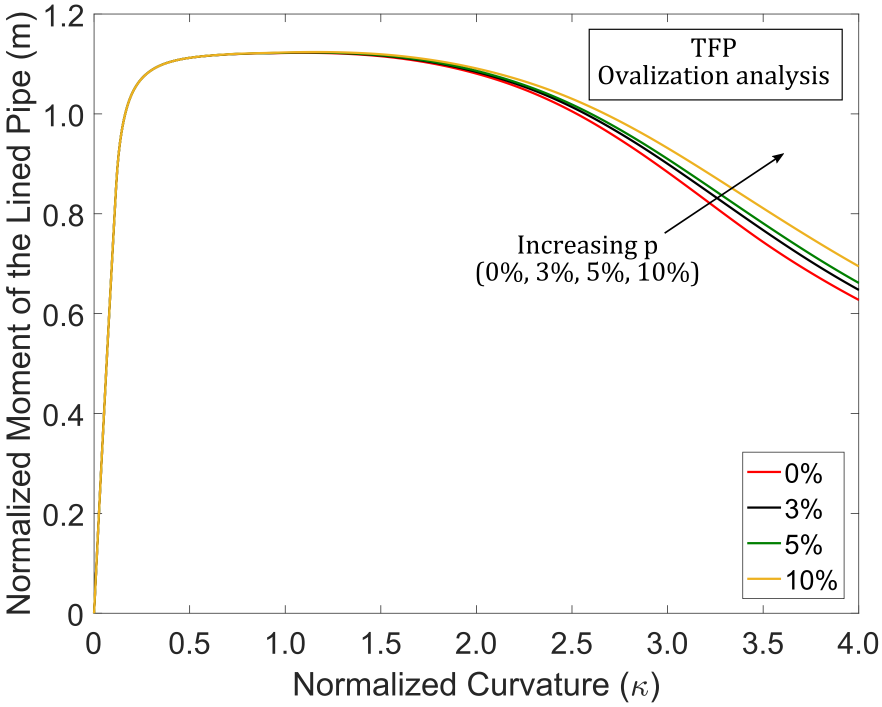

(a)

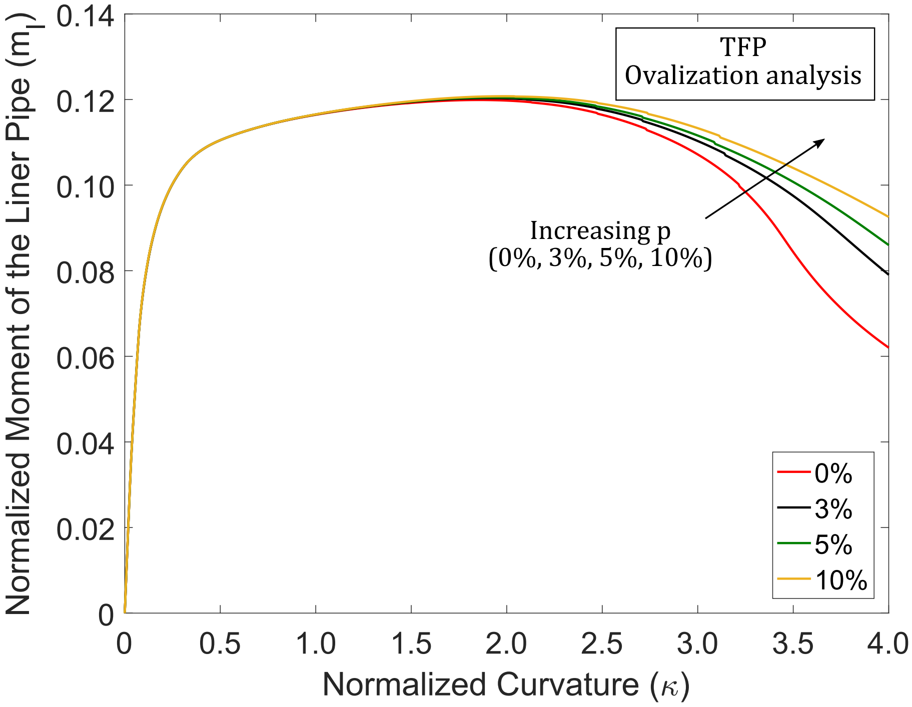

(b)

Figure 3.11 Bending moment for the entire lined pipe (TFP) and for the liner only, in terms of applied curvature for different levels of internal pressure; ovalisation analysis.

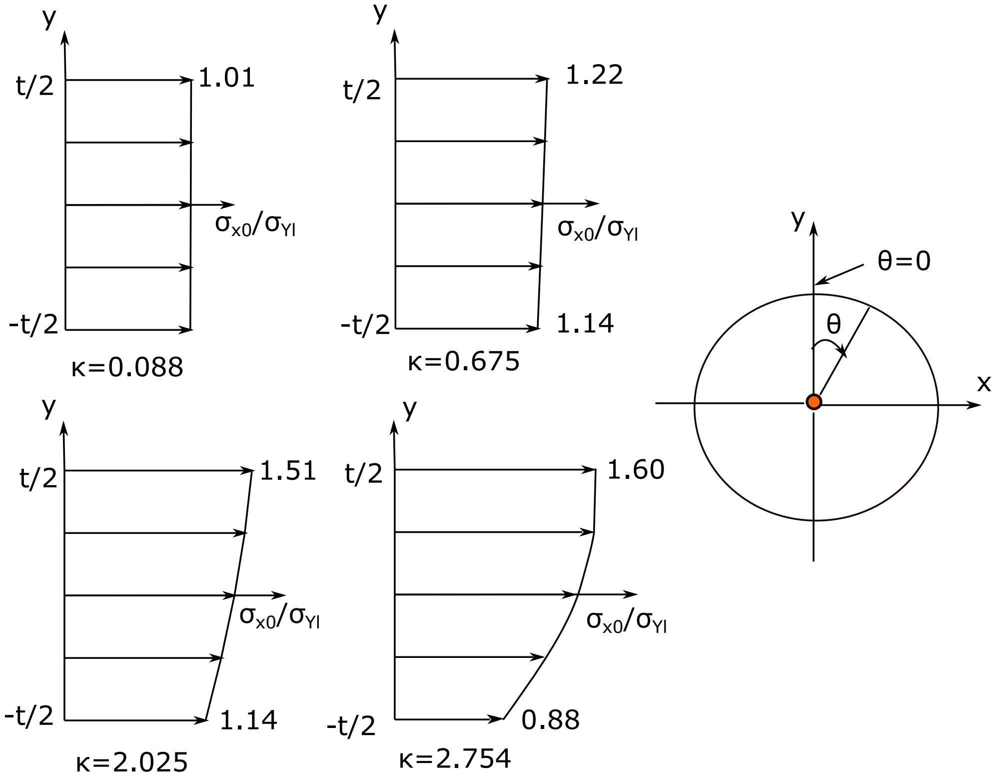

Figure 3.12 Variation of axial stress across the wall thickness at the most compressed location ($\theta = 0$) for different values of normalised curvature (κ); ovalisation analysis.

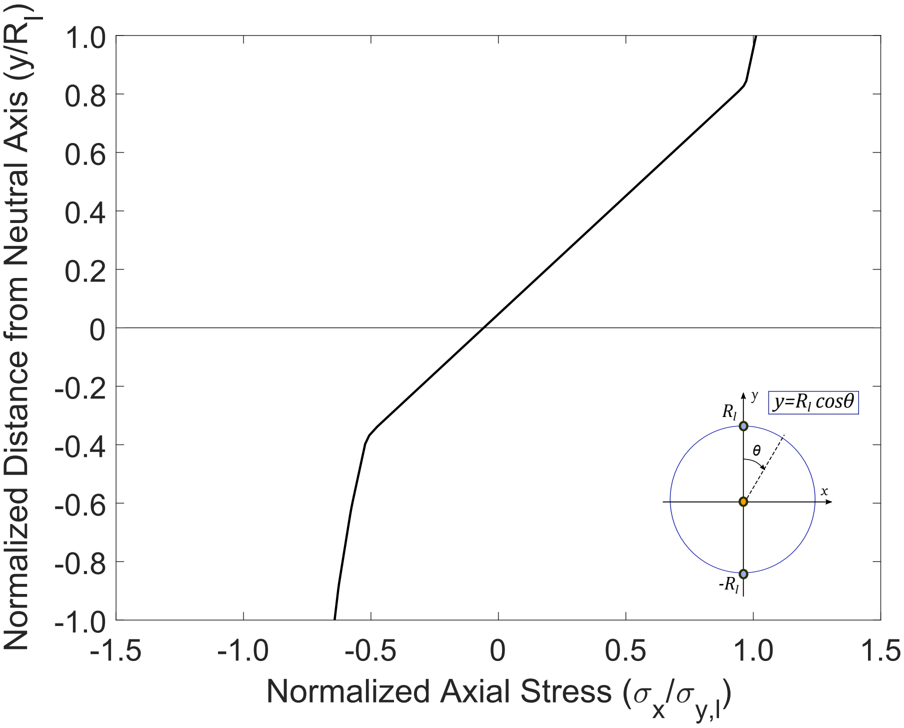

(a) $\kappa = 0.088$

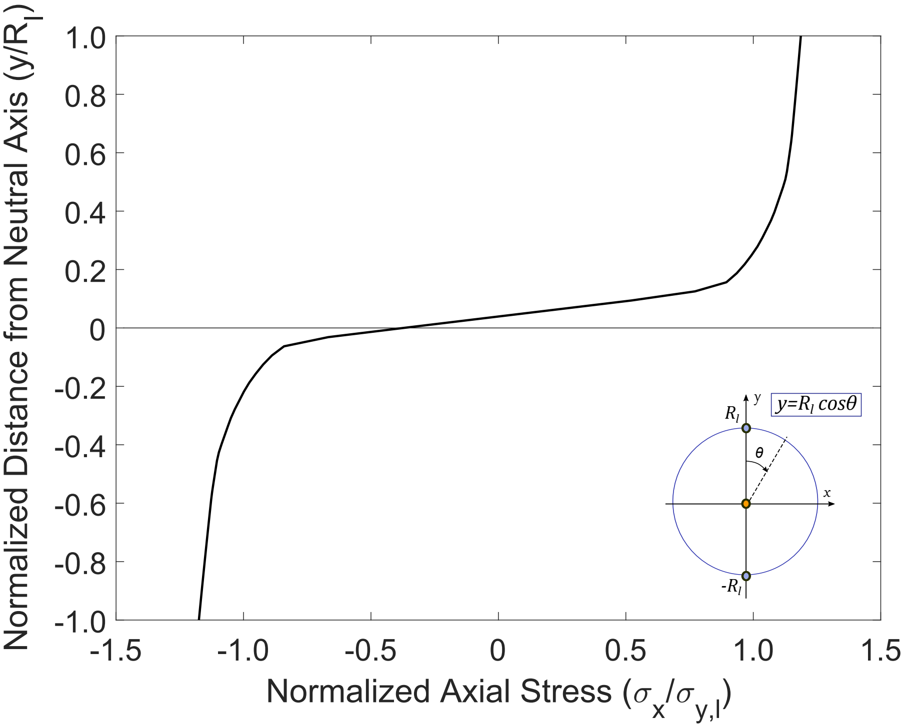

(b) $\kappa = 0.675$

Figure 3.13 Continues in the next page.

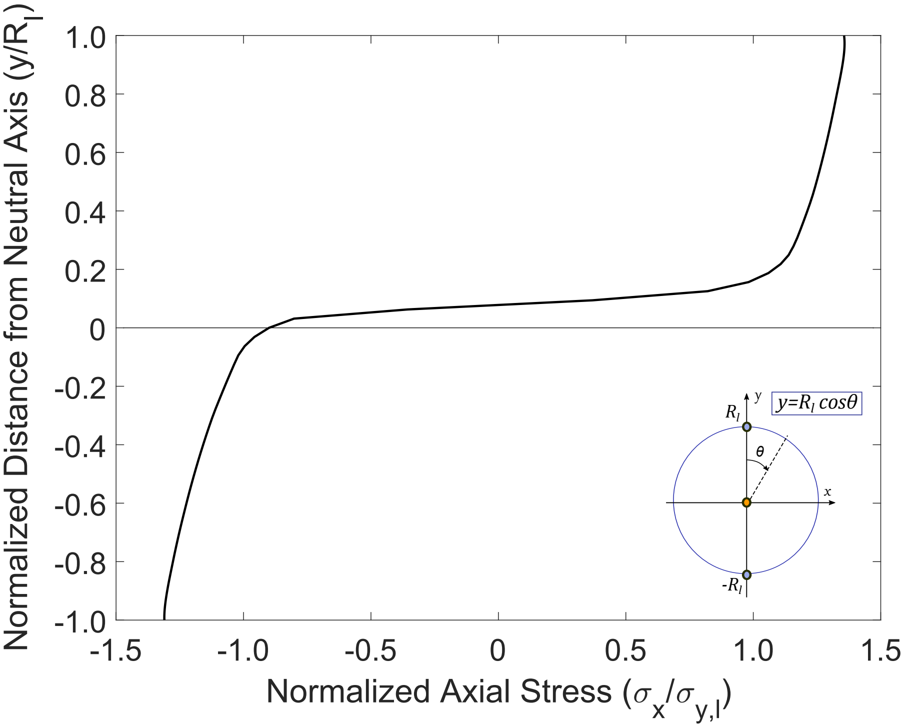

(c) $\kappa = 2.025$

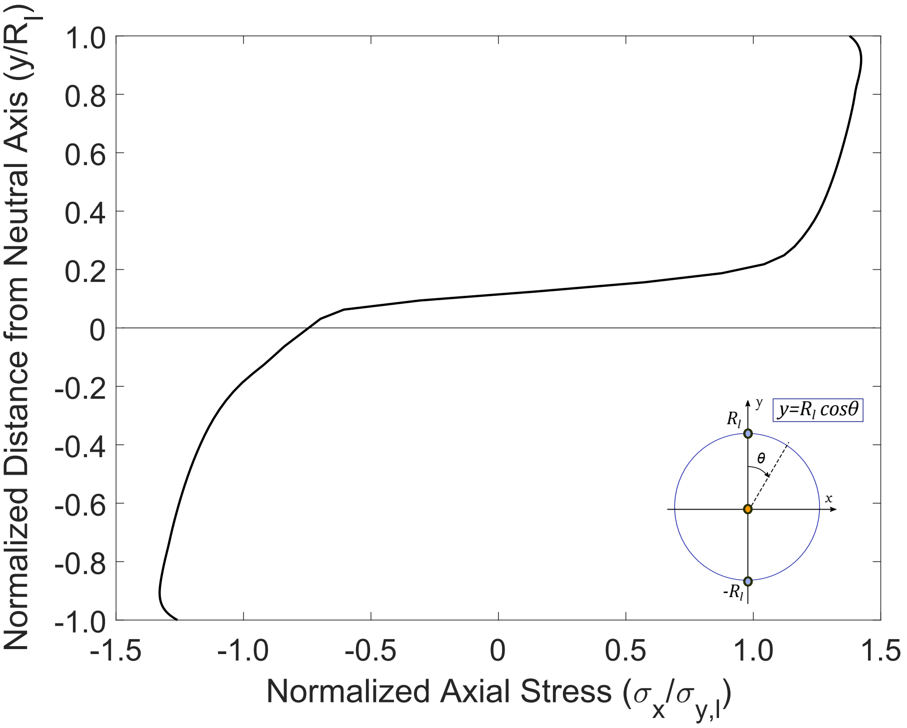

(d) $\kappa = 2.754$

Figure 3.13 Variation of average axial stress around the cross-section of the liner pipe for different values of curvature (κ); ovalisation analysis.

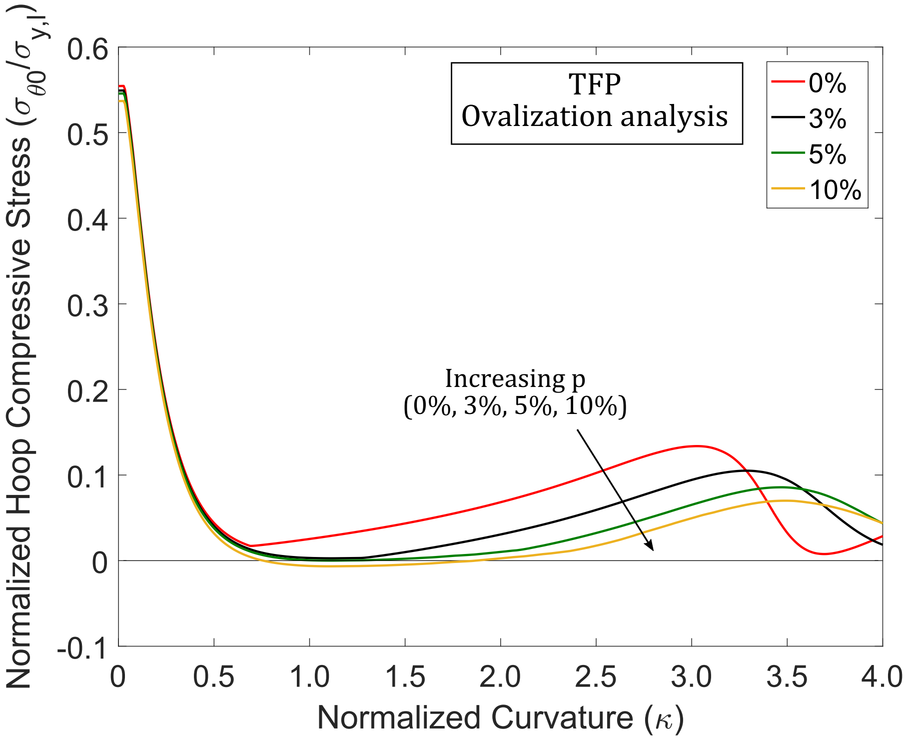

Figure 3.14 Variation of hoop stress in the liner pipe at $\theta = 0$, for different levels of internal pressure obtained from ovalisation analysis (hoop stresses are compressive).

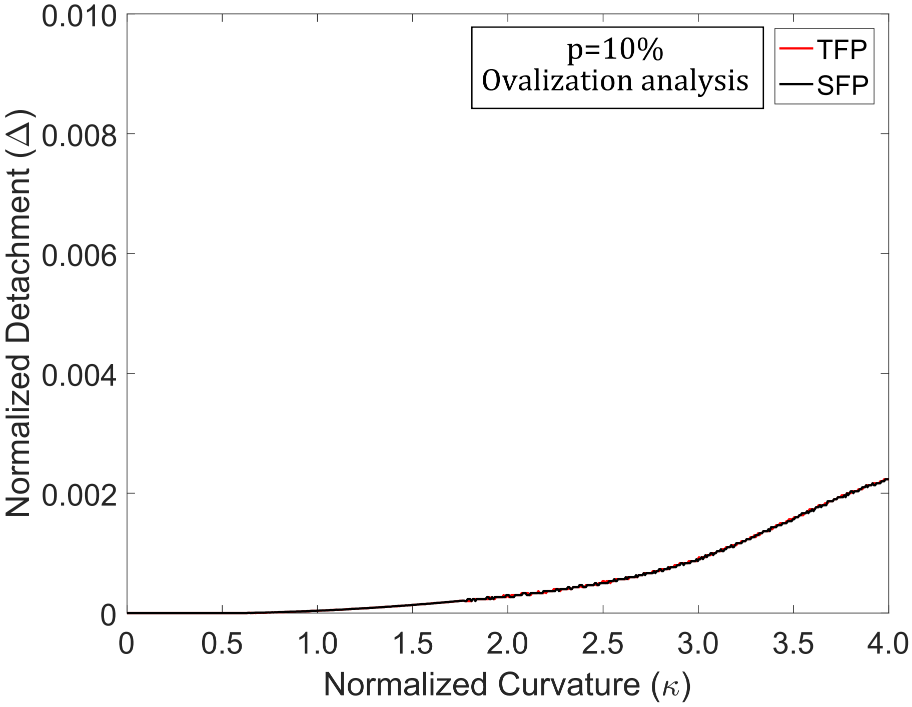

Figure 3.15 Comparison of liner detachment in SF and TF Pipes for $p = 10\%$; ovalisation analysis.

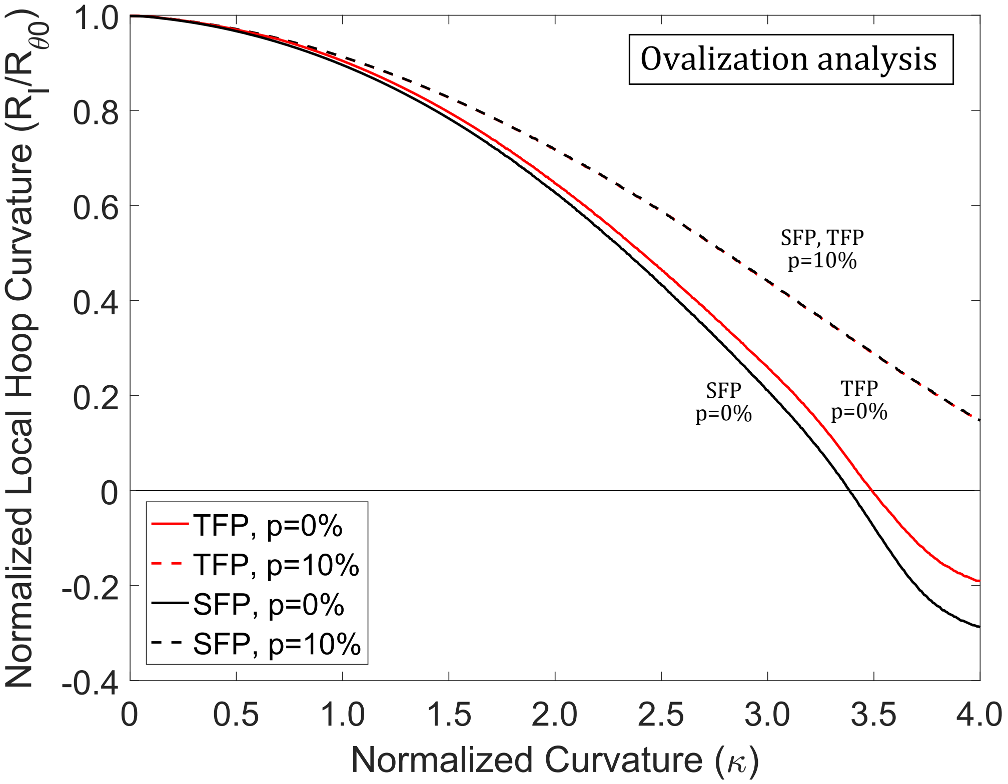

Figure 3.16 Comparison of normalised local hoop curvature at $\theta = 0$ between SF and TF Pipes, for $p = 0\%$ and $p = 10\%$; ovalisation analysis.

3.4.2 Buckling analysis

The mechanical behaviour of internally-pressurized steel lined pipes in terms of local buckling is investigated using the three-dimensional model shown in Figure 3.2, and the corresponding analysis will be referred to as “buckling analysis”. The results in this section refer to imperfection-free liners, whereas the effect of initial imperfections on pressurized bending response is examined in the following section 3.4.3. Figures 3.17a to 3.17d show the gradual detachment of the liner with increasing curvature along the pipe at $\theta = 0$ (the most compressed location of the cross-section) for SF and TF Pipes respectively, for zero and 10% level of internal pressure. In those figures, the vertical axis depicts the normalised detachment (Δ), and the normalised length (χ) spans along the pipe, as shown in Figure 3.3. In Figures 3.17a to 3.17d, the normalised length is also shown in the symmetric part ($\chi = -10$ to $\chi = 0$) mirroring the numerical results for visualization purpose.

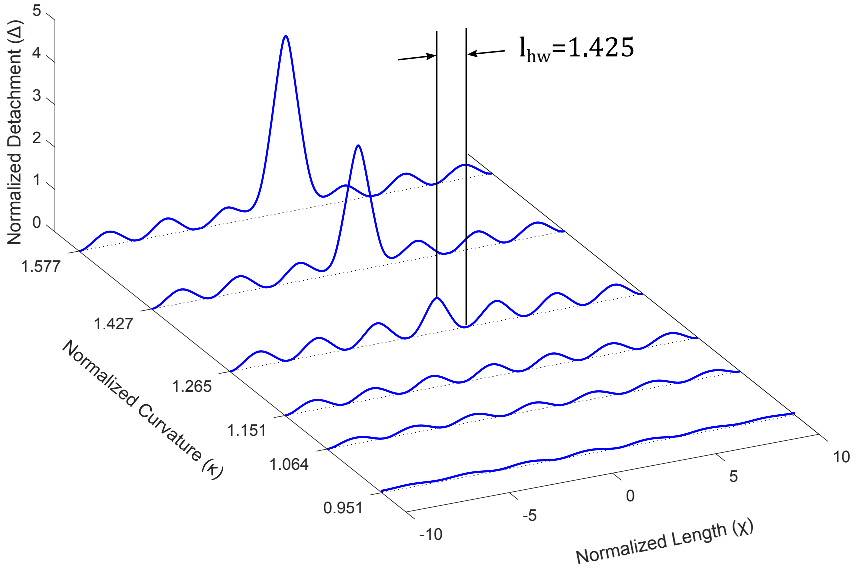

(a) Snug-fit pipe; $p = 0\%$.

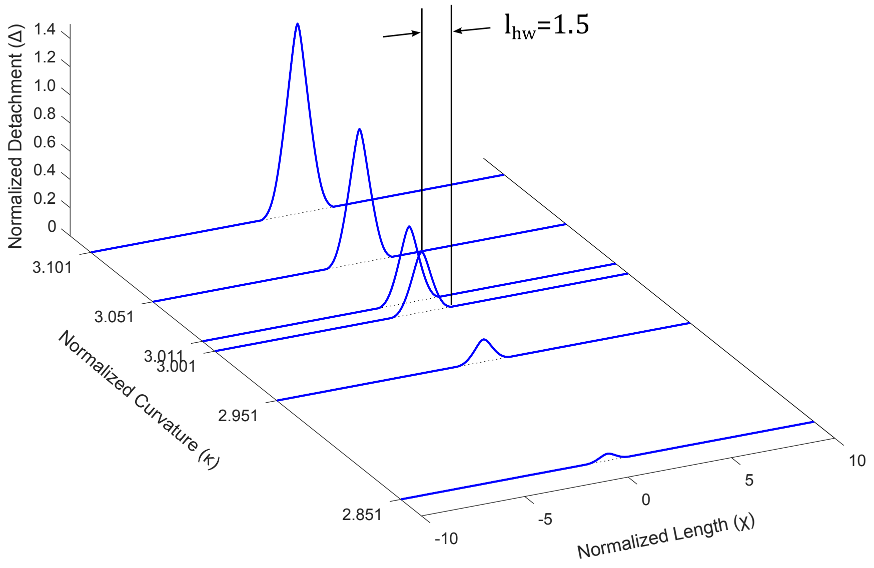

(b) Snug-fit pipe; $p = 10\%$.

Figure 3.17 Continues in the next page.

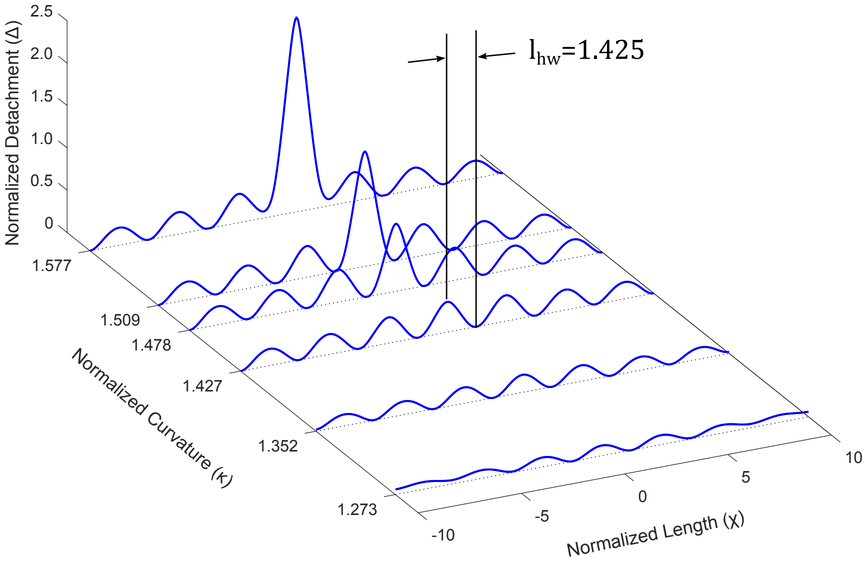

(c) Tight-fit pipe; $p = 0\%$.

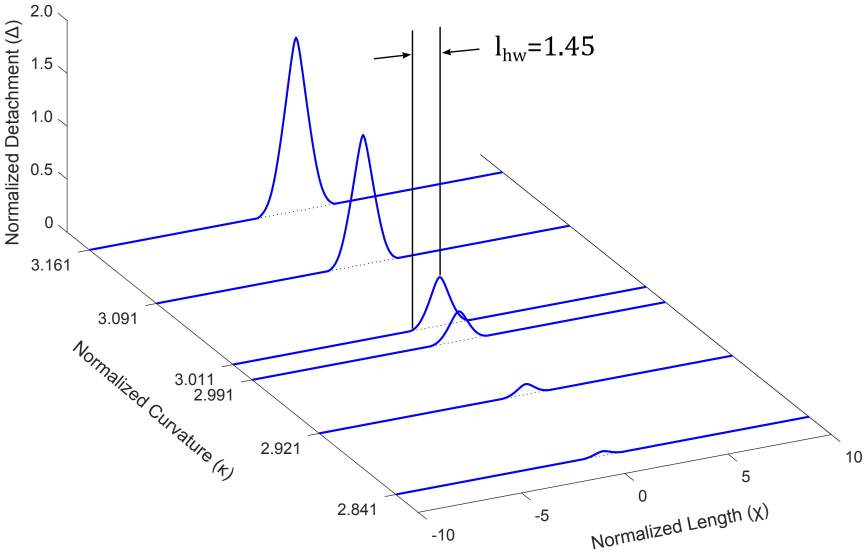

(d) Tight-fit pipe; $p = 0\%$.

Figure 3.17 Normalised detachment at $\theta = 0$ along SF and TF lined pipe under zero pressure and pressure equal to 10% of $P_{y,l}$.

It is observed that, soon after bending loading is applied, the liner ovalises more and detaches from the outer pipe. Furthermore, a quasi-uniform wrinkling is formed along the pipe due to the outer pipe confinement at the compression side, as shown in Figure 3.18a. This detachment and uniform wrinkling has been identified by Vasilikis and Karamanos (2012) as a first bifurcation for the non-pressurized case, and is also apparent herein for the presence of low levels of internal pressure up to $p = 10\%$. A second bifurcation shown in Figure 3.19 occurs at higher curvatures, also observed by Vasilikis and Karamanos (2012), leading to local buckling of the thin-walled liner pipe in the plastic range of the liner material into a diamond-type mode (Corona *et al.*, 2006; Ju and Kyriakides, 1991, 1992; Kyriakides and Ju, 1992; Tvergaard, 1983). As the level of internal pressure increases, detachment of liner pipe occurs at a later stage, which is beneficial for the pipe, enabling the pipe to deform at higher values of applied curvature without exhibiting local buckling. In Figures 3.17b and 3.17d (referring to SF and TF Pipes respectively) much higher curvature values are noticed, compared with the corresponding values observed in the absence of internal pressure (Figures 3.17a, 3.17c). The results show that increasing the internal pressure, the uniformly wrinkled configuration (shown in Figure 3.18a) tends to vanish, in a way that local buckling occurs rather abruptly at a very localized pattern (Figure 3.18b). The deformed configuration for all cases of internal pressure of TF Pipe are presented in Figure 3.19 at normalised curvature $\kappa = 3$, showing clearly the influence of pressure on the local buckling shape. Increasing the level of pressure, a reduction of the height of the main buckle (A) and of the four adjacent minor buckles (B) (presented in Figure 3.3) is observed, as shown in Figures 3.19, while the normalised detachment of the liner pipe from the outer pipe at normalised curvature $\kappa = 3$ for SF and TF Pipe is presented in Table 3.3 in more detail.

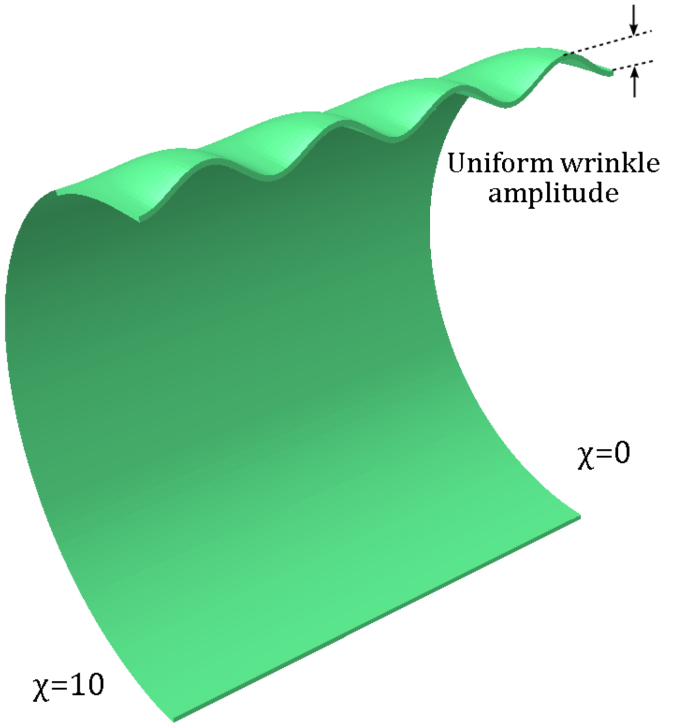

(a)

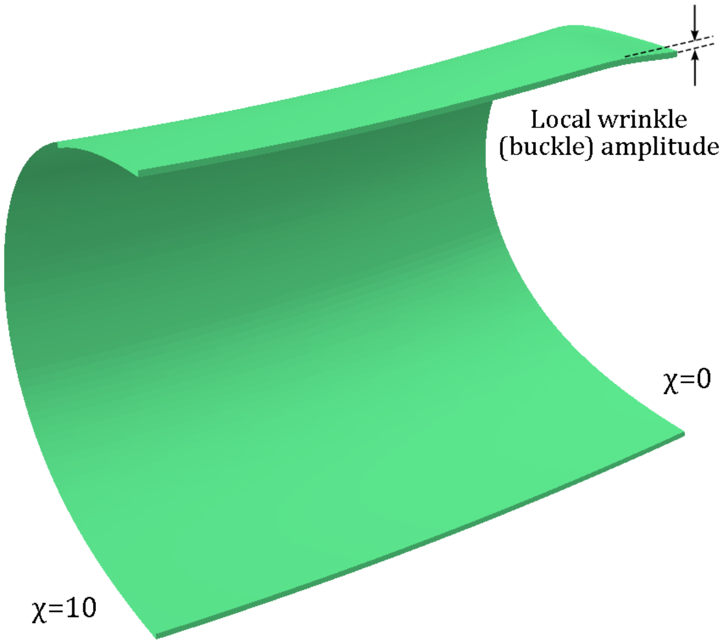

(b)

Figure 3.18 (a) Uniform wrinkling of liner pipe (low pressure levels), (b) localized buckling pattern of liner pipe (higher pressure levels).

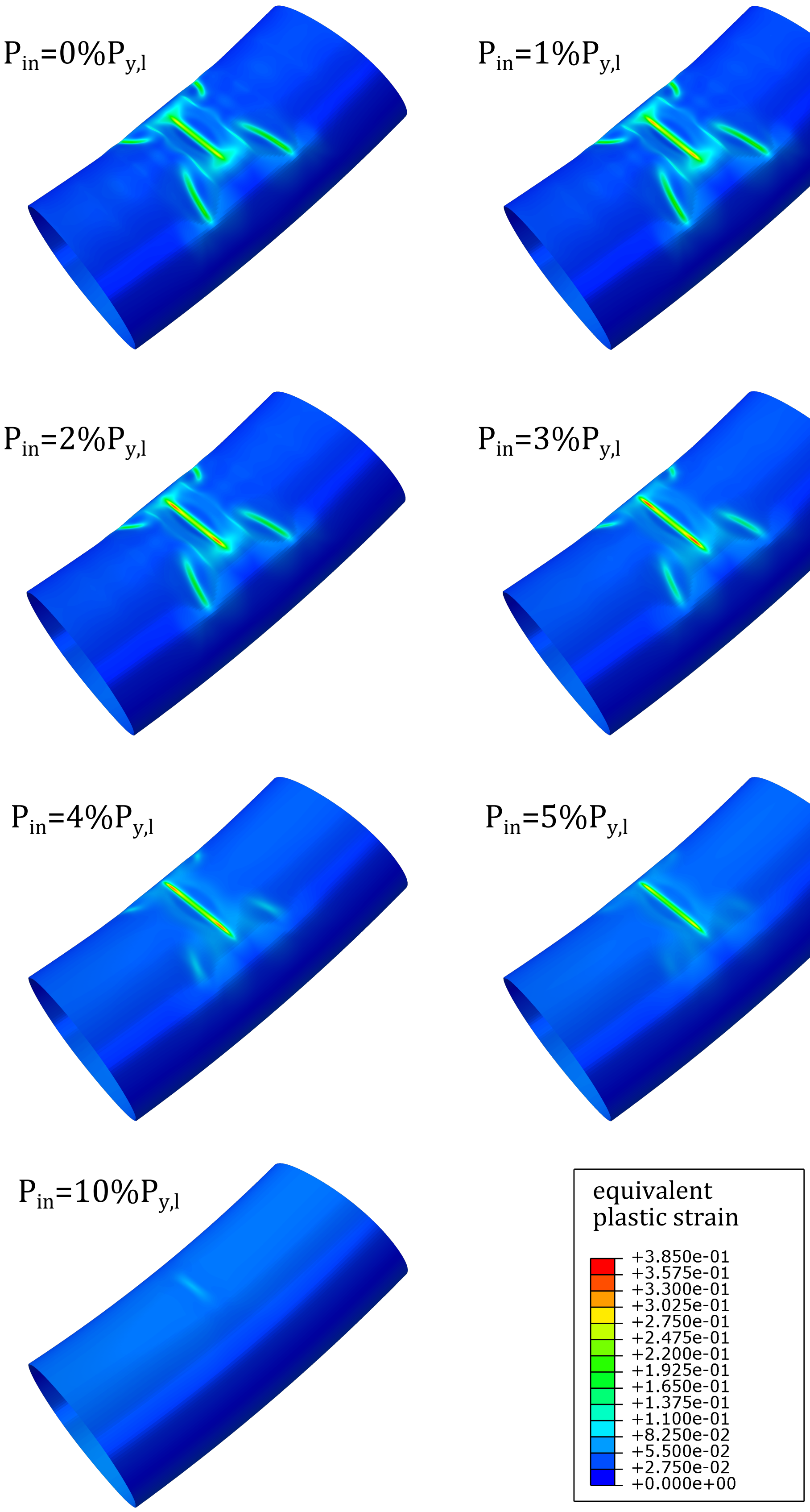

Figure 3.19 Liner buckled configuration for a TF Pipe, showing the distribution of equivalent plastic strain at normalised curvature $\kappa = 3$, for different levels of internal pressure.

Table 3.3 Normalised detachment (SF and TF Pipe) at main buckle (A) ($\chi = 0$) and curvature $\kappa = 3$ for different pressure levels.

Internal Pressure Level (p%)	Normalised Detachment of SFP (Δ%)	Normalised Detachment of TFP (Δ%)
0	853	751
1	824	761
2	731	710
3	640	633
4	542	538
5	444	439
10	43	36

At this point it is necessary to establish a definition of the "critical" curvature, which corresponds to failure of the structure beyond that value, so by referring to that value a quantitative comparison of different cases is possible. In case of zero internal pressure, the results in Figure 3.20 show that liner detachment initially increases slowly, forming a structurally stable uniform wrinkling. Beyond a specific value of curvature, the liner detachment increases rapidly, leading to diamond-type buckling mode of the liner pipe, an observation also reported in previous publications for thin-walled cylindrical shells (Kyriakides and Ju, 1992; Tvergaard, 1983). In particular, there is a value of curvature, at which the gradient of detachment ($d\Delta/d\kappa$) reaches its maximum value, as shown in Figure 3.20, corresponding also to the elastic-plastic bifurcation of the liner pipe (Gellin, 1980; Kyriakides and Shaw, 1982; Shaw and Kyriakides, 1985). This critical curvature definition is also in accordance with the results presented in Chapter 4, where the abrupt detachment of the liner pipe occurs at the same curvature that the bending moment of the liner drops sharply, indicating bifurcation instability of the pipe. Therefore, for the purpose of our study, this value of κ is considered as the critical (buckling) curvature of the liner, denoted as κ_{cr}, so that beyond this curvature the liner pipe is considered structurally unstable.

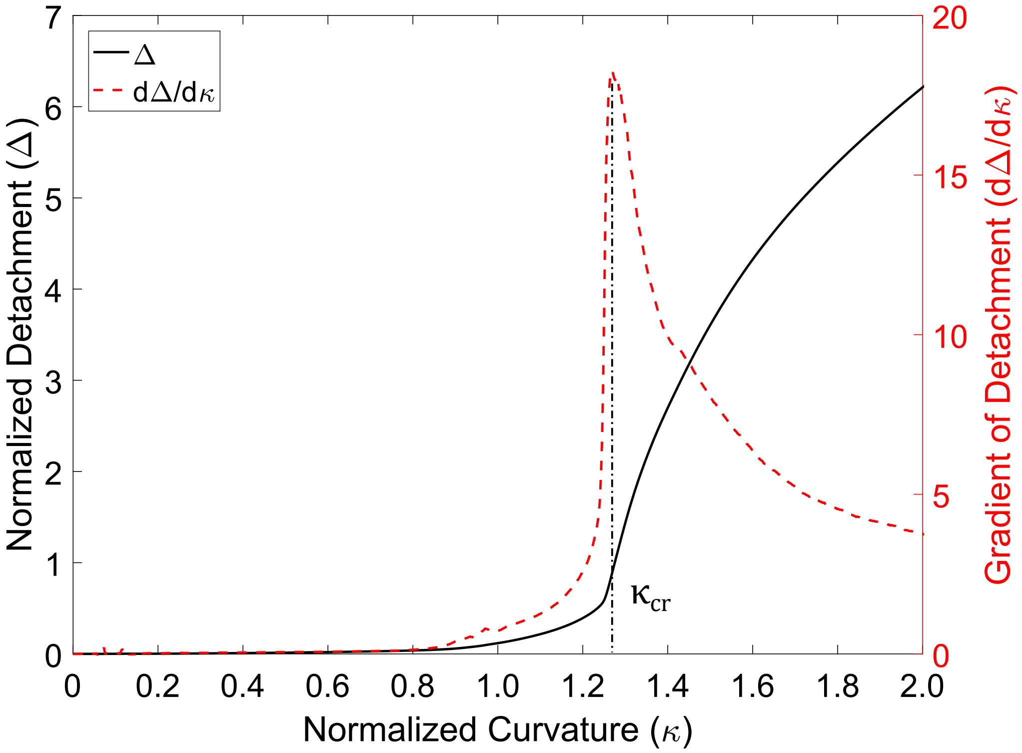

Figure 3.20 Variation of normalised detachment and gradient of detachment of SF Pipe without internal pressure at $\chi = 0$, in terms of normalised curvature.

Furthermore, the normalised half-wavelength ($l_{hw} = L_{hw}/\sqrt{D_{m,l}t_l}$) for non-pressurized SF and TF Pipes is equal to 1.425, as shown in Figures 3.17a and 3.17c, which is in good agreement with previous publications (Vasilikis, 2012; Vasilikis and Karamanos, 2012). These values are higher than the normalised half-wavelength of a single pipe exhibiting axisymmetric buckling, under axial compression and assuming elastic material behaviour (Timoshenko and Gere, 1961), which is equal to 1.222. This difference is attributed to both the lateral confinement of the liner pipe from the outer pipe and the inelastic behaviour of the liner material. In the case of 10% internal pressure level, the half-wavelength (l_{hw}) of the localized buckling pattern measured at the corresponding critical curvature value (κ_{cr}) is slightly increased, compared to the non-pressurized case, and it is equal to 1.5 and 1.45 for SF and TF Pipe, respectively (Figures 3.17b, 3.17d). This observation is in agreement with experimental and analytical results reported by Limam *et al.* (2010).

Figures 3.21 and 3.22 show the beneficial role of internal pressure on bending response in terms of the value of the critical curvature κ_{cr} and the results are summarized in Table 3.4, including the values of normalised detachment (Δ_{cr}), radius of curvature (ρ_{cr}) corresponding to the neutral axis of the pipe and global bending strain ($\varepsilon_{cr} = D_o/2\rho_{cr}$) at buckling for each type of pipe. It is clear that the critical curvature κ_{cr}

increases with increasing internal pressure significantly. More specifically, the κ_{cr} value for the SF Pipe is increased by 138% in the case of 10% pressure level, compared with the κ_{cr} value at zero pressure. For the TF Pipe the corresponding increase is 104%. Also, as the internal pressure increases, the critical curvature (κ_{cr}) values for the two pipes become quite similar. In the case of 10% internal pressure level, the critical curvature values are practically identical for SFP and TFP.

At this point, it should be noted that the beneficial effect of moderate levels of internal pressure during bending is clearly shown, but the critical curvatures for each internal pressure level and for both types of pipe are overestimated, due to the fact that the effect of manufacturing process on the material properties of the liner pipe is not taken into account. The influence of fabrication process on lined pipe bending response is investigated and presented in Chapter 4 in more detail.

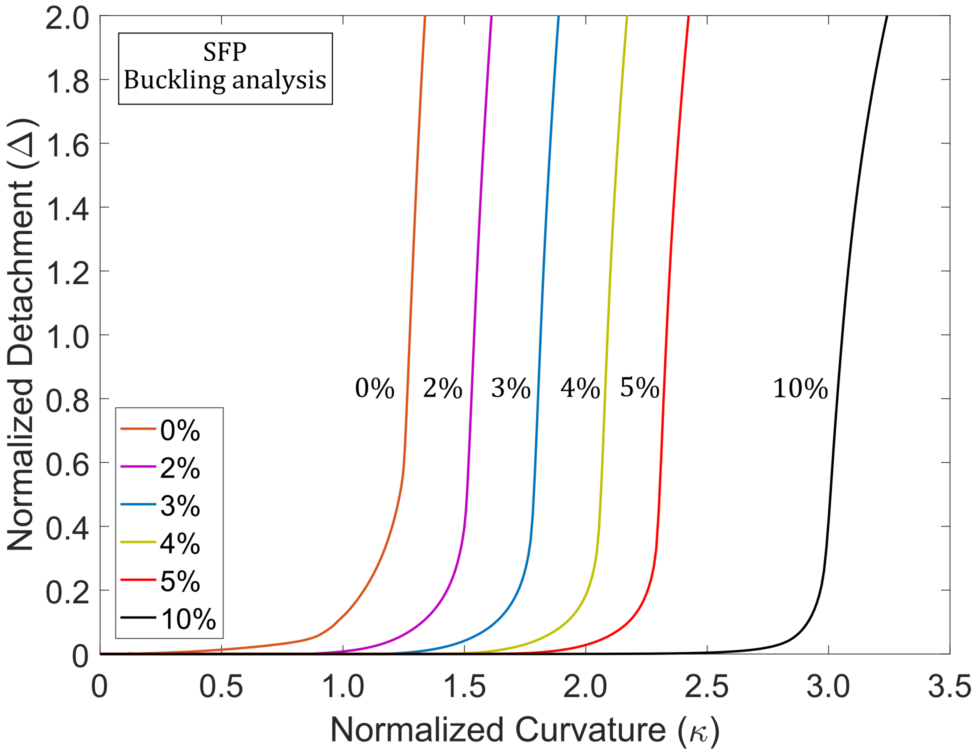

Figure 3.21 Normalised detachment at the centre of the main buckle ($\chi = 0$ and $\theta = 0$) of SF Pipes for different levels of internal pressure.

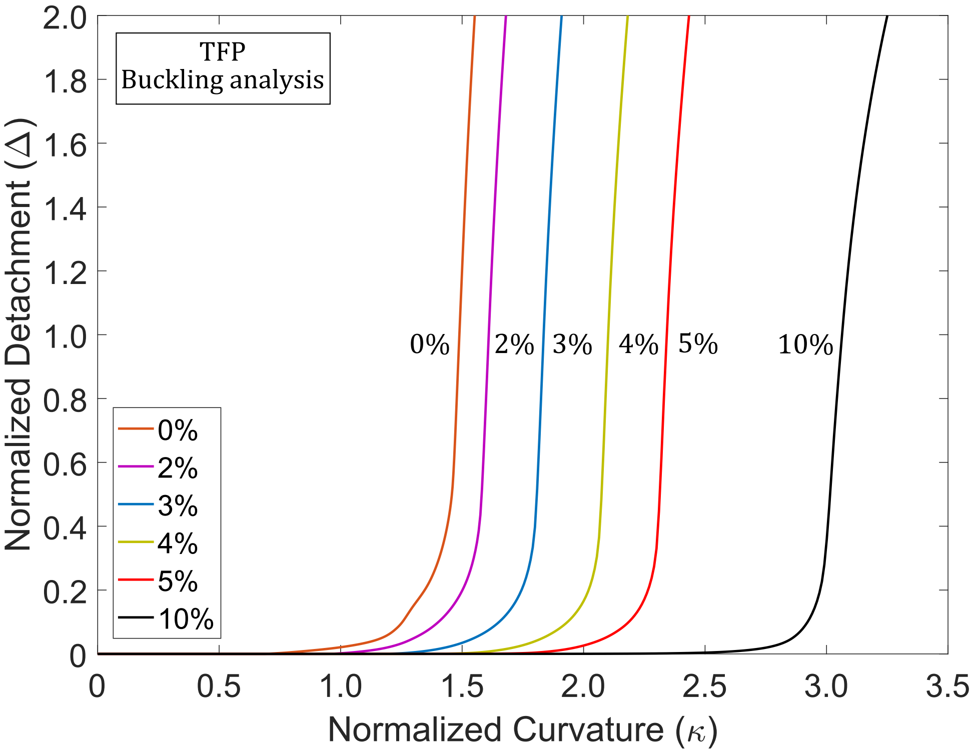

Figure 3.22 Normalised detachment at the centre of the main buckle ($\chi = 0$ and $\theta = 0$) of TF Pipes for different levels of internal pressure.

Table 3.4 Critical curvature, corresponding normalised detachment, radius of curvature and global bending strain for different pressure values of SF and TF Pipes.

Internal Pressure (p%)	Type of Pipe	Normalised Critical Curvature (κ_{cr})	Normalised Critical Detachment (Δ_{cr}%)	Buckling Radius of Curvature (ρ_{cr} mm)	Buckling Strain (ε_{cr} %)
0	SFP	1.265	81.7	5337	3.05
	TFP	1.478	79.7	4567	3.56
1	SFP	1.248	78.9	5409	3.00
	TFP	1.445	75.8	4672	3.48
2	SFP	1.534	88.8	4401	3.69
	TFP	1.602	86.9	4214	3.86
3	SFP	1.800	73.5	3750	4.33
	TFP	1.818	67.4	3713	4.38
4	SFP	2.075	72.0	3253	5.00
	TFP	2.082	64.1	3242	5.01
5	SFP	2.310	61.0	2922	5.56
	TFP	2.320	61.3	2910	5.58
10	SFP	3.011	53.9	2242	7.25
	TFP	3.011	46.0	2242	7.25

3.4.3 Imperfection sensitivity of pressurized lined pipes

The numerical results for the critical curvature value κ_{cr}, shown in Table 3.4 for each level of internal pressure, refer to imperfection-free (perfect) pipes. Focke (2007) detected initial wrinkles on the liner pipe after the manufacturing process, ranging from 4.7% to 9.3% of the liner pipe wall thickness. For these measurements, a laser trolley was developed, moving on wheels through the pipe. In order to scan the inner surface of the pipe, circumferential scans were performed at defined intervals along the pipe. Initial geometric imperfections are introduced to the liner pipe either during fabrication of the liner pipe or during the manufacturing process of the mechanically bonded lined pipe, when the liner establishes contact with the outer pipe. In may cases, the outer pipe is seamless fabricated from round billets, which are pierced at elevated temperature (Kyriakides and Corona, 2007), introducing a spiral-type geometric imperfection in the inner surface of the seamless pipe with a wavelength depending on fabrication process parameters (i.e. feed speed, piercer dimensions). This spiral imperfection is imprinted on the liner pipe during the manufacturing process of the lined pipe. A typical initial wrinkle amplitude is around 10% of the liner pipe wall thickness (Pépin *et al.*, 2017; Tkaczyk *et al.*, 2020), while experimental measurements presented by Harrison *et al.* (2016) verify the aforementioned liner pipe wrinkle amplitudes. Harrison *et al.* (2016) used custom scanning devices to measure the liner imperfections, characterised by trigonometric Fourier series. More specifically, two schemes were presented. The first involves a custom trolley that rides the internal surface of the liner pipe on wheels, performing circumferential scans of the inner surface. In the second, the pipe is fixed, while both the inner and the outer surface of the pipe are scanned, using non-contact instruments.

In the present section, sensitivity analysis of the bending response for different levels of initial geometric imperfection is conducted for the case of 10% internal pressure level. The shape of initial imperfection for both SF and TF Pipe refers to the liner (the outer pipe has no imperfections) and is assumed in the form of the buckling configuration of the corresponding imperfection-free lined pipe and its amplitude, normalised by the liner pipe wall thickness (t_l), is denoted as Δ_0. It is expected that this shape of imperfection simulates the worst-case imperfection scenario for the liner pipe. It should be noted that other types of imperfection, such as mismatch of material properties between consecutive pipe segments or fluctuation of the liner wall thickness value, are not considered in the present study. As shown in Figures 3.17b and 3.17d, the liner pipe at this level of pressure does not exhibit uniform wrinkling, but, instead, it buckles locally with a main buckle, as shown in Figure 3.18b. The deformed configuration of the "perfect" pipe is imported as initial shape of the imperfect lined pipe, assuming an initial wrinkle, and several imperfection amplitudes can be imposed through appropriate magnification. The initial imperfection amplitude Δ_0 ranges between 1% and 13.5% of the liner wall thickness t_l. It is noted though, that the wrinkled shape is imposed geometrically before initial pre-stressing is applied on the TF Pipe and prior to the application of internal pressure on both pipes. The influence of initial wrinkling imperfections on the bending response of both types of lined pipe is depicted in Figures 3.23 and 3.24 ($p = 10\%$).

In addition, Figure 3.25 presents the critical curvature for both types of pipe with respect to the value of the imperfection amplitudes (Δ_0) for pressurized and non-pressurized lined pipes. In the case of non-pressurized pipes a uniform wrinkling imperfection is considered, as shown in Figure 3.18a. With increasing imperfection amplitude, the critical curvature decreases, especially for SF Pipes. Furthermore, this imperfection sensitivity, for pressurized lined pipes, is significantly less pronounced for small values of Δ_0, compared to the one observed in the case of zero pressure as shown in Figure 3.25. The latter case has also been reported in the paper by Vasilikis and

Karamanos (2012). The difference between SFP and TFP results is due to the effects of pre-stressing on the initial imperfection amplitude. Upon application of pre-stressing, the initial value of imperfection Δ_0 is significantly reduced to a lower value, which may be referred to as "residual imperfection". The residual imperfection amplitude is significantly smaller compared to the Δ_0 value (as shown in Figure 3.26 and in Table 3.5). Furthermore, the presence of internal pressure further reduces the amplitude of this initial imperfection by a certain amount, also depicted in Figure 3.26 and Table 3.5. For initial imperfection of 10% amplitude, the κ_{cr} value decreases by 73% and 18% for SF and TF Pipe, respectively, with respect to the imperfection-free case. Table 3.6 summarizes the critical curvature κ_{cr}, with the corresponding value of detachment at buckling Δ_{cr}, in terms of the value of imperfection amplitude Δ_0.

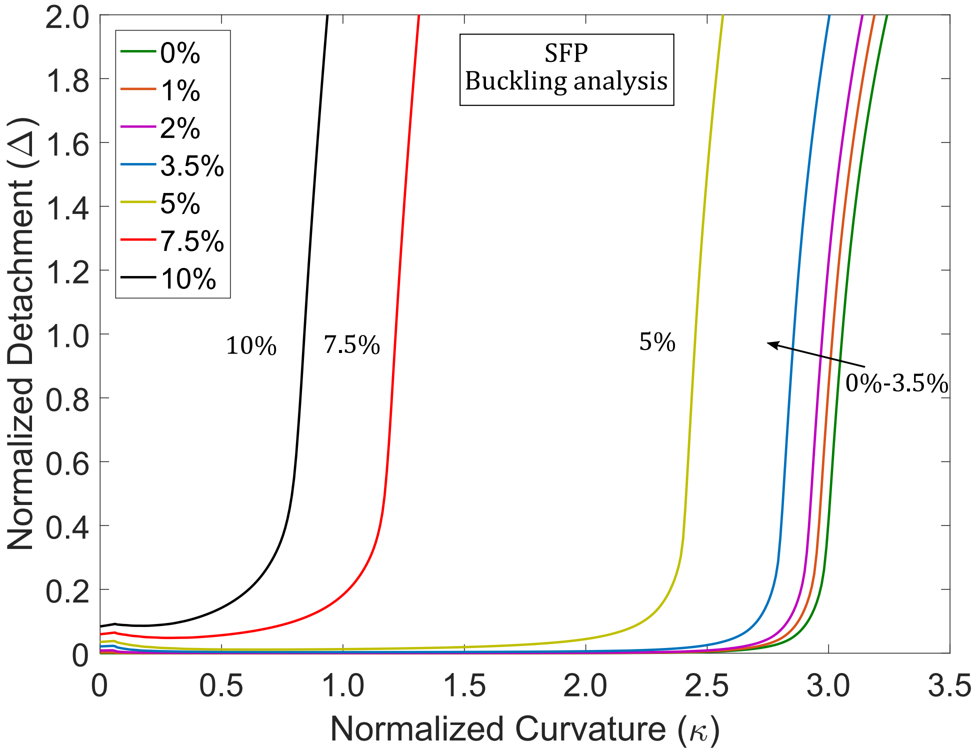

Figure 3.23 Development of liner detachment in SF Pipes with respect to applied curvature for different imperfection amplitudes ($p = 10\%$).

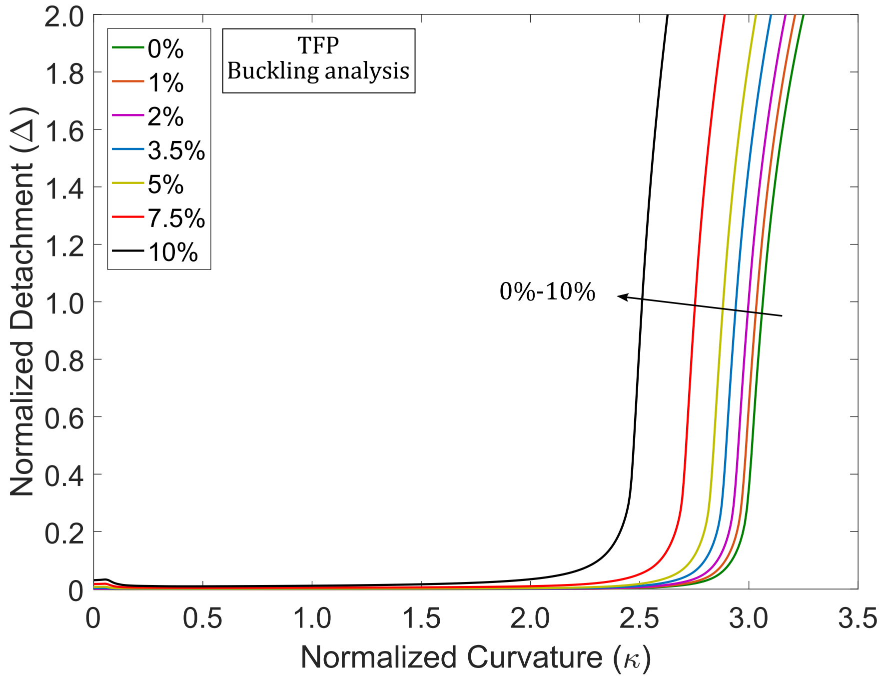

Figure 3.24 Development of liner detachment in TF Pipes with respect to applied curvature for different imperfection amplitudes ($p = 10\%$).

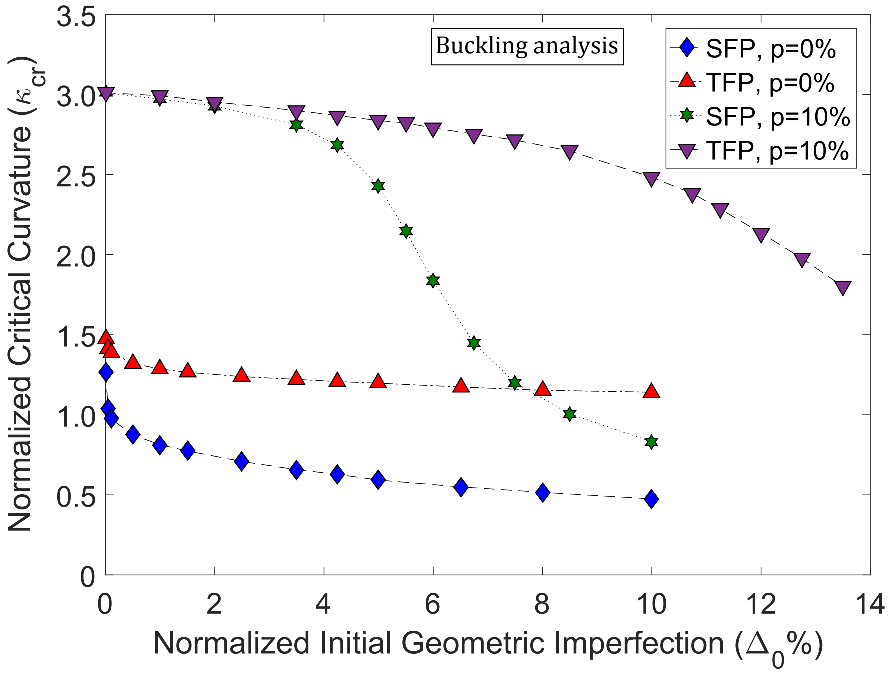

Figure 3.25 Variation of normalised value of critical curvature (κ_{cr}) of SF and TF Pipe in terms of initial imperfection amplitude ($p = 10\%$).

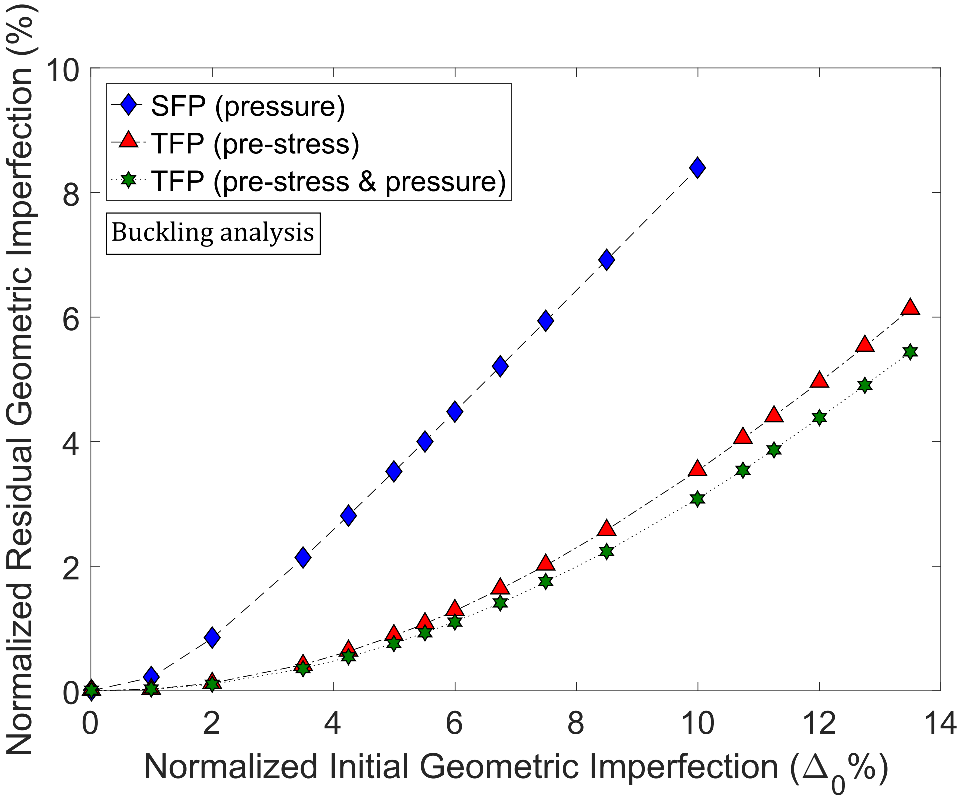

Figure 3.26 Normalised residual imperfection of SF and TF Pipes in terms of initial imperfection amplitude (Δ_0) for the case of $p = 10\%$.

Table 3.5 Residual imperfection amplitude in SF and TF Pipes with 10% internal pressure.

Initial Imperfection (Δ_0%)	Residual Imperfection of SFP	Residual Imperfection of TFP: After pre-stressing (before pressure)	Residual Imperfection of TFP: After pre-stressing and pressure
1.0	0.216	0.027	0.024
2.0	0.845	0.124	0.106
3.5	2.131	0.421	0.358
4.25	2.820	0.635	0.542
5.0	3.528	0.888	0.764
5.5	4.006	1.076	0.931
6.0	4.487	1.287	1.111
6.75	5.212	1.637	1.409
7.5	5.991	2.016	1.749
8.5	6.919	2.584	2.240
10.0	8.394	3.537	3.087
10.75	-	4.058	3.547
11.25	-	4.411	3.873
12.0	-	4.954	4.381
12.75	-	5.528	4.905
13.5	-	6.125	5.436

Table 3.6 Critical curvature and corresponding detachment for different imperfection amplitudes of SF and TF Pipes with 10% internal pressure level.

	SFP		TFP	
Initial Imperfection (Δ_0%)	Normalised Critical Curvature (κ_{cr})	Normalised Critical Detachment (Δ_{cr}%)	Normalised Critical Curvature (κ_{cr})	Normalised Critical Detachment (Δ_{cr}%)
0	3.011	53.9	3.011	46.0
1.0	2.971	51.8	2.992	55.1
2.0	2.928	49.9	2.953	51.8
3.5	2.810	45.8	2.899	53.2
4.25	2.683	50.9	2.868	49.8
5.0	2.428	69.0	2.837	47.8
5.5	2.146	67.2	2.822	56.0
6.0	1.836	76.7	2.791	47.8
6.75	1.445	70.4	2.752	49.0
7.5	1.199	77.4	2.715	53.1
8.5	1.006	85.1	2.647	60.8
10.0	0.832	88.1	2.483	63.6
10.75	-	-	2.381	68.7
11.25	-	-	2.285	66.4
12.0	-	-	2.135	71.2
12.75	-	-	1.976	81.1
13.5	-	-	1.800	80.5

3.5 Summary of results

In the case of non-pressurized lined pipes, it is shown that the liner pipe detaches from the outer pipe, upon applying monotonically increasing bending load, forming short-wave uniform wrinkles at the compression side. Further increase of the applied curvature results in local buckling of the liner pipe, characterized by a main buckle and four adjacent minor buckles. This is a phenomenon reported previously in experimental and numerical results, while it is verified in the present chapter in order to develop an accurate numerical model. Subsequently, different levels of internal pressure are applied followed by monotonic bending, showing that as the pressure level increases gradually the local buckling of the liner pipe delays significantly. In the case of internal pressure levels up to 4% of the liner pipe plastic pressure, at first uniform wrinkling (first bifurcation) and then local buckling (second bifurcation) is observed, similar to the non-pressurized lined pipe case. For pressure level equal to 10% of the liner pipe plastic pressure, the uniform wrinkling pattern vanishes and the lined pipe exhibits buckling quite suddenly in the form of a localized pattern. It is also important to mention that the maximum internal pressure level applied in the present study is chosen five times lower than the one reported in current industrial practices (50% of $P_{y,l}$), highlighting its beneficial effect on liner local buckling during monotonic bending.

Furthermore, it is shown that the liner pre-stressing, simulating the mechanical bonding due to manufacturing process, on the structural response of the lined pipe becomes smaller with increasing the level of internal pressure. In addition, the bending response of initially imperfect liner pipes is examined, in the absence of internal pressure. It is shown an important decrease on the critical curvature, even for small imperfection amplitudes. In the case of TF Pipes, the residual imperfection is significantly affected by pre-stressing playing a major role in the imperfection sensitivity of the liner pipe. On the other hand, for internally pressurized lined pipes, with pressure equal to 10% of the liner pipe yield pressure, the critical curvature decrease occurs in higher imperfection amplitudes, especially for TF Pipes, verifying the beneficial role of internal pressure.

Chapter 4

Influence of manufacturing process on lined pipe monotonic bending

4.1 Chapter outline

In the present chapter, a special-purpose finite element model is developed incorporating at the first stage the simulation of the manufacturing process of mechanically bonded lined pipes and proceeds to the modelling of their bending behaviour at the second stage of the analysis. The proposed model accounts for two methodologies of lined pipe fabrication, used by the pipeline industry, as discussed in previous publications as discussed in Chapter 1. The first methodology consists of hydraulic expansion of both pipes up to elastic or plastic deformation in the outer pipe, whereas the second methodology involves a thermo-hydraulic process, leading to the so-called "tight-fit pipe" (TFP). Upon completion of the simulation of the fabrication process, the present analysis proceeds in monotonic bending of the lined pipe, using the same finite element model, until structural failure of the liner occurs in the form of wrinkling. More specifically, the present analysis offers an integrated approach that employs a single finite element model, which assesses the manufacturing process and the structural bending in subsequent stages. Special emphasis is given on the material model of the liner and the outer pipe. Both materials are described using advanced plasticity models obeying non-linear kinematic hardening, capable of accounting for reverse plastic loading effects, and are calibrated with available experimental data. Parametric analyses are also conducted, considering the effect of initial radial gap of both pipes, different heating temperatures during the thermo-hydraulic expansion, geometric imperfections and the presence of internal pressure during bending. The effect of different temperature levels, accounting for either temperature-dependent or temperature-independent material of the liner pipe, is also investigated during the thermo-hydraulic expansion.

4.2 Material properties and numerical modelling

4.2.1 Lined pipe geometry and material properties

A lined pipe similar to the one examined in Chapter 3 is considered, after discussion with Vasilikis (2018), working in TechnipFMC as a Rigid Pipelines Development Engineer, in order to work with a real case scenario. The lined pipe consists of a thick-walled outer pipe, made of X70 steel grade, and a thin layer inner pipe, made of stainless steel 316L. The outside diameter (D_o) and wall thickness (t_o) of the outer pipe are equal to 12.75 *in* (323.85 *mm*) and 15.9 *mm*, whereas, the outside diameter (D_l) and thickness (t_l) of the liner are 289.25 *mm* and 2.8 *mm*, respectively, corresponding to an initial radial gap (g_0) between the liner and the outer pipe equal to 1.4 *mm* (50% of t_l). In the following sections, to examine the effect of initial radial gap, the outer diameter of the liner pipe is re-adjusted accordingly.

During the manufacturing process of a mechanically bonded lined pipe, the liner pipe deforms plastically in hoop direction during the pressurisation step, for all the examined cases, as shown later in section 4.3. However, in some cases reverse loading in hoop direction occurs even before monotonic bending is applied, such as the thermo-mechanical fabrication process presented in sections 4.3.3 and 4.3.4. In the aforementioned cases, the outer pipe deforms elastically, while in one of the hydraulically expanded cases, the outer pipe is loaded beyond the yield point in hoop direction. The plastic deformation in hoop direction results in expansion of the yield surface size, considering isotropic hardening of the materials, as described in section 2.5.2 and shown in Figure 2.3. The yield surface expansion results in increase of the yield stress in the axial direction as well, which affects the structural response of the lined pipe during monotonic bending. Furthermore, the Bauschinger effect will not be captured in the liner pipe for the thermo-mechanical manufacturing process, where reverse loading is noticed. Therefore, a kinematic hardening model is essential to obtain accurate numerical results.

The stress-strain curve of the X70 steel material of the seamless outer pipe is obtained from the test results reported by Herynk *et al.* (2007). Upon first yielding, the material exhibits negligible hardening up to 4.75% engineering strain, while the Bauschinger effect occurs during reverse plastic loading. Furthermore, Young's modulus E_o is equal to 210 *GPa*, the Poisson's ratio ν is equal to 0.3 and the yield stress $\sigma_{y,o}$ is 498 *MPa*. To simulate the material response of the pure X70 carbon steel, a J_2 (von Mises, 1928) cyclic plasticity model with non-linear kinematic/isotropic hardening is employed, which accounts for both the plastic plateau upon initial yielding, and the Bauschinger effect. This behaviour is captured by applying certain amendments to the original kinematic hardening rule proposed by Armstrong and Frederick (1966) (equation 2.25 with $M = 1$); this is a feature that is not included in built-in models of the commercial software ABAQUS. The modification of the hardening rule follows the proposal of Ucak and Tsopelas (2011), where a critical plastic strain ε_n is defined as the value at which the plastic plateau ends. If the equivalent plastic strain is lower than the critical strain value ε_n, a small value of hardening modulus C is assumed, representing the plastic plateau, and γ, which determines the rate of decrease of hardening, is equal to zero. For equivalent plastic strain values greater than ε_n or in case of reverse loading, different C and γ values are considered.

In multi-axis stress state, in case of unloading from the plastic plateau an angle-change criterion is established (Lee *et al.*, 2007), to identify the loading scenarios between plastic reloading and reverse plastic loading. Therefore, the angle between the direction of the last plastic loading vector in the plateau and the direction of the new plastic loading vector is calculated. Depending on this angle, the appropriate hardening values are adopted. The constitutive model is described in more detail by Chatzopoulou (2014); Chatzopoulou *et al.* (2016*a*,*b*), while the model is implemented in a user-subroutine (UMAT) for ABAQUS/Standard, using an integration methodology proposed by Hartmann and Haupt (1993). Table 4.1 presents the combined hardening parameters for the isotropic (equation 2.27) and kinematic (equation 2.25 with $M = 1$) hardening rules, calibrated with the test results reported by Herynk *et al.* (2007), while the corresponding stress-strain curve is presented in Figure 4.1. This figure also presents the cyclic response of an ABAQUS built-in model, considering J_2 plasticity with non-linear kinematic/isotropic hardening, using three back stresses (equation 2.25 with $M = 3$). The hardening parameters are $C^{1,2,3} = 425850; 10630; 7500\ MPa$, $\gamma^{1,2,3} = 2836.34; 208.4; 146$, $Q = -130\ MPa$ and $b = 10$; they are chosen to capture the hysteresis loop and the corresponding cyclic softening of the carbon steel material. It is shown that the built-in model may not be able to capture the severe discontinuity of the pure material upon first yielding and the Bauschinger effect at the same time, indicating that the built-in model is capable to simulate work-hardened carbon steels but not as-received materials, under cyclic loading. Finally, the yield stress of the ABAQUS built-in model is equal to 558 MPa at 0.2% residual plastic strain, compared to 498 MPa of the experimental behaviour (Herynk *et al.*, 2007), leading to a stiffer response during the first cycle.

Table 4.1 Combined hardening parameters of the user-subroutine, for the cyclic response of the outer pipe (L: loading, U: unloading, R: reloading, RL: reverse loading).

	Loading Path	C (MPa)	γ	Q (MPa)	b
$\varepsilon_p \leqslant \varepsilon_n$	L-U-R	1335	0	-132	10
	L-U-RL	26000	240		
$\varepsilon_p > \varepsilon_n$	L-U-R	1900	8		
	L-U-RL	26000	240		

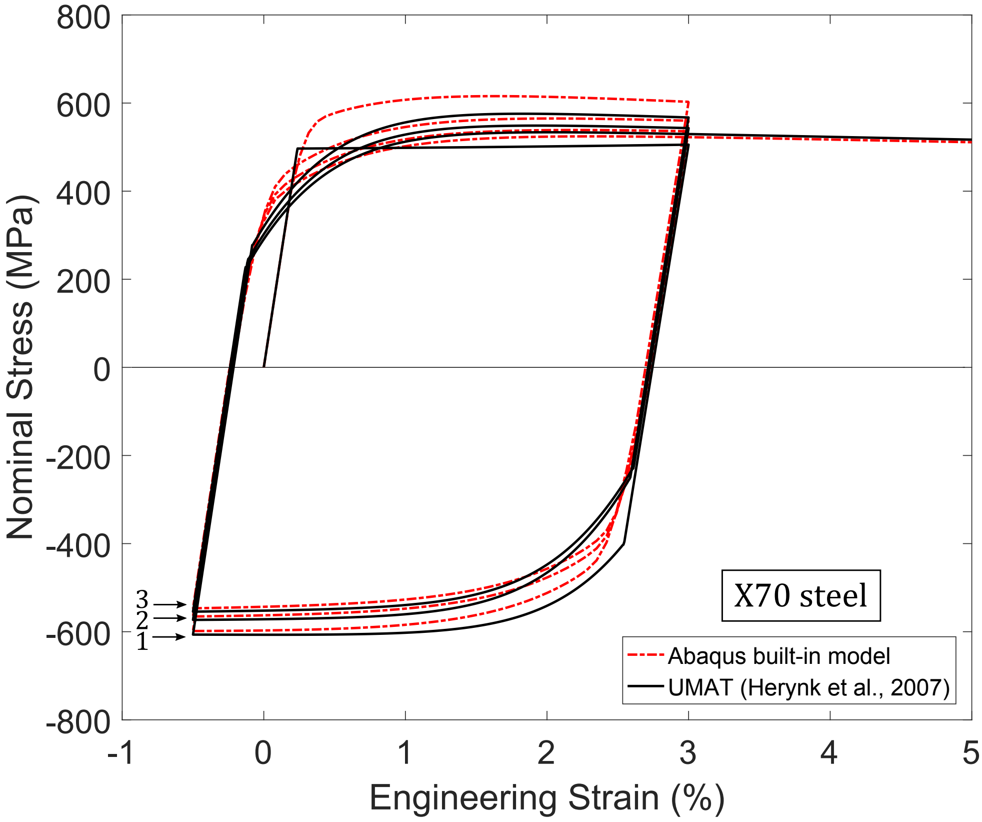

Figure 4.1 Stress-strain curve of outer pipe material (X70 carbon steel), comparing the user-subroutine with ABAQUS built-in model.

The stress-strain curve of the liner material is shown in Figure 4.2 (also called MAT-B in Chapter 5), and is based on experimental data provided by Vasilikis (2018). The Young's modulus E_l is equal to 193 GPa, the Poisson's ratio ν is equal to 0.3 and the yield stress of the liner material $\sigma_{y,l}$ is 260 MPa. At this point, it should be noted that in this case the yield stress of the liner pipe is quite higher than the as-received 316L material, which is equal to 205 MPa (Peckner and Bernstein, 1977). This is attributed to the electric resistance welded (ERW) liner pipe (Kyriakides and Corona, 2007), where the liner pipe material is hardened. To simulate the behaviour of this material, a J_2 (von Mises, 1928) plasticity model with non-linear kinematic/isotropic hardening is used, considering three back stresses (equation 2.25 with $M = 3$), built-in into ABAQUS/Standard. The plasticity model is calibrated with experimental data (Vasilikis, 2018), as shown in Figure 4.2, to determine the appropriate kinematic (C^q, γ^q) and isotropic (Q, b) hardening parameters to capture properly the hysteresis loop and the corresponding cyclic hardening of the liner pipe material. These parameters are $C^{1,2,3} = 15000; 23000; 1800\ MPa$, $\gamma^{1,2,3} = 1500; 250; 20$, $Q = 180\ MPa$ and $b = 5$.

Finally, the geometrical and material properties of both pipes are listed in more detail in Table 4.2. Also, in the majority of numerical analyses, the material properties of both pipes are assumed temperature-independent, while the influence of temperature-dependent material of both pipes on the mechanical bonding and subsequently on bending response is investigated in the parametric analysis section 4.5.3, as an attempt of refinement of the numerical model.

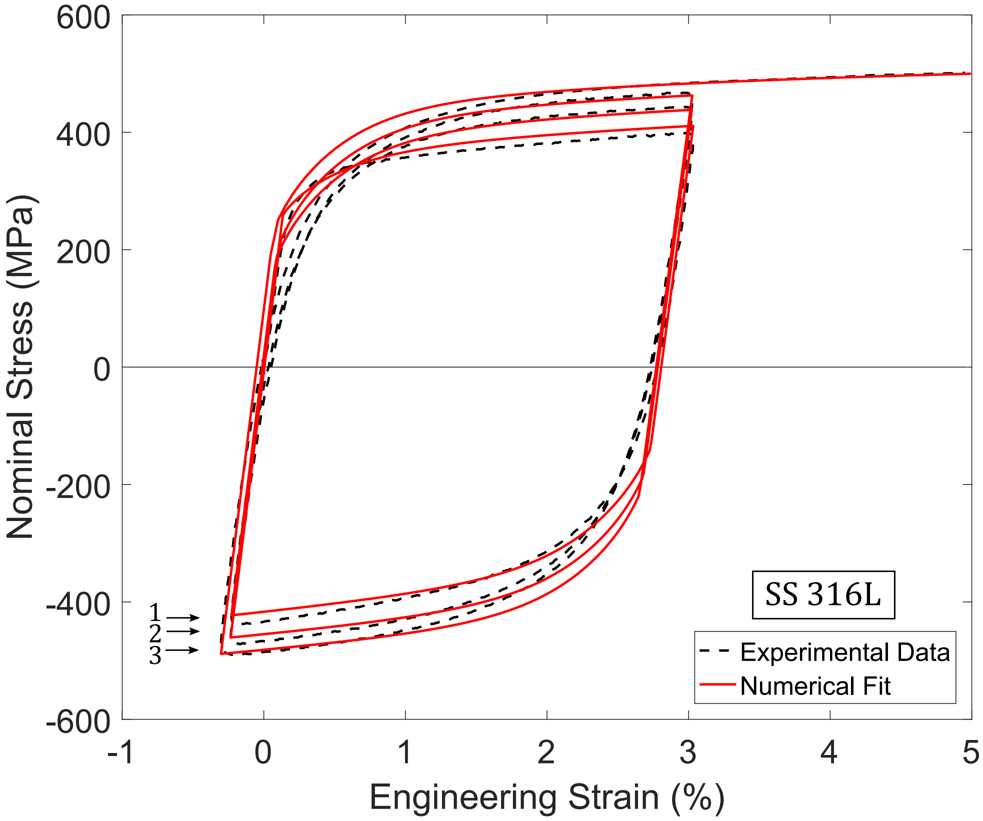

Figure 4.2 Stress-strain curve of liner pipe (Vasilikis, 2018).

Table 4.2 Geometric and material properties of the outer and liner pipe.

	Outer Diameter (mm)	Thickness (mm)	Young's Modulus (GPa)	Yield Stress (MPa)	Poisson's Ratio
Liner	289.25	2.8	193	260	0.3
Outer	323.85	15.9	210	498	0.3

4.2.2 Numerical modelling

In the present chapter, a numerical model, similar to the one presented in the previous chapter in section 3.2.2, is created as shown in Figure 4.3, using the general-purpose finite element software ABAQUS (Hibbitt *et al.*, 2016). A three-dimensional numerical model is developed representing a lined pipe segment of length $\chi = 15$, where $\chi = (L-z)/\sqrt{D_{m,l}t_l}$ is the dimensionless length parameter introduced in 3.2.2. As shown in the following section 4.4, the half-wavelength of the liner pipe on bending is affected by the manufacturing process. In the current analysis, a longer lined pipe segment is considered, compared with the numerical model presented in the previous chapter, which is similar to the length of the model presented by Yuan and Kyriakides (2014*a*,*b*, 2015) for more direct comparison with the present study. However, the liner pipe bending response is not affected by the change of length. In section 3.3.2, the numerical model used in the previous chapter, which considers normalised length $\chi = 10$ (seven half-wavelengths), presents identical results with the two half-wavelength long numerical model used by Vasilikis (2012), and also a good agreement with experimental tests (Focke, 2007; Hilberink, 2011).

Following the modelling presented in section 3.2.2, the analysis considers the half cross-section of the lined pipe using symmetry with respect to the y-z-plane of bending, as shown in Figure 4.3. In addition, x-y-plane symmetry is assumed in the $z = 0$ plane allowing only in-plane motion on the corresponding nodes, while in the $z = L$ plane, a reference node, in which the rotation is applied, is coupled with the nodes of the lined pipe cross-section, so that these nodes can slide on the rotated plane, allowing the lined pipe cross-section to ovalise freely, representing a segment of an infinite pipeline. The reference node at $z = L$ is simply supported, so that it is free to move in the z-direction and rotate about the x-axis, as shown in Figure 4.3. Furthermore, the same type of elements is used for both pipes (S4R for the liner and C3D20R for the outer pipe), considering the same mesh density. The half-circumference contains one hundred and fifty elements for the liner and outer pipe respectively, while in z-direction eighteen and six elements every half-wavelength λ_c are employed for the liner and outer pipe, respectively. The surface-to-surface contact is also considered frictionless.

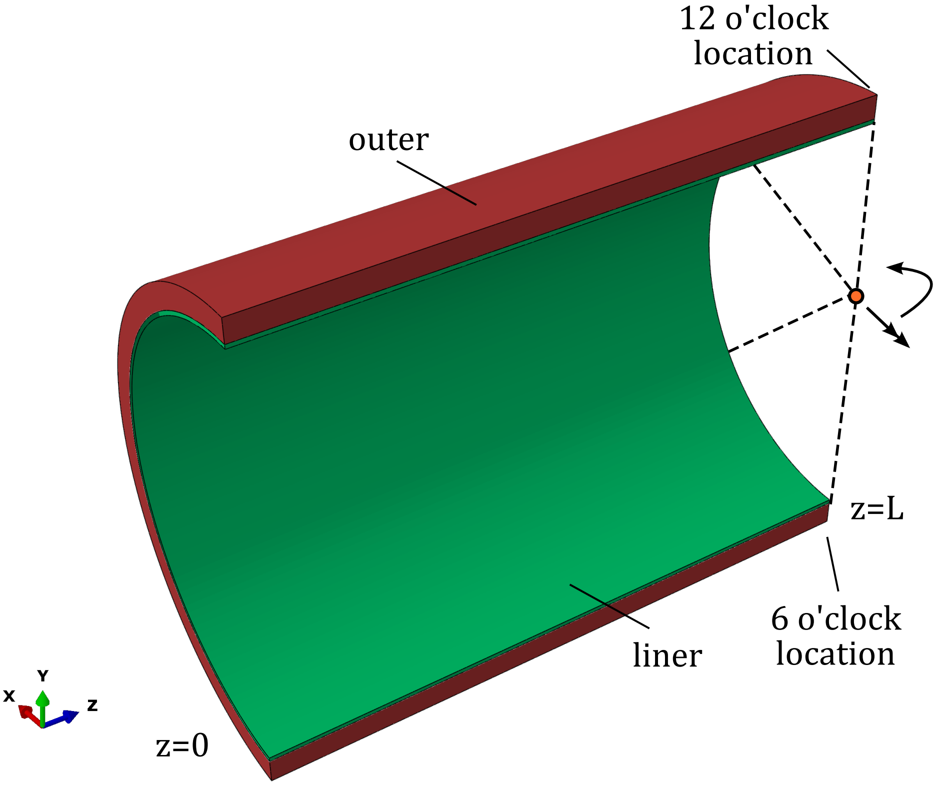

Figure 4.3 Three-dimensional numerical model of the lined pipe.

4.3 Simulation of different manufacturing processes

The present section of the thesis investigates contact pressure changes (or the bonding stresses) due to different manufacturing processes and the effect of these processes on the mechanical behaviour of the lined pipe under monotonic bending. Two different procedures of manufacturing are examined: (a) hydraulic expansion of both pipes up to elastic (section 4.3.1) or plastic deformation (section 4.3.2) in the outer pipe (the liner pipe deforms plastically in both cases) and (b) complete thermo-mechanical process of tight-fit pipes (TFP) (sections 4.3.3 and 4.3.4). Different values of initial radial gap (g_0) between the two pipes, are examined. For simulating the manufacturing process only (without analysing its effect on bending), a shorter version of the model presented in Figure 4.3 is employed for reducing computational cost. In this model a small value of L is employed, equal to 2% of the liner pipe diameter.

4.3.1 Elastically expanded

The elastically expanded process consists of inserting the liner into the outer, followed by the application of internal pressure (P_{in}) up to 80% (41.1 MPa) of the plastic pressure of the outer pipe ($P_{y,o} = 2\sigma_{y,o}t_o/D_{m,o}$, where $D_{m,o}$ is the mean diameter of the outer pipe, $D_{m,o} = D_o - t_o$). This manufacturing process will be referred to as "elastically expanded" in the sense that the word "elastically" refers to the outer pipe. As shown in Figure 4.4, the liner expands initially elastically and then plastically (⓪→①), establishing contact with the outer pipe. The response during manufacturing is axisymmetric, and therefore, no sliding occurs between the two pipes. Subsequently, both pipes expand together (①→②: the outer expands only linearly), followed by depressurization of both pipes (②→③).

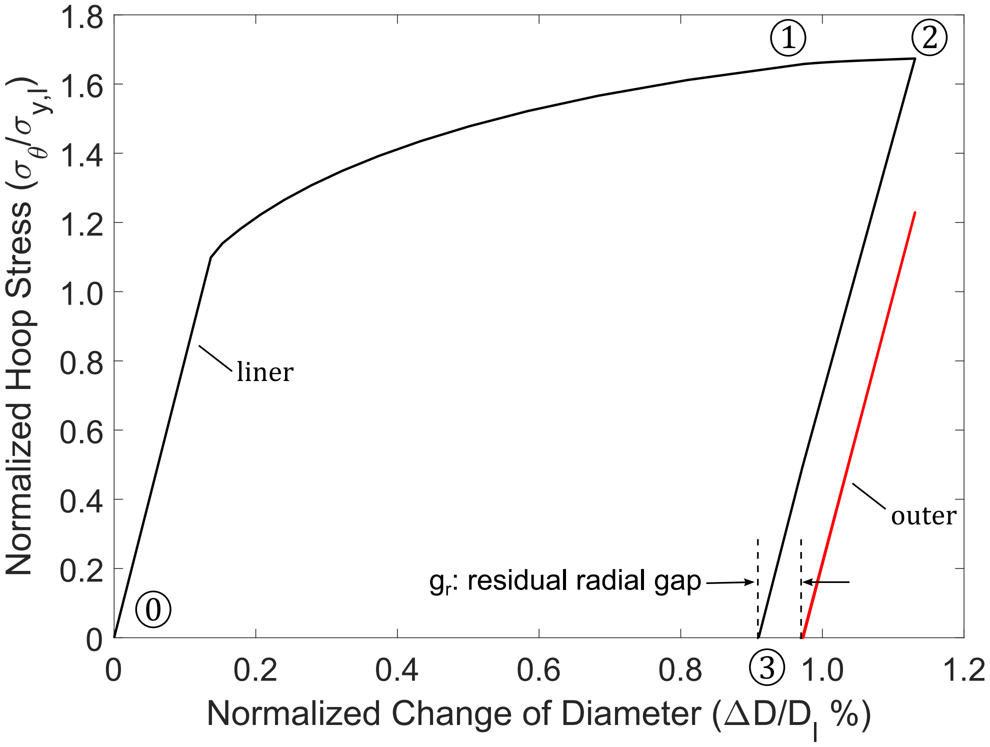

Figure 4.4 Normalised hoop stress with respect to normalised change in the diameter of both pipes (liner and outer), during elastic hydraulic expansion of the outer pipe.

Considering initial radial gap (g_0) values ranging from 35% to 75% of the liner wall thickness (t_l), and simulating the elastic hydraulic expansion manufacturing process, the residual radial gap (g_r) at the end of the process is calculated. The range from 35% to 75% of the liner thickness is a reasonable range for this initial gap, based on the information provided by the industry. Small values of initial radial gap may result in scoring of the liner, which is a type of damage of the liner while is inserted in the outer pipe. Considering small initial gap values, it might lead to longitudinal light scratches on the outer surface of the liner pipe, or uncontrolled galling of the liner. This may occur in case the pipes are axially misaligned during liner insertion or the pipe diameter and straightness tolerances are high. Liner galling may lead to build-up liner material between both pipes and indent the liner pipe during internal pressurisation. This type of damage is explained by Pépin *et al.* (2017), presenting also photographs of real cases.

On the other hand, considering higher gap values will increase the plastic deformation in the liner pipe during the manufacturing process, which affects significantly the bending performance, as shown in the following section 4.4. It is interesting to notice that the value of g_r is smaller by one order of magnitude, compared with the value of g_0, as shown in Figure 4.5, verifying the observation of industrial suppliers (Vasilikis, 2018).

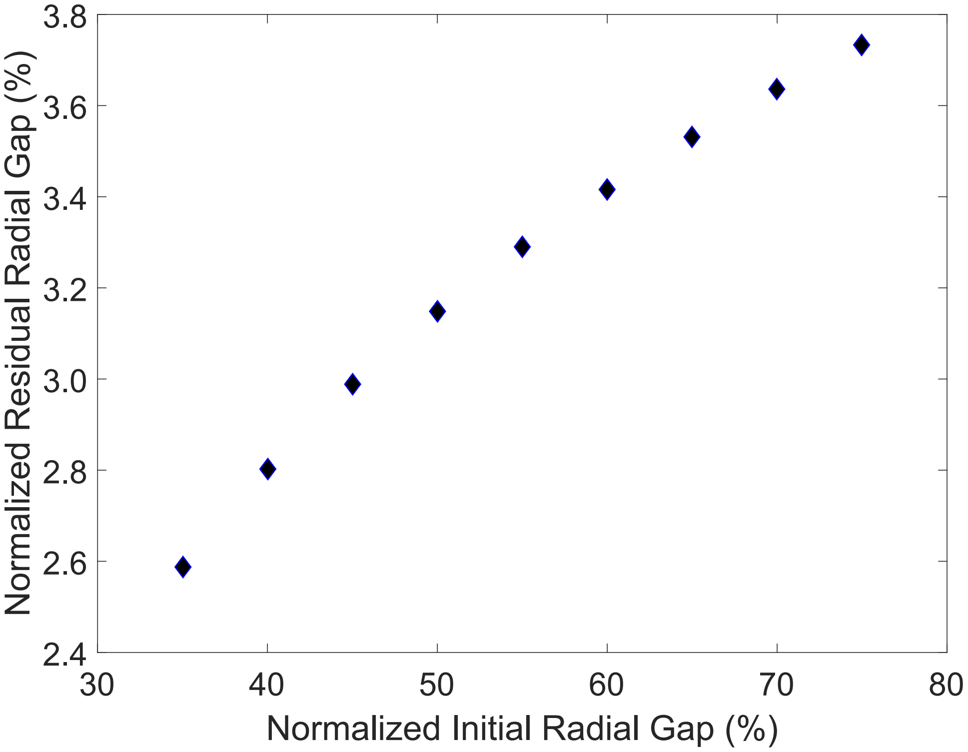

Figure 4.5 Residual radial gap (g_r) with respect to the initial radial gap (g_0), for elastic expansion of the outer pipe; gap values are normalised with liner thickness (t_l).

4.3.2 Plastically expanded

A variation of the aforementioned manufacturing process, consists of applying internal pressure during pressurization of the lined pipe that exceeds the plastic pressure of the outer pipe, equal to 59.9 *MPa* (117% of $P_{y,o}$). This manufacturing process will be referred to as “plastically expanded”. As shown in Figure 4.6, the liner expands initially elastically and then plastically (⓪→①), until the liner comes in contact with the outer pipe. Then both pipes expand together (①→②), and at the end of stage ② the outer pipe is also deformed plastically. This is followed by depressurization of both pipes (②→③). Due to the larger elastic deformation in the outer pipe, compared with the one in the liner pipe, after depressurization, the two pipes remain in mechanical bonding, and the contact pressure depends on the initial gap, as discussed later in section 4.3.5. During depressurization, the liner pipe does not exhibit any wrinkles.

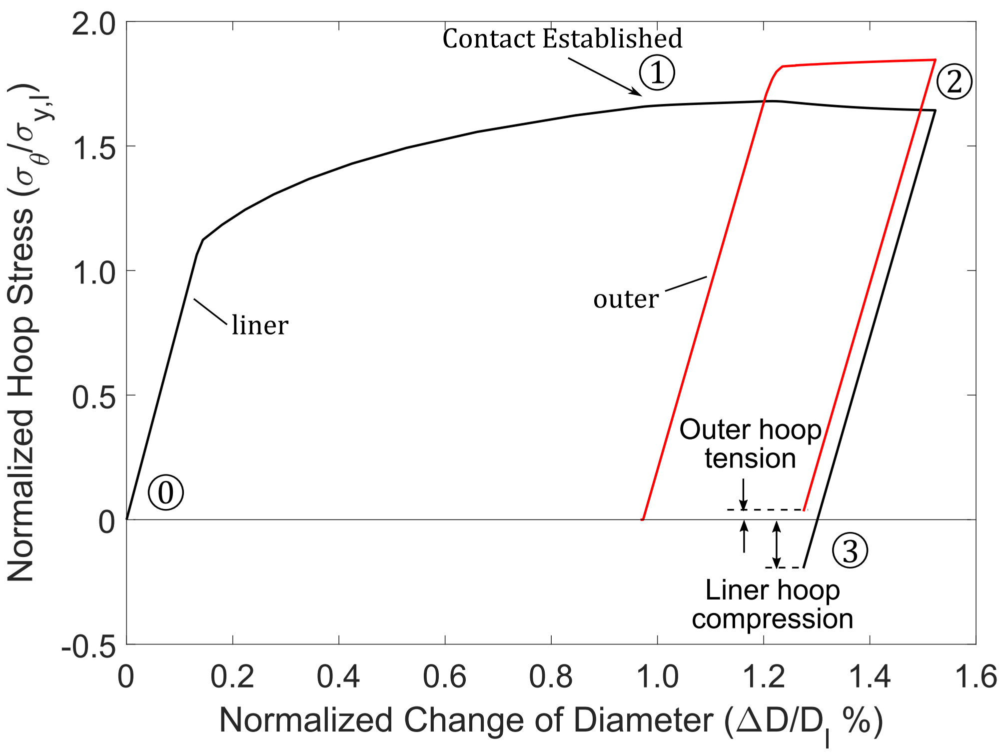

Figure 4.6 Normalised hoop stress with respect to normalised change in diameter of both pipes (liner and outer), during plastic hydraulic expansion of the outer pipe.

4.3.3 Fully heated Tight-Fit Pipe

Furthermore, the so-called TFP process is considered in the present study, which is a thermo-mechanical process. The thermal expansion coefficients are assumed $\alpha_l = 1.62 \times 10^{-5} K^{-1}$ (Atlas Specialty Metals, 2004) and $\alpha_o = 1.3 \times 10^{-5} K^{-1}$ (Focke, 2007) for the liner and the outer pipe respectively. In addition, the temperature through the thickness of both pipes is considered uniform, during the thermal expansion. The outer pipe is heated first up to $T_o = 680$ K (⓪→①), as presented in Figure 4.7. On this step, the liner pipe is slightly elongated, due to coupling between the outer and the liner pipe at $z = L$ through the reference node, resulting in a small diameter reduction. Subsequently, the liner is pressurized internally (①→②) up to $P_{in}/P_{y,l} = 5.94$ (31.4 *MPa*) (where $P_{y,l} = 2\sigma_{y,l}t_l/D_{m,l}$ is the plastic pressure of the liner pipe), comes in contact with the outer pipe (as also presented in Figure 4.7), followed by expansion of both pipes, while the temperature of the outer pipe is assumed constant in the current step. In this step, the liner pipe is heated, due to the contact with the outer pipe, up to the same temperature with the outer pipe ($T_l = T_o$, also referred to as the 100% case in section 4.5.3). The thermal hoop strain increases significantly, tending to increase the diameter of the liner pipe ($\varepsilon_{h,T} = (\Delta R_l / R_l)|_T$). Nevertheless, due to lateral confinement by the outer pipe, the liner hoop tension gradually decreases and hoop compression develops. This is represented by the sharp drop of the hoop stress of the liner shown in Figure 4.7. The analysis also shows that reverse plastic loading (RPL) occurs in the liner wall during the pressurization step, due to thermal hoop expansion and the lateral confinement and it is denoted by the horizontal arrow on the curve before the end of stage ②. After depressurization (③), there is residual hoop compression in the liner pipe, due to confinement by the outer pipe.

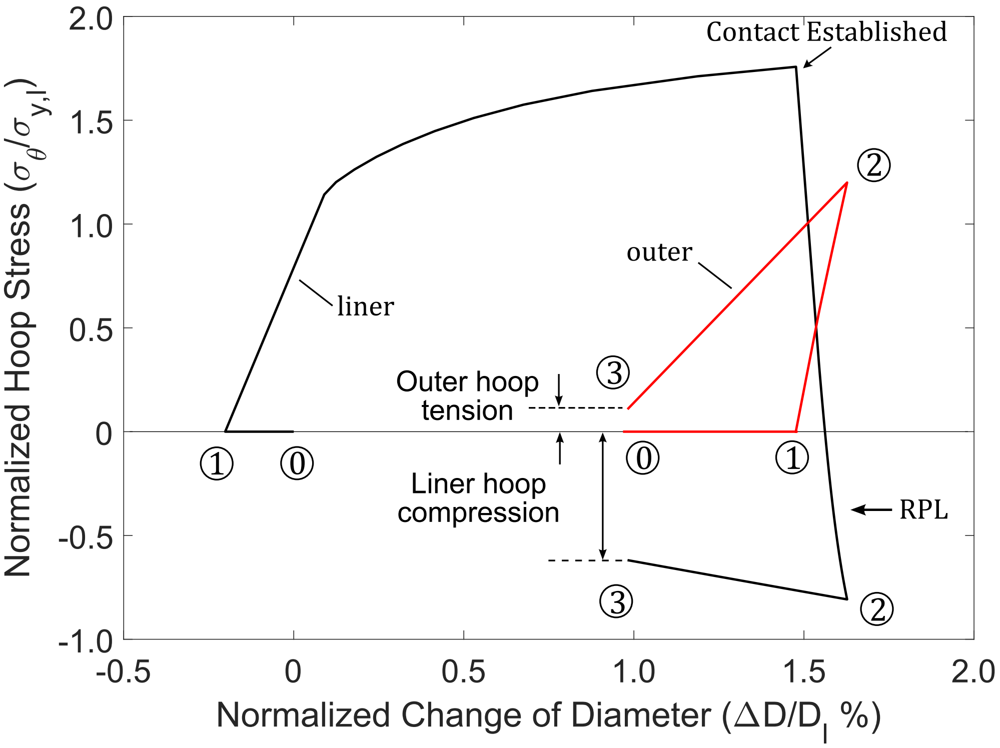

Figure 4.7 Tight-Fit Pipe manufacturing process with full heating of the liner pipe.

4.3.4 Partially heated Tight-Fit Pipe

Subsequently, an alternative process of a TF Pipe is also investigated in the present work (as shown in Figure 4.8), in which during the pressurization step (①→②) the liner is partially heated (denoted as TFP PH) up to $T_l = 388\ K$, assuming a liner temperature used in experimental tests (Focke, 2007; Hilberink, 2011) and numerical analyses (Naderi *et al.*, 2021). This value corresponds to 57% of the outer pipe's temperature (the term "partially" implies uniform heating of the liner pipe up to a lower temperature level from the T_o). In this case, the liner pipe exhibits less thermal hoop expansion, resulting in a smaller drop of the hoop stress, as shown in Figure 4.8. Reverse plastic loading (RPL) occurs during the depressurization step, as denoted with the horizontal arrow before the end of stage ③. At the end of the fabrication process (③), the liner pipe is in higher hoop compression stress, compared to the fully heated process (denoted as TFP FH). The initial temperature and the temperature after the depressurization step is $T_i = 298\ K$ for both pipes, for the thermo-hydraulic expansion cases.

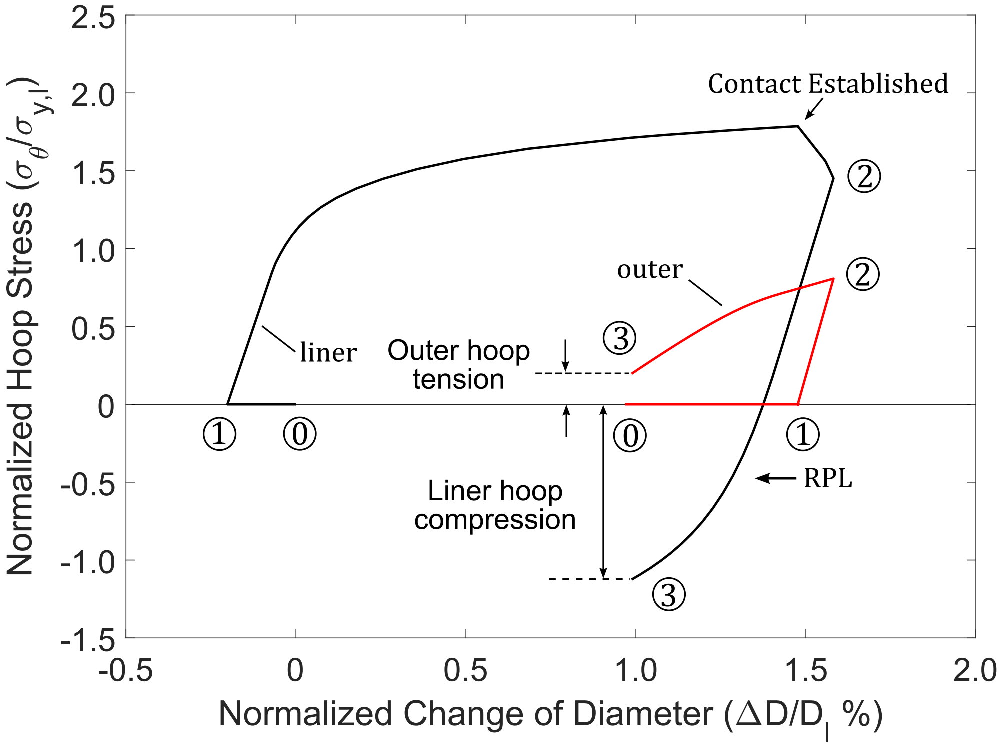

Figure 4.8 Tight-Fit Pipe manufacturing process with partial heating of the liner pipe.

4.3.5 Comparison of mechanical bonding between the manufacturing processes

In more detail, the residual compressive hoop stress of the liner pipe after the manufacturing process is presented in Figure 4.9, showing that the TFP manufacturing process with (full or partial) heating results in higher liner compression compared with the plastic expansion process. In addition, the fully heated TFP results in lower compression stress than the partially heated TFP. In this case, during the pressurization step, the total hoop strain of the liner pipe is the sum of a mechanical part ($\varepsilon_{h,M}$), due to hydraulic expansion and a thermal part ($\varepsilon_{h,T}$), due to the contact with the heated outer pipe ($\varepsilon_{h,Tot} = \varepsilon_{h,T} + \varepsilon_{h,M}$). The total hoop strain of the liner pipe is governed by the outer pipe, due to confinement. In this case, an increase of the thermal hoop strain results in a decrease of the mechanical hoop strain. The above results indicate that the level of mechanical bonding depends on the temperature level of the liner pipe and the mechanical hoop strain at the end of the pressurization step.

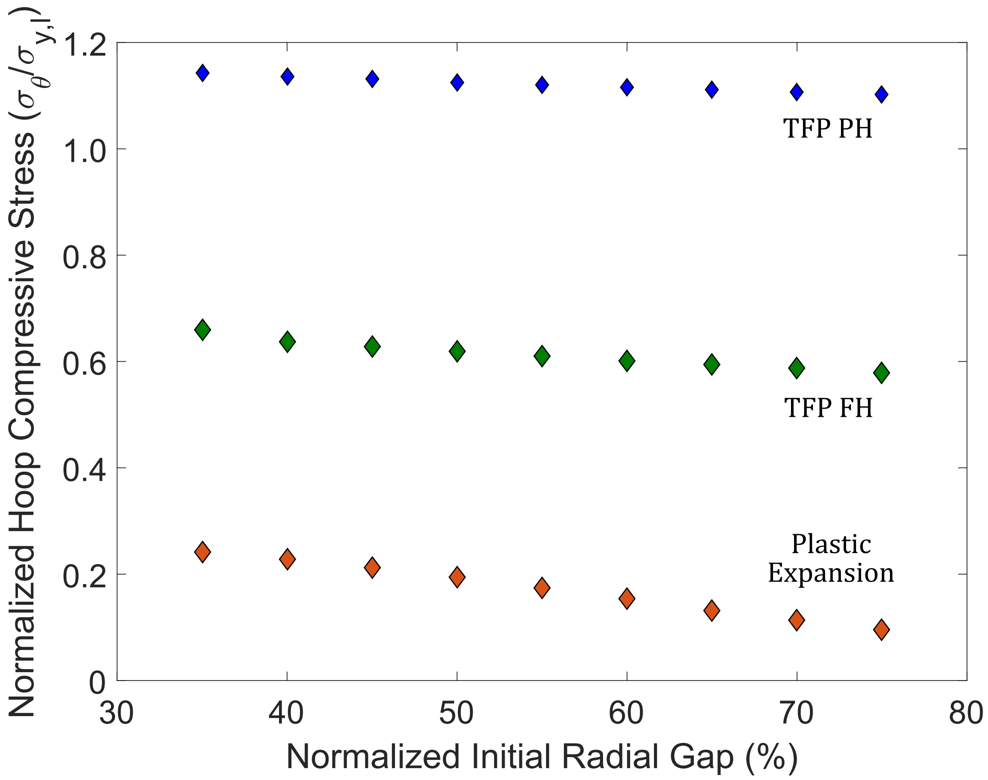

Figure 4.9 Liner compressive hoop stress (residual hoop stress) after different manufacturing processes.

An important observation refers to the material model used in the simulation of the manufacturing process. The results show that reverse plastic loading may occur during the manufacturing process and therefore consideration of the Bauschinger effect in material models is necessary. This implies that, the use of isotropic hardening for modelling the liner pipe material may not be adequate for simulating the manufacturing process. During the manufacturing process, the maximum hoop strain in the liner at stage ②, before depressurization is 1.12%, 1.51%, 1.61% and 1.57% for elastically, plastically, fully and partially heated TF Pipes, for an initial radial gap equal to 50% of liner thickness. For a gap equal to 75% of liner thickness the maximum hoop strain is 1.61%, 1.77%, 2.10% and 2.05%, respectively. During the pressurization, the liner pipe is subjected to tension in the hoop direction, while after the depressurization results in zero stress and elastic hoop compression for the elastically and plastically expanded lined pipes (as shown in Figures 4.4 and 4.6). In the case of the fully heated TF Pipes, during the pressurization step, and after contact between the two pipes is established, the liner pipe is gradually compressed, resulting in reverse plastic loading (RPL), as indicated by the arrow (➞) in Figure 4.7, whereas after depressurization, the liner is elastically compressed in the hoop direction. In the case of partially heated TF Pipes, after depressurization, the liner pipe exhibits reverse compressive plastic loading (RPL) as indicated in Figure 4.8.

4.4 Results on monotonic bending

In this section, the mechanical behaviour of steel lined pipes under monotonic bending is investigated, using the numerical model shown in Figure 4.3, considering the effect of different manufacturing processes. The manufacturing process is simulated in the first stage of the analysis, as described in the previous section, and it is followed by monotonic bending in the second stage of the analysis. The following results refer to imperfection-free lined pipes, whereas imperfect lined pipes are considered in the next section. The lined pipe normalised length, as already described in section 4.2.2, is equal to 15, as shown in Figure 4.10. In this figure, the model is mirrored (from $\chi = 0$ to $\chi = -15$) for visualization purposes. Previous publications (Vasilikis and Karamanos, 2012; Yuan and Kyriakides, 2014*a*) have demonstrated that, after applying bending, the liner pipe gradually detaches from the outer pipe, followed by the formation of a uniform wrinkling pattern at the compression zone leading to localized buckling with further increase of the curvature. Uniform wrinkling has been identified by Vasilikis and Karamanos (2012) as the first bifurcation, followed by a second bifurcation at higher curvatures leading to a main buckle (A), with four adjacent minor buckles (B), as shown in Figure 4.10, a result also verified by Yuan and Kyriakides (2014*a*, 2015) and in the present work as well.

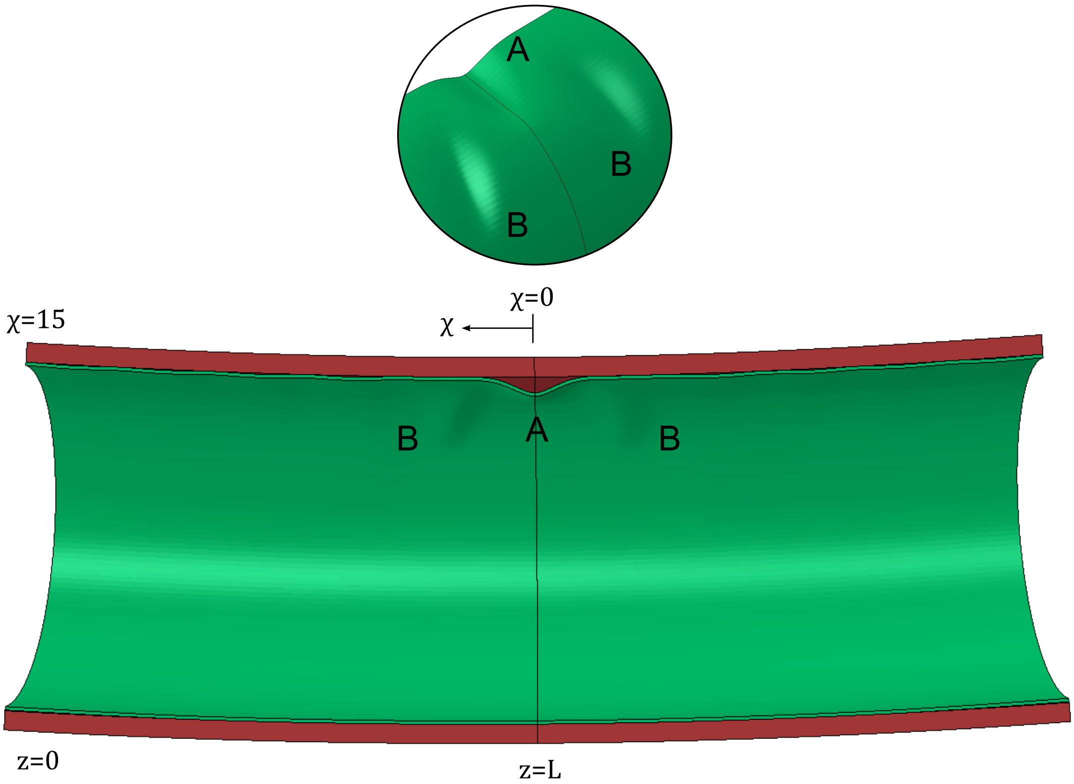

Figure 4.10 Localized buckling pattern of the liner pipe; buckle occurs at $\chi = 0$ location.

4.4.1 Effect of the different processes on liner buckling curvature

In the following, liner deformation is presented in terms of its detachment, which expresses its relative displacement with respect to the outer pipe. The maximum normalised detachment (Δ) of the liner pipe occurs at $\chi = 0$ location at the main buckle (A). It is shown in Figure 4.11 normalised by the wall thickness of the liner pipe (t_l), with respect to normalised curvature ($\kappa = k_r/k_o$; $k_r = \phi/L$, where ϕ is the rotation applied on the reference node at $z = L$; $k_o = t_o/D_{m,o}^2$), for the different manufacturing processes analysed earlier, and for the case of initial radial gap (g_0) equal to 50% of liner thickness.

The TFP with partial heating of the liner results in higher hoop compression of the liner, compared with the fully-heated TFP process, also noticed in the previous section. This observation may explain the results shown in Figure 4.11, where the abrupt detachment of the liner pipe in partially heated TFP occurs at higher curvature. It is shown in previous studies (Vasilikis and Karamanos, 2012) and in section 3.4.2 in the present study, the beneficial effect of prestressing the liner pipe on delaying the local buckling during bending. In case of Snug-Fit Pipe, where the liner is not compressed in hoop direction, the axial compression of the liner increases during bending and the material yields at $\sigma_x = -\sigma_{y,l}$, as shown in Figure 2.2b. In case of Tight-Fit Pipe, where hoop compression occurs in the liner pipe at the end of fabrication process, the liner pipe is under bi-axial compression during bending, while higher axial compressive stress is required ($\sigma_x < -\sigma_{y,l}$) to reach the yield surface. Therefore, higher bending is required to yield the liner pipe material and lead to local buckling eventually. For the same reason, the partially heated TF Pipes, where higher hoop compression occurs at the end fabrication compared to fully heated TH Pipes, present better bending performance delaying the abrupt liner detachment.

In addition, despite that the plastically expanded lined pipe results in mechanical bonding, the abrupt detachment of the liner from the outer pipe occurs earlier compared with the elastically expanded lined pipe, in which a residual radial gap (g_r) is observed. The abrupt detachment of liner pipe shown in Figure 4.11 is also associated with the drop of bending moment carried by the liner pipe. The latter is represented by normalised moment m_l, defined as $m_l = M_l/M_o$, where $M_o = \sigma_{y,o}D^2_{m,o}t_o$. This behaviour is shown in Figure 4.12, for each manufacturing process, for initial radial gap equal to 50% liner thickness, indicating the onset of local buckling of the liner pipe in a diamond-type mode.

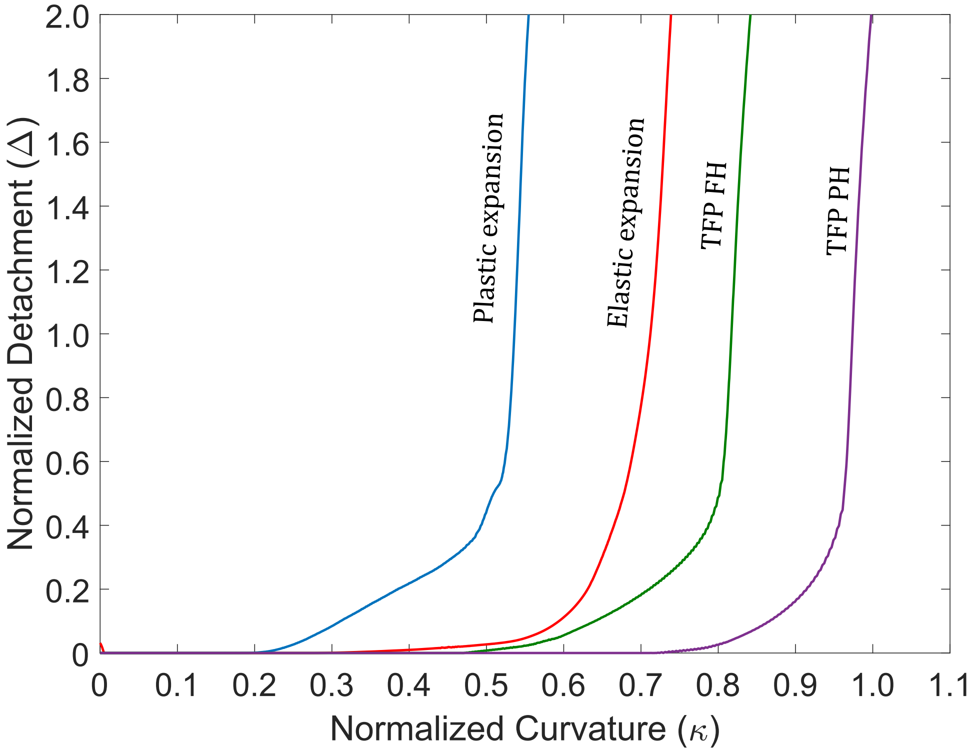

Figure 4.11 Evolution of detachment of liner pipe at $\chi = 0$ location, with respect to normalised curvature for different manufacturing processes, in case of 50% initial radial gap (g_0).

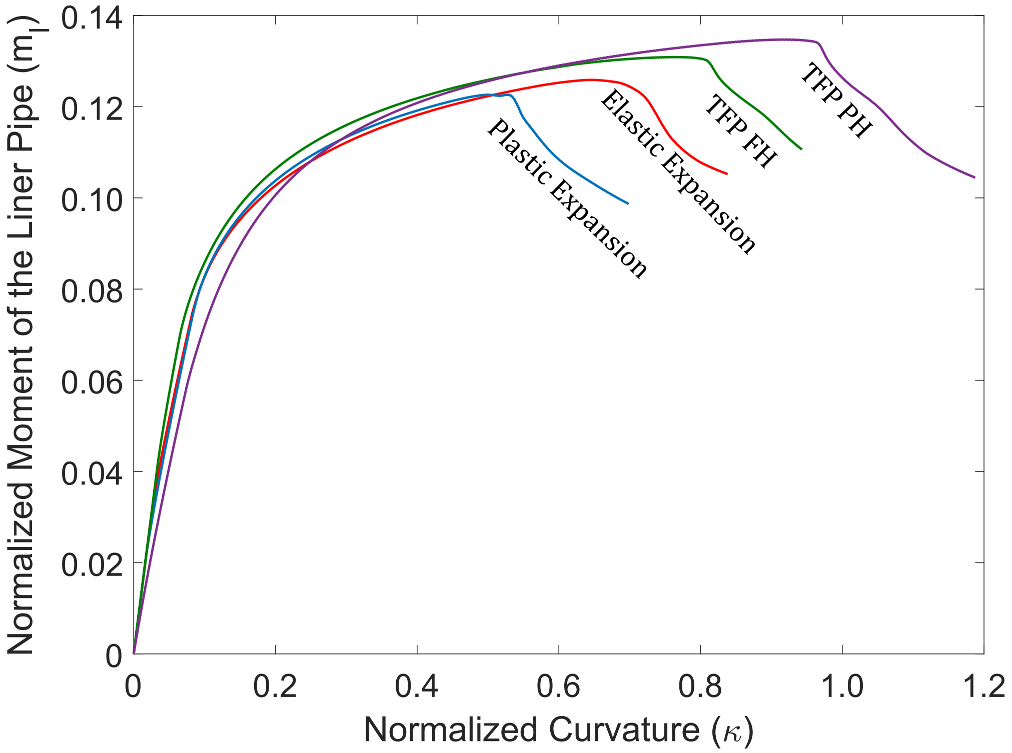

Figure 4.12 Normalised moment of the liner pipe, with respect to normalised curvature for different manufacturing processes, in case of 50% initial radial gap (g_0).

The "critical" curvature (κ_{cr}) is defined as the curvature at which the slope of the detachment-curvature diagram ($d\Delta/d\kappa$) reaches its maximum, a definition introduced in the previous chapter (section 3.4.2). As shown in Figure 4.11, the detachment of the liner pipe increases rapidly after a specific curvature value, leading to local buckling of the liner pipe. The value of "critical" curvature from the above definition corresponds to the abrupt drop of moment of the liner pipe, as shown in Figure 4.12. Based on the above failure criterion, Figure 4.13 presents the critical curvature of the lined pipe from each manufacturing process and for different values of initial radial gap (g_0). The results show that the TFP manufacturing process with partial heating of the liner pipe results in higher critical curvature values compared with all the other manufacturing processes. In addition, the plastically-expanded lined pipe exhibits the lowest critical curvature values, due to the excessive plastic deformation of the liner pipe. In more detail, the critical buckling curvature of partially-heated TFP is 17%, 28% and 57% higher than the corresponding value for fully heated TFP, elastically expanded and plastically expanded lined pipes, respectively, assuming a 50% value of initial radial gap, due to bi-axial compression during bending as explained previously. The results are summarized in Table 4.3, including the values of normalised detachment (Δ_{cr}), radius of curvature (ρ_{cr})

corresponding to the neutral axis of the pipe and global bending strain ($\varepsilon_{cr} = D_o/2\rho_{cr}$) at buckling, for each fabrication process.

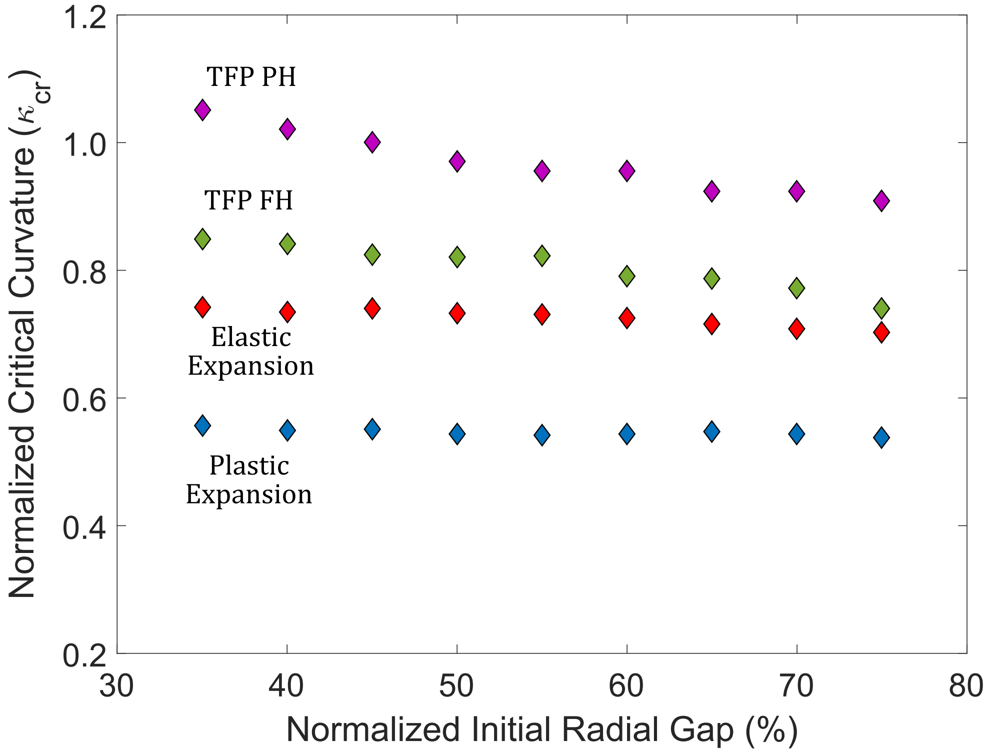

Figure 4.13 Critical curvature in terms of initial radial gap size for different manufacturing processes.

Table 4.3 Critical curvature, corresponding normalised detachment, radius of curvature and global bending strain for different fabrication processes.

Manufacturing Process	Normalised Critical Curvature (κ_{cr})	Normalised Critical Detachment ($\Delta_{cr}\%$)	Buckling Radius of Curvature (ρ_{cr} mm)	Buckling Strain (ε_{cr} %)
Plastic Expansion	0.543	138	10986	1.47
Elastic Expansion	0.732	172	8144	1.98
Fully Heated TFP	0.821	121	7261	2.23
Partially Heated TFP	0.971	82	6145	2.63

4.4.2 Influence of manufacture processes on liner wave-length

In addition to the critical bending curvature (κ_{cr}), the manufacturing process may affect the buckling wavelength (L_{hw}). The results herein are reported in normalised form ($l_{hw} = L_{hw}/\sqrt{D_{m,l}t_l}$). For the fully and partially heated TF Pipes, the normalised half-wavelength is equal to 1.375, while for elastically expanded and plastically expanded pipes the corresponding values are somewhat smaller, equal to 1.3 and 1.225, respectively. As the plastification of the liner increases, the normalised half-wavelength is further reduced. Furthermore, considering the TFP manufacturing process, the normalised half-wavelength has a somewhat lower value compared with the value of 1.425 reported in previous work by Vasilikis and Karamanos (2012) and in section 3.4.2 as well. It should be noted though that in these works the manufacturing process has been taken into account only indirectly, assuming an initial hoop stress. The normalised half-wavelength of the liner pipe is presented in Figure 4.14, showing also the gradual liner detachment with increasing curvature along the liner pipe, for each manufacturing process.

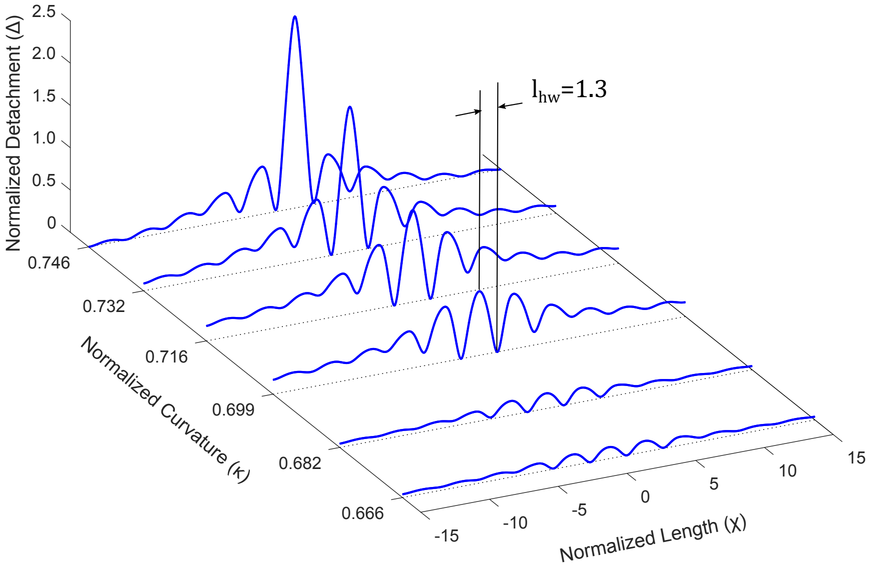

(a) Elastically expanded lined pipe (referring to the outer pipe).

Figure 4.14 Continues in the next page.

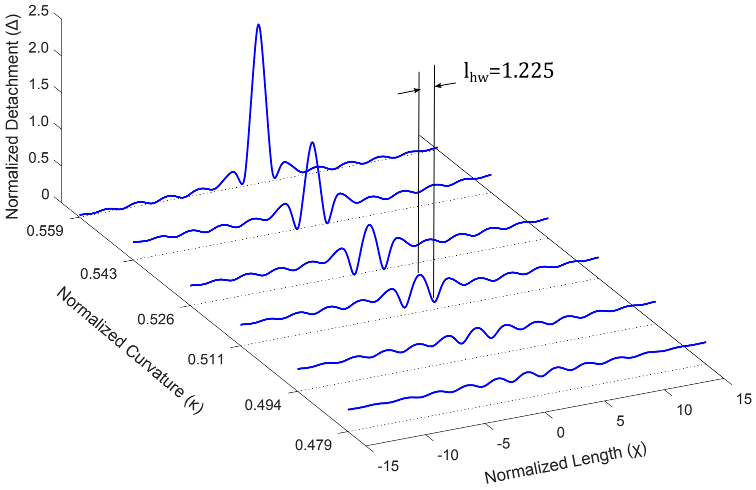

(b) Plastically expanded lined pipe (referring to the outer pipe).

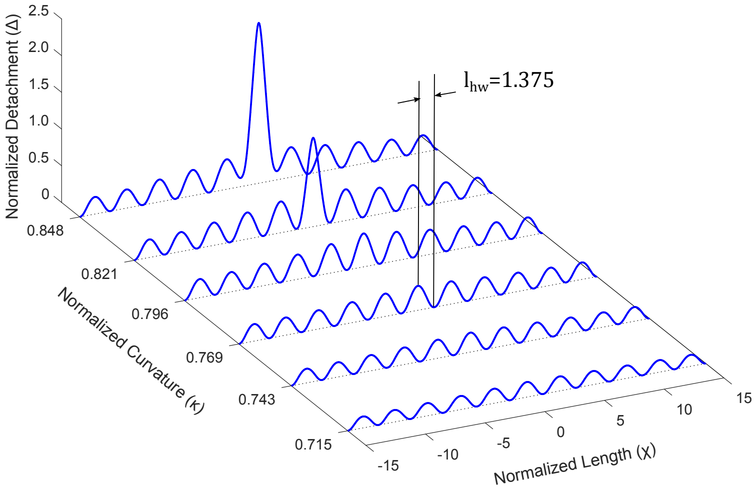

(c) Fully heated TF Pipe.

Figure 4.14 Continues in the next page.

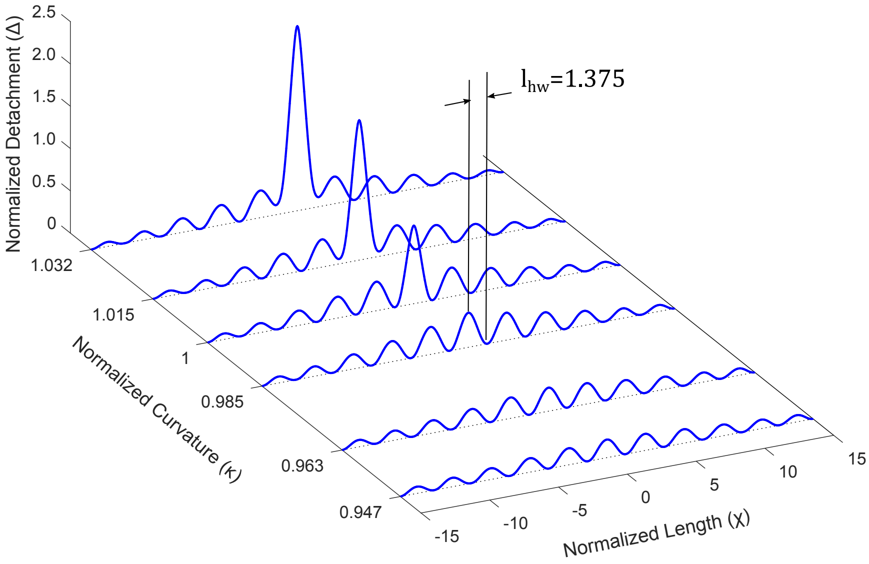

(d) Partially heated TF Pipe.

Figure 4.14 Normalised detachment along the liner pipe at the compression side for each manufacturing process.

4.4.3 Influence of fabrication numerical modelling on liner buckling performance

At this point, additional analysis is conducted, comparing the influence of the detailed manufacturing process modelling, assumed in the present chapter, with the simpler mechanical bonding modelling considered in Chapter 3.

The bending performance of a lined pipe is examined, considering the geometric and material characteristics of the present chapter, as presented in section 4.2, while the mechanical bonding is achieved following the simpler bonding modelling presented in chapter 3 (section 4.2). An initial hoop compressive stress is applied on liner pipe, followed by an unloading step and leading to residual hoop compression equal to the fully heated TF Pipe case presented in 4.4.1, for initial radial gap equal to 50%. In this case, it should be noted that the outer diameter of the liner pipe is readjusted accordingly, considering zero initial gap between both pipes, such as in Chapter 3.

Following the critical curvature definition, adopted in the present study, the liner pipe buckles locally at normalised curvature equal to 1.119, compared with the fully heated TF Pipe where the liner detaches abruptly at curvature value equal to 0.821 (as shown in Figures 4.11 and 4.13). The results show that accounting for the plastic deformation in the liner pipe during the manufacturing process, the buckling response of the liner pipe is affected, leading to decreasing the critical curvature by 31%. Therefore, the proper modelling of the fabrication process affects significantly the bending response of the lined pipe.

4.5 Parametric analysis

In the following sections, the effect of different parameters on the bending response of mechanically bonded pipes is investigated. Imperfection sensitivity analysis of the liner pipe is considered in the form of the buckling configuration of the imperfection-free liner pipe, examined in the previous section 4.4. Subsequently, the structural stability of the liner pipe in the presence of moderate levels of internal pressure is examined. Finally, the influence of the maximum liner temperature, during the thermo-hydraulic manufacturing process, on bending performance is investigated.

4.5.1 Imperfection sensitivity analysis

In the present section, the mechanical behaviour of lined pipes in the presence of geometrical initial imperfections of the liner pipe is investigated for elastically expanded, plastically expanded and fully heated TF Pipes. The shape of the initial geometric imperfection of the liner pipe is based on the buckling pattern of the imperfection-free lined pipe of the corresponding manufacturing process, normalised by the liner pipe wall thickness (t_l). The shape of the imperfection is presented in Figure 4.15 and it has the form of buckling mode of the corresponding “perfect” pipe. Therefore, it is expected that the buckled configuration of each lined pipe (elastically expanded, plastically expanded and fully heated TF Pipes) simulates the worst case scenario for the imperfection sensitivity analysis. The imperfection values range from zero to 10% of liner pipe wall thickness, while these values are classified as acceptable by DNV-OS-F101 (2013) guidelines, representing real case scenarios.

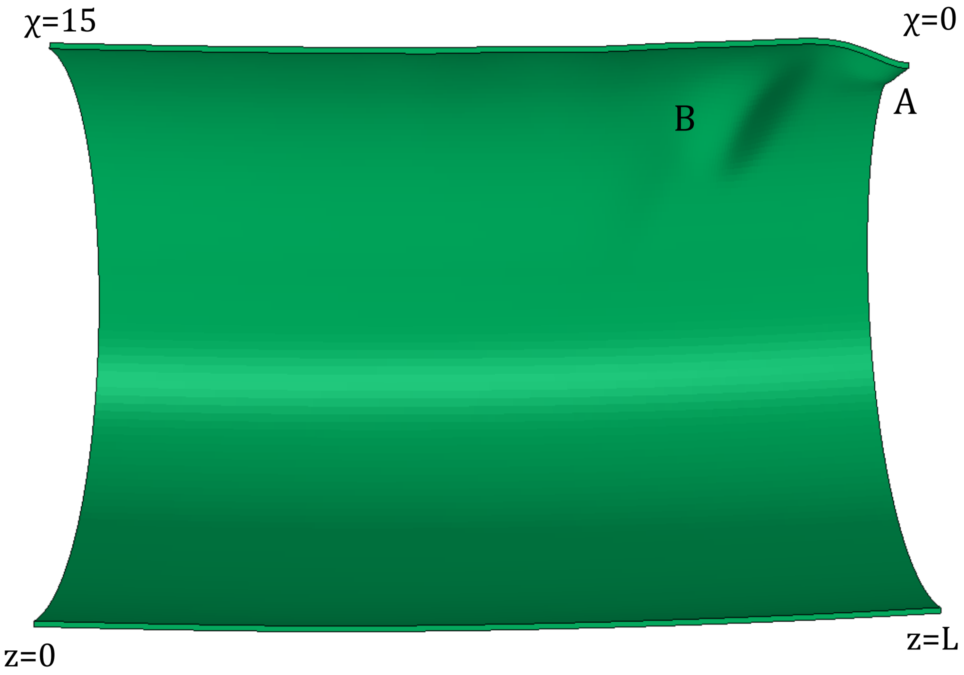

Figure 4.15 Geometric configuration of the initial imperfection of the liner pipe.

In the case of elastically expanded lined pipes, after depressurization, a residual imperfection with amplitude Δ_r is observed, as shown in Figure 4.16, in terms of the initial imperfection amplitude, while for the other two cases the residual imperfection after the manufacturing process is negligible for the entire range of initial imperfection amplitude considered. The effect of the initial geometric imperfection, assuming the maximum value of amplitude ($\Delta_0 = 10\%$), is presented in Figures 4.17, 4.18, showing its influence on the liner pipe detachment (Δ) from the outer pipe and the liner pipe moment (m_l). The solid curves correspond to imperfection-free liner, while the dashed curves refer to imperfect liner, respectively. In Figure 4.19, the critical curvature values of the different examined types of manufacturing processes for the case of 50% initial radial gap (g_0) are presented. For the case of the elastically expanded and plastically expanded pipes, a significant reduction of the critical curvature value occurs with increasing initial imperfection Δ_0, an observation which is consistent with the results reported in previous publications (Vasilikis and Karamanos, 2012, 2013). This reduction is more significant for small values of Δ_0, and less pronounced for larger values of Δ_0. It is interesting to note that a 10% initial imperfection, results in a 36% and 26% decrease of critical curvature for the case of the elastically expanded and plastically expanded pipes, respectively. On the other hand, the mechanical behaviour of the fully heated TF Pipes is less sensitive to initial geometric imperfections, resulting in a 9%

decrease for the same imperfection size (10%). The critical curvature (κ_{cr}) for different values of initial geometric imperfection amplitude and fabrication cases is summarized in Table 4.4.

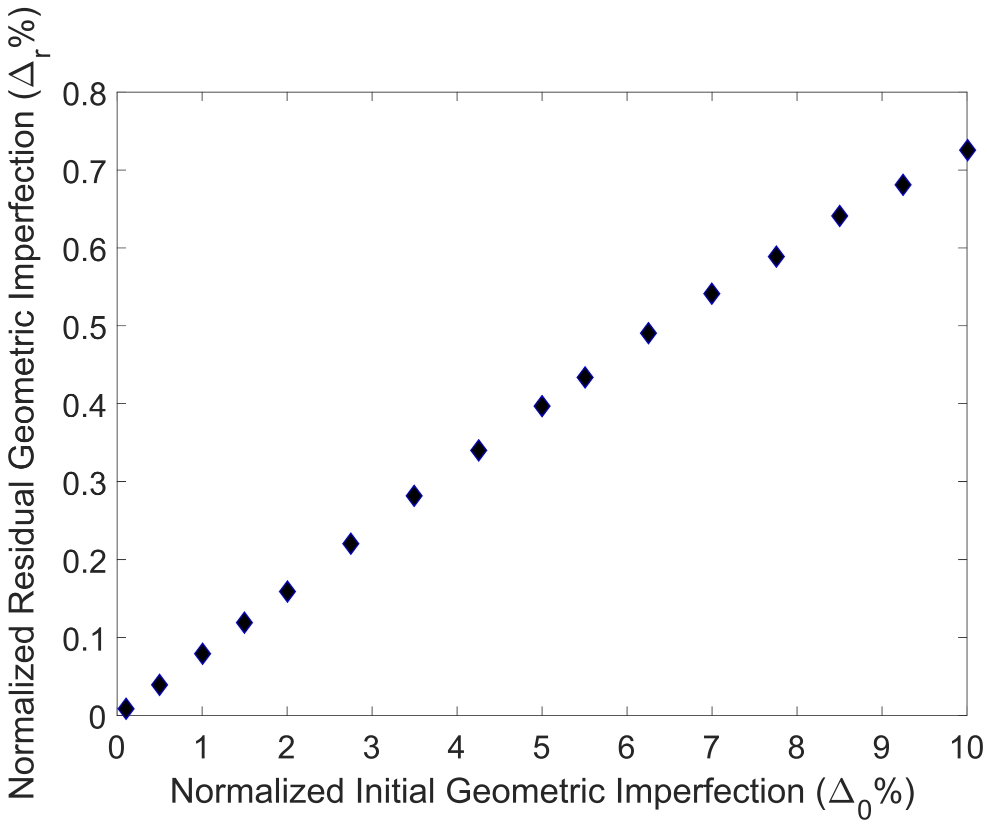

Figure 4.16 Normalised residual imperfection (Δ_r) of elastically expanded lined pipes (referring to the outer pipe) with respect to normalised initial imperfection (Δ_0).

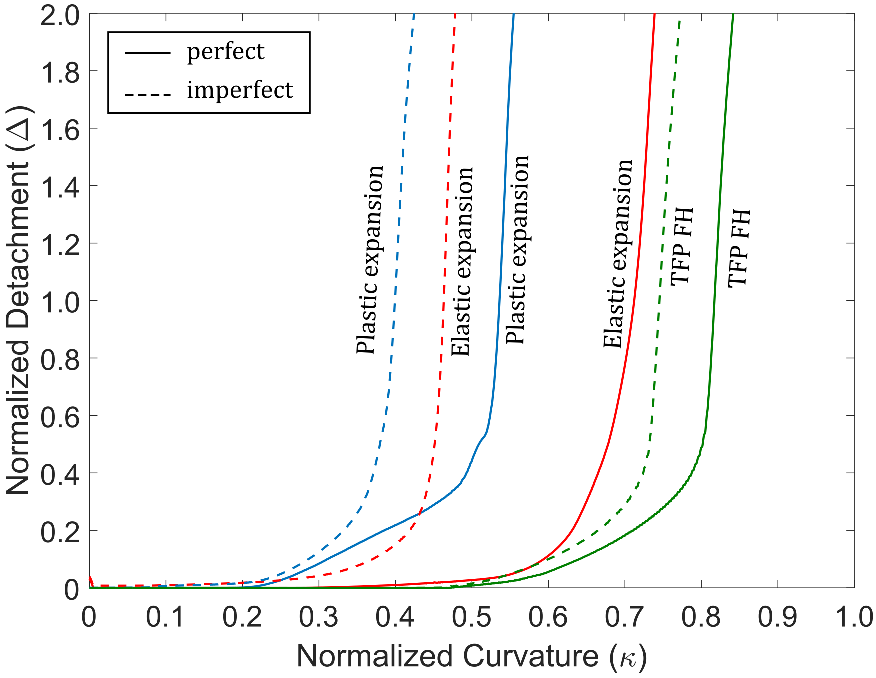

Figure 4.17 Normalised detachment (Δ) with respect to normalised curvature (κ) for the different manufacturing processes for zero and 10% initial imperfection.

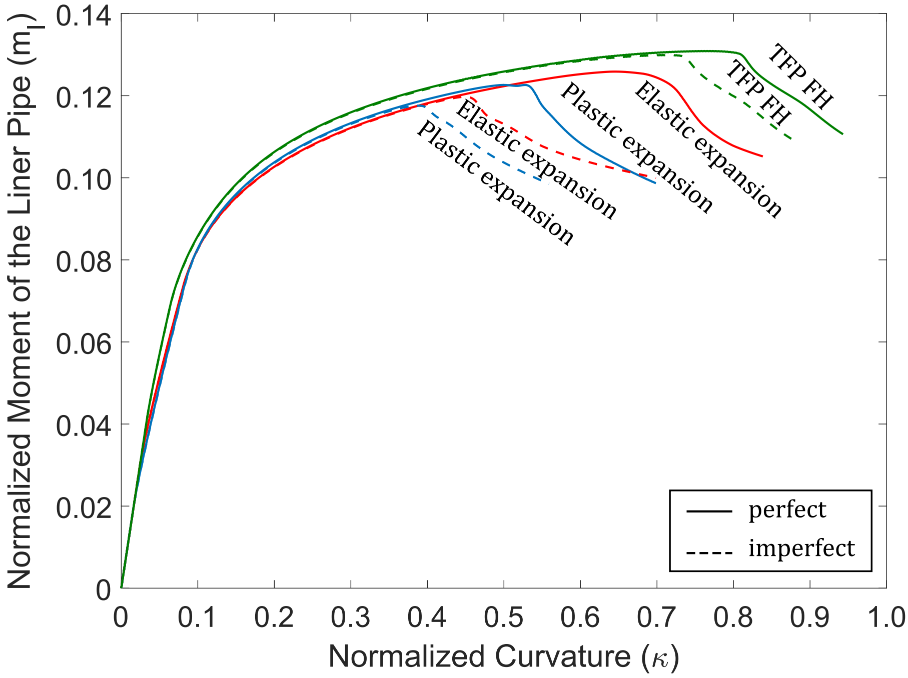

Figure 4.18 Normalised moment of the liner pipe (m_l), with respect to normalised curvature (κ) for the different manufacturing processes for zero and 10% initial imperfection.

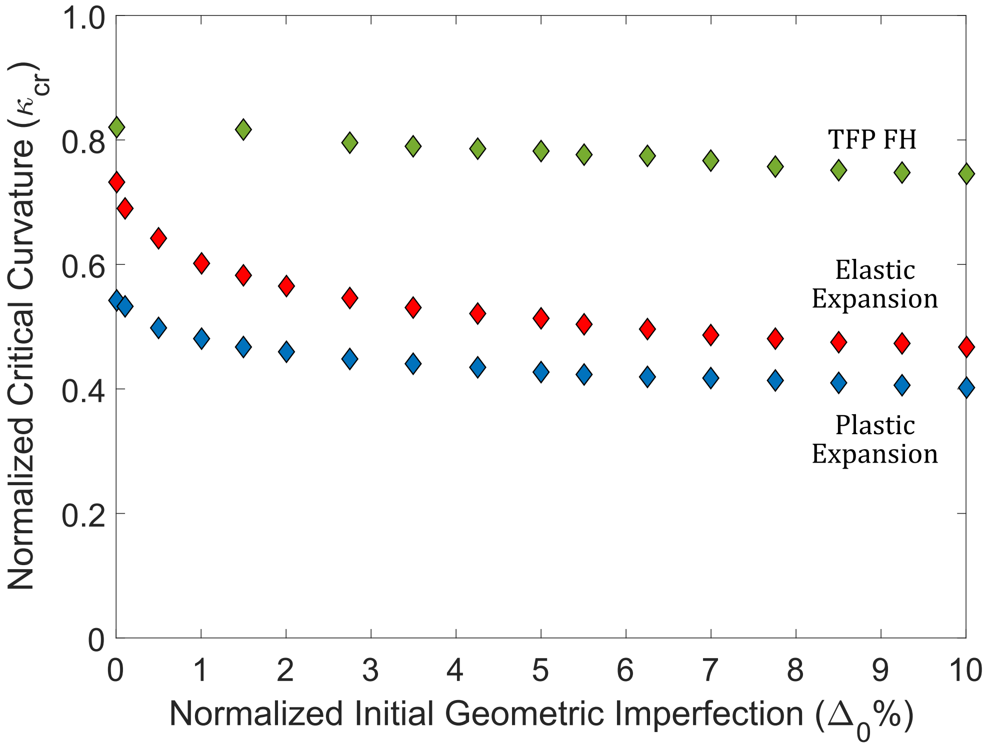

Figure 4.19 Normalised critical curvature in terms of initial imperfection amplitude for hydraulically expanded and fully heated TF lined Pipes.

Table 4.4 Critical curvature (κ_{cr}) for different imperfection amplitudes (Δ_0) for different fabrication processes.

Imperfection Amplitude (Δ_0%)	Critical Curvature (κ_{cr}) Elastic Expansion	Plastic Expansion	TFP FH
0.1	0.689	0.533	0.821
0.5	0.643	0.497	-
1.0	0.603	0.481	-
1.5	0.582	0.468	-
2.0	0.565	0.460	0.816
2.75	0.546	0.448	-
3.5	0.531	0.440	0.796
4.25	0.521	0.434	0.790
5.0	0.513	0.427	0.786
5.5	0.503	0.424	0.782
6.25	0.495	0.420	0.776
7.0	0.487	0.418	0.774
7.75	0.481	0.413	0.767
8.5	0.475	0.409	0.757
9.25	0.473	0.406	0.751
10.0	0.467	0.402	0.747

4.5.2 Internally pressurized lined pipes

The effect of internal pressure (P_{in}) on the bending response of mechanically bonded lined pipes is investigated in the present work and its beneficial role on the critical curvature is demonstrated in Chapter 3. In the present section, lined pipes fabricated through different manufacturing procedures (namely, plastically expanded, partially heated and fully heated TF Pipes), and initial radial gap equal to 50%, are subjected to pressurized bending. The pressure is applied after the manufacturing process and is held constant during the monotonic bending process. The pressure level is 10% of the liner pipe yield pressure ($P_{y,l} = 2\sigma_{y,l}t_l/D_{m,l}$, where $D_{m,l}$ is the mean diameter of the liner pipe). A tensile force (F_p) is also applied on the reference node in the $z = L$ plane, equal to the applied internal pressure times the internal cross-section of the liner ($F_p = P_{in}\pi(D_l - 2t_l)^2/4$) in order to simulate the force at the two capped ends due to the internal pressure. This force is referred to as "capped-end force", and remains constant during bending, but follows the orientation of reference node (follower force).

The normalised amplitude of detachment (Δ) of the liner pipe is presented in Figure 4.20, showing that in the presence of internal pressure the abrupt detachment of the liner occurs at higher values of curvature for all three fabrication procedures. In Figure 4.21, the normalised moment of the liner pipe is presented, showing that the sharp drop of each case occurs at higher curvature values a result compatible with the one in Figure 4.20. The critical curvature (κ_{cr}) of the plastically expanded, fully and partially heated TF pressurized pipes is increased by 27%, 143% and 115%, respectively. As already presented in more detail in the previous chapter (section 3.4.2), despite the low level of internal pressure, the critical curvature (κ_{cr}) increases significantly. In the case of plastically expanded lined pipes, the increase of critical curvature is considerably less pronounced, compared to the other two manufacturing cases. This is attributed to the excessive plastic deformation of the liner pipe during the manufacturing process and the significantly lower mechanical bonding between the liner and the outer pipe at the end of fabrication, compared to partially heated and fully heated TF Pipes. The results are summarized in Table 4.5, including the values of normalised detachment, radius of curvature corresponding to the neutral axis of the pipe and global bending strain (ε_{cr}) at the buckling stage, for each fabrication process.

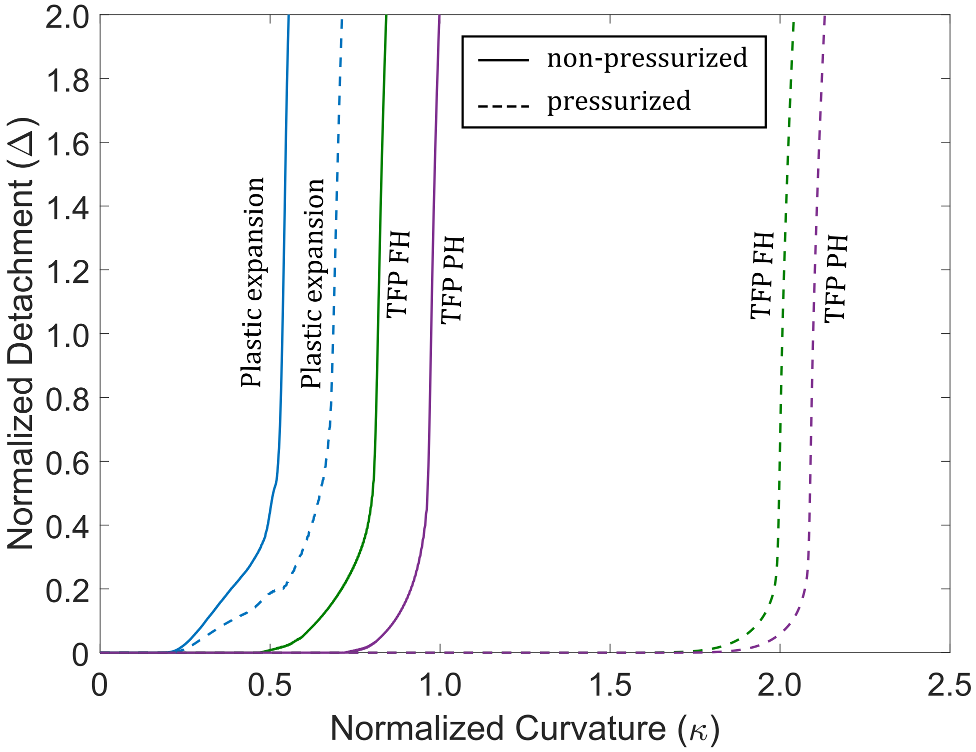

Figure 4.20 Normalised detachment (Δ) with respect to normalised curvature (κ) for the different manufacturing processes for zero and 10% internal pressure.

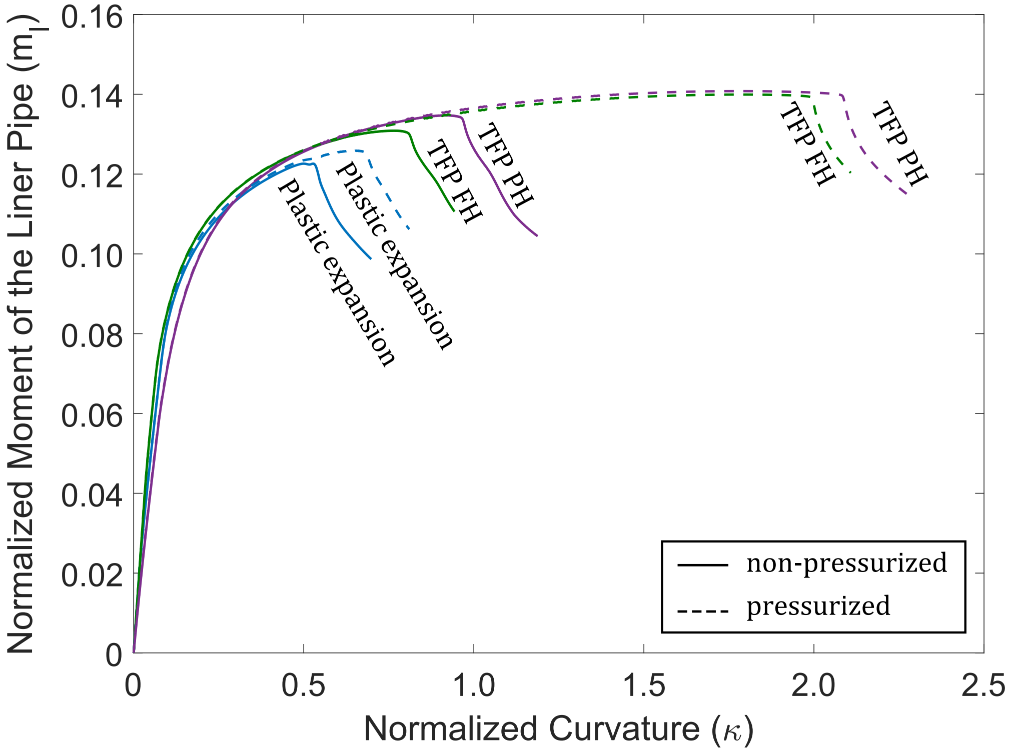

Figure 4.21 Normalised moment of the liner pipe (m_l), with respect to normalised curvature (κ) for the different manufacturing processes for zero and 10% internal pressure.

Table 4.5 Critical curvature, corresponding normalised detachment, radius of curvature and global bending strain for different fabrication processes in case of 10% internal pressure.

Manufacturing Process	Normalised Critical Curvature (κ_{cr})	Normalised Critical Detachment ($\Delta_{cr}\%$)	Buckling Radius of Curvature (ρ_{cr} mm)	Buckling Strain (ε_{cr} %)
Plastic Expansion	0.689	113	8657	1.87
Fully Heated TFP	2.000	58	2982	5.43
Partially Heated TFP	2.091	59	2852	5.67

4.5.3 Effect of liner pipe temperature in Tight-Fit Pipes

The effect of the temperature level of the liner pipe on the final state of stress of the partially heated TF Pipes is also investigated. In the previous results, the partially heated liner pipe is examined only for temperature equal to 57% ($T_l = 388\ K$) of the fully heated TF Pipes. In the present section, other temperatures levels ranging from 57% to 100% of the temperature used in the fully heated TF Pipe (where the temperature of the liner pipe is equal to the outer pipe's T_o), are investigated. In the following, the temperature will be denoted as a percent, referring to the percentage of the liner temperature with respect to the temperature of the outer pipe. In this section three types of analysis are adopted, considering (a) temperature-independent material properties of both pipes (as described in section 4.2.1), (b) temperature-dependent material properties of the liner pipe and (c) temperature-dependent material properties for both pipes. The latter cases (b) and (c) should be regarded as an attempt for refinement of the present model.

4.5.3.1 Temperature-independent material properties

Figure 4.22 presents the normalised hoop compression of the liner pipe of partially heated TF Pipes after the manufacturing process, with respect to different temperature levels of the liner on the pressurization step. The results are obtained with the assumption of temperature-independent material properties. For temperatures varying from 57% to 92% of T_o the hoop compression of the liner decreases slightly as the temperature increases, while the residual compressive stress is higher than the yield stress ($\sigma_{y,l}$) of the liner. These cases follow corresponding paths of hoop stress of the liner pipe with respect to diameter change as shown in Figure 4.8. For 96% and 100% temperature levels, the hoop compressive stress decreases significantly resulting in stress smaller than the yield stress. As explained previously in section 4.3.5, during the pressurization step the thermal part of the hoop strain of the liner pipe increases significantly while the mechanical part decreases resulting in plastic hoop compression. After the depressurization, the hoop stress of the liner pipe is in the elastic region, as shown in Figure 4.7, justifying the sharp drop of hoop compressive stress of the liner pipe in Figure 4.22. Figures 4.23 and 4.24 present the detachment and the corresponding moment of the liner pipe, showing the abrupt liner detachment (and the corresponding sharp drop of the bending moment of the liner) in higher curvature values as the maximum temperature of the liner decreases. The critical curvature, as defined in Chapter 3 (section 3.4.2), is presented in Figure 4.25, while the results are also summarized in Table 4.6, including the values of normalised detachment, radius of curvature corresponding to the neutral axis of the pipe and global bending strain (ε_{cr}) at the buckling stage for each fabrication process.

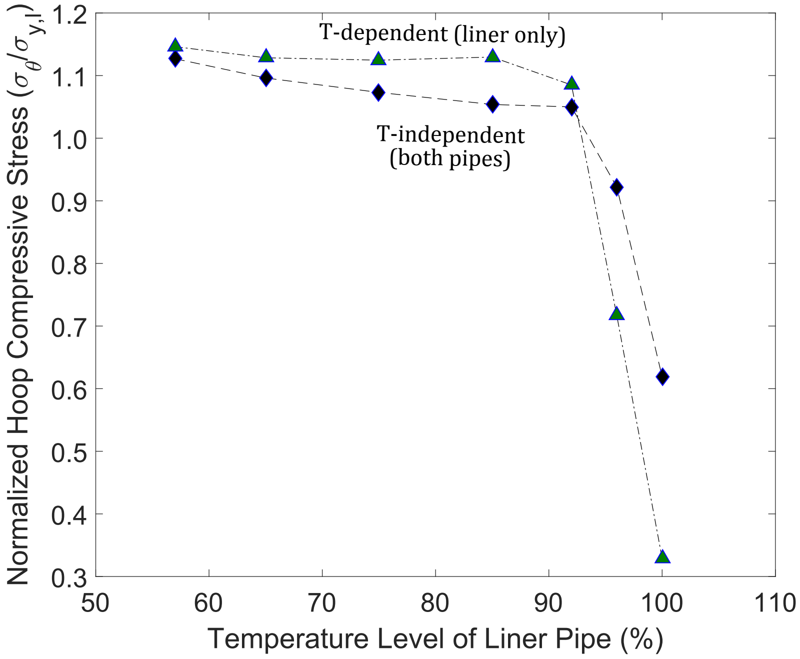

Figure 4.22 Liner compressive hoop stress (residual hoop stress) with respect to the liner pipe temperature during pressurization, for temperature-dependent and temperature-independent liner material.

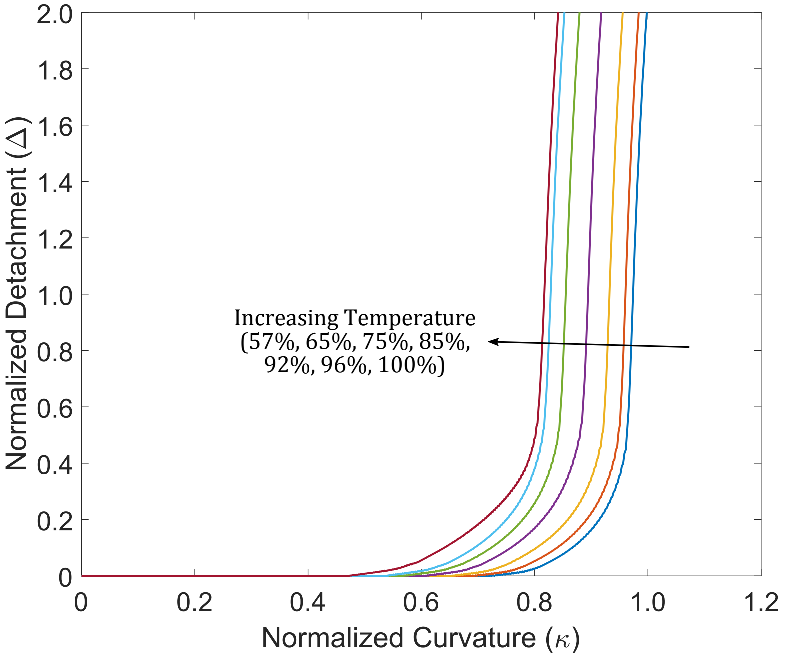

Figure 4.23 Normalised detachment (Δ) with respect to normalised curvature (κ) for the different temperature levels of the liner pipe for the partially heated TF Pipes, considering temperature-independent liner material.

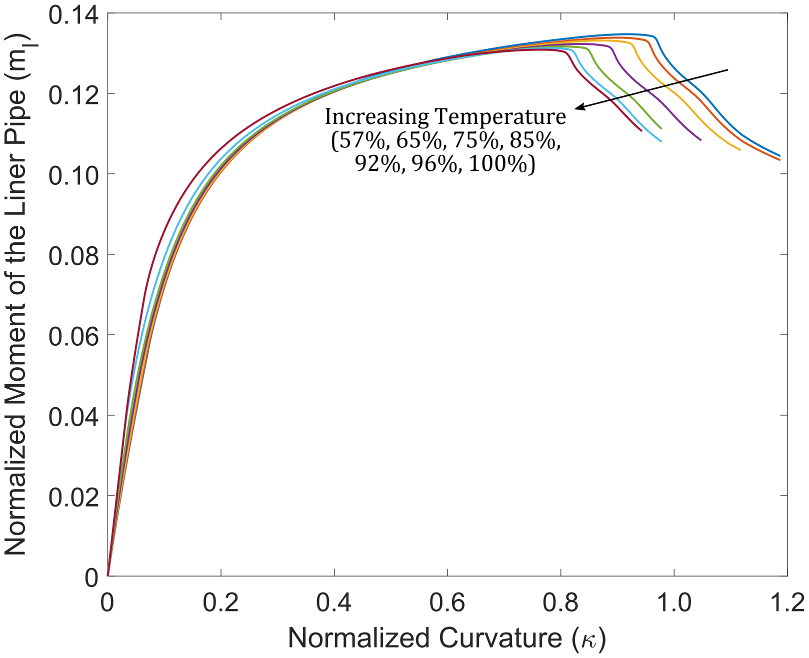

Figure 4.24 Normalised moment of the liner pipe (m_l), with respect to normalised curvature (κ) for the different temperature levels of the liner pipe for the partially heated TF Pipes, considering temperature-independent liner material.

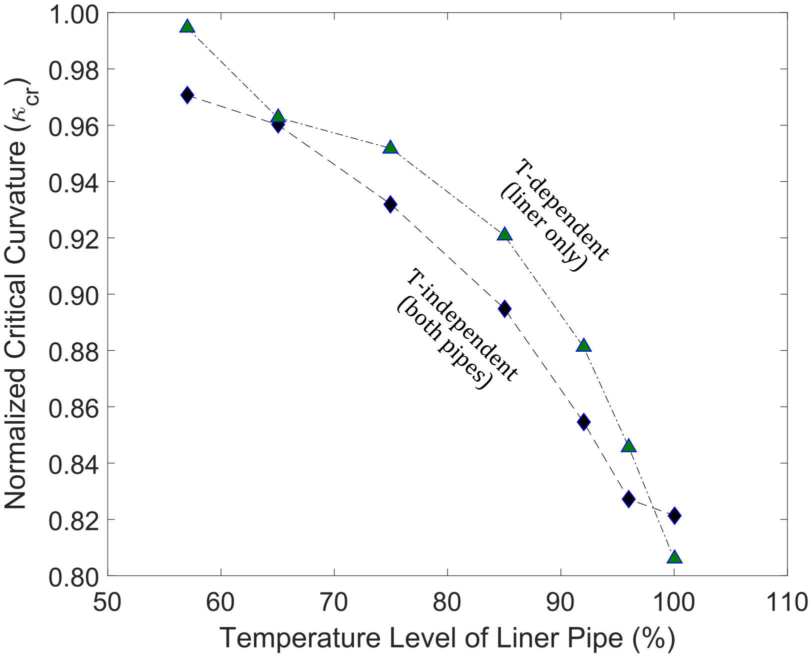

Figure 4.25 Normalised critical curvature (κ_{cr}) in terms of different temperature levels of the liner pipe for the partially heated TF Pipes, for temperature-dependent and temperature-independent liner material.

Table 4.6 Critical curvature, corresponding normalised detachment, radius of curvature and global bending strain for different temperature levels of the liner pipe for the partially heated TF Pipes.

Temperature Level of the Liner (%)	Normalised Critical Curvature (κ_{cr})	Normalised Critical Detachment ($\Delta_{cr}\%$)	Buckling Radius of Curvature (ρ_{cr} mm)	Buckling Strain (ε_{cr} %)
57	0.971	82	6145	2.63
65	0.960	99	6212	2.61
75	0.932	99	6400	2.53
85	0.895	103	6665	2.43
92	0.855	98	6979	2.32
96	0.827	94	7211	2.25
100	0.821	121	7261	2.23

4.5.3.2 Temperature-dependency of liner pipe

All previous results on TF Pipes have been obtained under the assumption that the material properties are not affected by the level of temperature. In the present section, the mechanical behaviour of the liner pipe is also investigated assuming temperature-dependent Young's modulus (E_l), yield stress ($\sigma_{y,l}$) and thermal expansion coefficient (α_l) of the liner pipe, in an attempt to refine of the numerical model, while the outer pipe is still considered temperature-independent.

The dependency of Young's modulus, yield stress and thermal expansion coefficient on the temperature adopted in the present study is the one proposed by Alain *et al.* (1997); Atlas Specialty Metals (2004); Hong *et al.* (2003), shown in Table 4.7. In Figure 4.22, the normalised hoop stress of the liner pipe, after the manufacturing process, is presented for partially heated TF Pipes, taking into account the temperature-dependent material properties of the liner pipe. The residual hoop compression of the liner pipe, when temperature-dependent liner pipe material properties are considered, is higher compared with the temperature-independent liner material, for temperature levels T_l varying from 57% to 92% of T_o, as the Young's modulus and yield stress of the liner pipe decreases. However, for temperature level T_l near the 100% level, the residual hoop compression of the liner decreases, resulting in lower compression values compared with the temperature-independent case. For this high-temperature range, the thermal expansion coefficient of the liner (α_l) also increases, resulting in higher thermal hoop strain, and lower mechanical bonding.

Table 4.7 Material properties of the liner pipe with respect to the temperature level.

Temperature of the liner T_l (K)	Young's Modulus E_l (MPa)	Yield Stress $\sigma_{y,l}$ (MPa)	Thermal Expansion Coefficient α_l ($10^{-5}K^{-1}$)
273-298	193000	260	1.59
298-373	180306	181.45	
373-448			
448-474	178322		1.62
474-557	171394	150.23	
557-574	170141		
574-588	163064		
588-659			1.75
659-674	161989		
674-768	154971	133.96	
768-811	-		
811-872	-		-

Figure 4.25 shows the critical curvature (κ_{cr}) with respect to different temperature levels of the partially-heated liner pipe, considering temperature-dependent liner pipe material properties. For temperature levels ranging from 57% to 96% of T_o, the critical curvature values are higher compared to the corresponding κ_{cr} values obtained assuming temperature-independent liner pipe material properties. For the case of temperature-dependent properties, the values of Young's modulus and yield stress of the liner are lower compared with the temperature-independent case, resulting in higher residual hoop compression of the liner pipe, as shown in Figure 4.22, and critical curvature values, respectively. For fully heated liner pipe, the critical curvature is lower in the temperature-dependent case. This is attributed to the fact that the residual hoop compression, after the manufacturing process, is 52% lower than the corresponding value obtained by the temperature-independent case.

Finally, the difference of the critical curvature value obtained considering temperature-dependent and temperature-independent material properties of the liner, ranges from 0.27% to 3.08%, leading to the conclusion that the assumption of temperature-independent material of the liner yields very reasonable results, and can be used for obtaining reliable estimates of liner buckling curvature. However, the material of the outer pipe is considered temperature-independent; this is an assumption which is examined in the following section 4.5.3.3.

4.5.3.3 Temperature-dependency of both pipes

At elevated temperatures, the material properties of the carbon steel is also affected, reducing its stiffness and strength. In this section, both pipes are assumed temperature-dependent, aiming at simulating a closer to reality scenario, identifying also the influence of the outer pipe temperature dependency on the mechanical bonding of both pipes and the buckling performance of the liner pipe under monotonic bending.

Two different cases are investigated considering both temperature dependent and temperature independent material properties of the outer pipe, while the liner pipe material is assumed temperature dependent. This analysis is aimed at identifying the influence of temperature dependency of the outer pipe material on the mechanical bonding of the pipes and the buckling performance of the liner pipe. In this section, the outer pipe material is modelled with the ABAQUS built-in plasticity model, as described in section 4.2.1 and shown in Figure 4.1. Furthermore, the dependency of Young's modulus (E_o) and yield stress ($\sigma_{y,o}$) of the outer pipe adopted in the present study follows the provisions of the European Standard (EN-1993-1-2, 2005), as shown in Table 4.8. For the liner pipe material, the plasticity model described in section 4.2.1 is employed, accounting for temperature-dependent material properties as shown in Table 4.7.

Table 4.8 Material properties of the outer pipe with respect to the temperature level (EN-1993-1-2, 2005).

Temperature of the outer T_o (K)	Young's Modulus E_o (GPa)	Yield Stress $\sigma_{y,o}$ (MPa)
298-373	210	558
373-473	189	452
473-573	168	343
573-680	147	235

Figure 4.26 presents the liner hoop compressive stress for the case of temperature dependent and temperature independent outer pipe material at the end manufacturing process, with respect to different temperature levels of the liner pipe during pressurisation. When the material properties of the outer pipe are considered temperature-independent,

the outer pipe deforms elastically throughout the fabrication process, resulting in identical hoop compression in the liner pipe, such as in the analysis presented in Figure 4.22 in section 4.5.3.2. It should be noted that in the current analysis the outer pipe is described by the ABAQUS built-in model, while in section 4.5.3.2 the user-subroutine is used. However, the outer pipe deforms elastically in both cases, leading to identical response. In the temperature-dependent case, the stiffness and strength of the outer pipe are reduced significantly, and the outer pipe deforms plastically during the fabrication process, while the hoop compression of the liner pipe is not significantly affected, compared to the temperature-independent outer pipe material. Figure 4.26 shows an identical liner hoop compression for temperature levels up to 92% of the outer pipe temperature, while in higher temperature levels the liner hoop compression increases slightly, leading to higher mechanical bonding.

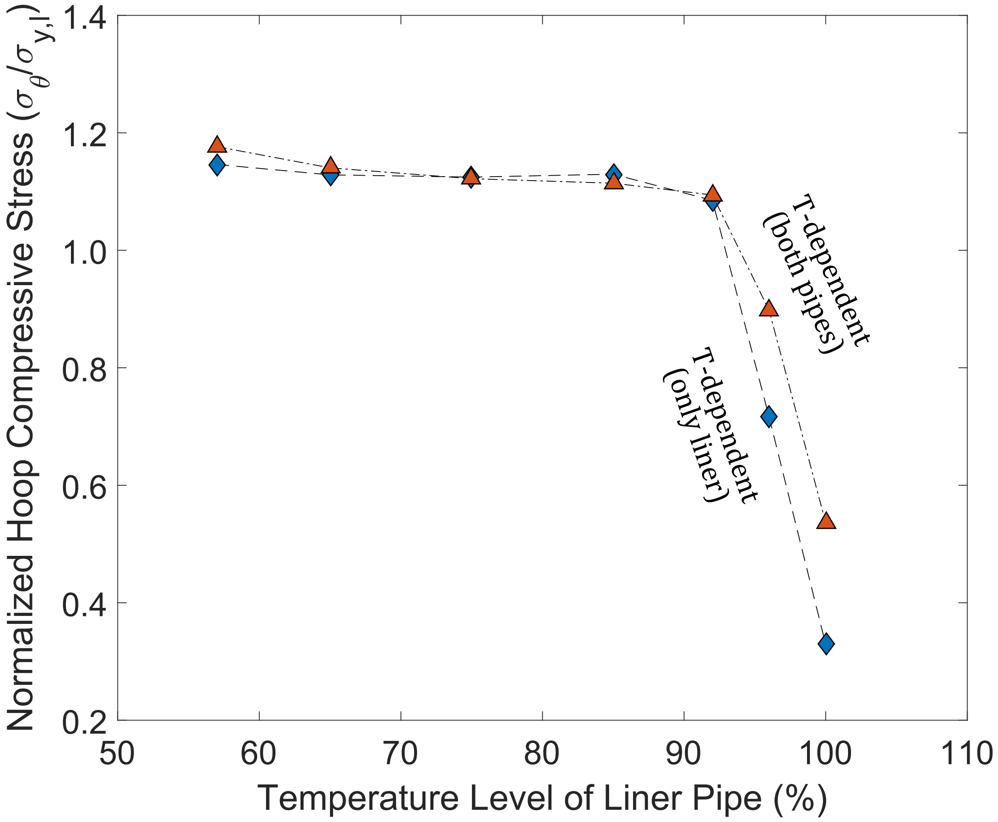

Figure 4.26 Liner compressive hoop stress (residual hoop stress) with respect to the liner pipe temperature during pressurization, considering temperature-dependent materials for both pipes.

The bending response is also investigated for the temperature dependent and temperature independent properties of the outer pipe, considering liner temperature equal to 57% (partially heated) and 100% (fully heated) of the outer pipe. Following the buckling definition established in section 3.4.2, in partially heated pipes the critical curvature κ_{cr} is calculated equal to 1.001 and 1.030, for temperature-independent and temperature-dependent outer pipe material. On the other hand, for fully heated TF Pipe the critical curvature is calculated equal to 0.797 and 0.831, respectively. This increase on the curvature values is attributed to the slight increase on liner hoop compression, as shown in Figure 4.26, for each case. It should be noted that lined pipe bending occurs after cooling down the pipe at $T_i = 298\ K$, as described in sections 4.3.3 and 4.3.4. Therefore, the decrease of stiffness and strength of both pipes at elevated temperature levels occurs only during the manufacturing process. The temperature dependency of the outer pipe material leads to plastic deformation in the outer pipe during the fabrication process, which also affects slightly the stress state during bending. However, the liner pipe buckles locally at very low curvature levels, resulting in very small influence of prior plastic deformation in the outer pipe during fabrication process

4.6 Summary of results

At the beginning of the present chapter, purely mechanical and thermo-mechanical processes for lined pipe fabrication are simulated. In the case of elastically expanded lined pipes, and for initial radial gap ranging from 35% to 75% of the liner pipe wall thickness, a residual radial gap is observed at the end of the manufacturing process, resulting in a lined pipe with no mechanical bonding. On the other hand, plastically expanded lined pipes, as well as fully and partially heated TFP result in contact between the liner and the outer pipe, associated with hoop compression of the liner pipe. The results indicate that the TFP process induces higher hoop stress than the plastically expanded lined pipe, while the mechanical bonding of partially heated TFP is higher than the one in fully heated TFP. In thermo-hydraulic expanded pipes, reverse plastic loading of the liner material has been detected during the manufacturing process, implying that a cyclic-plasticity model should be used in the finite element model.

In the following, the bending behaviour of lined pipes, is investigated, accounting for their manufacturing process. The main purpose of this analysis is the calculation of the critical curvature of the liner under monotonic bending. The results show that TF Pipes buckle at higher curvature compared with the hydraulically expanded pipes, especially when partial heating of the liner occurs, highlighting the important influence of prestressing of the liner pipe. In the case of plastically expanded lined pipes, the critical curvature value is lower than that of the corresponding elastically expanded lined pipes. With increasing plastic deformation of the liner, the critical curvature and the corresponding half-wavelength of the wrinkled liner decrease, implying that, during manufacturing, the plastic deformation of the liner pipe has a significant effect on its structural performance; this should be major parameter for the fabrication process.

In initially imperfect elastically expanded lined pipes, a residual geometric imperfection is observed after manufacturing, while for plastically expanded and fully heated TF Pipes, the residual imperfection is negligible. The critical curvature of hydraulically expanded pipes (both elastic and plastic) is imperfection sensitive, especially for small values of imperfection amplitude. The imperfection sensitivity of fully heated TF Pipes is less pronounced, due to the smooth inner surface of the outer pipe.

The beneficial effect of internal pressure on bending response has been verified. This benefit has been more significant in fully and partially heated TF Pipes, but it is less pronounced in plastically expanded lined pipes, due to excessive plastic deformation of the liner pipe induced by the manufacturing process.

Finally, the influence of different levels of liner temperature on the bending response of partially heated TF Pipes is investigated, assuming both temperature-independent and temperature-dependent material properties. Under both assumptions, the residual compression and the corresponding critical curvature of the liner pipe decreases as the maximum temperature of the liner pipe increases. In case of temperature-dependent materials, the outer pipe deforms inelastically during the manufacturing process, due to the reduced strength at elevated temperature levels. However, the hoop compression in the liner pipe and the corresponding buckling response are not affected significantly. Considering temperature-dependent outer pipe material, it leads to plastic deformation in the outer pipe during the manufacturing process, which also affects the stress state during bending. However, the influence on liner pipe buckling response is rather small, concluding that the assumption of temperature independent outer pipe material may lead to reasonable results.

Chapter 5

Cyclic bending of steel lined pipes

5.1 Chapter outline

The present study investigates the structural behaviour of lined pipes, subjected to cyclic loading conditions, representing loading conditions imposed by the reeling installation process. Those loading conditions are associated with maximum curvature values lower than the “critical” curvature determined by monotonic loading (sections 3.4.2 and 4.4). The study uses a single numerical model that simulates the manufacturing process of a mechanically bonded lined pipe in its first stage and proceeds to its cyclic loading in the second stage of the analysis, taking into account the entire plastic loading history of the liner pipe during the fabrication process, including possible reverse plastic loading. Advanced finite element models are employed to simulate the outer pipe and liner response, including pipe wall wrinkling and local buckling, as well as its post-buckling behaviour. The analyses are aimed at simulating the mechanical performance of a mechanically bonded lined pipe subjected to five bending cycles, i.e. the two bending cycles during reeling (Figure 1.3a), and three additional cycles, associated with the case of a failure-repair scenario. The results pinpoint the severe effect of cyclic loading on localized buckling of the liner pipe. Several analyses are conducted, considering different bending curvature ranges, as an attempt to quantify the influence of different reel and aligner radii. The effect of reverse bending during cyclic loading, the influence of geometric imperfections of the liner pipe, the effect of different values of liner wall thickness, the presence of low levels of internal pressure during cyclic bending and the effect of different manufacturing parameters are also examined in detail in the present chapter.

5.2 Material properties and numerical modelling

5.2.1 Lined pipe geometry and material properties

In the present chapter, the analysis is conducted using a similar lined pipe considered in the previous chapter, as presented in section 4.2.1 (Table 4.2). The outside diameter (D_o) and wall thickness (t_o) of the thick-walled outer pipe are equal to 12.75 *in* (323.85 *mm*) and 15.9 *mm* (0.63 *in*), whereas, the outside diameter (D_l) and thickness (t_l) of the thin-walled liner are 288.97 *mm* (11.38 *in*) and 2.8 *mm* (0.11 *in*), respectively, corresponding to an initial radial gap (g_0) between the liner and the outer pipe equal to 1.54 *mm* (55% of t_l), following the initial gap range examined in the previous chapter.

The stress-strain curve used for simulating the X70 steel material of the seamless outer pipe is shown in Figure 4.1, using the user-subroutine (UMAT) presented in 4.2.1. The use of a UMAT is dictated by the presence of plastic plateau, in carbon steel upon first yielding, and the Bauschinger effect during reverse loading. Unfortunately, ABAQUS built-in models can not model both features. The model implemented in the UMAT accounts for a J_2 plasticity model with non-linear kinematic/isotropic hardening. The cyclic response of the X70 carbon steel material is calibrated with experimental data reported by Herynk *et al.* (2007), while the material and hardening parameters of this model are presented in Tables 5.1 and 4.1, respectively.

Table 5.1 Geometric and material properties of the outer and liner pipe.

	Outer Diameter (*mm*)	Thickness (*mm*)	Young's Modulus (*GPa*)	Yield Stress (*MPa*)	Poisson's Ratio
Liner	288.97	2.8	193	260	0.3
Outer	323.85	15.9	210	498	0.3

Furthermore, the geometric and material parameters of the liner pipe are summarised in Table 5.1. To simulate the behaviour of liner pipe material, the ABAQUS/Standard built-in model, as described in section 4.2.1, is used. It consists of a J_2 (von Mises, 1928) plasticity model with non-linear kinematic/isotropic hardening, considering multiple back stresses. Two sets of kinematic hardening parameters C^q and γ^q (Chaboche, 1986; Lemaitre and Chaboche, 1994) are considered, namely MAT-A and MAT-B. Both material sets are calibrated with experimental data provided by Vasilikis (2018), and are capable of predicting the cyclic strain-controlled response quite satisfactorily, as shown in Figures 5.1 and 4.2. The MAT-A kinematic hardening parameters used for the cyclic response of the liner pipe are $C^{1,2,3,4} = 202000; 16000; 800; 150$ *MPa* and $\gamma^{1,2,3,4} = 2800; 150; 3; 1$, while the corresponding MAT-B hardening parameters are the same that used in section 4.2.1 ($C^{1,2,3} = 15000; 23000; 1800\ MPa$ and $\gamma^{1,2,3} = 1500; 250; 20$). The cyclic hardening of the liner pipe 316L material is modelled using the same isotropic hardening parameters in both material sets ($Q = 180\ MPa$ and $b = 5$).

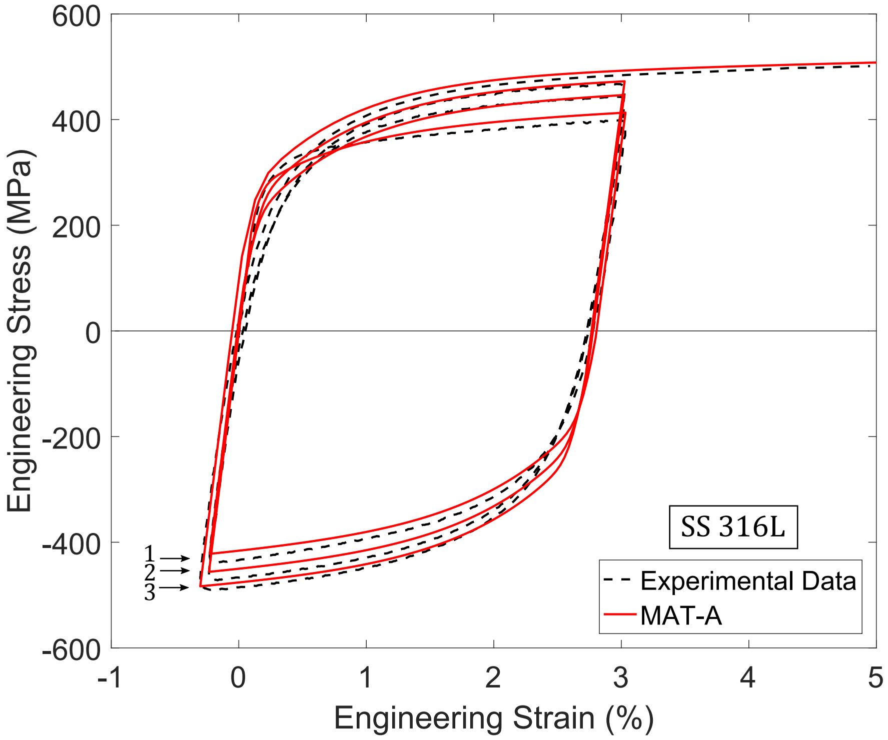

Figure 5.1 Experimental cyclic stress-strain curve of liner pipe (Vasilikis, 2018) and numerical fitting with MAT-A properties.

However, the material sets MAT-A and MAT-B predict a significantly different rate of accumulation of plastic strain under non-symmetric stress controlled loading conditions, referred to as material ratcheting (Bari and Hassan, 2002; Chaboche and Nouailhas, 1989*a*,*b*) and this may be a significant factor in cyclic loading. To elucidate this issue stress-controlled simulations are conducted for both materials A and B, imposing the loading conditions reported in the tests by Kang and Gao (2005). In those tests, 316L stainless steel coupons are cyclically loaded, applying a number of cycles with four consecutive stress amplitudes, as shown in Table 5.2. Figure 5.2 presents the evolution of axial average strain (ratcheting) in those tests, defined as $\varepsilon_r = (\varepsilon_{max} + \varepsilon_{min})/2$, where ε_{max} and ε_{min} are the maximum and minimum axial strains recorded in each cycle. The results in Figure 5.2 show that, despite the fact that MAT-A and MAT-B predict in a very similar manner the strain-controlled loops in Figures 5.1 and 4.2, their prediction of the stress-controlled response is quite different. More specifically, the predicted strains of MAT-A set is in very good agreement with strain observed in the experiment, while the ratcheting rate of MAT-B is significantly lower.

Based on material ratcheting predictions in 316L stainless steel specimens, MAT-A set of parameters is used in the majority of the analyses that follow, whereas MAT-B set is used only for comparison purposes in a small number of cases. The sensitivity of material parameters on the mechanical response of the liner under cyclic loading is examined in section 5.3.

Table 5.2 Loading conditions of mean (σ_m) and amplitude (σ_α) stress history.

Number of Cycles	Mean Stress ($\sigma_m/\sigma_{y,l}$)	Amplitude ($\sigma_\alpha/\sigma_{y,l}$)
30	0	±1.03
10	0.21	±1.03
10	0.35	±1.03
10	0.56	±1.03

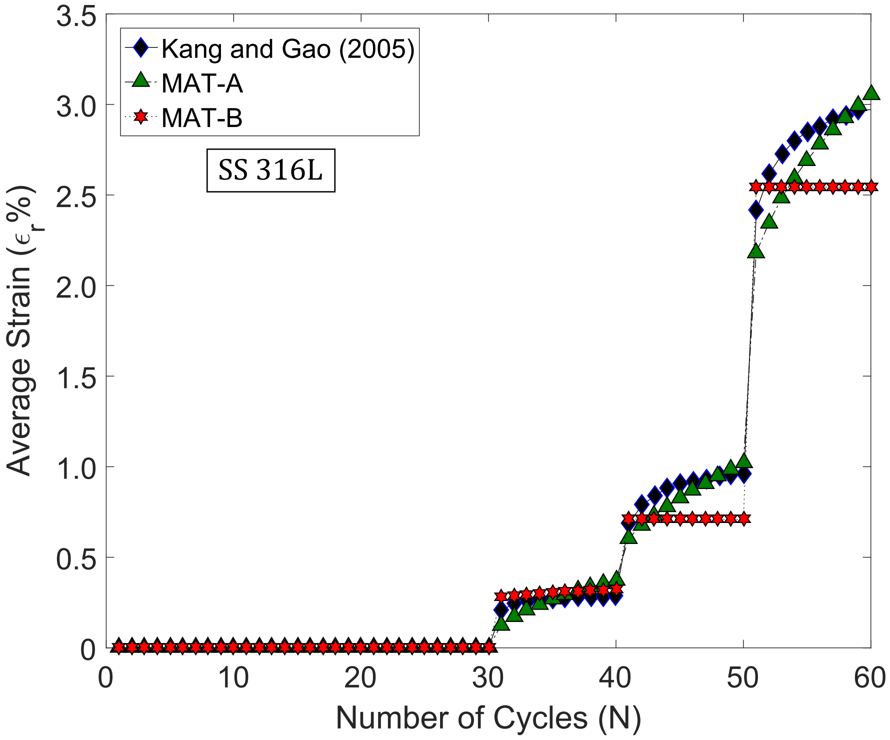

Figure 5.2 Evolution of average strain with respect to the number of cycles in stainless steel 316L; experimental results from Kang and Gao (2005) and predictions from MAT-A and MAT-B.

5.2.2 Numerical modelling and manufacturing process description

In the present chapter, the analyses are performed using the numerical model presented in section 4.2.2 and shown in Figure 4.3. The three-dimensional numerical model represents of a lined pipe segment of length $\chi = 15$ ($\chi = (L-z)/\sqrt{D_{m,l}t_l}$), while the rest of the modelling parameters, such as boundary conditions, type of elements, mesh density of each pipe and the interaction between both pipes follows the modelling parameters as described in detail in section 4.2.2.

Furthermore, prior to simulating the cyclic bending of a lined pipe, the manufacturing process is modelled. In the first stage, the thermo-hydraulic manufacturing process is simulated, proceeding to the cyclic response of the lined pipe in the second stage of the analysis. The complete process of the tight-fit pipe fabrication is described in more detail in section 4.3.3, and is also shown in Figure 4.7. Moreover, the material properties of both pipes are considered temperature-independent; this assumption may not influence the mechanical bonding of both pipes and the corresponding bending response significantly, as already demonstrated in the previous chapter in section 4.5.3.3. The fully heated tight-fit pipe is used for all the analyses presented in the current chapter, while the effect of different fabrication processes on the cyclic response of a lined pipe is examined in section 5.4.6.

5.3 Numerical results for a geometrically perfect lined pipe

In the current section, the cyclic loading behaviour of a mechanically bonded lined pipe is investigated, using the three-dimensional lined pipe model shown in Figure 4.3. In the first part of the analysis, the thermo-hydraulic (TFP) manufacturing process, with heating temperature of the liner pipe equal to the outer pipe temperature, is simulated, as described in section 4.3.3 (Figure 4.7). Subsequently, in the second part of the analysis, the lined pipe is subjected to five consecutive bending cycles representing an installation/repair scenario.

During reeling, the pipeline goes through two main bending cycles, while in a case where a serious defect is detected, the installation process is stopped so that the pipe is repaired (Vasilikis, 2018). In this case, the pipeline is spooled and unspooled again passing through the aligner, the reel and the straightener, adding three bending cycles until the repaired pipeline leaves the reeling vessel. Therefore, a total of five cycles are considered.

The vales of curvature κ are equal to $k_r = \phi/L$, where ϕ is the rotation range applied on the reference node at $z = L$ and are normalised by the curvature-like parameter $k_o = t_o/D^2_{m,o}$. The loading path has been chosen so that the applied curvature ranges $\Delta\kappa$ represent a pipe passing through a reeling (Cycles 1 and 2) and repair scenario (Cycles 3, 4 and 5), with a global bending strain $\varepsilon_b = D_o/2\rho$ (where ρ is the radius of curvature corresponding to the neutral axis of the pipe). In the analysis presented in current section, the ε_b value is equal to 1.59%, and is referred to as “Case I”, while the applied curvature for each cycle is shown in Table 5.3 in more detail. In the case of reeling, this corresponds to reel (R_{reel}) and aligner ($R_{aligner}$) radii equal to 10 m, which is a typical value in practical reeling applications [Chapter 2 in the book by Kyriakides and Corona (2007)]. Furthermore, a negative curvature is applied, representing the deformation that the pipe undergoes passing through the straightener during the reeling process. In the present section, the pipes are considered imperfection-free, while the influence of initial geometric imperfections of the liner pipe is investigated in section 5.4.3.

Table 5.3 Normalised curvature and global bending strain for the five bending cycles in Case I.

Number of Cycle	Normalised Curvature (κ)	Bending Strain (ε_b %)
1	0 → 0.587	0 → 1.59
	0.587 → 0	1.59 → 0
2	0 → 0.587	0 → 1.59
	0.587 → -0.133	1.59 → -0.72
	-0.133 → 0	-0.72 → 0
3	0 → 0.587	0 → 1.59
	0.587 → 0	1.59 → 0
4	0 → 0.587	0 → 1.59
	0.587 → 0	1.59 → 0
5	0 → 0.587	0 → 1.59
	0.587 → -0.133	1.59 → -0.72
	-0.133 → 0	-0.72 → 0

In Figure 5.3, the total moment applied on the double-walled pipe is presented with respect to the number of bending cycles. The value of moment is normalised by $M_o = \sigma_{y,o}D^2_{m,o}t_o$, where $D_{m,o}$ is the mean diameter of the outer pipe, so that $m = M_{Total}/M_o$.

The detachment of the liner pipe from the outer pipe at 12 o'clock location reaches its maximum value at $\chi = 0$ and is presented in Figure 5.4, normalised by the wall thickness of the liner pipe (t_l), with respect to the number of bending cycles. The 12 o'clock position (Figure 4.3) corresponds to the side of the lined pipe that is compressed first during cyclic bending loading (positive curvature values), and represents the side of the pipe that is in contact with the reel and the aligner in the case of reeling. Figure 5.5 presents the corresponding buckling configurations of the liner pipe at 12 o'clock location, showing that during the first two bending cycles a uniform wrinkling pattern develops along the compression side of the liner with amplitude less than the wall thickness of the liner pipe ("a", "b"). In the last three cycles, the detachment increases rapidly ("c") leading to local buckling of the liner and the formation of a main buckle A with four minor adjacent buckles B ("d", "e", "f"), as shown in Figure 5.6.

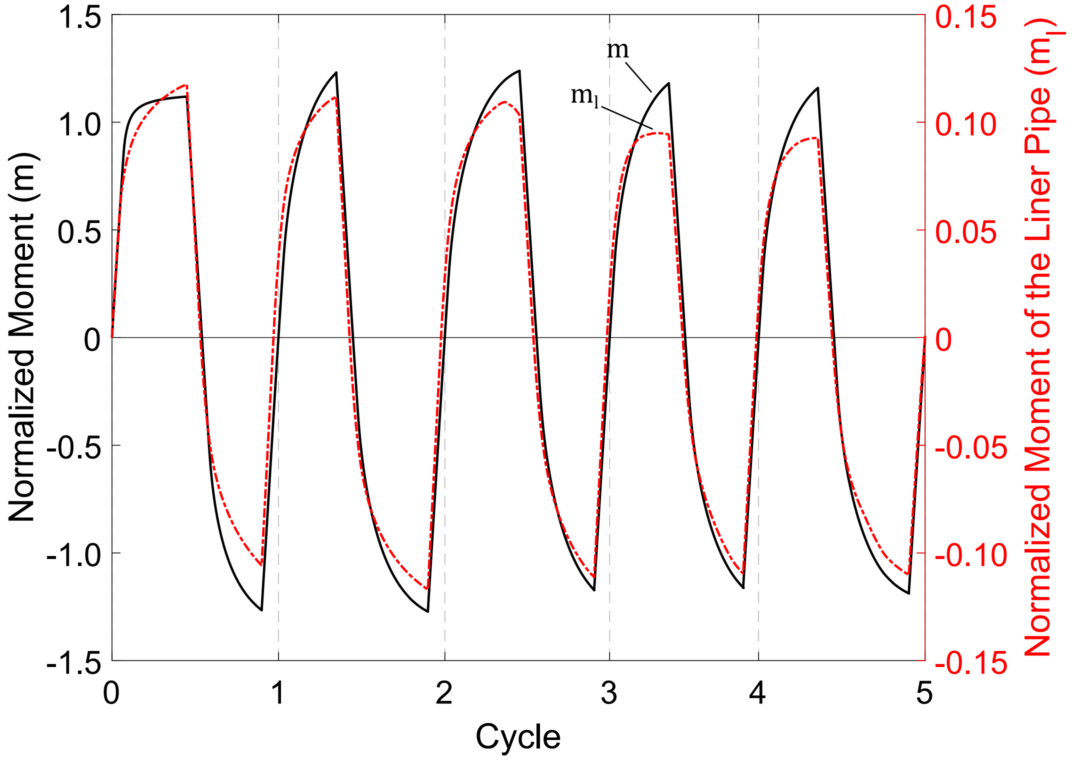

Figure 5.3 Normalised bending moments of the lined (bi-material) pipe (m) and the liner pipe (m_l) for loading Case I, with respect to the number of cycles.

Liner pipe detachment at $\chi = 0$ and 6 o'clock location is also presented in Figure 5.4, with respect to the number of bending cycles. The 6 o'clock position (Figure 4.3) corresponds to the side of the lined pipe that exhibits tension during initial bending. At the end of the second cycle, the liner pipe is slightly detached from the outer pipe, while at the end of the third cycle the liner pipe has developed some small wrinkles ("a"), as shown in Figure 5.7. Subsequently, during the fourth cycle (“b”), four adjacent local buckles B develop on the liner pipe. Buckles B are completely formed at the end of the fifth cycle, representing the reverse bending of the pipe on the straightener (“c”) at the end of the repair.

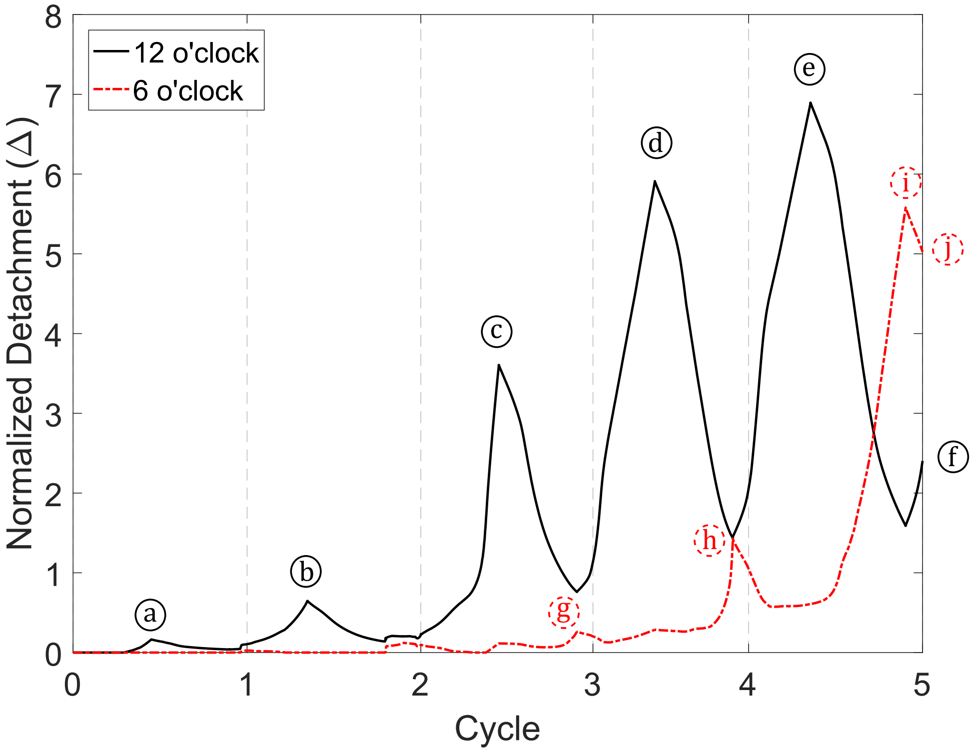

Figure 5.4 Normalised detachment at 12 and 6 o’clock positions of the liner pipe, with respect to the number of cycles (Case I).

The results presented in Figure 5.4 indicate that the detachment of the liner pipe is larger at the 12 o’clock position, than the one at the 6 o’clock position, because the cyclic loading is non-symmetric. The evolution of detachment is also presented at 6 o’clock on the fifth cycle; bending deformation is not so severe on this side of the pipe, compared to 12 o’clock location. Finally, the bending moment carried by the liner pipe is plotted in Figure 5.3, with respect to the number of bending cycles, showing that the bending moment of the liner pipe exhibits a significant reduction on the third cycle, leading to local buckling in a diamond-type mode. The detachment at the 12 o’clock location increases rapidly on the same curvature value of the third cycle, as shown in Figure 5.4, leading to the buckling pattern “c” of Figure 5.5. Therefore, the last three cycles are considered important for the liner pipe, in terms of local buckling, while a low amplitude wrinkling is developed during the first two cycles.

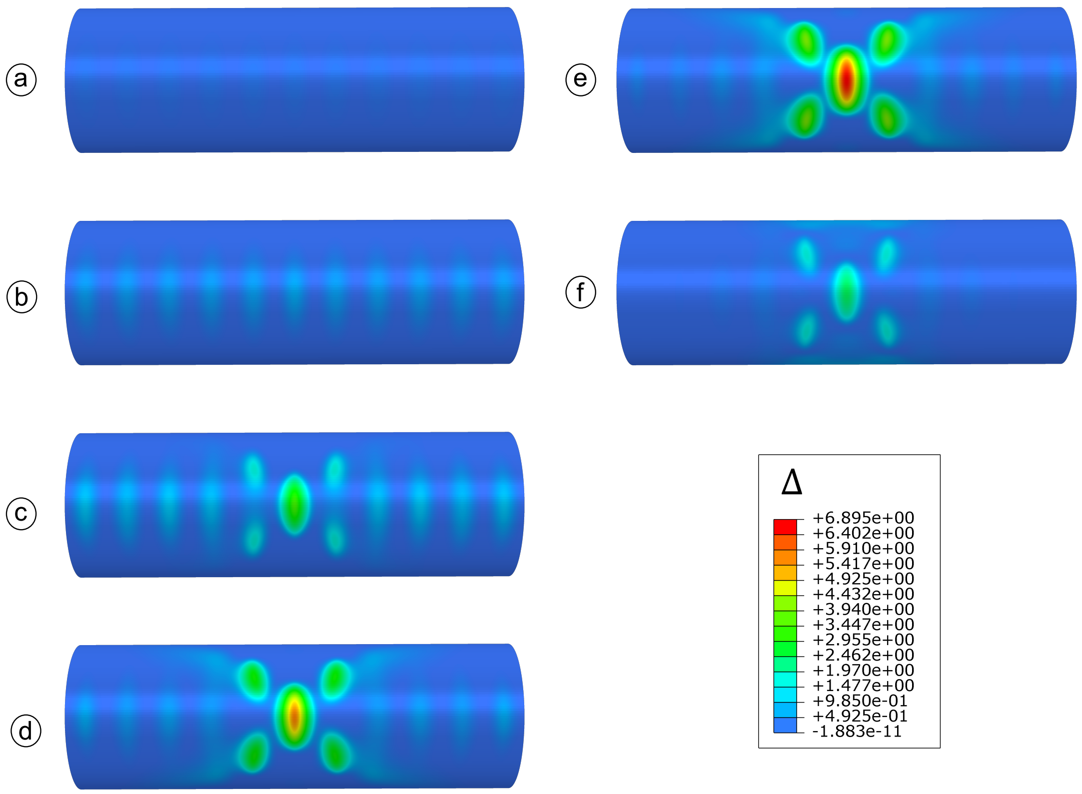

Figure 5.5 Sequence of liner pipe deformation and detachment (Δ), presenting the buckling configuration during cyclic bending, at 12 o'clock location; the configurations of this figure correspond to the stages of Figure 5.4.

Finally, the effect of material parameters (MAT-A and MAT-B sets) on cyclic response is investigated, in an attempt to examine the sensitivity of results to small variations of material properties. In each case, the lined pipe is fully heated following the manufacturing process described in section 4.3.3 and subsequently loading Case I is applied (Table 5.3). Figure 5.8 presents the normalised detachment of the liner at 12 o'clock location for the two sets of material parameters MAT-A and MAT-B, with respect to the loading cycles. There is a striking difference of structural response obtained from the two sets of material properties. Using MAT-B properties, the liner pipe undergoes significantly smaller liner deformation and its gradual detachment develops with a significantly lower rate than the MAT-A case, as shown in Figure 5.8. More specifically, at the third cycle the detachment of the liner pipe using MAT-B properties is 81% lower compared to the MAT-A case. In terms of liner local buckling, the liner pipe using MAT-A set buckles locally during the third cycle, while in the case of MAT-B material properties the liner pipe buckles locally at a later stage during the fourth cycle, highlighting the effect of material parameters on the cyclic response.

This is attributed to the substantially lower rate of ratcheting predicted by MAT-B in comparison with MAT-A (see Figure 5.2). Those results indicate that material ratcheting has a paramount effect on the prediction of cyclic bending response of lined pipes and should be taken into account for calibrating the material model, using appropriate data from stress-controlled cyclic material testing. Given the fact that the stress-controlled material response of MAT-A is closer to the experimental data as discussed in section 5.2.1, MAT-A properties are considered more reliable in representing the response of 316L liner material, and will be employed exclusively for the following parametric analyses.

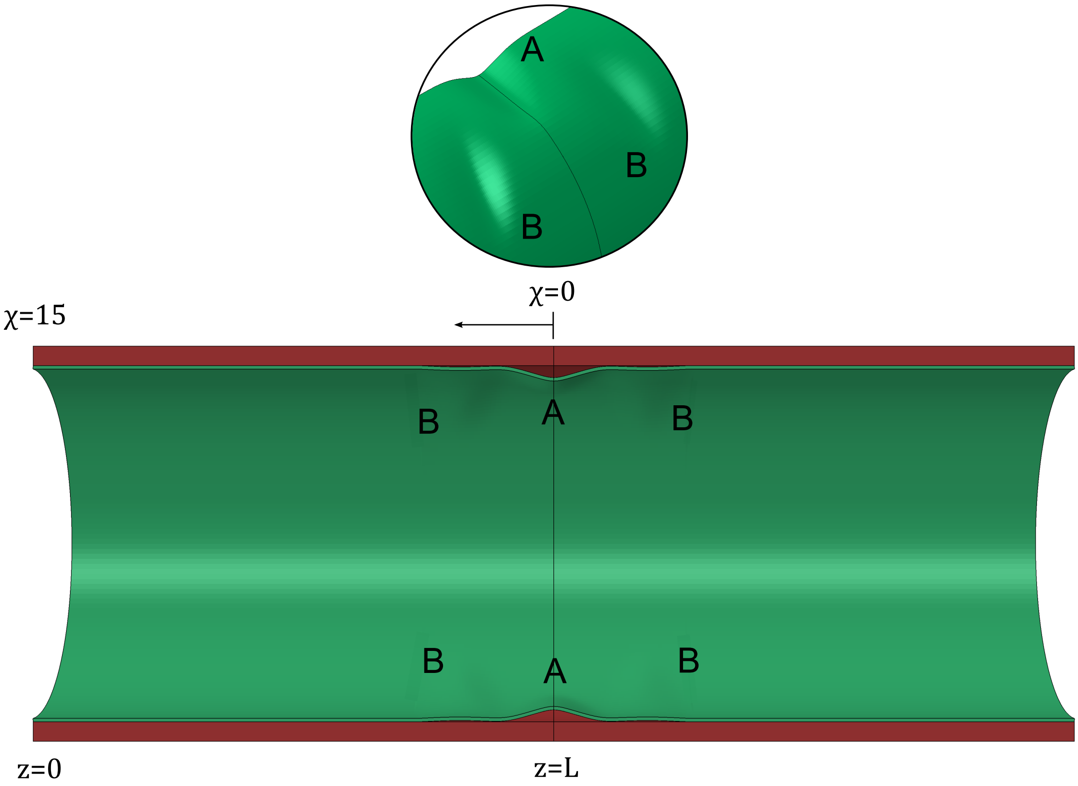

Figure 5.6 Local buckling of the liner pipe at $\chi = 0$ location.

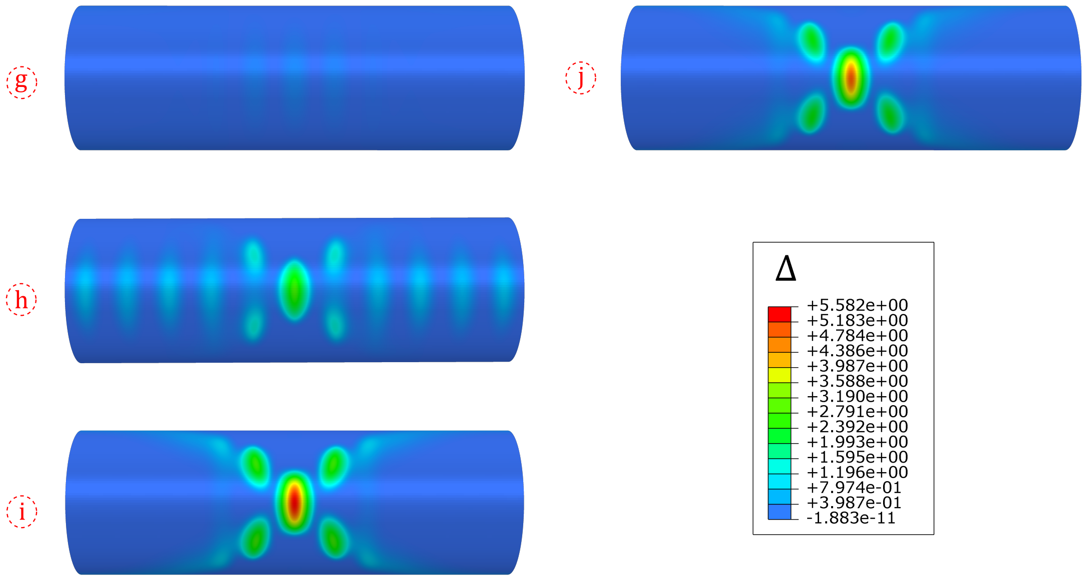

Figure 5.7 Sequence of liner pipe deformation and detachment (Δ), presenting the buckling configuration during cyclic bending, at 6 o'clock location; the configurations of this figure correspond to the stages of Figure 5.4.

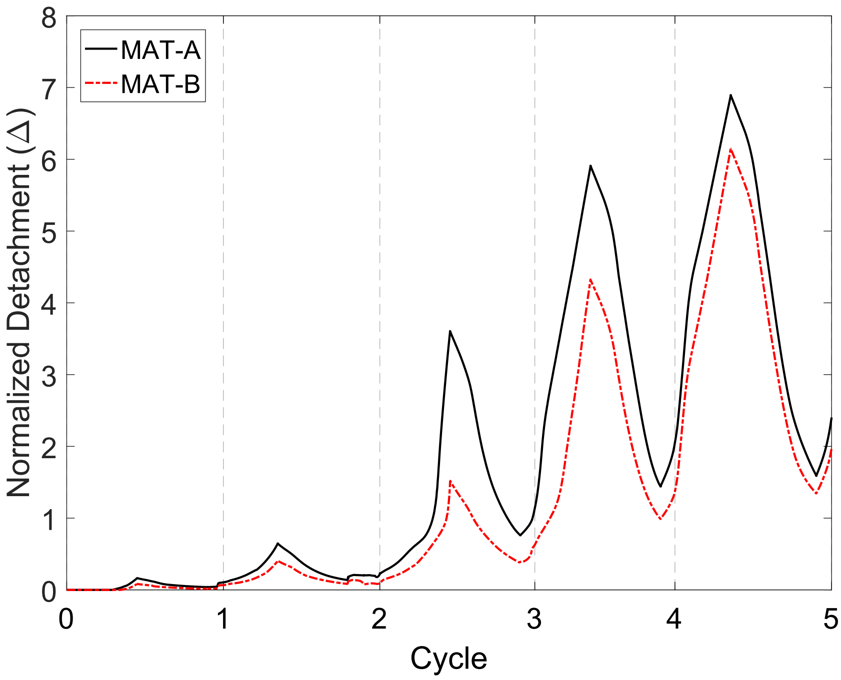

Figure 5.8 Effect of material properties on the mechanical response of lined pipes; normalised detachment of the liner pipe (Δ) at 12 o'clock location, with respect to loading cycles, for loading Case I.

5.4 Influence of various parameters on structural response

In the following sections, the influence of several parameters on the cyclic response of lined pipes is examined. The effect of different loading cases on the cyclic performance of the liner pipe is investigated first. Imperfection sensitivity of the liner pipe is also considered in the form of two initial geometric configurations. Subsequently, the structural stability of the liner pipe under cyclic loading is examined assuming different wall thickness values, including the effect of moderate levels of internal pressure. Finally, the influence of different types of manufacturing processes on the cyclic performance of the liner pipe is analysed.

5.4.1 Cyclic loading under non-negative bending curvature

In addition to Case I loading, presented in section 5.3, alternative loading sequences are also considered in the present section. In Case II, the lined pipe undergoes five consecutive bending cycles, with bending strain that ranges from zero to the maximum bending strain of Case I ($\varepsilon_b = 1.59\%$). The exact loading sequence in terms of the corresponding applied curvatures and bending strains with respect of the number of cycles are presented in Table 5.4. The main feature of this loading case is the absence of negative curvature. Therefore, comparison of the results from loading Cases I and II would indicate the effect of straightener during the reeling process on liner buckling. In this comparison, the thermo-mechanical manufacturing process is followed, as described in section 4.3.3, and the liner pipe is considered free of geometrical imperfections.

Figure 5.9 presents the normalised moment of the lined and liner pipe, with respect to the number of cycles, while the normalised detachment of the liner pipe from the outer pipe is shown in Figure 5.10. The results show that the detachment of the liner pipe under loading Case II is lower compared with the one under Case I. More specifically, the normalised detachment of the liner at points “c”, “d” and “e” in Figures 5.4 and 5.10, is decreased by 50%, 20% and 8%, respectively, in Case II with respect to Case I. The different buckling performance of the liner for the two loading cases is more apparent in Figures 5.5 and 5.11. In both loading cases, the liner pipe buckles locally, forming one main (A) and four minor (B) buckles. In Case I, this occurs at the third cycle (bending configuration “c” in Figure 5.5), whereas in Case II it occurs at the fourth cycle (bending configuration “d” in Figure 5.11).

Table 5.4 Normalised curvature and global bending strain for the five bending cycles in Case II.

Number of Cycle	Normalised Curvature (κ)	Bending Strain (ε_b %)
1	0 → 0.587	0 → 1.59
	0.587 → 0	1.59 → 0
2	0 → 0.587	0 → 1.59
	0.587 → 0	1.59 → 0
3	0 → 0.587	0 → 1.59
	0.587 → 0	1.59 → 0
4	0 → 0.587	0 → 1.59
	0.587 → 0	1.59 → 0
5	0 → 0.587	0 → 1.59
	0.587 → 0	1.59 → 0

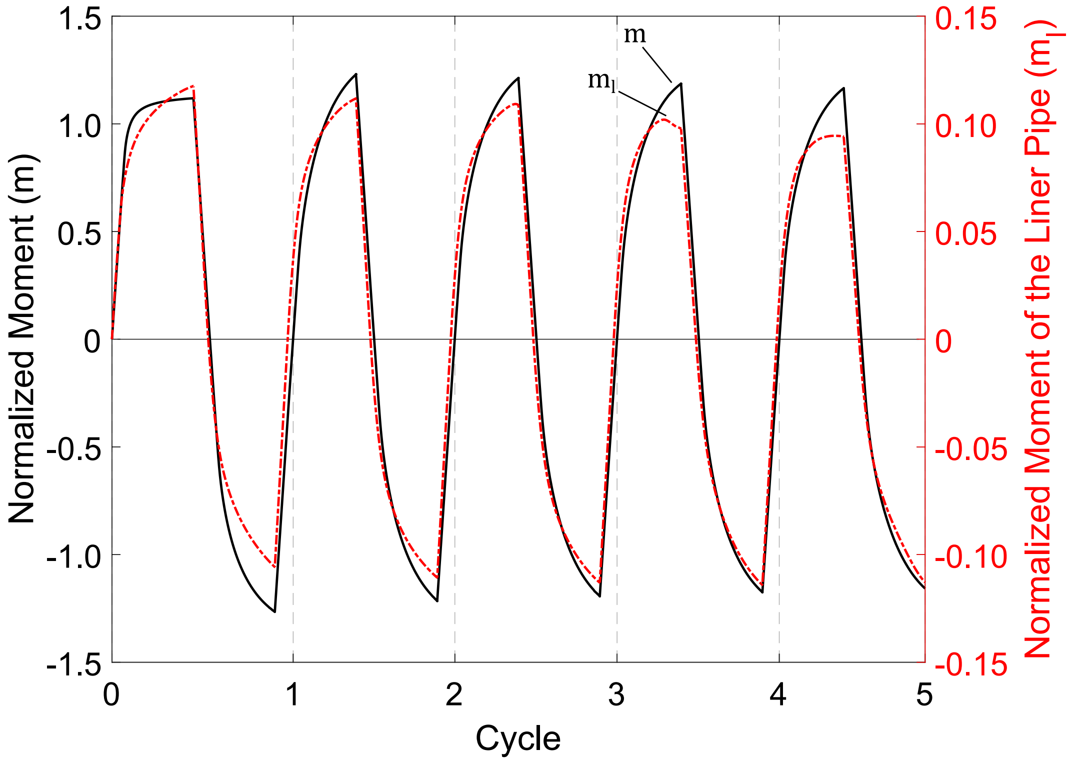

Figure 5.9 Normalised bending moments of the lined (bi-material) pipe (m) and the liner pipe (m_l) for loading Case II, with respect to the number of cycles.

The difference of liner detachment amplitude between the two loading cases is apparent in Figures 5.12 and 5.13, where the horizontal axis represents the number of cycles. In each bending cycle there are four loading stages, namely bending of the pipe, unloading, reverse bending and unloading. The present numerical results on the evolution of liner detachment in Figures 5.12 and 5.13 are qualitatively in accordance with the ones presented by Tkaczyk *et al.* (2011). Furthermore, the liner detachment at 12 o'clock position (Figure 5.12) in loading Case II is significantly reduced highlighting the influence of negative curvature values imposed by the straightener on liner buckling performance. Furthermore, at the end of the fifth cycle, the liner pipe has a much smaller wrinkling amplitude at the 6 o'clock position in Case II than in Case I (Figure 5.13).

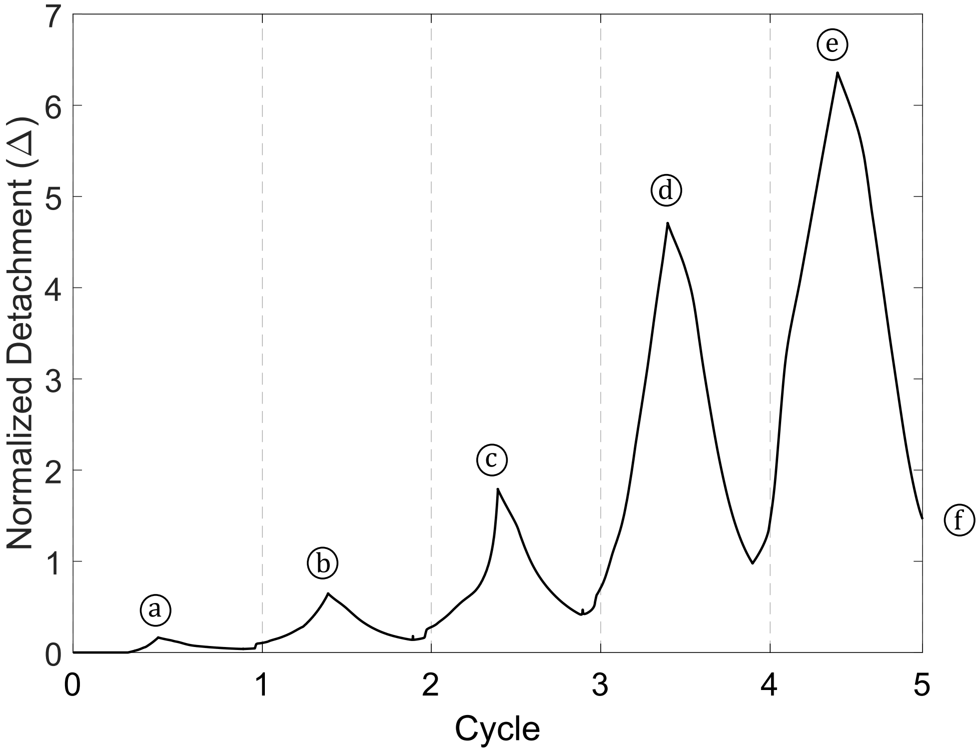

Figure 5.10 Normalised detachment (Δ) at 12 o'clock location, with respect to the number of cycles (Case II).

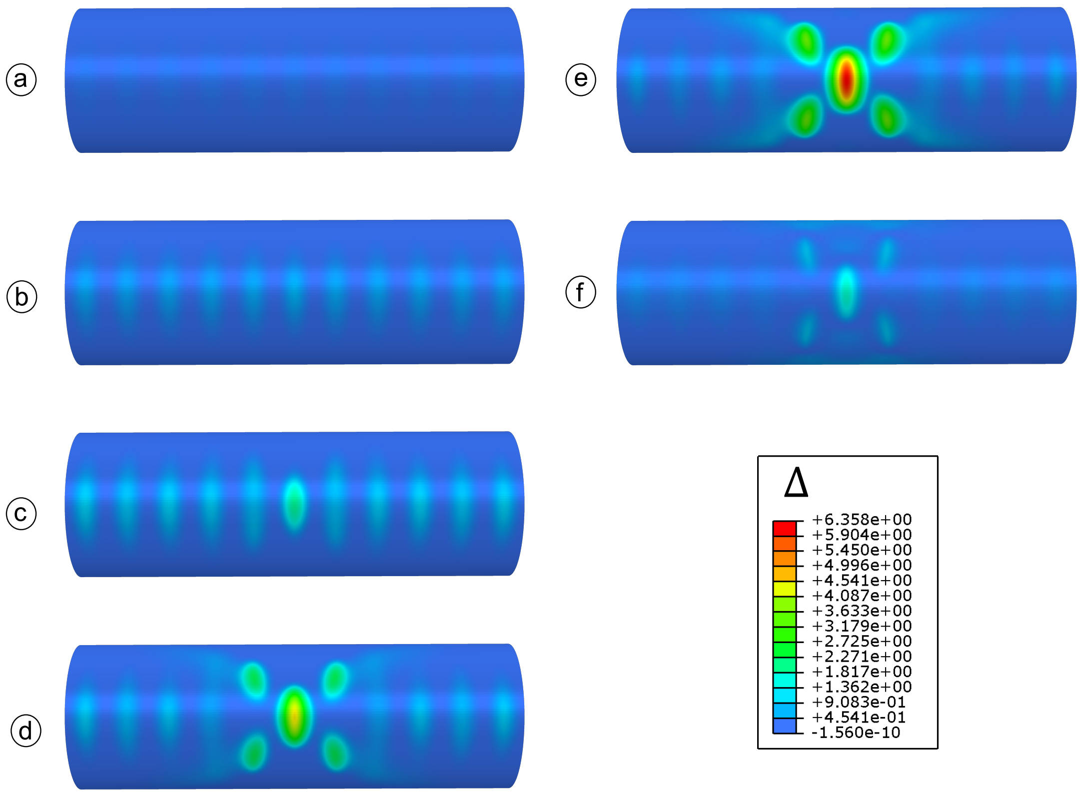

Figure 5.11 Sequence of liner pipe deformation and detachment (Δ), presenting the buckling configuration during cyclic bending at 12 o'clock location, for loading Case II; the configurations of this figure correspond to the stages of Figure 5.10.

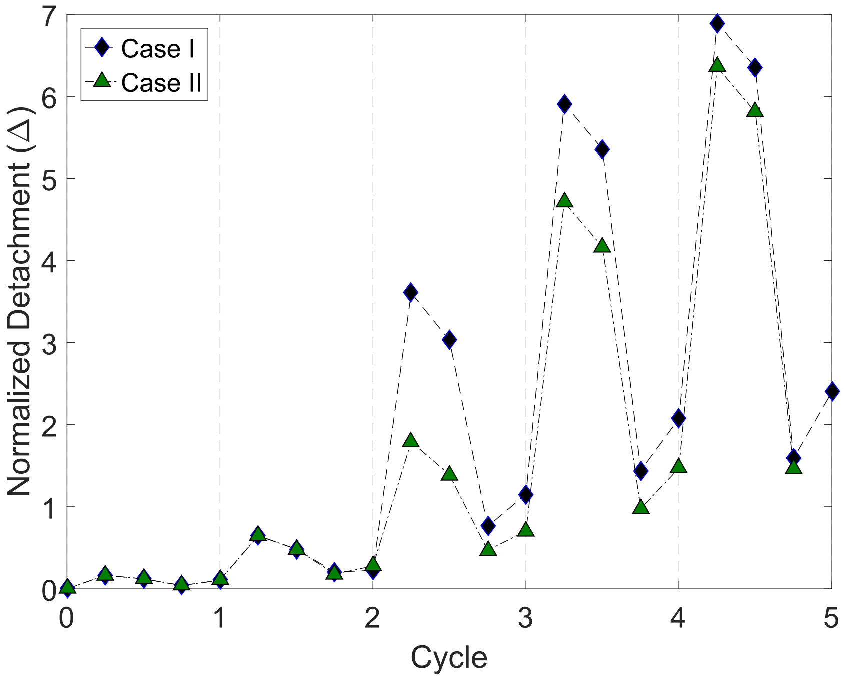

Figure 5.12 Normalised detachment of the liner pipe at 12 o'clock position, with respect to loading cycles, for loading Cases I and II.

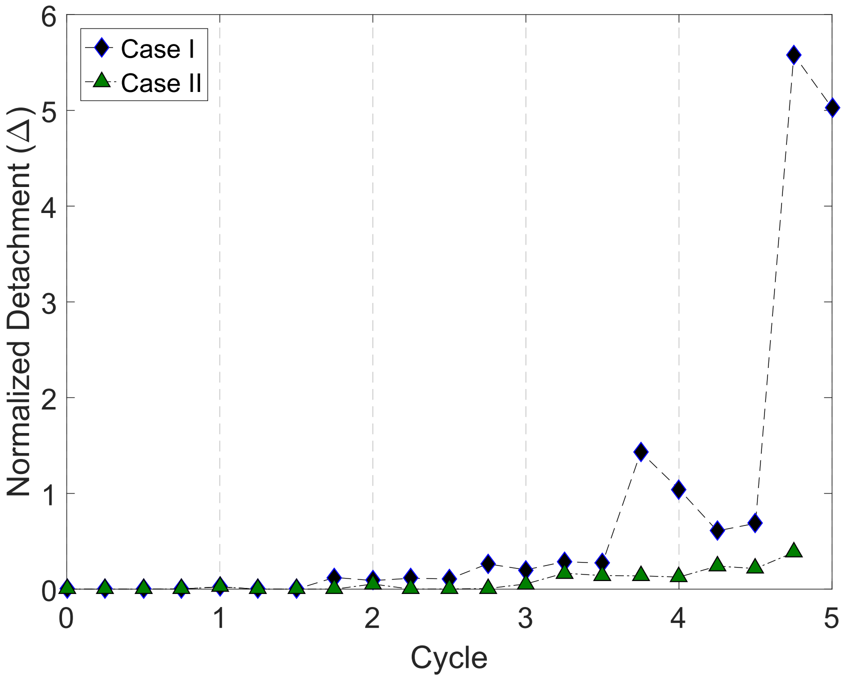

Figure 5.13 Normalised detachment of the liner pipe at 6 o'clock position, with respect to loading cycles, for loading Cases I and II.

5.4.2 Application of different bending loading cases

The effect of different values of maximum bending strain during the five loading cycles is also investigated, considering two additional loading cases. Those involve non-negative bending strain cycles, with the purpose of identifying the effect of different bending strain ranges, compared with the strain range of Case II. Case III consists of five cycles with bending strain that ranges from zero to 1.93% (cycles 1, 4) and 1.59% (cycles 2, 3, 5); the loading path is presented in more detail in Table 5.5. The maximum values of strain represent a reel/aligner radius equal to 8.23 *m* ($\varepsilon_b = 1.93\%$) and 10 *m* ($\varepsilon_b = 1.59\%$) respectively. Furthermore, Case IV consists of five cycles with bending strain ranging from zero to 1.93% (cycles 1, 4) and from zero to 1.25% (cycles 2, 3, 5), and the loading path is presented in detail in Table 5.6. Case IV represents a reel and aligner radii equal to 8.23 *m* ($\varepsilon_b = 1.93\%$) and 12.79 *m* ($\varepsilon_b = 1.25\%$), respectively. In both additional cases, the bending strain values represent real case scenarios (Chapter 2 in the book by Kyriakides and Corona (2007)). In all the above cases, imperfection-free lined pipes are considered.

Table 5.5 Normalised curvature and global bending strain for the five bending cycles in Case III.

Number of Cycle	Normalised Curvature (κ)	Bending Strain (ε_b %)
1	0 → 0.711	0 → 1.93
	0.711 → 0	1.93 → 0
2	0 → 0.587	0 → 1.59
	0.587 → 0	1.59 → 0
3	0 → 0.587	0 → 1.59
	0.587 → 0	1.59 → 0
4	0 → 0.711	0 → 1.93
	0.711 → 0	1.93 → 0
5	0 → 0.587	0 → 1.59
	0.587 → 0	1.59 → 0

The normalised bending moment of the lined pipe for Cases III and IV is presented in Figures 5.14 and 5.15, with respect to loading cycles. In these figures, the normalised bending moment carried by the liner pipe is also depicted. The results show that, in both cases, the liner pipe undergoes a uniform wrinkling pattern at the end of the second cycle. In Case III the liner buckles locally at the beginning of the third cycle, associated with the slight drop of moment of the liner pipe shown in Figure 5.14. In Case IV, uniform wrinkling does not grow further during the second and third cycle, due to the low value of the maximum normalised curvature ($\kappa = 0.462$), while during the fourth cycle the liner pipe buckles locally, at a value of normalised curvature equal to 0.711, corresponding to reel radius equal to 8.23 m.

Table 5.6 Normalised curvature and global bending strain for the reeling and repair cycles in Case IV.

Number of Cycle	Normalised Curvature (κ)	Bending Strain (ε_b %)
1	0 → 0.711	0 → 1.93
	0.711 → 0	1.93 → 0
2	0 → 0.462	0 → 1.25
	0.462 → 0	1.25 → 0
3	0 → 0.462	0 → 1.25
	0.462 → 0	1.25 → 0
4	0 → 0.711	0 → 1.93
	0.711 → 0	1.93 → 0
5	0 → 0.462	0 → 1.25
	0.462 → 0	1.25 → 0

The normalised detachment of liner pipe for the different non-negative bending loading cases (II, III, IV) is also presented in Figure 5.16. In all cases, during the first two cycles, the liner detaches from the outer pipe forming short-wave uniform wrinkles, which may be considered an acceptable situation during reeling of a lined pipe. This is more apparent in Case III, which involves a more severe loading history than Cases II and IV, resulting in 87% larger detachment than the other two cases. At the fourth cycle, in all cases, the liner pipe exhibits significant detachment from the outer pipe leading to local buckling.

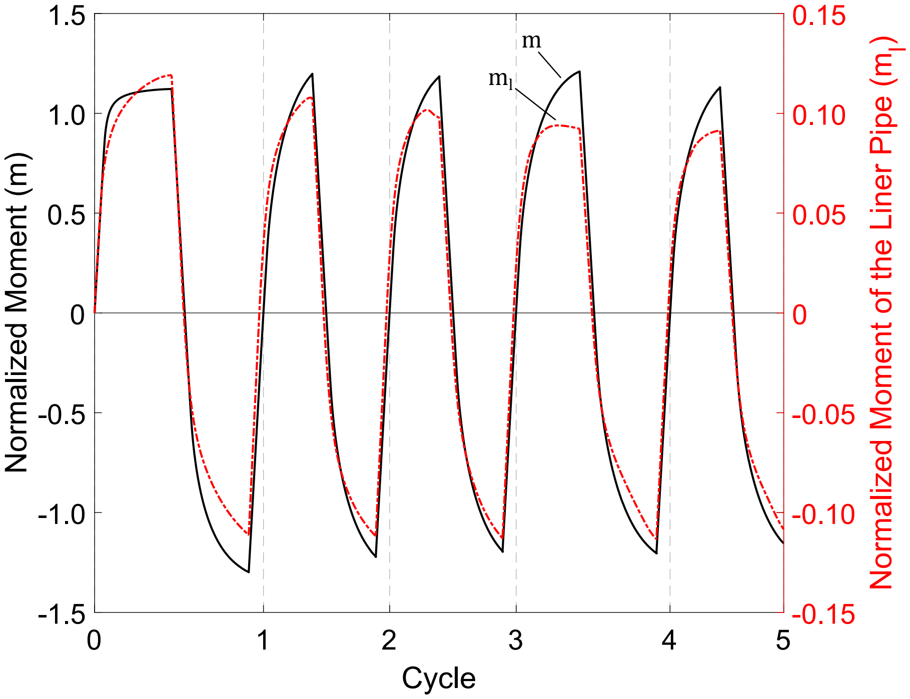

Figure 5.14 Normalised bending moments of the lined (bi-material) pipe (*m*) and the liner pipe (m_l) for loading Case III, with respect to the number of cycles.

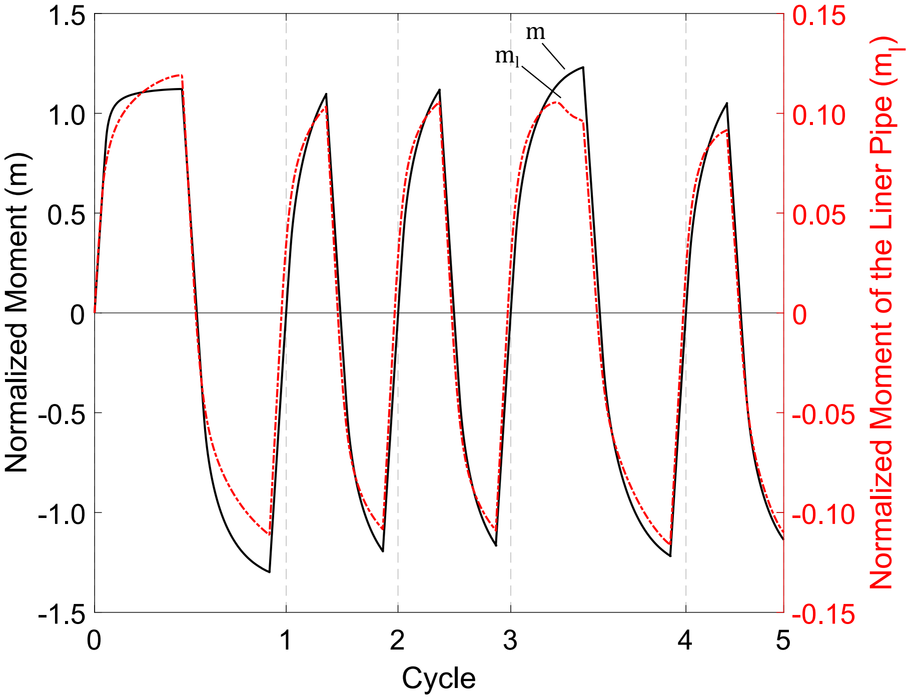

Figure 5.15 Normalised bending moments of the lined (bi-material) pipe (*m*) and the liner pipe (m_l) for loading Case IV, with respect to the number of cycles.

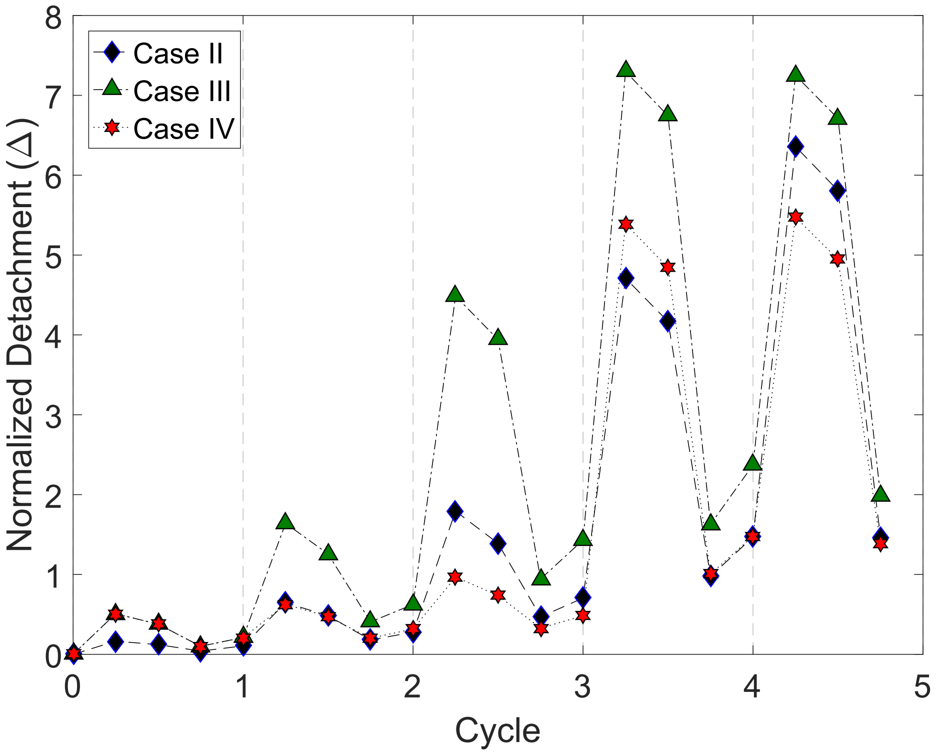

Figure 5.16 Normalised detachment of the liner pipe at 12 o'clock position, with respect to loading cycles, for loading Cases II, III and IV.

5.4.3 Buckling of imperfect liner pipe

In the present section, sensitivity analysis of the cyclic bending performance of a lined pipe in the presence of initial geometric imperfections is conducted. The initial imperfection refers to the liner pipe only, while the outer pipe is considered geometrically perfect. Two shapes of geometric imperfections are examined. The first configuration is a uniform wrinkling pattern of the liner pipe, called "IMP-1" and shown in Figure 5.17a. The second type of imperfection is the buckling configuration of the liner, observed in the previous analyses, with a main buckle (A) and four minor buckles (B), called "IMP-2" and shown in Figures 5.17b. In both cases, the imperfect shapes refer to wrinkles with amplitude at 12 and 6 o'clock locations of the liner, and maximum value (Δ_0) equal to 10% of the wall thickness of the liner pipe (t_l) at $\chi = 0$ location. For both types of imperfection, to conduct a fair comparison the same manufacturing process is followed, as described in section 4.3.3, and the lined pipe is subjected to loading Case II, as presented in section 5.4.1 and Table 5.4.

The normalised bending moment of the liner pipe, for the pipe with perfect liner and the two different types of imperfection, is presented in Figure 5.18. For the perfect and the IMP-1 cases, the liner pipe develops a uniform wrinkling pattern, at the end

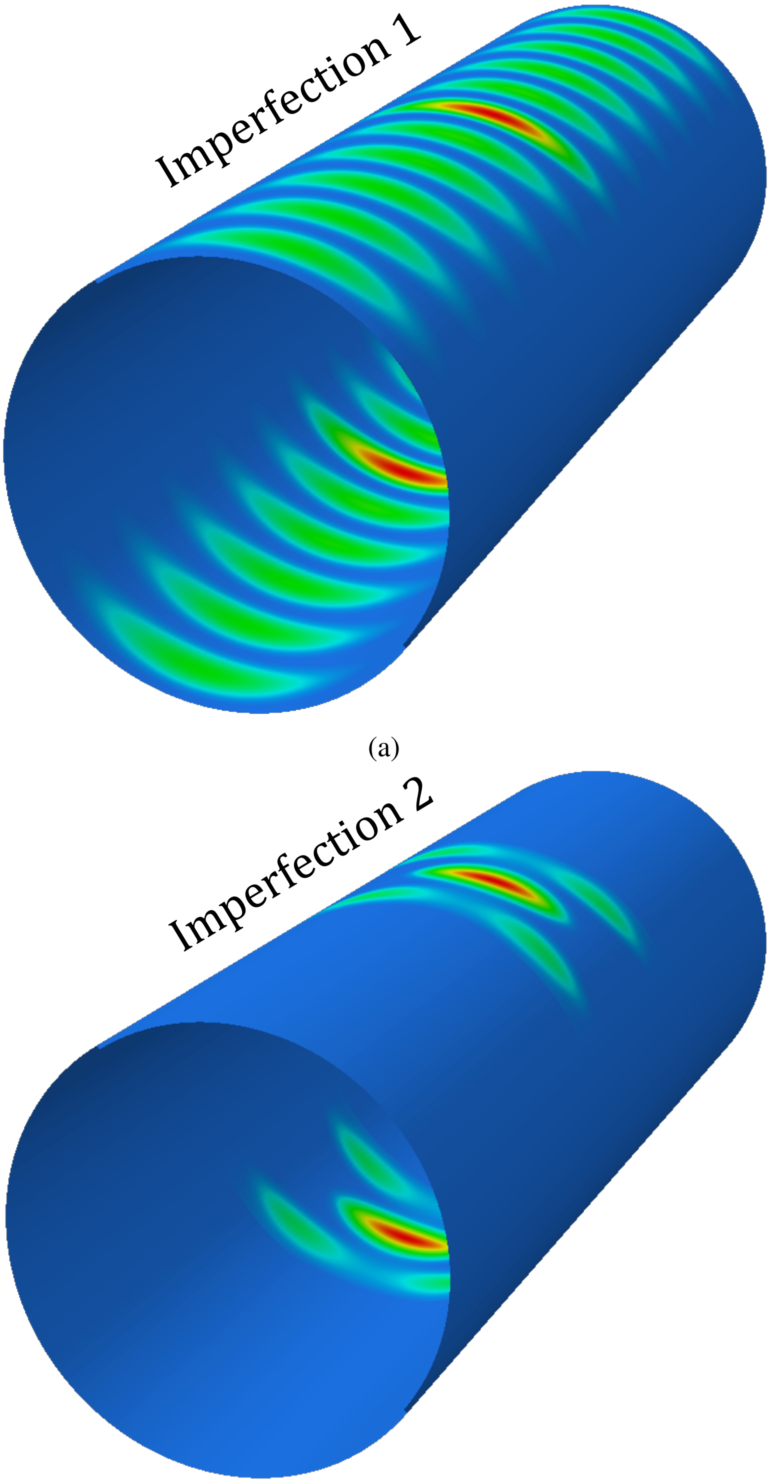

(a)

(b)

Figure 5.17 Initial geometric configurations of both types of imperfection of the liner pipe.

of the second cycle. In the case of imperfection 1, the liner pipe buckles locally at the beginning of the third cycle. In Figure 5.18, the moment of liner exhibits a slight drop, indicating liner local buckling, which is in accordance with the results in Figure 5.19, where a rapid increase of detachment is observed. For the case of a perfect liner pipe, buckling occurs at a latter stage (fourth cycle), as shown in Figures 5.9 and 5.18 where the moment of the liner drops gradually and the corresponding detachment increases (Figures 5.10, 5.19). On the other hand, in the IMP-2 case the liner pipe starts to develop a local buckling pattern at 12 o'clock location at the end of the second cycle. Figure 5.18 shows that the bending moment of the liner for the IMP-2 is slightly lower. This result is consistent with the curves in Figure 5.19, where at the third cycle, the detachment of the liner pipe increases more rapidly and corresponds to 44% and 93% larger value, compared with the IMP-1 and perfect cases, respectively. This result shows that IMP-2 corresponds to the worst case scenario in terms of the imperfection sensitivity of the liner pipe, and is in accordance with observations reported in previous publications (Vasilikis, 2012; Vasilikis and Karamanos, 2012) and in the previous Chapters 3 and 4. It should be noted that the worst case scenario is determined in terms of liner detachment, which is assumed as the performance criterion of interest in lined pipes. Early stage liner detachment may lead to local buckling in a diamond-type mode, which is as the main limit state. This might lead to cracking of the liner pipe under operational thermo-mechanical loads, resulting in corrosion of the outer pipe with significant environmental impact.

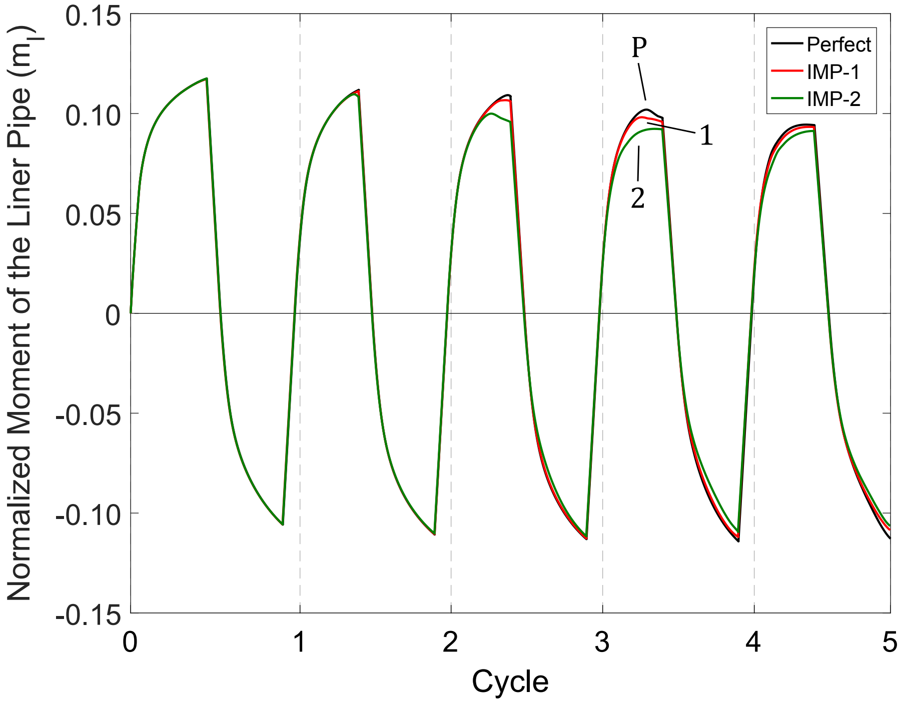

Figure 5.18 Normalised bending moments of the liner pipe (m_l) for the perfect and imperfect liners, with respect to loading cycles, for loading Case II.

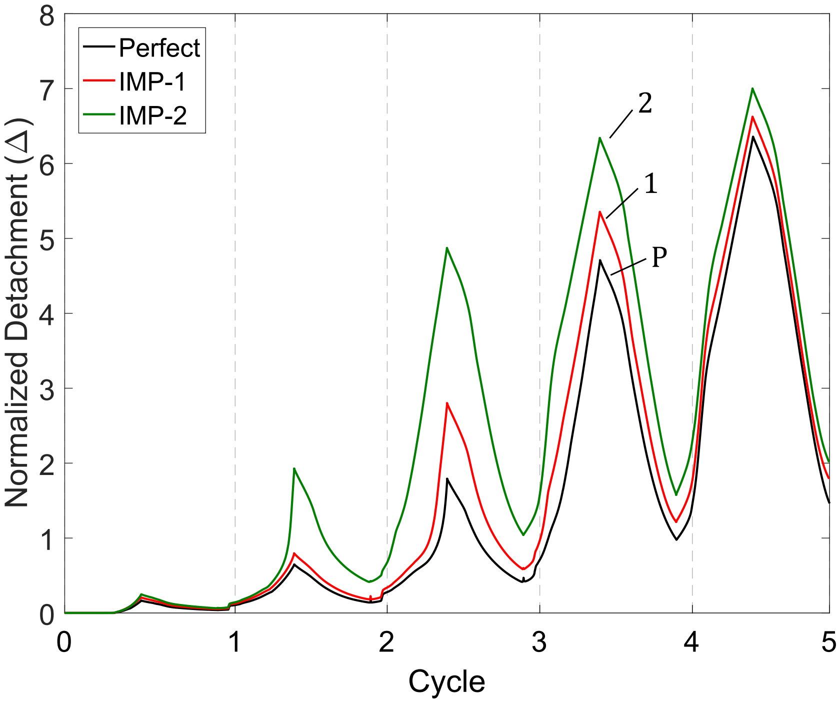

Figure 5.19 Normalised detachment of the liner pipe (Δ) for the perfect and imperfect liners, with respect to loading cycles, for loading Case II.

5.4.4 Liner pipe wall thickness

Numerical analyses with different values of wall thickness of the liner pipe have been conducted, in order to investigate its effect on the cyclic response of the liner pipe. It is expected that increasing liner wall thickness, the detachment of the liner pipe would be retarded, delaying or even preventing buckling of the liner pipe during the five loading cases. In addition to the base case (also called $t_{l,A}$ in the current section) as described in section 5.2.1, three different pipes are examined, considering liners with increased wall thickness by 25% ($t_{l,B} = 3.5\ mm$), 50% ($t_{l,C} = 4.2\ mm$) and 100% ($t_{l,D} = 5.6\ mm$). In the present analyses, liners are considered geometrically perfect, while the internal pressure during the manufacturing process is properly adjusted, in order to result in equal equivalent mechanical bonding conditions at the end of the process, i.e. in a hoop compression equal to the same percentage of the yield stress of the liner ($\sigma_\theta/\sigma_{y,l}$). The loading path applied in the present study is the one Case II, presented in detail in Table 5.4.

Figure 5.20 shows the bending moment, carried by the liner pipe, with respect to the applied curvature. For consistency, moment and curvature values are normalised by $M_o = \sigma_{y,o} D_{m,o}^2 t_o$ and $k_o = t_o/D_{m,o}^2$, respectively. As expected, there is an increase of liner moment as the liner wall thickness increases. Furthermore, liner detachment evolution normalised by the wall thickness of the base case ($t_{l,A}$), with respect to five bending cycles, is presented in Figure 5.21 for each case. As already mentioned in section 5.4.1, the liner pipe with wall thickness equal to $t_{l,A}$ results in uniform wrinkling during the second bending cycle, and buckles locally during the fourth cycle, an event that corresponds to moment drop. However, assuming wall thickness values equal to $t_{l,B}$ and $t_{l,C}$, the liner pipe presents uniform wrinkling of significantly smaller amplitude at the end of the fifth cycle, as shown in Figure 5.22, while the corresponding moment is slightly reduced per cycle, due to wrinkling and small increase of detachment. The decrease of liner detachment in each case, is compared with the base case (thickness equal to $t_{l,A}$), and the comparison depicted in Figures 5.21 and 5.22, shows that for the case of $t_{l,D}$ the liner pipe has a very good performance, with slight detachment from the outer pipe. At the end of the second cycle, the normalised detachment of the liner pipe is 34%, 44% and 50% lower for $t_{l,B}$, $t_{l,C}$ and $t_{l,D}$, respectively, compared with the base case $t_{l,A}$. Before the end of the fifth cycle, the corresponding differences in the detachment amplitude are 140%, 163% and 184% due to local buckling of the liner pipe in the base case ($t_{l,A}$). As a result, considering slightly thicker liner than the base case, the lined pipe is capable of undergoing five loading cycles with only minor wrinkling.

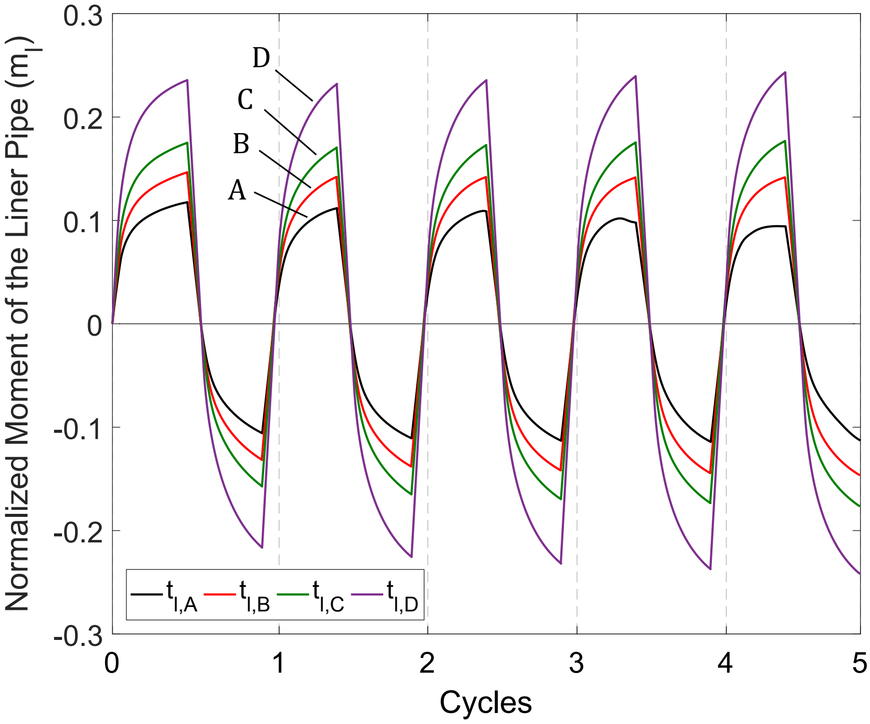

Figure 5.20 Normalised bending moments of the liner pipe (m_l) for different wall thickness values of liners, with respect to loading cycles, for loading Case II.

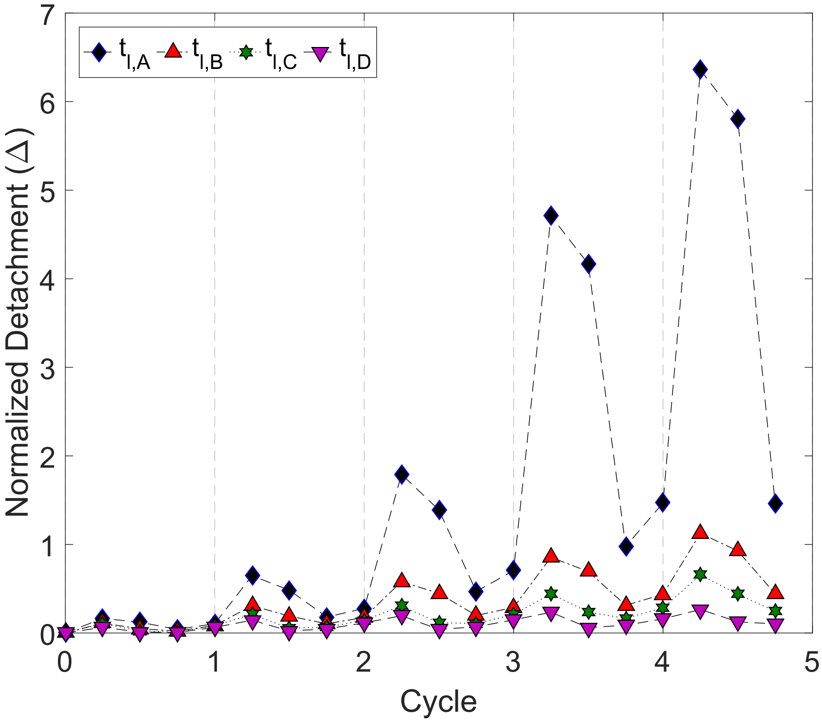

Figure 5.21 Normalised detachment of the liner pipe (Δ) for different wall thickness values of liners, with respect to loading cycles, for loading Case II.

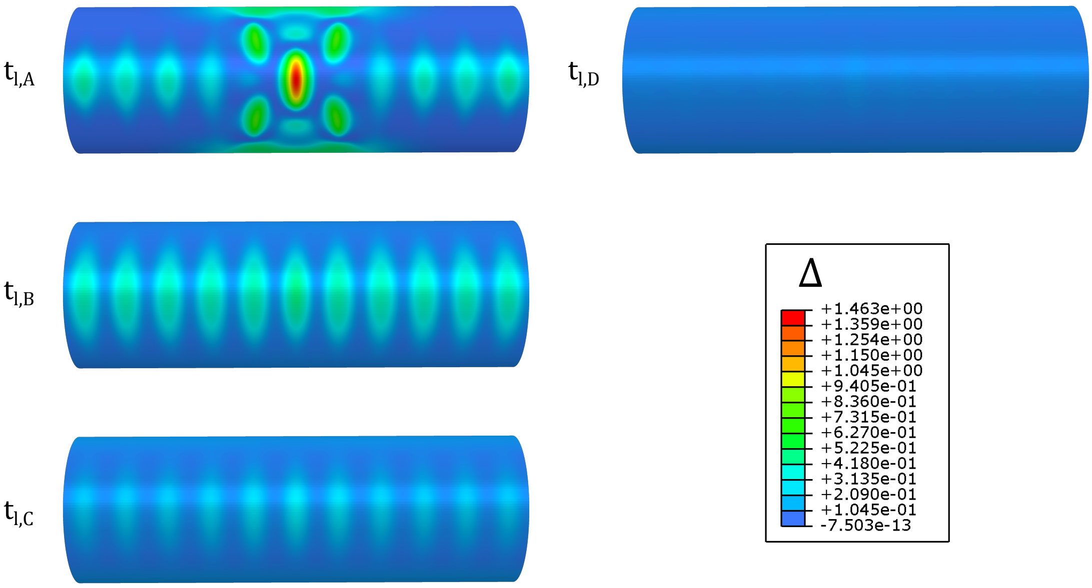

Figure 5.22 Sequence of liner pipe deformation and detachment (Δ), presenting the buckling configuration at the end of fifth cycle at 12 o'clock location, for different liner wall thickness values, for loading Case II.

5.4.5 Cyclic response under internal pressure

The cyclic bending response of a lined pipe under moderate level of internal pressure is investigated. Internal pressure is aimed at preventing detachment and, eventually, buckling of the liner pipe, without increasing the liner wall thickness. The beneficial effect of moderate level of internal pressure on monotonic bending response is examined extensively in the previous chapters (sections 3.4.2 and 4.5.2). Moreover, the cyclic response of lined pipes under high level of internal pressure has also been examined in previous publications (Sriskandarajah *et al.*, 2013*b*; Toguyeni and Banse, 2012), showing its beneficial role.

In the present work, the effect of low level pressure on cyclic response is investigated. An imperfection-free lined pipe is considered for the purposes of this investigation, as described in section 5.2.2. In the analysis procedure, after the end of the thermo-hydraulic manufacturing process, internal pressure 0.5 MPa is applied, equal to 10% of the plastic pressure of the liner pipe ($P_{y,l} = 2\sigma_{y,l}t_l/D_{m,l}$, where $D_{m,l}$ is the mean diameter of the liner pipe). A tensile force (F_p) is also applied on the reference node in the $z = L$ plane (as shown in Figure 4.3), equal to the product of the internal pressure times the internal cross-section of the liner ($F_p = P_{in}\pi(D_l - 2t_l)^2/4$) in order to simulate the force at the two capped ends due to the internal pressure. This force, often referred to as "capped-end force", follows the orientation of reference node (follower force). The internal pressure and the magnitude of capped-end force remain constant during cyclic bending. In this analysis, Case II loading path is applied.

In Figure 5.23, the normalised bending moment of the liner pipe (m_l) under pressurized and non-pressurized conditions is plotted, with respect to the loading cycles. In the case of non-pressurized lined pipe, the liner pipe detaches from the outer pipe, buckles locally, and exhibits a drop of moment at the fourth cycle, as shown in Figure 5.23 and described in more detail in section 5.4.1. On the other hand, in the presence of a moderate level of internal pressure, the liner pipe does not detach from the outer pipe during the five bending cycles and local buckling is prevented.

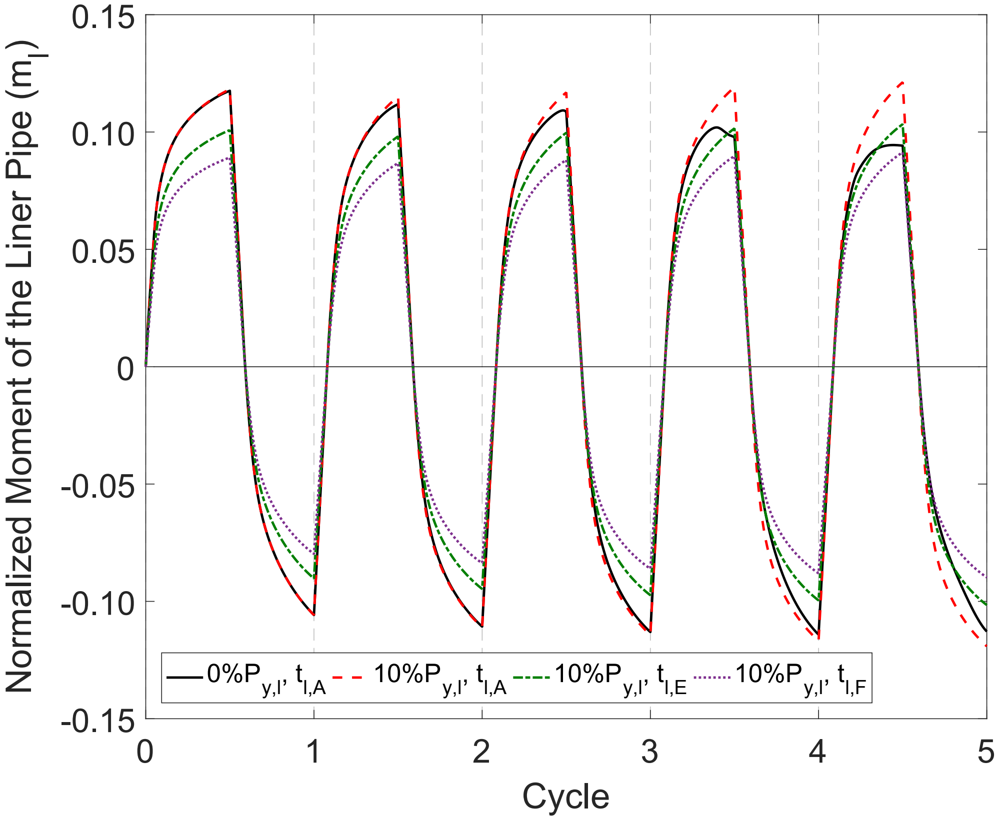

Figure 5.23 Normalised bending moments of the liner pipe (m_l) for pressurized, non-pressurized and different wall thickness values of liner pipes, with respect to loading cycles (loading Case II and pressure equal to 0.5 *MPa* for all the pressurized pipes).

To elucidate this issue, and examine the combined effect of pressure and liner thickness on cyclic bending response, keeping the level of pressure constant (0.5 *MPa*), the mechanical behaviour of thinner liners is investigated. This analysis can be regarded as an attempt to reduce the cost of a lined pipe. Two additional values of thickness are examined, reducing the base case $t_{l,A}$ by 15% ($t_{l,E} = 2.38$ *mm*) and 25% ($t_{l,F} = 2.1$

mm). The thermo-hydraulic manufacturing process is taken into account for each case, adjusting the fabrication pressure in order to obtain an equivalent mechanical bonding in terms of the $\sigma_\theta/\sigma_{y,l}$ ratio at the end of the process. Following the simulation of the fabrication process, internal pressure and the corresponding capped-end force are applied to the desired level (0.5 *MPa*), which are kept constant throughout the subsequent application of five bending cycles. Figure 5.23 presents the normalised moment of each liner pipe. In both cases, no liner pipe detachment has been detected, verifying the beneficial effect of this moderate level of internal pressure on detachment and local buckling. Therefore, applying an internal pressure at a level of 10% of $P_{y,l}$ constitutes a promising solution for preventing liner buckling under cyclic loading. These results could motivate the industry at establishing new practices during reeling of lined pipes. This argument is investigated further in the next chapter in section 6.4.6 using a more rigorous three-dimensional reeling model.

Finally, additional analyses are performed, with internal pressure ranging from 5% (0.25 *MPa*) to 8% (0.41 *MPa*) of the liner pipe plastic pressure ($P_{y,l}$). The liner pipe wall thickness is equal to $t_{l,A}$, and the Case II loading path is applied. Initially, the fully heated thermo-hydraulic manufacturing process is performed in the analysis, followed by the application of internal pressure. Figure 5.24 presents the liner detachment during spooling of the fifth cycle at 12 o'clock location, for different internal pressure levels. The results show that for internal pressure equal to 8% of Py,l, the liner pipe does not detach from the outer pipe, similar to the case of 10% pressure level. For pressure level equal to 5%, the liner pipe exhibits very small amplitude wrinkling. The corresponding maximum value of Δ is equal to 0.448, and occurs during spooling of the fifth cycle. Furthermore, at the end of loading a negligible liner detachment is detected with a value of Δ equal to 0.091. The numerical results indicate that in the case of the minimum internal pressure level examined in the present study (5% of $P_{y,l}$), local buckling of the liner is prevented, while the 8% pressure level could be considered as the minimum pressure level which provides zero liner detachment during Case II loading.

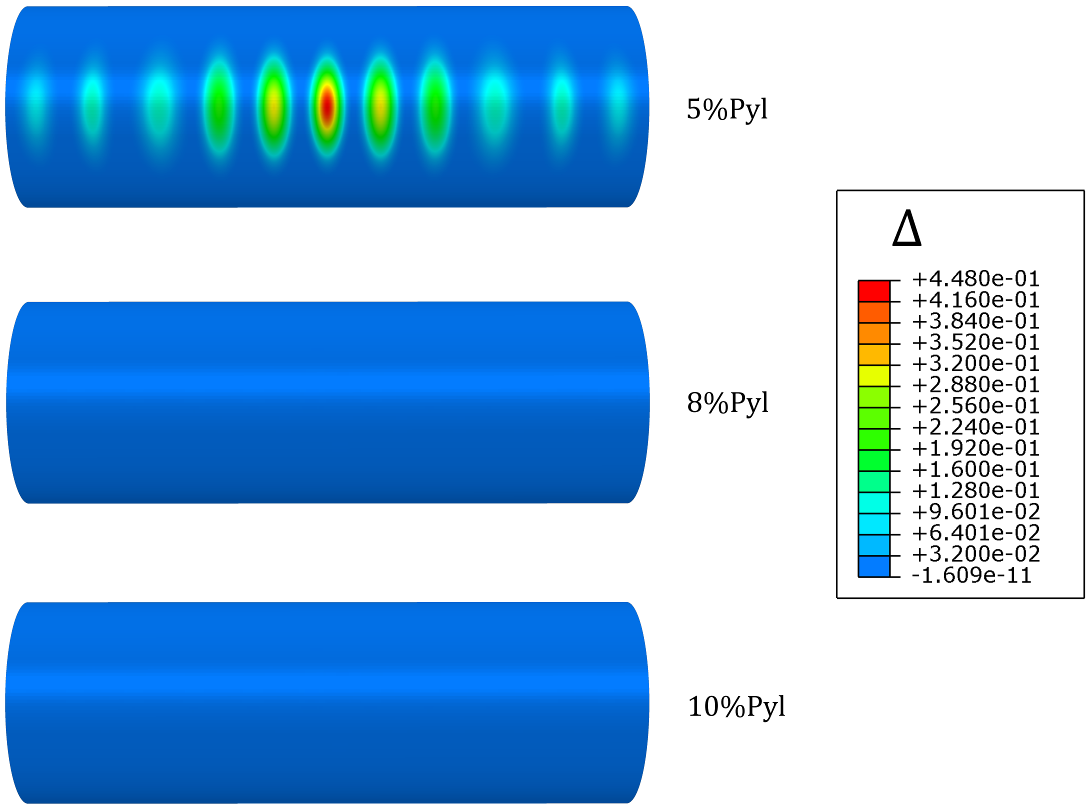

Figure 5.24 Sequence of liner pipe deformation and detachment (Δ); buckling configuration during spooling of fifth cycle at 12 o'clock location, for different internal pressure values (loading Case II).

5.4.6 Alternative manufacturing processes

The lined pipes, examined in the previous sections, are manufactured through the thermo-hydraulic process. In that process, the liner reaches the temperature of the outer pipe during the pressurization step. This case is referred to as fully heated tight-fit pipe (TFP FH), and is described in detail in section 4.3.3. In Chapter 4, it was demonstrated that the type of manufacturing process, as well as the value of several parameters within a certain process may affect bending response by a substantial amount. In the present section, the cyclic loading performance of lined pipes is examined, considering an alternative thermo-mechanical process and a purely mechanical process. The lined pipes are assumed geometrically perfect, having the same geometrical and material properties described in section 5.2.1 and summarized in Table 5.1, and are subjected to the Case II loading path.

The thermo-hydraulic fabrication process is discussed in more detail in section 4.3.4, while Figure 4.8 presents the response of both pipes during the fabrication process. During the pressurization step (①→②) the liner is partially heated (denoted as TFP PH) up to $T_l = 388\ K$, which is 57% of the outer pipe's temperature. It is noted that the term "partially" implies uniform heating of the liner pipe up to a lower temperature level than T_o. In this case, the liner pipe exhibits a smaller amount of thermal hoop expansion, resulting in a smaller drop of the hoop stress, as shown in Figure 4.8. Reverse plastic loading (RPL) occurs during the depressurization step, as denoted by the horizontal arrow before the end of stage ③. At the end of the fabrication process (③), the liner pipe is at higher hoop compression stress, compared to the fully-heated process (TFP FH).

In addition, a purely hydraulic manufacturing process is also simulated, consisting of applying internal pressure during pressurization of the lined pipe that exceeds the plastic pressure of the outer pipe, equal to 59.9 MPa (117% of $P_{y,o}$). The pipe fabricated through this manufacturing process will be referred to as "plastically expanded". 4.6 shows that the liner expansion is initially elastic, and subsequently inelastic (⓪→①), until the liner establishes contact with the outer pipe. Then both pipes expand together (①→②), and at the end of stage ② the outer pipe is also deformed plastically. This is followed by depressurization of both pipes (②→③). After depressurization, due to the larger elastic deformation in the outer pipe, compared with the one in the liner pipe, the two pipes remain in mechanical bonding, and the contact pressure depends on the size of the initial gap, as reported in sections 4.3.2 and 4.3.5.

In Figures 5.25, 5.26, the normalised bending moment and the corresponding liner detachment are plotted for the different manufacturing processes, with respect to the bending cycles. The case of fully heated TF Pipe has been examined in detail in section 5.4.1. In this pipe, the liner wrinkles at the end of the second cycle, which is associated with the slight drop in the liner bending moment shown in Figure 5.25, while local buckling occurs in the fourth cycle. In the case of partially heated TF Pipe, the liner detaches in the second cycle and develops wrinkles of lower amplitude size, compared with those of the fully heated TF Pipe, as shown in Figure 5.26. In this case, the liner exhibits a localized buckling pattern at the fifth cycle, while the bending moment of the liner pipe presents a slight drop, which is also shown in Figure 5.25. This result is in accordance with the superior structural response of partially heated TF Pipe during monotonic bending, as presented in section 4.4.1. Increasing the hoop compression of the liner pipe at the end of fabrication process leads to an increase of the axial compression, due to von Mises (1928) yield criterion (Figure 2.2b).

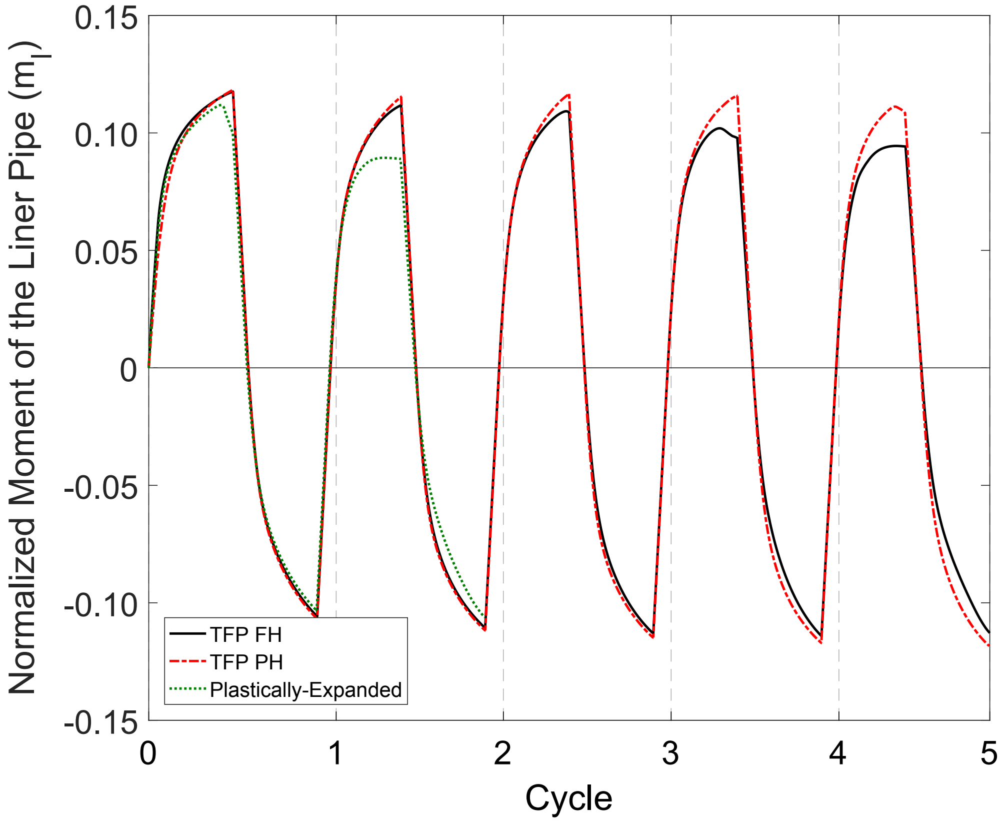

Figure 5.25 Normalised bending moments of the liner pipe (m_l) for different manufacturing processes, with respect to loading cycles, for loading Case II.

On the other hand, the cyclic response of plastically expanded lined pipes is quite different. In this case, local buckles develop in the liner pipe very soon, during the first cycle, in a pattern with a main buckle with the adjacent four minor buckles. This means that -practically- liner buckling initiates under monotonic loading conditions, before even reverse loading is applied, and this is presented in Figures 5.25, 5.26 by the moment drop and the abrupt increase of the detachment. This early-stage buckling of the liner pipe is attributed to the severe plastic deformation of the liner pipe during the manufacturing process. Beyond the second cycle, excessive deformation occurs and, therefore, the plastically expanded pipe is examined only on the first two loading cycles, which results in 160% and 193% larger detachment than the fully heated and partially heated TFP, respectively.

The previous observations indicate superior performance of partially heated TF Pipes, compared with the one of fully heated TF Pipes and poor performance of plastically expanded pipes against structural instability. Those conclusions are in accordance with those reported in the previous Chapter 4 (section 4.4) that refers to monotonic bending of the lined pipes under consideration.

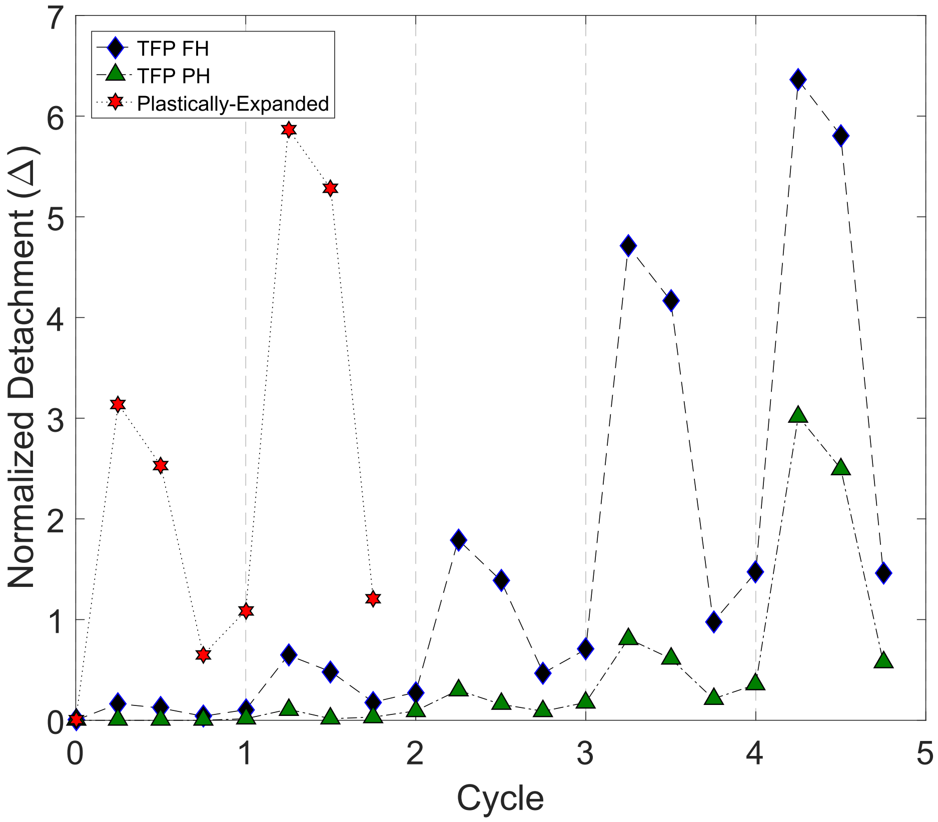

Figure 5.26 Normalised detachment of the liner pipe (Δ) at 12 o'clock position, for different manufacturing processes, with respect to loading cycles, for loading Case II.

5.5 Summary of results

In the present chapter, the structural behaviour of mechanically bonded lined pipes is examined, subjected to five bending cycles, representing offshore reeling installation conditions and the subsequent repair cycles in the case of a failure/repair scenario. A three-dimensional model is created, simulating in the first stage of the analysis, the manufacturing process with a thermo-mechanical expansion (TFP FH) of the lined pipe as base case, and in the second stage, the cyclic bending response. The numerical results refer to 12.75 *in* diameter pipe, with a thickness equal to 15.9 *mm*. The results underline the significant effect of liner material properties, especially its ratcheting behaviour, on lined pipe cyclic response. This indicates the importance of performing both stress-controlled and strain-controlled material tests to determine the appropriate values of material parameters. The influence of negative bending curvature is examined, representing the load imposed by the straightener during reeling installation. Compared to bending cycles with non-negative curvature, it is found that local buckling of the liner occurs at an early stage, immediately after the end of the negative curvature application, and leads to the development of significantly higher detachment at both 12 and 6 o'clock locations. Furthermore, the influence of two different shapes of initial geometric imperfection of the liner pipe is analysed, considering imperfection amplitude equal to 10% of liner wall thickness. It is shown that pipes with uniform wrinkling imperfection, buckle during the fourth cycle, similar to the imperfection-free pipe. On the other hand, in liners with imperfection in the form of the local buckling shape, earlier buckling occurs, at the beginning of the third cycle, indicating that this is the worst imperfection case. Several pipes with increased wall thickness of the liner pipe, up to twice the thickness of the base case ($t_{l,A}$), were also considered. In all those cases, no local buckling is detected during the five loading cycles, despite the observation of a slight detachment. The cyclic response of internally pressurized lined pipes, under relatively low level of pressure (5%, 8% and 10% of $P_{y,l}$), verified the beneficial effect of pressure. The results show that in the case of 5% of $P_{y,l}$, a negligible liner detachment is detected, while local buckling of the liner pipe is prevented. Furthermore, the 8% pressure level could be considered as the minimum pressure level which provides zero detachment during the five bending cycles, even for liners with quite small thickness. Finally, the manufacturing process is also shown to influence significantly the structural instability of the liner under cyclic loading. Partial heating of the liner (TFP PH) results in higher hoop compression of liner by the outer pipe at the end of the process, due to smaller amount of thermal expansion of the liner pipe, and for this case local buckling occurs at a later stage than the fully heated case. On the other hand, a purely hydraulic process, in which the fabrication pressure induces plastic deformation in the outer pipe, results in premature local buckling of the liner due to the severe plastic deformation of the liner material during manufacturing.

Chapter 6

Reeling of lined pipes and its influence on liner buckling

6.1 Chapter outline

The work in the present chapter investigates the structural response of lined pipes during spooling-unspooling and straightening, representing the loading conditions during the reeling installation process. Those loading cycles impose a maximum curvature value lower than the "critical" curvature that causes liner local buckling under monotonic loading (sections 3.4.2 and 4.4). The present study uses a single numerical model that starts with the simulation of the manufacturing process of a mechanically bonded lined pipe and proceeds to its reeling performance in the second stage of the analysis, taking into account the entire plastic loading history of the liner pipe during the fabrication process, including possible reverse plastic loading. An advanced finite element model is developed to model the mechanical response of the outer and the liner pipe, capable of simulating possible pipe wall wrinkling and local buckling, as well as its post-buckling behaviour. The analyses are aimed at simulating the mechanical performance of a mechanically bonded lined pipe subjected to five spooling-unspooling loading cycles, i.e. the two cycles during reeling (Figure 1.3a), and three additional cycles, associated with the case of a failure/repair scenario. The effect of straightener at the end of reeling is also simulated, using a three-point bending scheme. The results pinpoint the severe effect of cyclic loading on localized buckling of the liner pipe. Several analyses are conducted, considering different reel diameter values, as an attempt to quantify its influence on liner buckling response. The effect of straightener during reeling, the structural response of the liner under different back tension levels, the influence of geometric imperfections of the liner pipe, the effect of different values of liner wall thickness and the presence of low levels of internal pressure during reeling are also investigated in detail in the present study.

6.2 Material properties and numerical modelling

6.2.1 Lined pipe geometry and material properties

In the following analyses, the same material and geometric properties considered in the previous chapter are used, as shown in Table 5.1, and the structural response of a lined pipe during reeling is investigated. The lined pipe consists of a thick-walled outer pipe, made of X70 carbon steel material, and a thin-walled inner pipe, made of stainless steel 316L. The user-subroutine (UMAT) is used for the outer pipe considering the same material parameters, described in more detail in section 4.2.1, while the stress-strain of the outer pipe is shown in Figure 4.1. Furthermore, the non-linear kinematic/isotropic hardening plasticity (built-in) ABAQUS model is used for the liner pipe, as described in section 5.2.1, considering the MAT-A material parameters, which account accurately for the plastic strain accumulation under non-symmetric stress controlled loading conditions (Kang and Gao, 2005), as presented in Figure 5.2.

6.2.2 Finite Element Modelling

In the present chapter, a three-dimensional numerical model is developed to simulate the reeling process of a lined pipe, using the general-purpose finite element software ABAQUS (Hibbitt *et al.*, 2016) and considering non-linear geometry in the description of parts of the numerical model. The reel is represented as a circular rigid surface of radius R_{reel}, which constitutes a major loading parameter, defined in the following sections. The total length of the lined pipe is equal to one hundred and fifty (150) times the outer diameter of the outer pipe (D_o). One end of the lined pipe is kinematically connected to the reel, as shown in Figure 6.1, while the other end is placed between rollers, allowing only horizontal displacement of the pipeline. Furthermore, the lined pipe is incrementally reeled around the reel by applying an appropriate rotation ω (shown in Figure 6.1), while a constant tensile force, called “back tension”, is applied at the other end during the reeling process. Finally, the model considers half the cross-section, using symmetry with respect to the y-z-plane of bending, as shown in Figure 6.2.

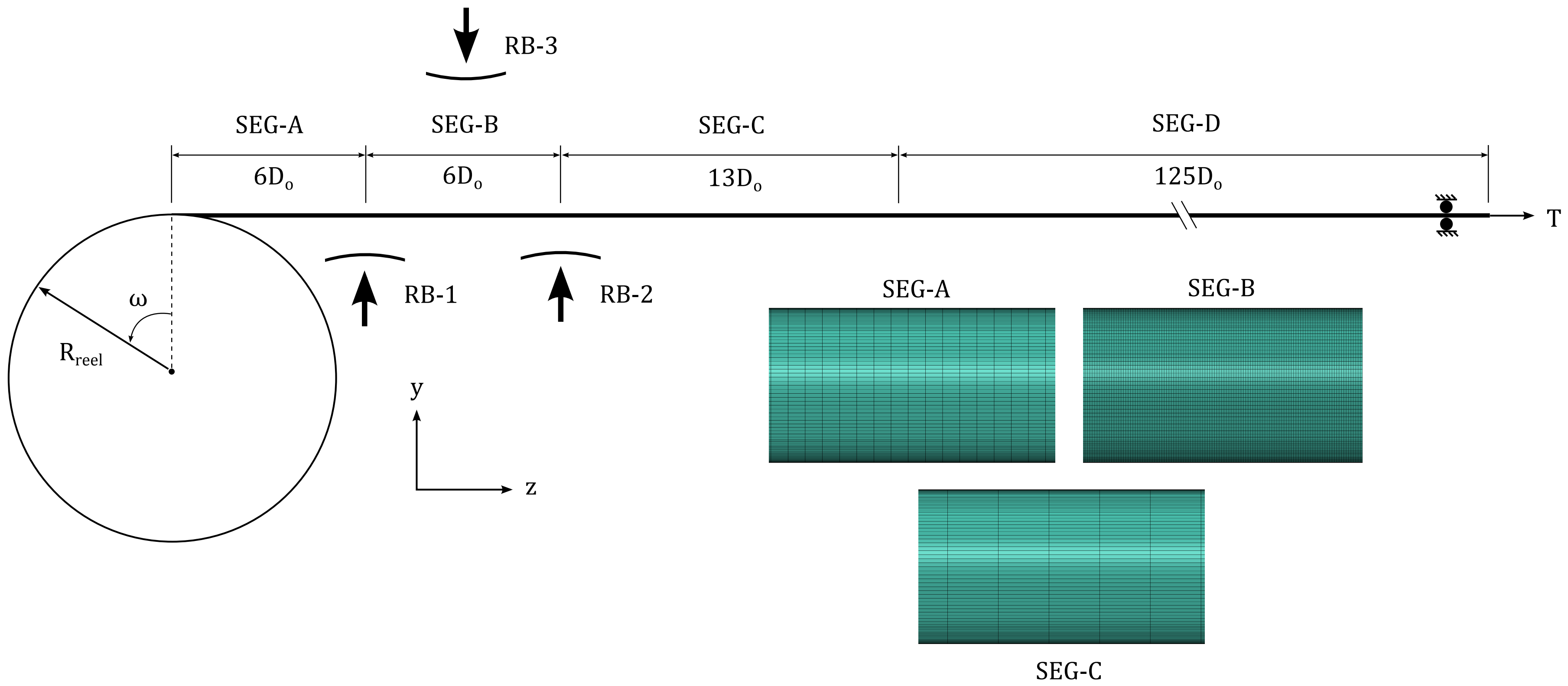

Figure 6.1 Schematic representation of the reel-lined pipe model.

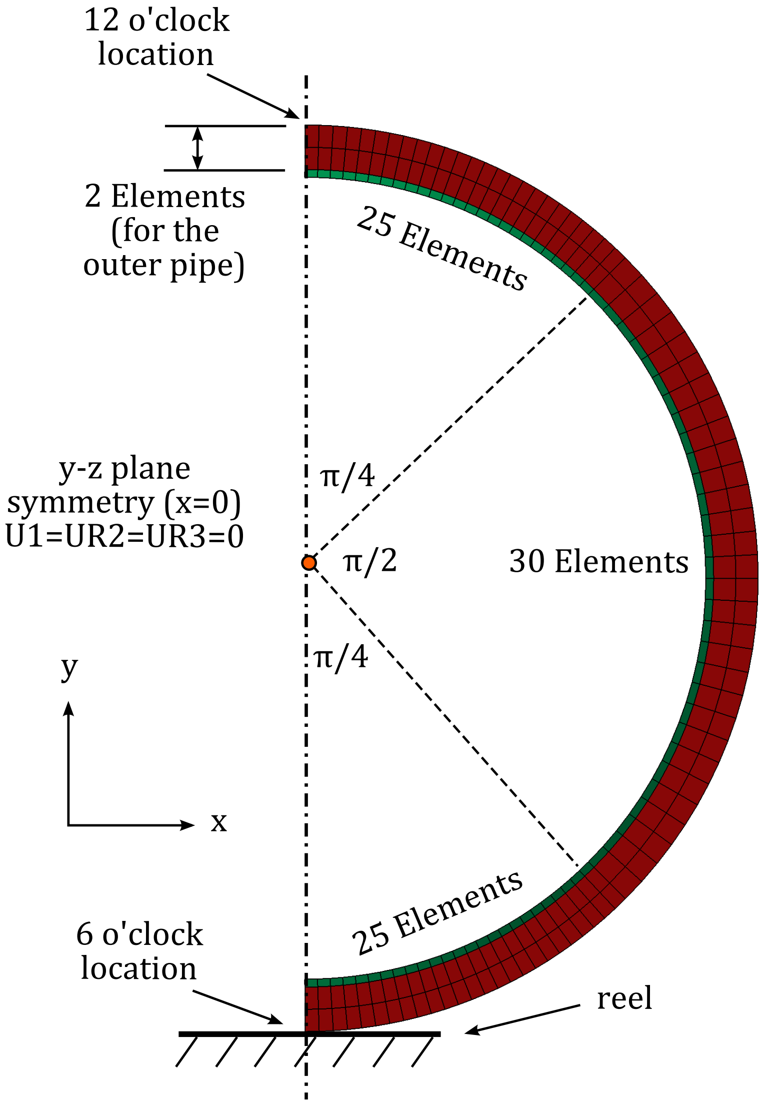

Figure 6.2 Lined pipe cross-section mesh (for SEG-A, SEG-B and SEG-C sections).

The thin-walled liner pipe is modelled with four-node linear shell elements (S4), while the outer pipe is modelled with eight-node linear solid elements (C3D8). In the present research, the objective is to simulate the winding-unwinding and straightening effect of the reeling installation method on the buckling response of the liner pipe. As already presented in previous publications (Vasilikis, 2012; Vasilikis and Karamanos, 2013; Yuan, 2015; Yuan and Kyriakides, 2014*a*) and also in Chapters 3, 4 and 5, short-wave wrinkles develop at the compression side of the liner pipe, which grow further with gradual increase of the applied curvature, leading to local buckling of the liner pipe. In order to capture the buckling phenomena and the accurate wavelength of the liner pipe while optimizing computational efficiency, the lined pipe should be modelled with the appropriate mesh following similar density mesh to those used by Yuan and Kyriakides (2020).

The lined pipe is divided into four segments (SEG-A, SEG-B, SEG-C and SEG-D), as shown in Figure 6.1. SEG-A is an "entry section" connected to the reel with six outer diameters (D_o) length, containing sixty elements on the axial direction (z-axis) for both pipes. The "test section", denoted as SEG-B, follows, containing three hundred and six hundred elements in the axial direction for the outer and the liner pipe, respectively. At this point, it should be noted that the liner pipe in SEG-B section has been initially modelled with three hundred elements, following the work reported by Yuan and Kyriakides (2020), and four hundred elements in the axial direction (denoted as "MA"). However, this discretization was not able to produce converged results for liner wrinkling at 6 o'clock location, as shown in Figure 6.3. Using five hundred and six hundred elements, also called "MB" and "MC", similar results were obtained. Six hundred elements are considered in the present study. The length of SEG-B is equal to six times the diameter of the outer pipe. Subsequently, a section with coarser mesh than the SEG-B section follows; it has forty four elements in the axial direction for the outer and the liner pipe with thirteen outer diameters length. In those three sections, the number of elements around the circumference is equal to eighty for each pipe. In order to simulate the formulation of local buckling at 12 and 6 o'clock location of the cross-section, a finer mesh is adopted containing twenty five elements for $0 \leq \theta \leq \pi/4$ and $3\pi/4 \leq \theta \leq \pi$, while thirty elements are used for $\pi/4 \leq \theta \leq 3\pi/4$, as shown in Figure 6.2. Summarizing, SEG-A section contains $\{z, \theta, t\} = \{60, 80, 2\}$ elements for the outer pipe and $\{60, 80, 1\}$ elements for the liner pipe, SEG-B contains $\{300, 80, 2\}$ and $\{600, 80, 1\}$ elements, while SEG-C contains $\{44, 80, 2\}$ and $\{44, 80, 1\}$ elements for both the outer and the liner pipe, respectively.

An additional "trailing section" (denoted as SEG-D) is considered following the SEG-C section, in order to simulate that the SEG-B, which is the pipe segment that the results are extracted from, experiences the loads that are representative during an actual reeling process. Beam elements could have been used to reduce the computational cost, but the ovalisation of the pipe will not be described accurately and that may also affect the deformation of SEG-B and SEG-C section. Therefore, solid and shell elements are used for the outer and liner pipe, respectively, similar to the previous sections of the pipe. The elements in SEG-D section do not establish contact with the reel, so a coarser mesh is considered containing $\{z, \theta, t\} = \{105, 12, 1\}$ elements for the outer and the liner pipe, respectively, while the length of SEG-D section is equal to one hundred and twenty five (125) outer diameters. The outer and the liner pipe elements in this section are connected with the corresponding elements of SEG-C section of the lined pipe, using the "Tie Constraint" feature in ABAQUS.

In addition, three circular rigid surfaces, denoted as RB-A, RB-B and RB-C, are developed, capable of performing three point bending on SEG-B section after the winding-unwinding cycles. The three point bending represents the straightener, as shown in Figure 1.3 schematically, resulting in zero residual curvature before the pipeline leaves the vessel. The complete reeling process is investigated, including the effect of straightening, and is presented later in the present chapter in section 6.3.

Finally, contact between the outer and the liner pipe is modelled using a surface-to-surface interaction, with finite-sliding contact, allowing for separation and frictionless sliding/rotation without penetration between the two surfaces, an assumption also used in previous works (Vasilikis, 2012; Vasilikis and Karamanos, 2012; Yuan, 2015; Yuan and Kyriakides, 2014*a*) and in the previous chapters (sections 3.2.2, 4.2.2 and 5.2.2). Furthermore, contact between the rigid surfaces and the deformable lined pipe is modelled considering the rigid surfaces as "master" and the pipe as "slave" surface, using an exponential softening contact pressure-overclosure algorithm in ABAQUS with 0.7 *MPa* and 0.001 *mm* (Yuan and Kyriakides, 2020) as representative pressure and clearance values, respectively. All contacts in the present model are considered frictionless.

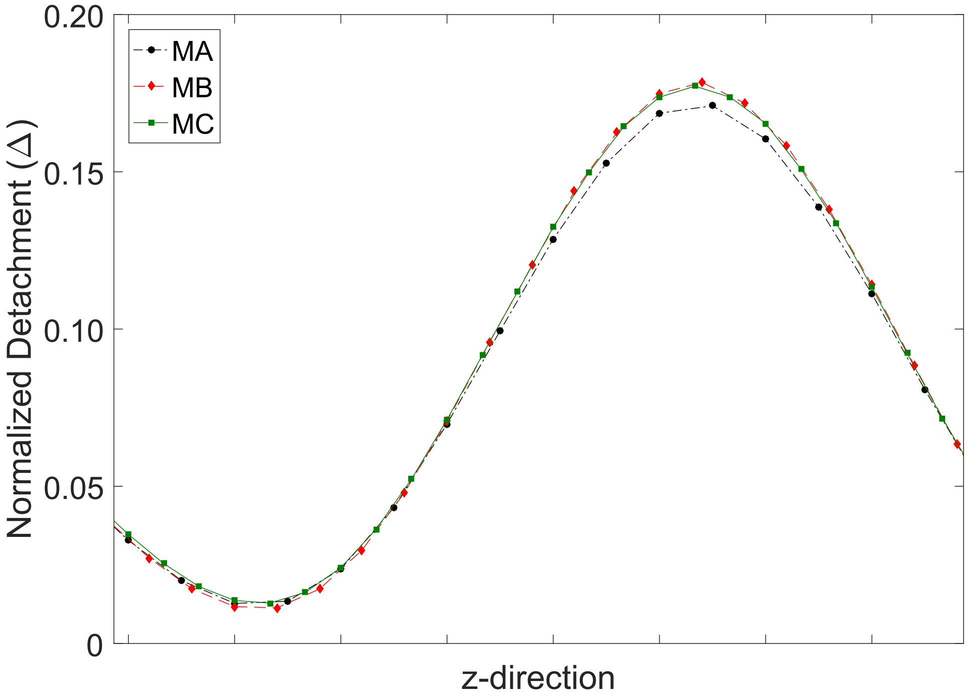

Figure 6.3 Liner wrinkle amplitude at 6 o'clock location in SEG-B section, for different mesh densities in the axial direction.

6.3 Reeling of geometrically perfect lined pipes

In the present section, the structural response of a mechanically bonded pipe during reeling is investigated, using the three-dimensional model shown schematically in Figure 6.1 and presented in detailed in section 6.2.2. In the first part of the analysis, the thermo-mechanical (TFP) manufacturing process is simulated, as described in section 4.3.3 and shown in Figure 4.7, while in the second part of the analysis, the lined pipe is subjected to five winding-unwinding cycles representing a real installation-repair scenario. As mentioned previously in section 5.3, if a serious defect is detected, the installation process is stopped and the pipe is repaired. In this case, except for the two main bending cycles of reeling, the pipeline is spooled and unspooled again passing through the aligner, the reel and the straightener, adding three bending cycles until the repaired pipeline leaves the reeling vessel.

The present model is a useful addition in the knowledge of the effect of reeling on pipelines structural performance. Extensive numerical models have been reported examining the mechanical behaviour of single wall pipes during spooling/unspooling on a drum (Liu and Kyriakides, 2017; Liu *et al.*, 2017, 2015), while more recently Yuan and Kyriakides (2020) presented numerical results on spooling monotonically a double-walled pipe onto a reel. The present study constitutes an attempt to develop a more complex numerical model, which considers the plastic deformation of the liner pipe during the manufacturing process, and simulates further the cyclic response of lined pipe under five cycles, accounting also the significant influence of straightener on liner buckling.

Considering a reel radius R_{reel} equal to 10 m, which is a typical value in practical applications (Kyriakides and Corona, 2007), the spooling process is simulated by applying a rotation $\omega = 45°$, as shown in Figure 6.1, subjecting the lined pipe to global bending strain $\varepsilon_b = D_o/(2R_{reel} + D_o)$ equal to 1.59%. The angle ω is chosen so that the test section SEG-B, where the results are extracted from, is fully wound onto the reel and a significant part of the SEG-C section is also in contact with the reel, as shown in Figure 6.4, ensuring that further rotation of the reel will not affect the SEG-B section. In addition, at the end of the second and fifth cycle, a three point bending of the lined pipe is performed, simulating pipeline straightening. The RB-1 and RB-2 rigid surfaces are located at the beginning and at the end of SEG-B section, while RB-3 translates downwards at y direction bending the lined pipe. The RB-3 translation is appropriately chosen in order to obtain local curvature equal to zero at the end of straightening process, in the middle section of SEG-B segment (black cross in Figure 6.4).

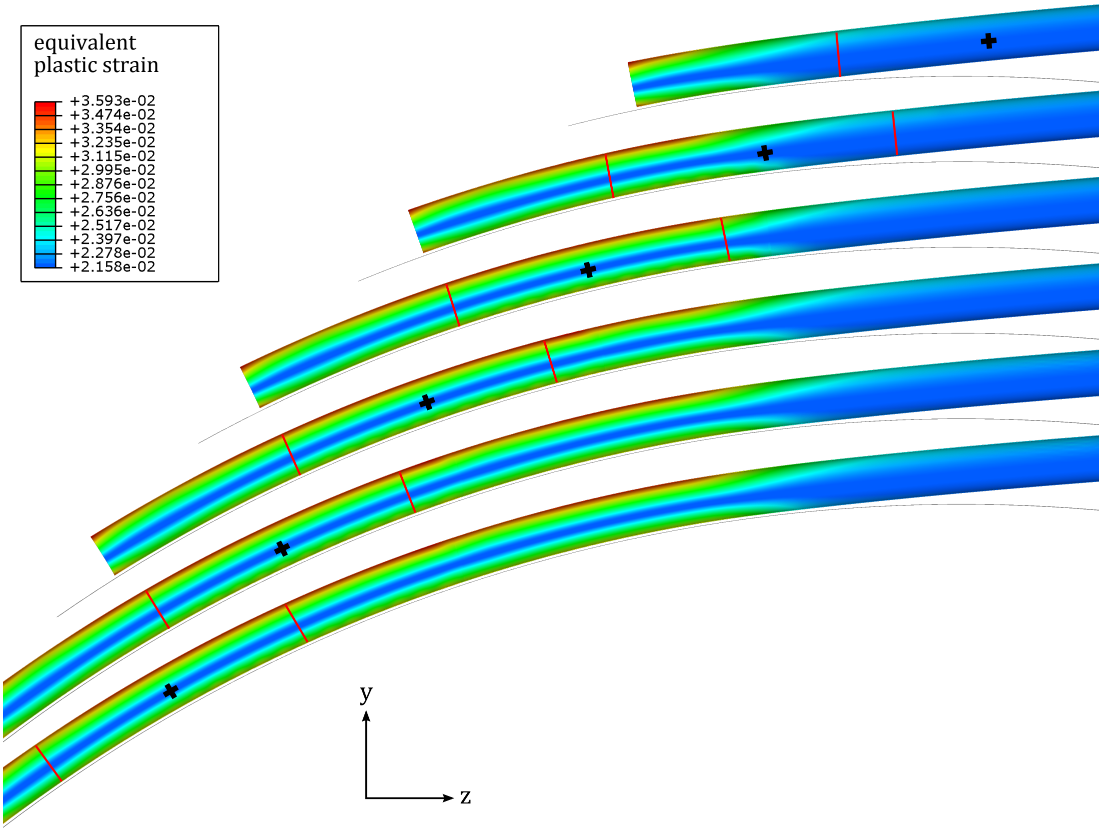

Figure 6.4 Sequence lined pipe configurations during spooling onto a reel; the colour contours represent the equivalent plastic strain (ε_q).

During reeling, a constant "back tension" force is applied to control the configuration shape of the pipeline free span, and avoid local buckling (Brown *et al.*, 2004; DNV-OS-F101, 2013; Kyriakides, 2017; Manouchehri, 2012). Therefore, a back tension force is applied in the present study, which is equal to 2% of the yield tension of the outer pipe ($T_p = \sigma_{y,o} \pi D_{m,o} t_o$, where $D_{m,o} = D_m - t_o$ is the mean diameter of the outer pipe), following typical values used in the industry (Vasilikis, 2018) and in previous publications (Liu and Kyriakides, 2017). This is in agreement with the expression presented by Manouchehri (2012), calculating the back tension force according to the plastic moment of the outer pipe (the outer pipe in this case) over the radius of the reel. The aforementioned loading is referred to as "Reeling Case I". In the present section, the pipes are considered imperfection-free, while the influence of geometric imperfections of the liner pipe is investigated in the following section 6.4.4.

In Figure 6.5, the total bending moment on the double-walled pipe is presented with respect to the number of cycles. The moment is calculated in the middle section of the SEG-B segment (denoted with a black cross in Figure 6.4), summing the axial stress resultants acting on each node of the cross section multiplied by their distance from mid-surface. The value of bending moment is normalised by $M_o = \sigma_{y,o} D_{m,o}^2 t_o$, where $D_{m,o}$ is the mean diameter of the outer pipe, so that $m = M_{Total}/M_o$. As the reel incrementally rotates, the pipeline arches upwards, and the total moment increases reaching a maximum value, which corresponds to the point where the middle of the SEG-B segment establishes contact with the reel. During unwinding, as the pipeline is lifted off the reel, the bending moment drops and becomes negative, due to straightening of the pipeline and the applied back tension force.

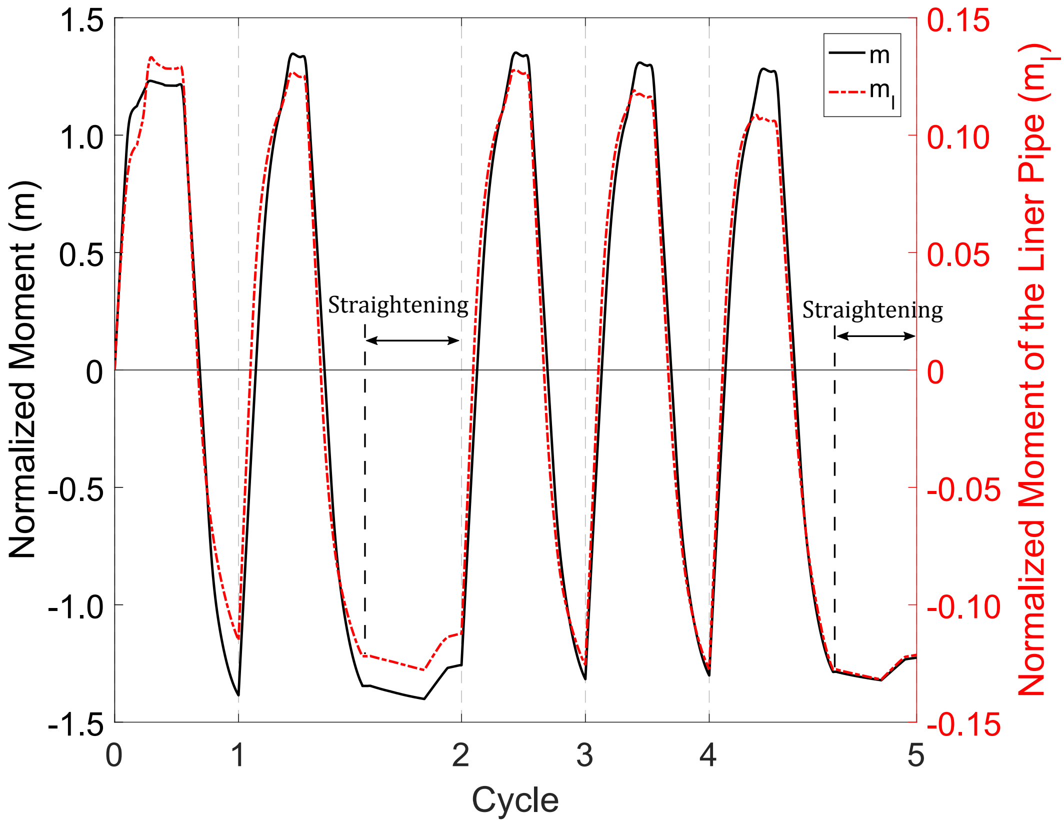

Figure 6.5 Normalised bending moments of the bi-material lined pipe (m) and the liner pipe (m_l), with respect to the number of cycles, for loading Reeling Case I.

Subsequently, Figure 6.6 presents the maximum detachment of the liner pipe from the outer pipe at 6 o'clock location with respect to the bending cycles. The detachment is calculated in the middle of SEG-B segment and normalised by the wall thickness of the liner pipe (t_l). The 6 o'clock location corresponds to the side of the lined pipe that is compressed first during reeling and establishes contact with the reel, as shown in Figure 6.2. Figure 6.7 shows the corresponding buckling patterns of the liner at 6 o'clock location, indicating that during the first two reeling cycles a uniform wrinkling is formed along the compression side of the liner pipe with amplitude less than the wall thickness of the liner pipe (configurations “a” and “b”). Moreover, the normalised half-wavelength is equal to 1.373 ($l_{hw} = L_{hw}/\sqrt{D_{m,l}t_l}$, where $D_{m,l}$ is the mean diameter of the liner pipe), which is in accordance with previous results presented in the previous chapters.

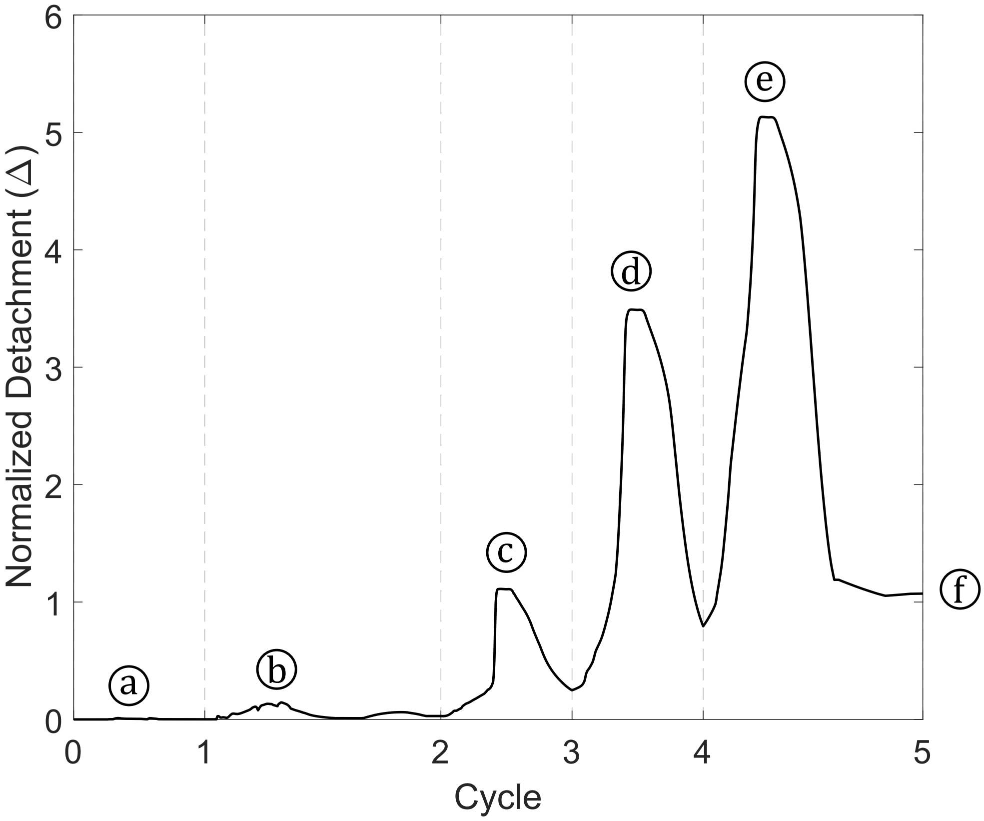

Figure 6.6 Liner normalised detachment (Δ) at 6 o’clock location, with respect to the number of cycles, for loading Reeling Case I.

During the repair cycles, the liner pipe detaches rapidly (“c”) and local buckling begins to develop, as shown in Figure 6.8. In particular, during the last two cycles of repair the liner pipe buckles locally forming a main buckle A and four adjacent minor buckles B (configurations “d”, “e”, “f”). The minor buckles are not symmetric around the main buckle A, compared with previous publications (Vasilikis and Karamanos, 2012, 2013; Yuan and Kyriakides, 2014*a*) nor with the results presented in Chapters 3, 4 and 5 in the present work, where a pure bending model is used. This asymmetry is attributed to the non-uniform curvature experienced by the current pipe segment, as the pipeline engages the reel. This observation is also presented in Figure 6.9, where a part of the SEG-B segment is shown at 6 o’clock location during the five reeling cycles. At this point, it should be highlighted that liner pipe collapse in a diamond-type buckling mode is considered as the main limit state of lined pipes. This performance criterion is considered unserviceable and might lead to cracking of the liner pipe under operational thermo-mechanical loads, resulting in corrosion of the outer pipe. Therefore, in case that the pipeline undergoes only the reeling cycles with global bending strain $\varepsilon_b = 1.59\%$, assuming that the failure scenario does not happen, the liner pipe ends with minor wrinkling. Furthermore, the normalised bending moment carried by the liner pipe (m_l) is presented in Figure 6.5, with respect to the reeling cycles, showing that the moment of the liner pipe gradually reduces during the fourth cycle, where the liner detachment is abruptly increased, leading to a diamond-type local buckling of the liner pipe (configuration “d” of Figure 6.8).

In addition, the ovalisation of the outer pipe is presented in Figure 6.10, calculated in the middle section of SEG-B segment (black cross in Figure 6.4). It is defined as $\zeta_o = (D_{m,o,h} - D_{m,o,v})/(D_{m,o,h} + D_{m,o,v})$, where $D_{m,o,h}$ and $D_{m,o,v}$ are the deformed horizontal and vertical mean diameters of the outer pipe, a definition also used by API RP 1111 (1999); Kyriakides and Corona (2007); Murphey and Langner (1985). A gradual increase of the ovalisation is observed during winding, while a small local spike occurs when the cross-section establishes contact with the reel. The ovalisation of the outer pipe cross-section remains constant with further rotation of the reel. During unwinding, the ovalisation is initially constant when the cross-section remains in contact with the reel. When the cross-section loses contact with the reel, a local spike is shown, an observation reported in previous publications (Kyriakides, 2017; Liu *et al.*, 2017). As the unwinding proceeds, gradual decrease of the ovalisation is followed. At the second reeling cycle, the ovalisation of the outer pipe is equal to 0.59%, before straightening, and increases to 0.86% afterwards, showing the influence of straightener on cross-sectional ovality. The effect of “straightener” is also shown at the end of the fifth cycle, where the ovality increases from 1.17% to 1.32%.

The values of curvature k are normalised by the curvature-like parameter $k_o = t_o/D_{m,o}^2$, where t_o and $D_{m,o}$ is the wall thickness and the mean diameter of the outer pipe, respectively, so that $\kappa = k/k_o$. Figure 6.11 presents the local curvature κ of the outer pipe calculated on the neutral axis of the pipe in the middle of SEG-B section (black cross in Figure 6.4) by fitting three nearby nodes of the outer pipe on a circle with local radius equal to $1/(\kappa k_o)$. Initially, the local curvature increases during winding, reaching a maximum curvature value on the first $2\pi R_{reel}$ pipeline length, which is in contact with the reel. With continuing spooling and packing the pipeline on the drum, the applied curvature gradually decreases. Subsequently, during unwinding, the pipeline loses contact with the reel, the local curvature decreases, and residual local curvature exists at the end of each cycle. These values range from 0.088 to 0.120, depending on the cycle, while the local curvature is zero at the end of the second and fifth cycle after performing the straightening of the pipeline.

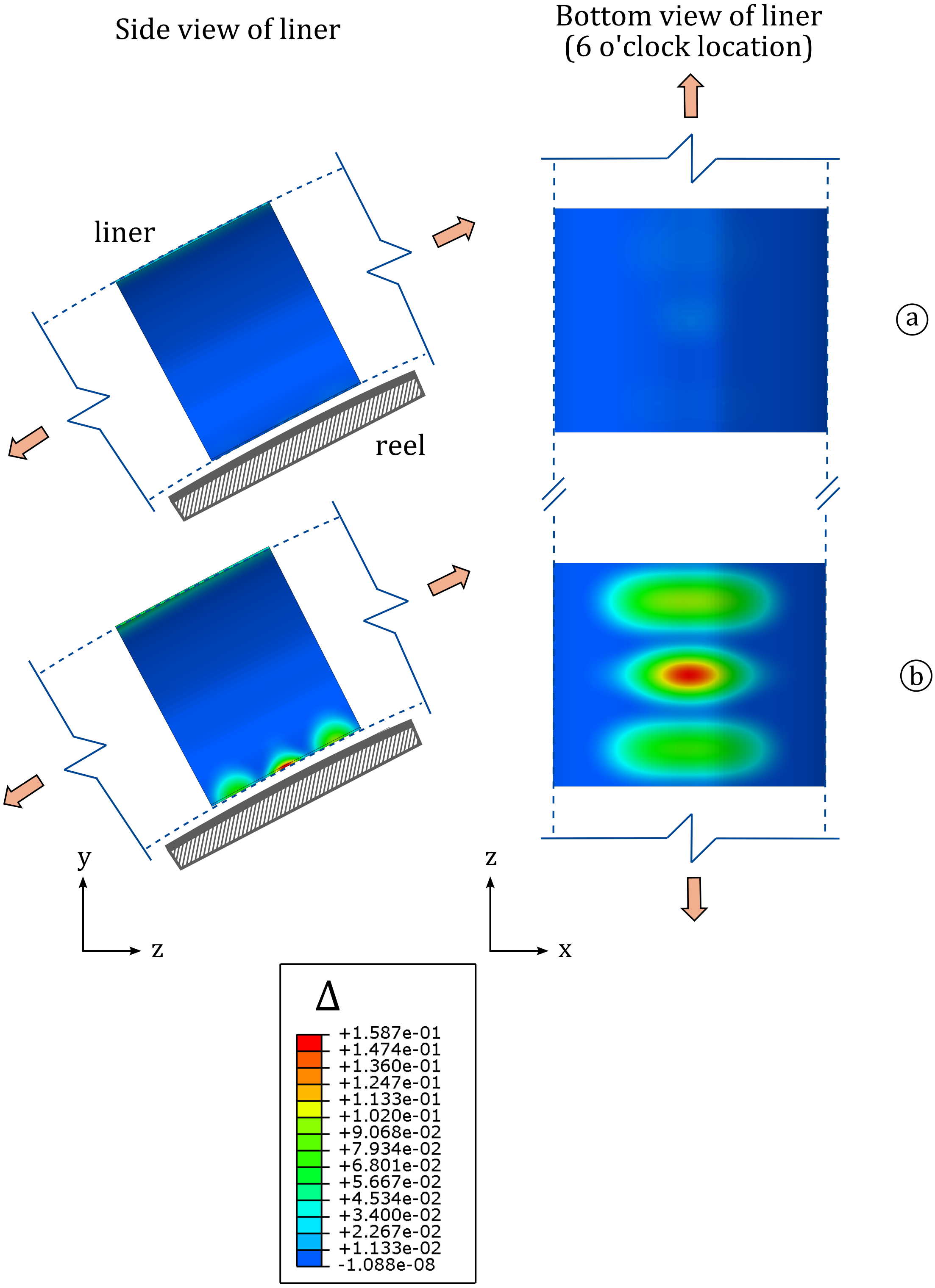

Figure 6.7 Sequence of liner pipe deformation and normalised detachment (Δ), at 6 o'clock location; the configurations of this figure correspond to stages "a" and "b" of Figures 6.6, which are the regular installation cycles.

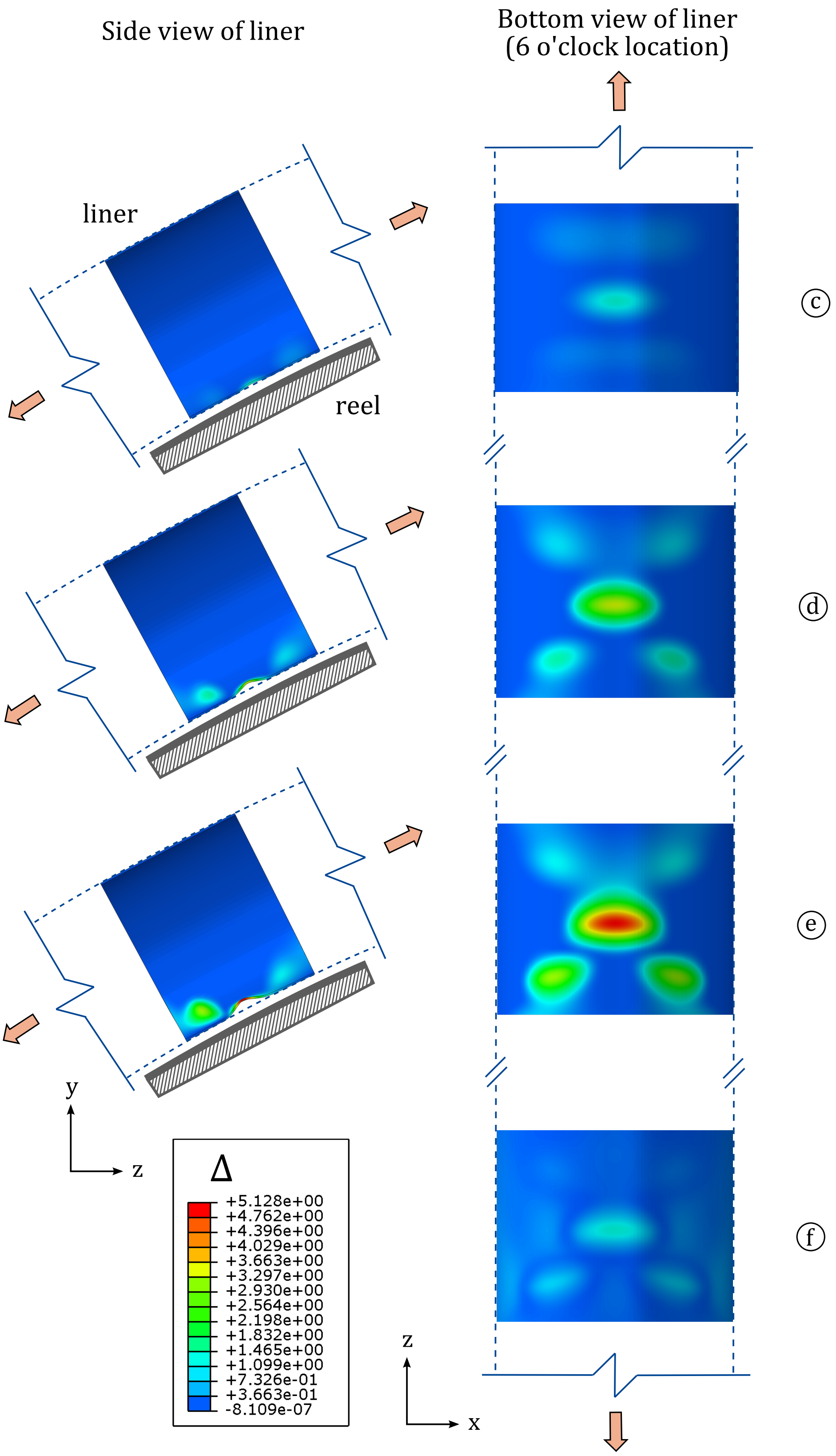

Figure 6.8 Sequence of liner pipe deformation and normalised detachment (Δ), at 6 o'clock location; the configurations of this figure correspond to stages “c”-“f” of Figure 6.6, which refer to the last three cycles because of repair.

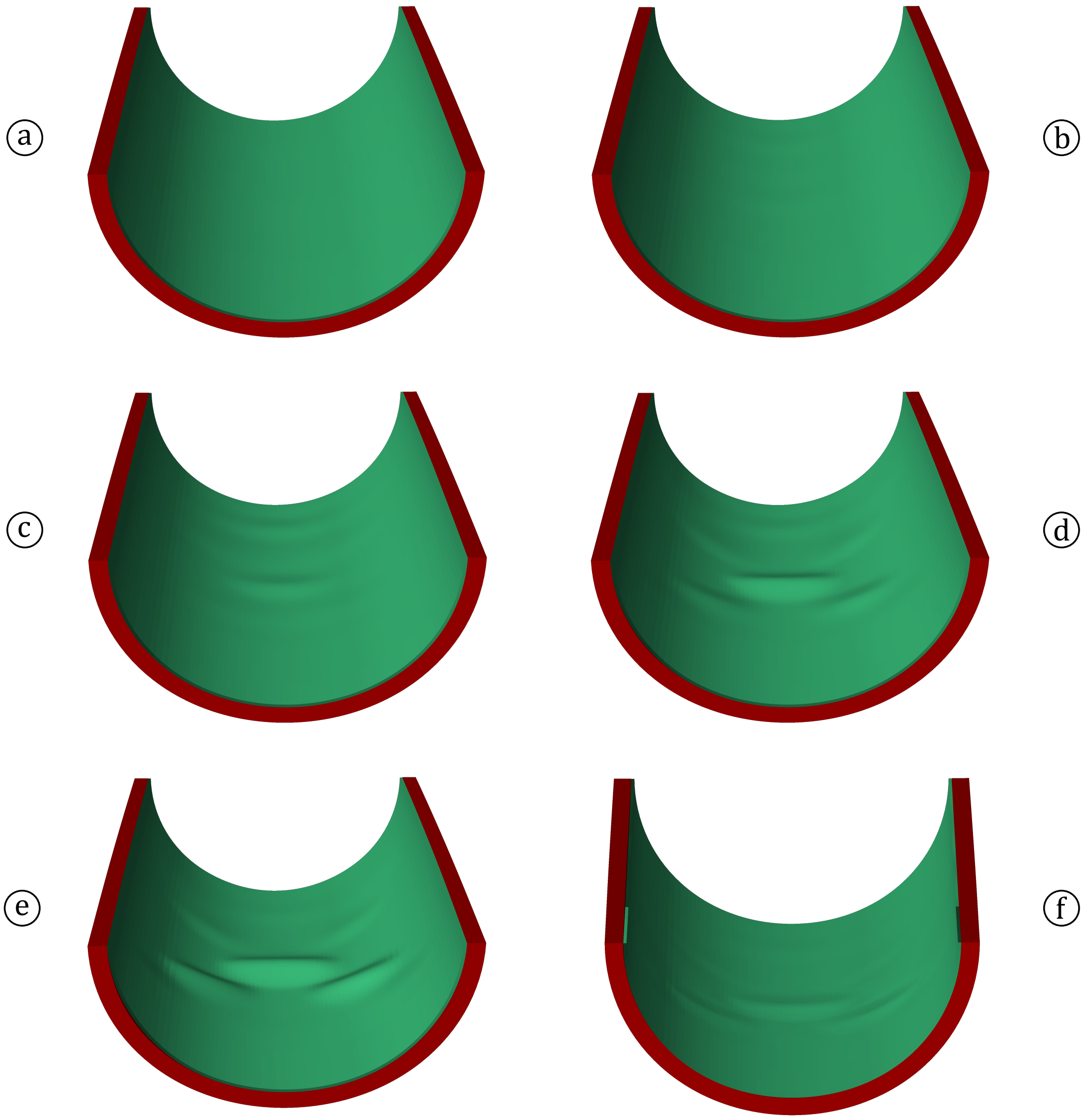

Figure 6.9 Three-dimensional configuration of the buckled liner pipe, for the deformation configurations shown in Figures 6.7 and 6.8; half of the pipe is shown referring to the part in contact with the reel.

Finally, Figure 6.12 presents the evolution of liner detachment for the complete reeling model for Reeling Case I loading, presented in the current chapter in section 6.2.2, compared with the pure cyclic bending model, employed in Chapter 5, under Case I loading. At this point, it should be also noted that the 6 o'clock location in the present chapter (Figure 6.2) corresponds to the 12 o'clock location in Chapter 5 (Figure 4.3). In both loading cases, the pipe is geometrically perfect, and is manufactured using the fully heated TFP process. In the present case, the liner detachment in each cycle is significantly lower than the one calculated with the pure bending model. In the pure bending model, the applied curvature on the pipe ranges from zero to the maximum value ($\kappa \in [0, 0.587]$, with curvature range $\Delta\kappa = 0.587$), while in the present case a residual curvature is observed during unwinding ($\kappa \in [\kappa_{res}, 0.587]$, where $\kappa_{res} > 0$ and curvature range $\Delta\kappa = 0.587 - \kappa_{res} < 0.587$); as a result, the pipeline is cyclically loaded under a smaller curvature range, leading to a smaller strain range, and therefore the evolution of plastic deformation in the liner pipe is also lower, delaying the formation of local buckling. It should be also noted that using the present model, the liner pipe during unwinding does not develop wrinkles or local buckles at the opposite location (the 12 o'clock location shown in Figure 6.2). This is different than the response of the pipe under pure bending model; this difference is attributed to the residual curvature after unwinding. The smaller curvature range loading results in a lower rate of plastic strain accumulation in the liner pipe; as a result the formation of local buckling at 12 o'clock location is not developed during the five cycles.

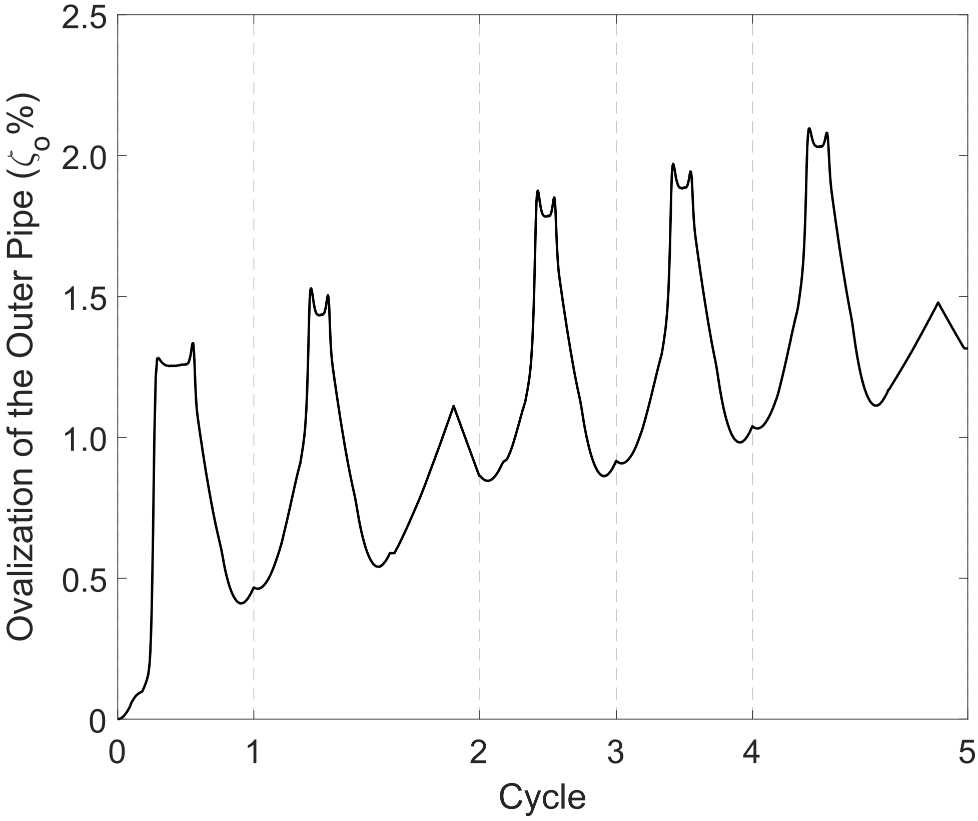

Figure 6.10 Ovalisation (ζ_o) of the outer pipe at the SEG-B section, with respect to the number of cycles, for Reeling Case I.

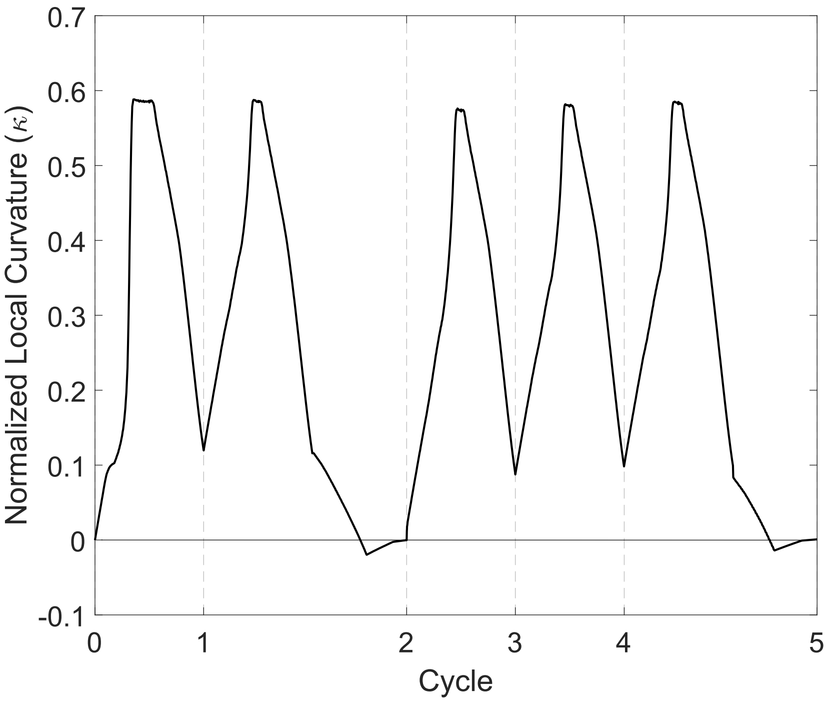

Figure 6.11 Local curvature (κ) of the lined pipe at the SEG-B section, with respect to the number of cycles, for loading Reeling Case I.

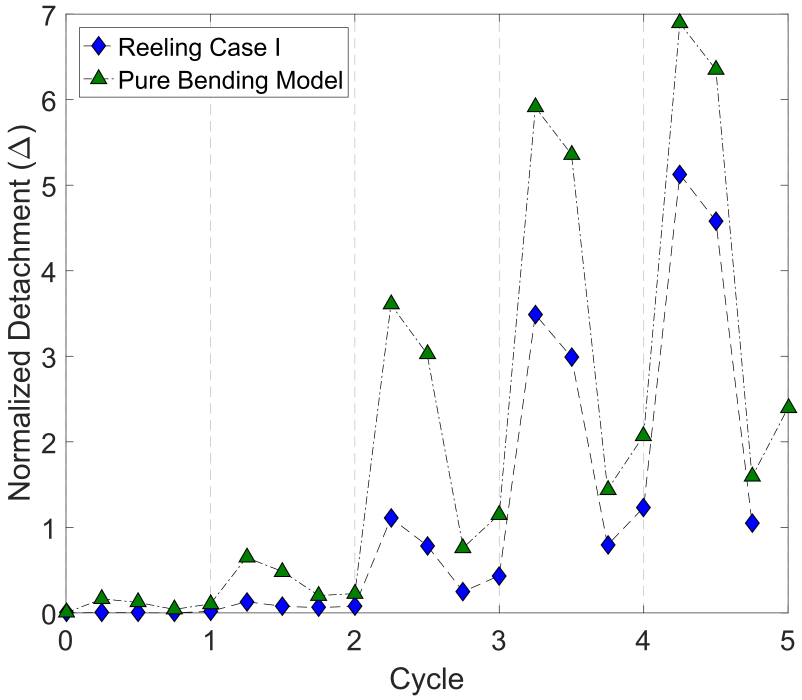

Figure 6.12 Normalised detachment of liner pipe at 6 o'clock position with respect to loading cycles for Reeling Case I, compared with the corresponding cyclic bending Case I from Chapter 5 using a pure bending model.

6.4 Effect of various parameters on lined pipe reeling

In the following sections, the effect of several parameters on the reeling performance of lined pipes is investigated. The influence of straightening and different reel diameters on the buckling response of the liner pipe are investigated first. The effect of different back tension forces is also examined, while imperfection sensitivity of the liner pipe is considered assuming an initial configuration of the liner with geometric imperfections. Finally, the structural stability of the liner pipe during reeling is examined assuming different wall thickness values of the liner pipe, while the effect of moderate levels of internal pressure is also investigated.

6.4.1 Effect of straightener on liner buckling

In addition to Reeling Case I, analysed in the previous section 6.3, an alternative loading case is also investigated in the present section, referred to as Reeling Case II. In this case, the mechanically bonded pipe undergoes five consecutive reeling cycles, in the absence of straightener, which is performed in the current analysis by a three point bending at the end of the second and fifth cycle. The reel diameter (R_{reel}) equals to 10 m ($\varepsilon_b = 1.59\%$) and the back tension force is 2% of the yield tension (T_p) of the outer pipe, and remains constant during the five reeling cycles. The main feature of Reeling Case II is the absence of negative curvature values on SEG-B segment of the pipe. Therefore, the comparison of the numerical result from Reeling Cases I and II would indicate the influence of straightener on liner pipe buckling. The fully heated thermo-mechanical manufacturing process, presented in section 4.3.3, is considered, and both pipes are assumed free of geometric imperfections.

Figure 6.13 presents the normalised bending moment of the lined pipe and the liner pipe calculated in the middle section of SEG-B segment, with respect to the number of reeling cycles. A reduction on the liner bending moment occurs during the fourth cycle, while the moment drop on the fifth is more pronounced, indicating significant detachment of the liner pipe, associated with local buckling. Accounting for this issue, the normalised detachment of the liner pipe is presented in Figure 6.14, showing a significant increase of the maximum liner detachment on the fourth reeling cycle. At this stage, the liner pipe starts buckling locally, forming a main buckle with four minor adjacent buckles. Figures 6.7 and 6.15 present the buckling configurations of the liner pipe during the five reeling cycles, showing the formation of a uniform wrinkling of the liner pipe at the 6 o'clock location during the first three cycles, while the liner pipe buckles locally during the last two cycles. Figure 6.14 also presents the difference in liner detachment amplitude between the Reeling Cases I and II to highlight the effect of reverse bending on liner buckling response. The detachment in Reeling Case I is significantly more pronounced during the last three cycles, after straightening the pipeline at the end of the second cycle, showing its significant influence on liner pipe buckling response. More specifically, liner detachment during spooling in Reeling Case II is 74%, 36% and 17% lower than in Reeling Case I at the third, fourth and fifth cycle, respectively.

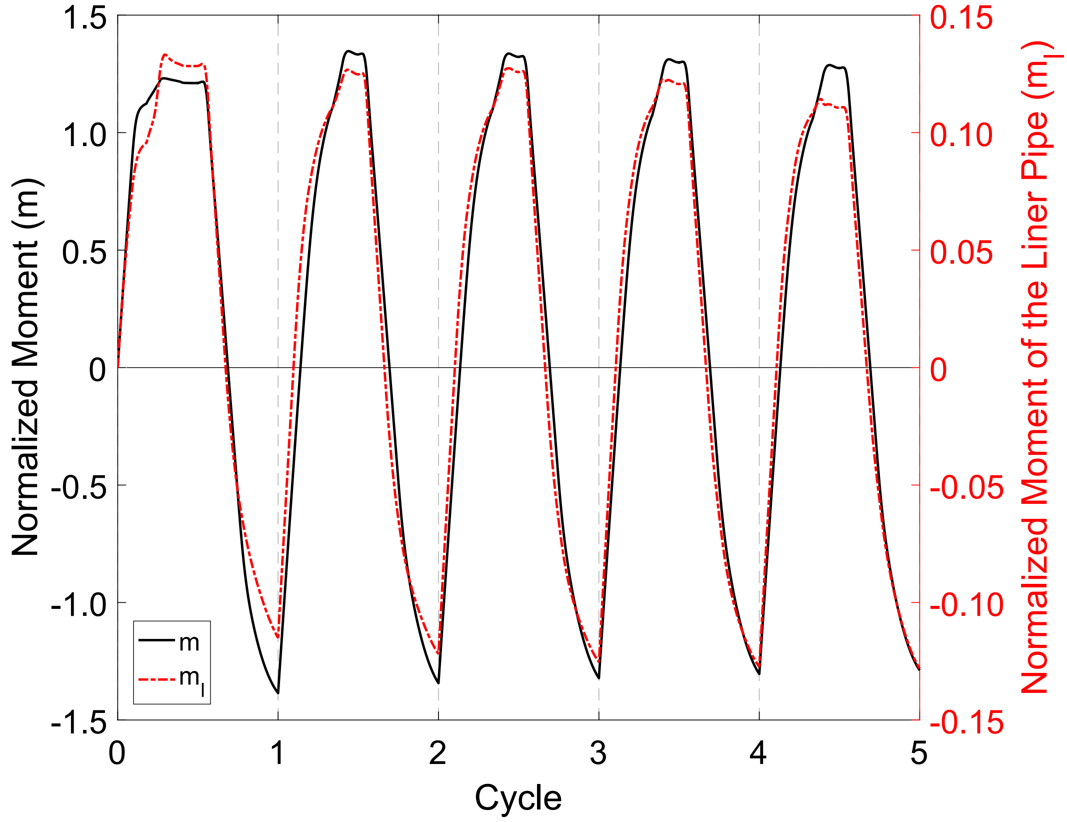

Figure 6.13 Normalised bending moments of the lined (bi-material) pipe (m) and the liner pipe (m_l), with respect to the number of cycles, for Reeling Case II.

Furthermore, the ovalisation of the outer pipe, with respect to the reeling cycles, is presented in Figure 6.16 for Reeling Case II, showing a lower increase rate compared with the Reeling Case I. The ovalisation in Reeling Case II is equal to 0.51% and 0.75% at the end of the second and fifth cycle, respectively, and reaches a maximum value equal to 1.7% during spooling of the fifth cycle. In Reeling Case I, the corresponding values are 0.87%, 1.32% and 2.10%. Finally, Figure 6.17 shows the evolution of local curvature of the outer pipe at the middle section of SEG-B segment. The local curvature measured ranges between a residual value, which equals to $\kappa = 0.120$, and the maximum curvature value during spooling ($\kappa = 0.587$).

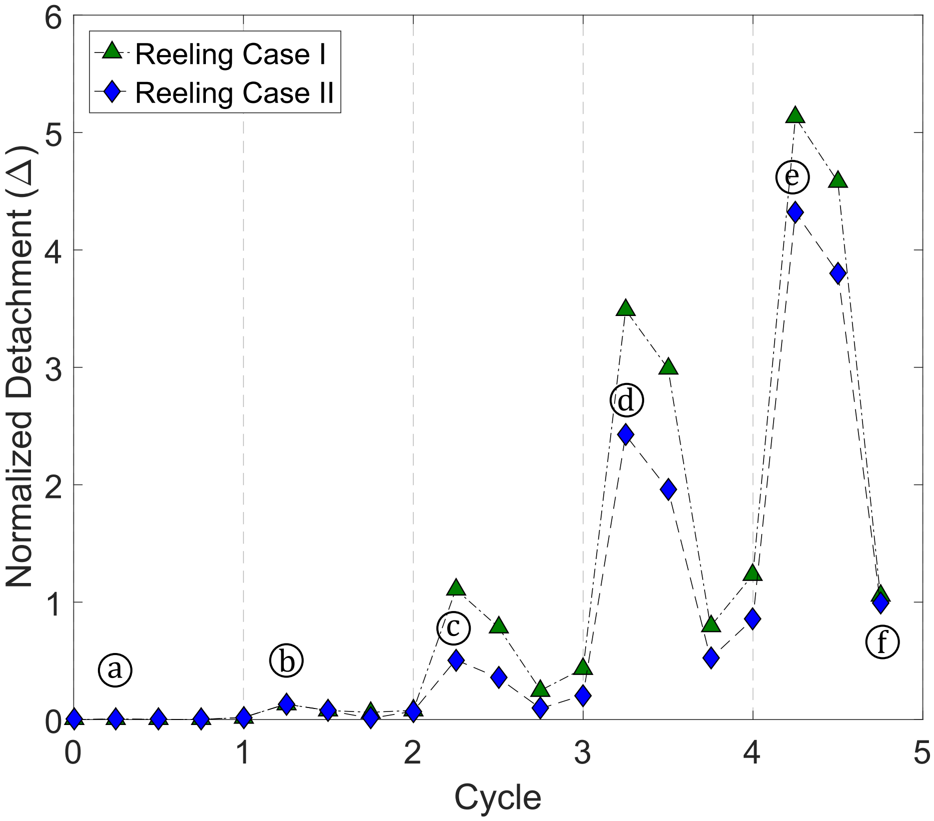

Figure 6.14 Normalised detachment of the liner pipe at 6 o'clock position, with respect to loading cycles, for Reeling Cases I and II.

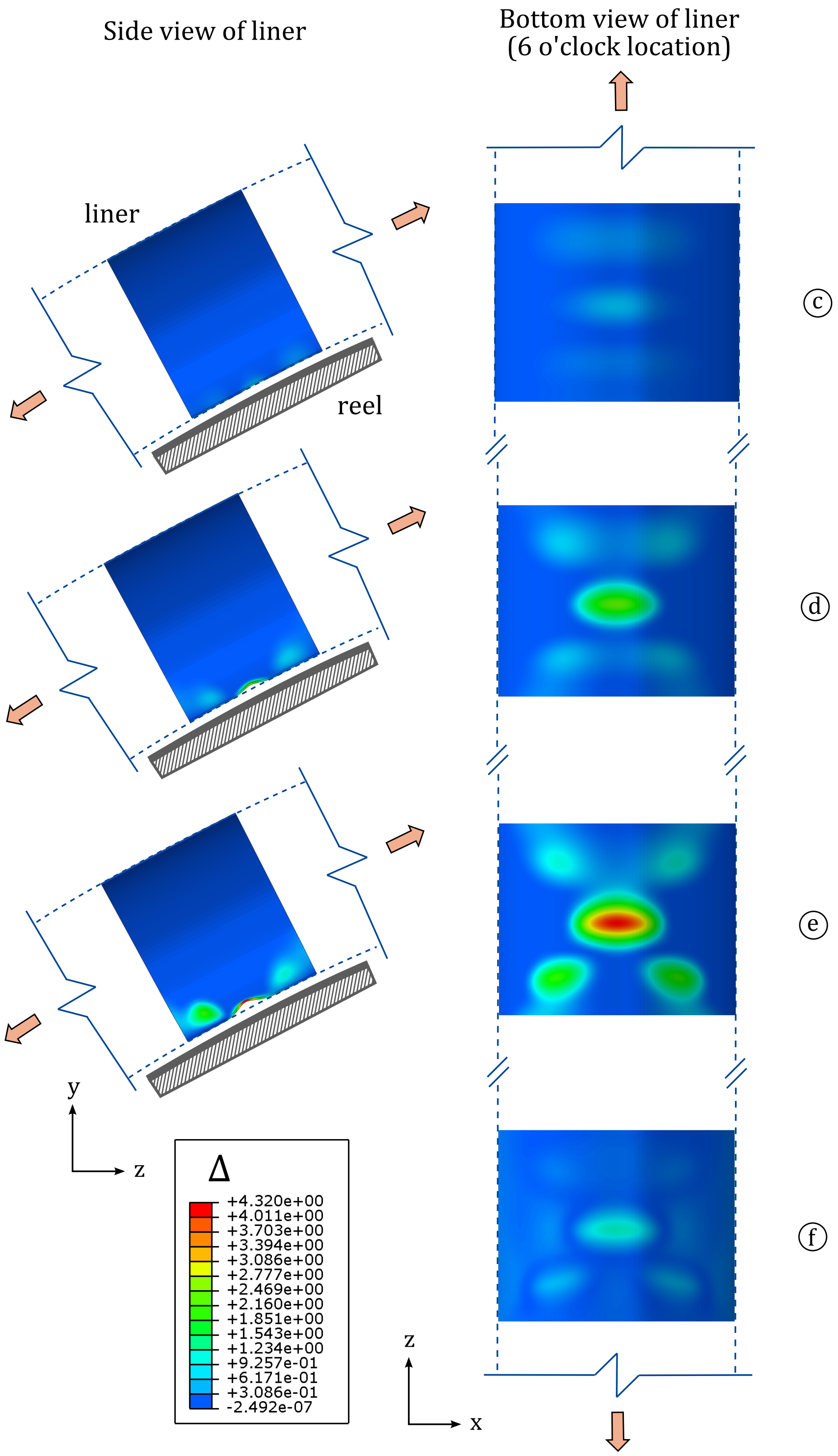

Figure 6.15 Sequence of liner pipe deformation and normalised detachment (Δ), at 6 o’clock location; the configurations of this figure correspond to stages “c”-“f” of Figure 6.14, which refer to the last three cycles because of repair.

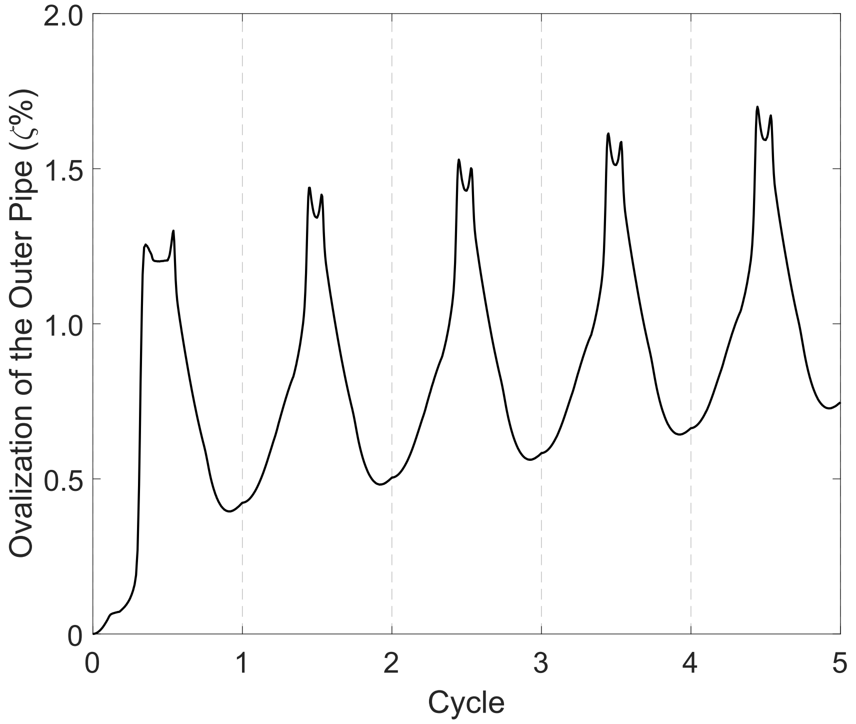

Figure 6.16 Ovalisation (ζ_o) of the outer pipe at the SEG-B section, with respect to the number of cycles, for Reeling Case II.

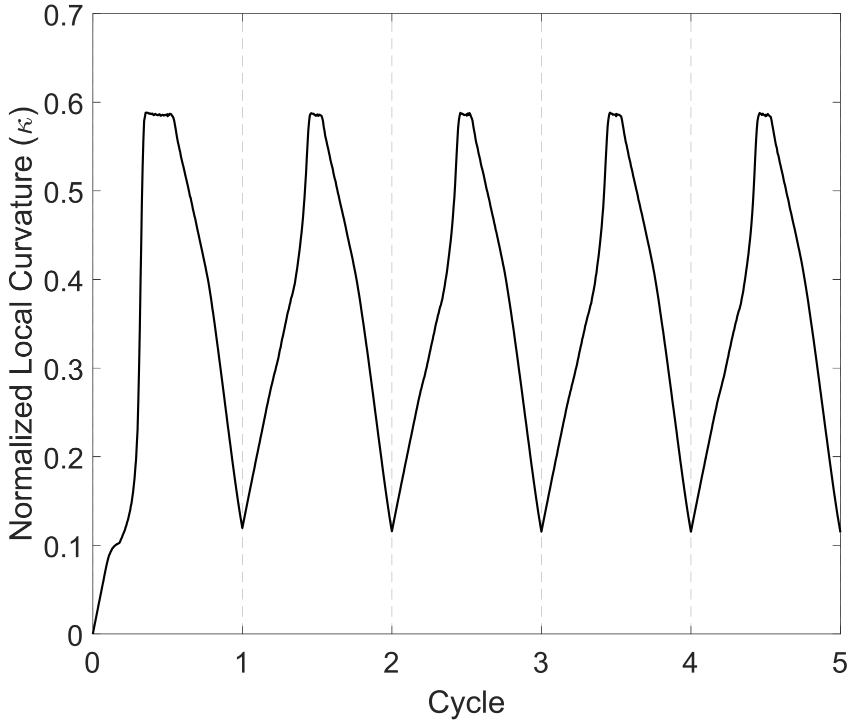

Figure 6.17 Local curvature (κ) of the lined pipe at the SEG-B section, with respect to the number of cycles, for Reeling Case II.

6.4.2 Different reel diameter values

The influence of different global bending strains, considering different reel diameters, on liner pipe buckling during the five loading cycles is also investigated. Two additional loading cases are examined in the present paragraph aimed at identifying the effect of reel size, and are compared with Reeling Case II, and they are denoted as Reeling Case III and IV. In Reeling Case III, the reel radius is equal to $8.23\ m$, corresponding to global bending strain $\varepsilon_b = 1.93\%$, while Reeling Case IV consists of a reel with radius $12.79\ m$ and $\varepsilon_b = 1.25\%$, respectively. The choice of the specific bending strain ε_b values is related to reeling vessel characteristics, presented by Kyriakides and Corona (2007). In both cases, the fully heated thermo-mechanical manufacturing process is followed, presented in section 4.3.3, and both pipes are considered imperfection-free. The back tension force is equal to 2% of yield tension T_p, while the reel maximum rotation (ω) is adjusted to 55° and 36° for Reeling Cases III and IV, in order to wind and unwind the same pipeline length.

Figure 6.18 presents the normalised bending moment of the liner pipe (m_l), with respect to the reeling cycles. A slight drop of moment is observed in the fourth cycle, where the liner detachment increases significantly and uniform wrinkling of the liner pipe leads to local buckling (configuration “d” in Figure 6.15), while local buckling is completely formed in the fifth cycle and the corresponding moment drop is more pronounced. In Reeling Case III, the moment of the liner pipe drops abruptly in the third cycle, indicating local buckling of the liner pipe. This result is verified in Figure 6.19, where the normalised detachment of the liner pipe for the different loading cases, with respect to the reeling cycles, is presented. In this case, uniform wrinkling of the liner is developed during the second cycle, local buckling occurs during the third cycle, and therefore, the last two cycles may not be performed. In Reeling Case IV, the maximum value of liner moment remains unchanged through the reeling cycles. A slight detachment is observed in Figure 6.19, resulting in a very low amplitude wrinkling formation. More specifically, in Reeling Case III, the liner detachment during spooling of the third cycle is 156% and 192% larger than the corresponding detachment in Reeling Case II and IV, respectively. The results indicate that for global bending strain ε_b values equal to 1.59% and 1.93%, the liner pipe forms uniform wrinkling during the reeling cycles and buckles locally during repair, while for $\varepsilon_b = 1.25\%$ the liner pipe undergoes five cycles avoiding local buckling.

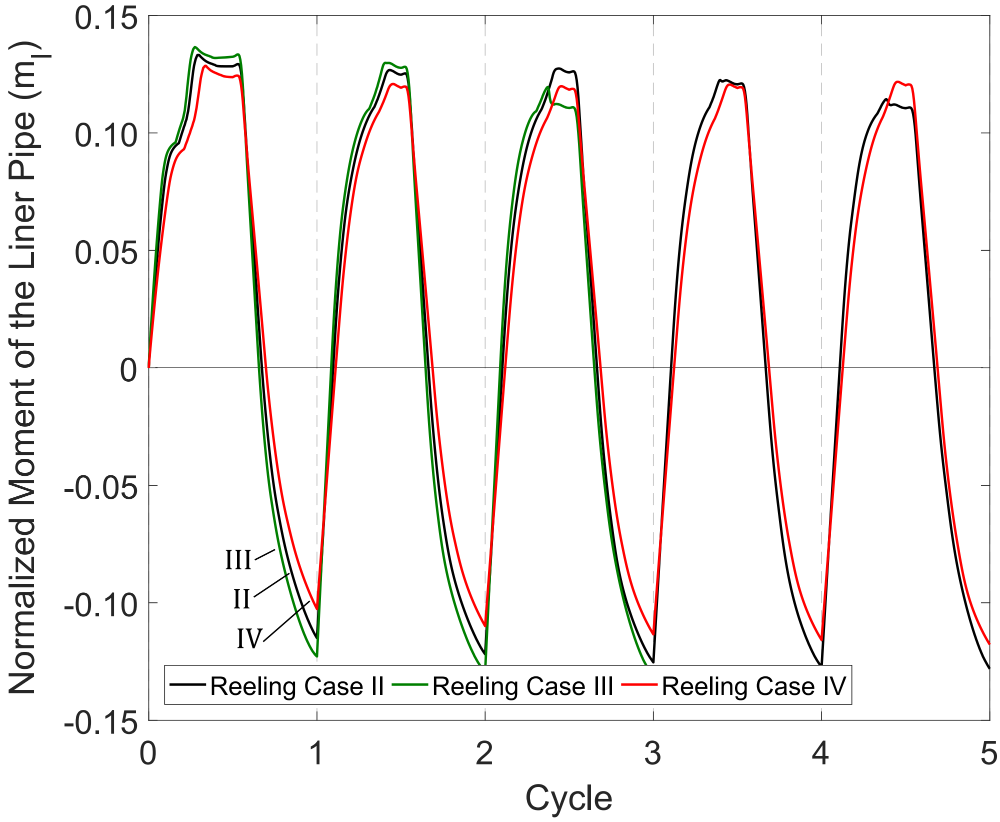

Figure 6.18 Normalised bending moment of the liner pipe (m_l), with respect to the number of cycles, for Reeling Cases II, III and IV.

In addition, Figure 6.20 depicts the local curvature of the outer pipe (κ), calculated on the neutral axis of the pipe in the middle section of SEG-B segment, fitting a circle on three nearby nodes of the pipe in each Reeling Case (II, III and IV), with respect to the reeling cycles. A residual local curvature is observed for all three cases during unspooling, equal to $\kappa = 0.120$, while the maximum curvature value on the lined pipe during spooling is 0.587, 0.711 and 0.462, for Reeling Cases II, III and IV, respectively. Reducing the reel radius, the applied curvature range increases, resulting in increasing the rate of plastic strain accumulation in the liner pipe and earlier formation of local buckling. The effect of reel diameter on the ovalisation of the outer pipe (ζ_o) is also presented in Figure 6.21, with respect to the reeling cycles. Increasing the reel diameter, the outer pipe ovalisation increases significantly. More specifically, cross-sectional ovality at the end of the third cycle equals to 0.58%, 1.02% and 0.28% for Reeling Cases II, III and IV, while the maximum ovalisation value during the same cycle is 1.53%, 2.28% and 0.94%, respectively.

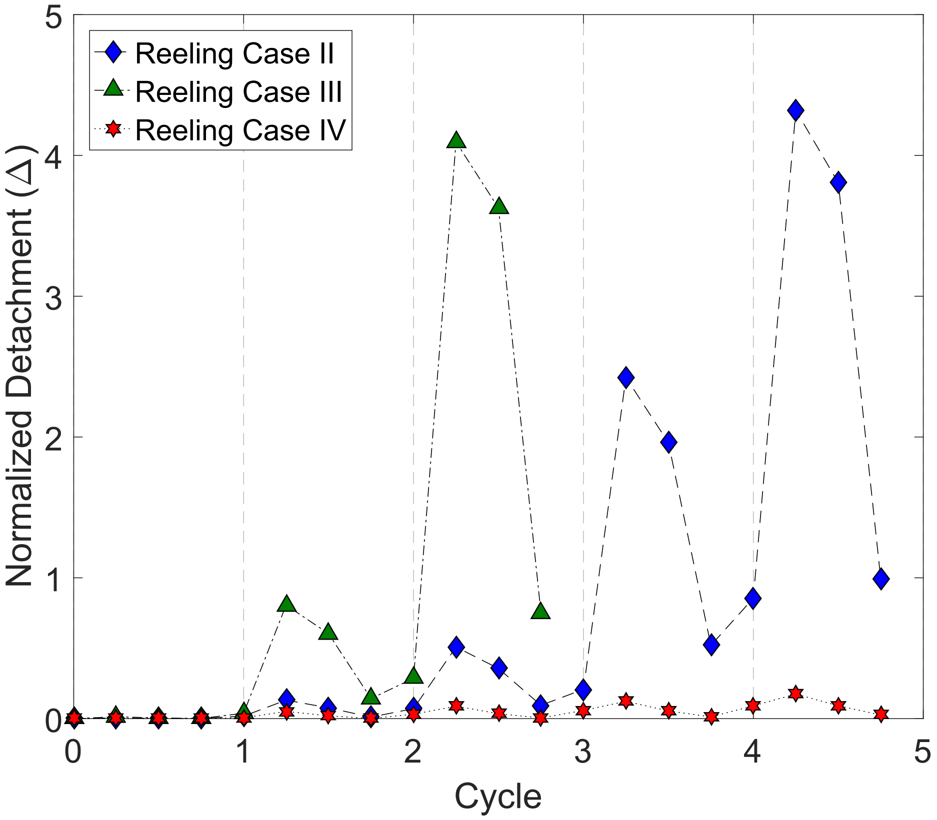

Figure 6.19 Normalised detachment of the liner pipe (Δ), with respect to the number of cycles, for Reeling Cases II, III and IV.

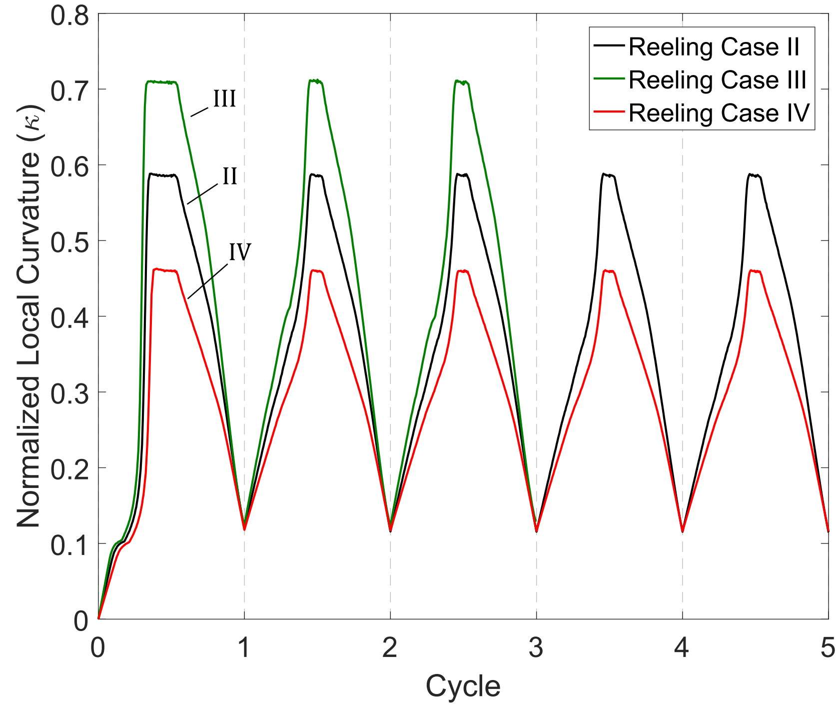

Figure 6.20 Local curvature (κ) of the lined pipe in SEG-B section, with respect to the number of cycles, for loading Reeling Cases II, III and IV.

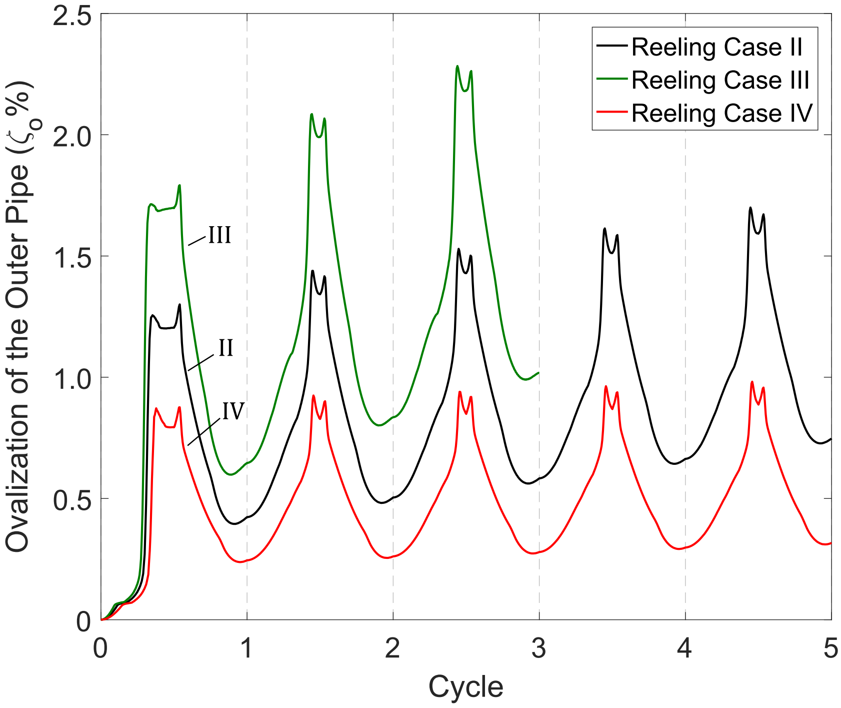

Figure 6.21 Ovalisation (ζ_o) of the outer pipe in SEG-B section, with respect to the number of cycles, for Reeling Cases II, III and IV.

6.4.3 Influence of back tension

In the previous sections, back tension is considered equal to 2% of the yield tension of the outer pipe ($T_p = \sigma_{y,o} \pi D_{m,o} t_o$, where $D_{m,o}$ is the mean diameter of the outer pipe), which is a typical value used in practice (Liu and Kyriakides, 2017; Manouchehri, 2012; Vasilikis, 2018). However, Manouchehri (2012) reported that in several cases, the back tension force is higher than the ratio of plastic moment of the pipe over the reel radius, to achieve efficient packing and avoid local buckling on the reel. In this section, different levels of back tension, varying from 1% to 10% of yield tension T_p, are applied examining its effect on liner detachment evolution, compared with the base case presented in section 6.4.1. In this parametric investigation, Reeling Case II is considered. Furthermore, it is assumed that the pipe is fabricated with the fully heated thermo-mechanical manufacturing process, presented in section 4.3.3 in detail, and it is free of geometric imperfections.

Figure 6.22 presents the variation of local curvature (κ) of the pipeline at segment SEG-B, with respect to the loading cycles, for back tension levels equal to 1%, 2%, 4%, 7% and 10% of the yield tension T_p of the outer pipe cross-section. The results show that the back tension level affects significantly the residual local curvature at the end of each cycle. The value of residual curvature, for back tension level equal to 1%, 2%, 4%, 7% and 10%, is 0.143, 0.120, 0.076, 0.040 and 0.004, respectively, while the maximum curvature observed in all the different levels of back tension is 0.587; this corresponds to the curvature value of the first $2\pi R_{reel}$ pipeline length, which is in contact with the reel. Once this pipeline length is wound, the pipe is bent under a larger radius of curvature ($R_{reel} + D_o$), decreasing the maximum curvature that the pipeline is bent at.

This observation is also shown in Figure 6.23, where the shape of the pipeline during spooling and unspooling is presented for 1% and 10% levels of tension. At the end of unspooling, the pipeline is straighter for the case of 10% T_p than the case of 1% T_p and the corresponding residual curvature value is very small. The results indicate that the increase of tension during spooling controls pipeline curvature as it engages with the reel, reducing the transition length of the pipe. This observation is shown in Figure 6.23, where in the case of 1% T_p the pipeline is arched upwards and the local curvature gradually increases as a pipe cross-section approaches the reel, until the cross-section is fully wound and the maximum curvature value is reached. On the other hand, in the case of 10% T_p the pipeline is straighter during spooling, indicating very small value of local curvature of a cross-section far from the reel. Approaching the reel, the curvature of a cross-section remains small, due to the high tensile force value; it increases to the maximum just before is wound onto the reel. A similar observation was reported by Liu and Kyriakides (2017) for single wall pipes.

Furthermore, the ovalisation of the outer pipe (ζ_o) for various values of back tension is presented in Figure 6.24, with respect to the reeling cycles. It is shown that increasing the back tension, pipeline ovalisation also increases, a result also mentioned in previous publications (Kyriakides, 2017; Liu *et al.*, 2017). The inelastic response of thick-walled pipes, under combined bending on a stiff curved surface and axial tension, has been investigated extensively by Dyau and Kyriakides (1992) and Kyriakides *et al.* (1994). The distributed transverse load on the reel is equal to the tension force times the bending curvature. The transverse force, due to contact with the stiff curved surface, increases the cross-sectional ovalisation of the bent pipe, compared with the response of a stand alone pipe under bending. Therefore, increasing the initial tensile force the cross-sectional ovalisation of the bent pipe also increases. Experimental and analytical results that verify this argument are presented in more detail by Kyriakides and Corona (2007).

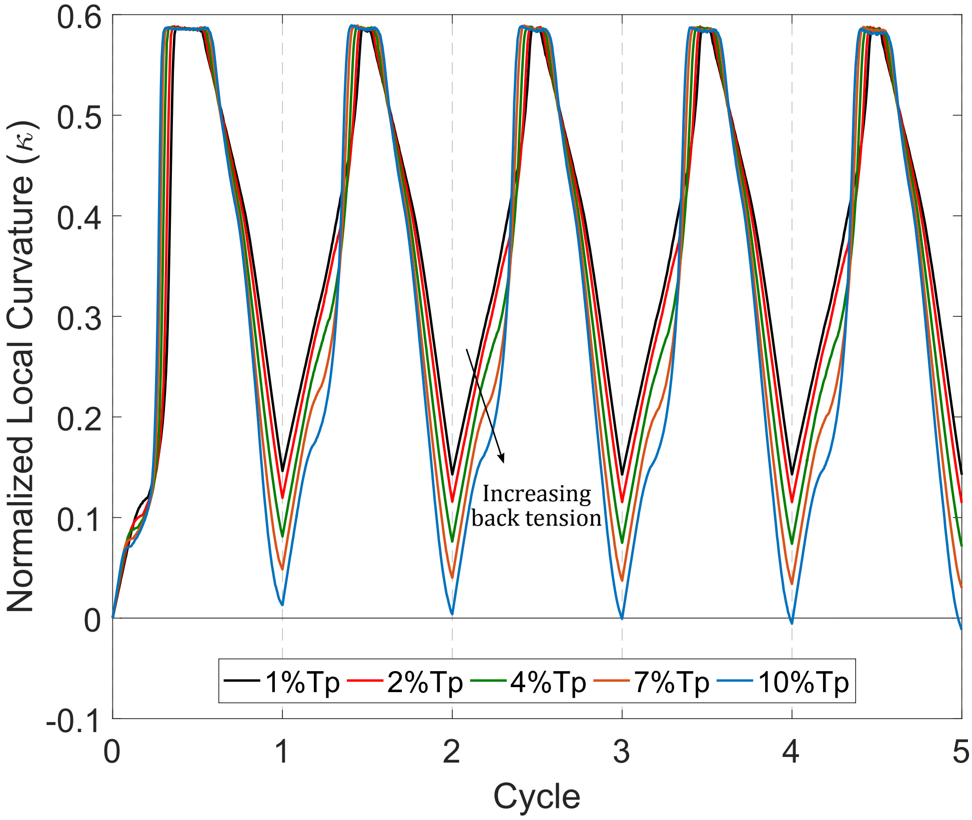

Figure 6.22 Local curvature (κ) of the lined pipe at the SEG-B section with respect to the number of cycles, for different values of back tension, and for Reeling Case II.

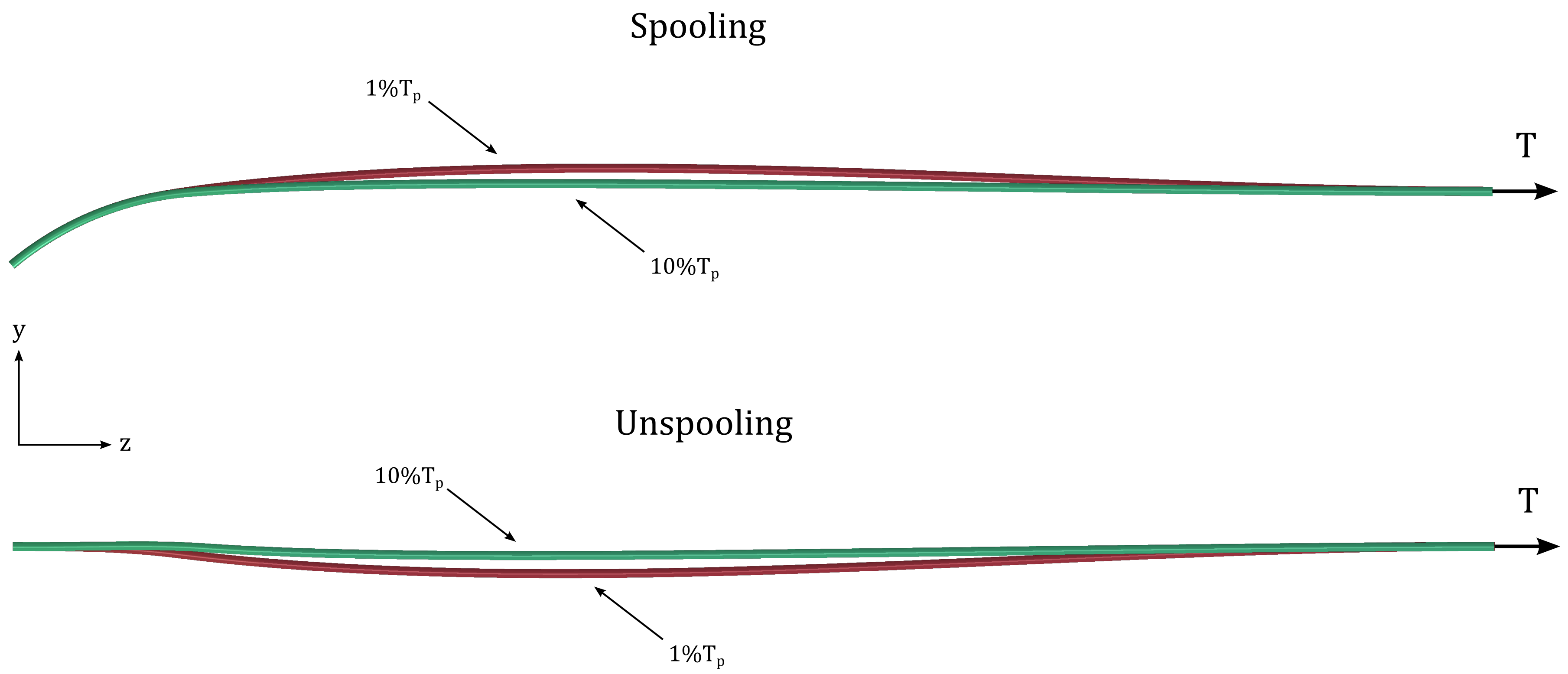

Figure 6.23 Configuration shapes of lined pipe segment for 1% and 10% levels of tension during spooling and unspooling of the first cycle (Reeling Cases II).

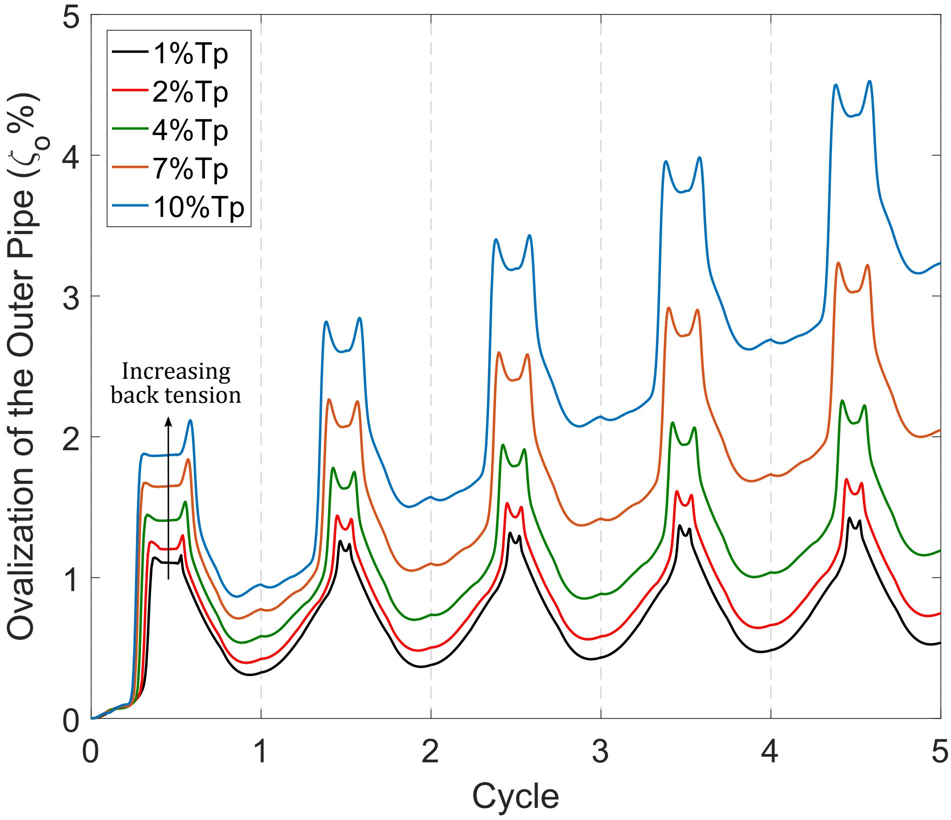

Figure 6.24 Ovalisation (ζ_o) of the outer pipe at the SEG-B section for different back tensions, with respect to the number of cycles, for Reeling Cases II.

At the end of the fifth cycle, cross-sectional ovality of the outer pipe in the middle of the SEG-B segment is 0.54%, 0.78%, 1.19%, 2.05% and 3.23% for back tension level equal to 1%T_p, 2%T_p, 4%T_p, 7%T_p and 10%T_p, respectively, while the corresponding maximum value equals to 1.43%, 1.70%, 2.26%, 3.24% and 4.53%; these values explain the significant influence of back tension on pipe ovalisation, while the cross-sectional ovality of the pipeline is strongly related to the external collapse pressure (Chatzopoulou *et al.*, 2016*a*; Kyriakides *et al.*, 1989; Liu *et al.*, 2017).

Finally, Figure 6.25 presents the detachment of the liner pipe from the outer pipe for 1%, 2% and 4% of yield tension T_p, over the loading cycles. The results show that increasing the back tension level, liner detachment also increases, and as a result, the liner pipe buckles locally at an earlier stage. During the fourth cycle spooling, and for the case of 2%T_p and 4%T_p back tension, the liner detachment is 95% and 114% higher than in the case of 1%T_p back tension. Increasing the back tension, the cross-sectional ovalisation of the outer pipe increases, which ovalises further the liner pipe, due to confinement, reducing its bending stiffness. Moreover, the applied curvature range also increases, justifying the higher liner detachment values. This observation is also shown in Figure 6.22, where the maximum curvature value corresponds to the pipeline segment which is in contact with the reel, while the minimum value of the curvature reduces as back tension increases, amplifying the curvature range applied on the pipe. On the other hand, increasing the back tension level further, a decrease on liner detachment is observed. Figure 6.26 shows the liner detachment for back tension levels equal to $4\%T_p$, $7\%T_p$ and $10\%T_p$, with respect to the loading cycles. During spooling on the fourth cycle, for $7\%T_p$ and $10\%T_p$ levels, the liner detachment is 24% and 173% lower than the one that occurs at the $2\%T_p$ level. Furthermore, increasing the applied back tension, the compression at 6 o'clock location decreases during spooling. More specifically, during spooling on the first cycle, the longitudinal strain of the liner pipe in the middle section of SEG-B (black cross in Figure 6.4) at 6 o'clock location, is equal to -1.34%, -1.26%, -1.17%, -1.06% and -0.96%, for 1%, 2%, 4%, 7% and 10% of tension level, respectively. For $1\%T_p$, $2\%T_p$ and $4\%T_p$ levels, the increasing curvature range is shown to affect the increasing liner detachment. On the other hand, considering the 4%, 7% and 10% levels, the rate of plastic strain accumulation in the liner pipe decreases with increasing back tension, delaying liner detachment and local buckling formation.

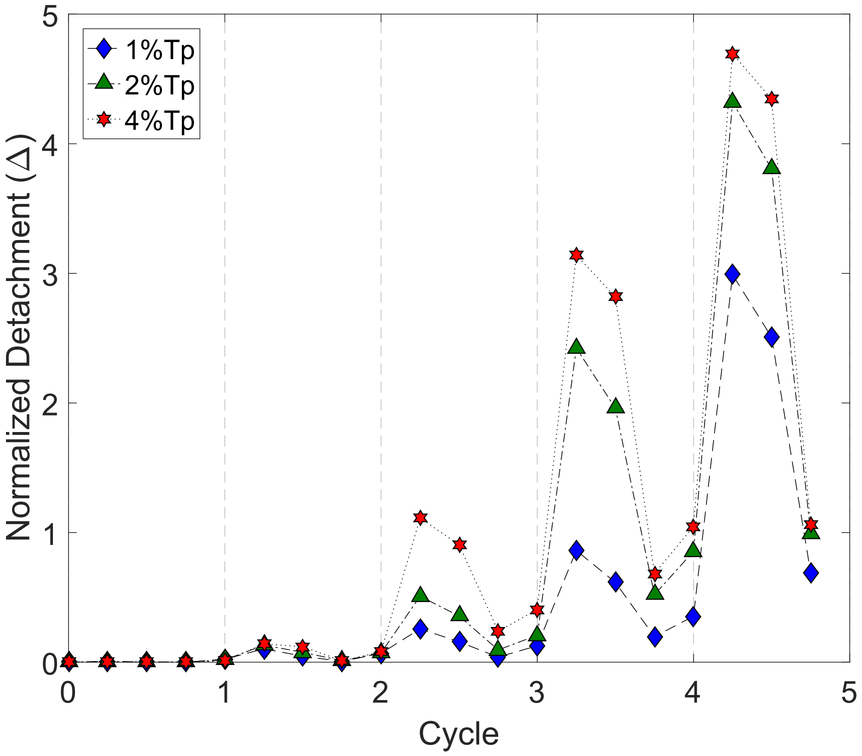

Figure 6.25 Normalised detachment of the liner pipe (Δ) with respect to the number of cycles, for back tension levels equal to 1%, 2% and 4% of yield force T_p, for Reeling Case II.

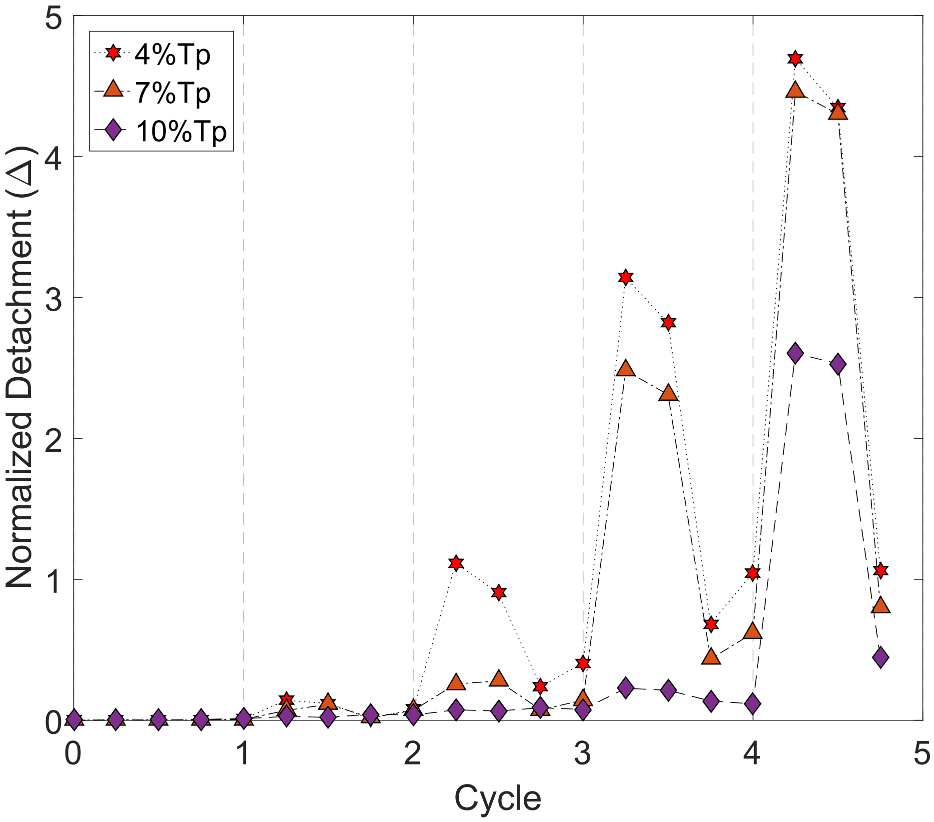

Figure 6.26 Normalised detachment of the liner pipe (Δ) with respect to the number of cycles, for back tension levels equal to 4%, 7% and 10% of yield force T_p, for loading Reeling Cases II.

6.4.4 Reeling of imperfect liner pipe

A sensitivity analysis is conducted on the reeling performance of lined pipes in the presence of initial geometric imperfections. Those imperfections refer to liner pipe only, while the outer pipe is considered geometrically perfect in its initial state. The shape configuration of the initial imperfection is a uniform wrinkling pattern, as shown in Figure 6.27, similar to the liner pipe wrinkles observed in the analysis, described in section 6.4.1. Initial wrinkles of small amplitude on the liner pipe are noticed in experimental test specimens (Focke, 2007). The initial wrinkles are assumed at 6 and 12 o'clock locations of the liner, where local buckling might occur under cyclic loading. The imperfection is considered in SEG-B section, with maximum value (Δ_0) equal to 10% of the liner pipe wall thickness (t_l), while the rest of liner sections are considered geometrically perfect. The loading scheme is the one followed in Reeling Case II, with back tension equal to 2% of yield tension T_p.

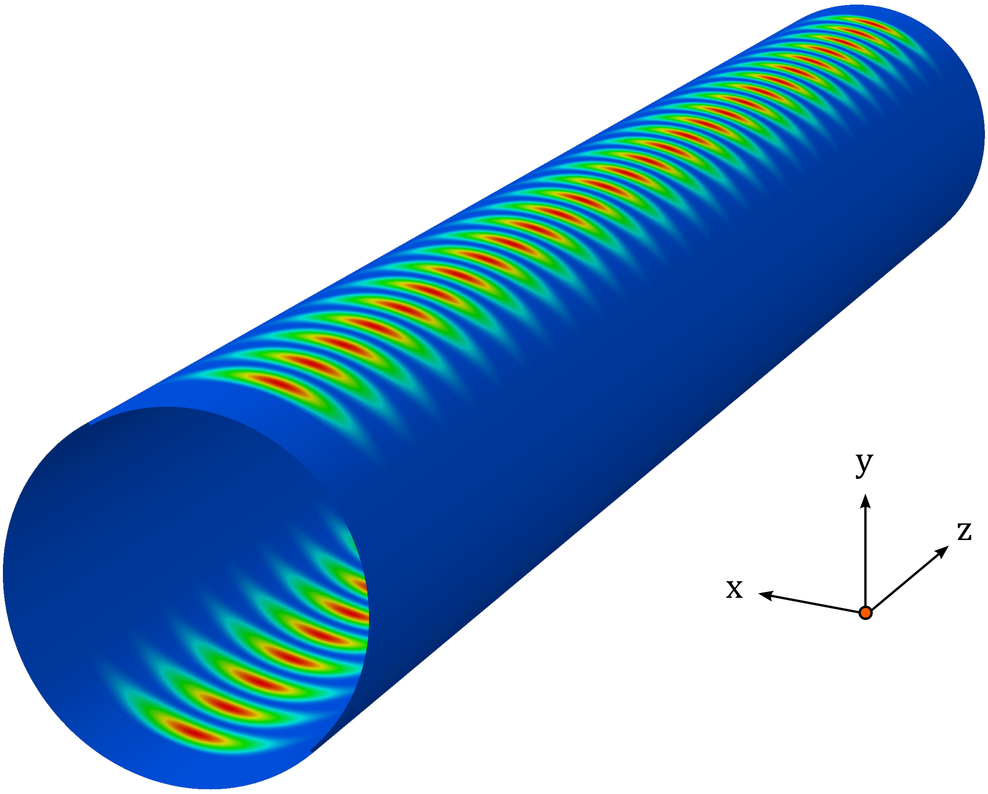

Figure 6.27 Initial configuration of liner pipe imperfection (SEG-B section).

Figure 6.28 presents the normalised bending moment of the liner pipe (m_l) for the perfect and imperfect liner, with respect to the loading cycles. In the absence of imperfections, the liner pipe exhibits uniform wrinkling during the first three cycles, and buckles locally at the fourth cycle, showing a slight moment drop. For imperfect liner, the bending moment of the liner slightly drops earlier, during the third cycle, indicating the formation of a local buckle. This observation is also verified in Figure 6.29, where the normalised detachment of the liner pipe, with respect to the loading cycles, is presented. An abrupt increase on liner detachment occurs in the third cycle, while the detachment of the imperfect liner, during spooling in the third, fourth and fifth cycle, is 82%, 28% and 9% higher than the detachment of the perfect liner pipe, respectively. More specifically, the imperfect liner buckles locally in an earlier stage, at the third cycle, while the geometrically perfect liner forms a low amplitude wrinkling presenting the highest detachment difference. During spooling of the fourth cycle, the already buckled imperfect liner presents a high detachment value, while the perfect liner start forming local buckling, reducing the detachment difference between both cases. During the final cycle, both liners buckle locally, showing negligible difference on the detachment values. One should notice that the initial imperfection amplitude of the liner pipe reduces significantly during the manufacturing process. Assuming a rough inner surface of the outer pipe, which may be the case in seamless pipes due to their fabrication process, the geometric imperfection can be affected on the liner pipe, resulting in local buckling at an earlier stage, during the first two cycles. This is a real case scenario that is recommended for further study in section 7.3.

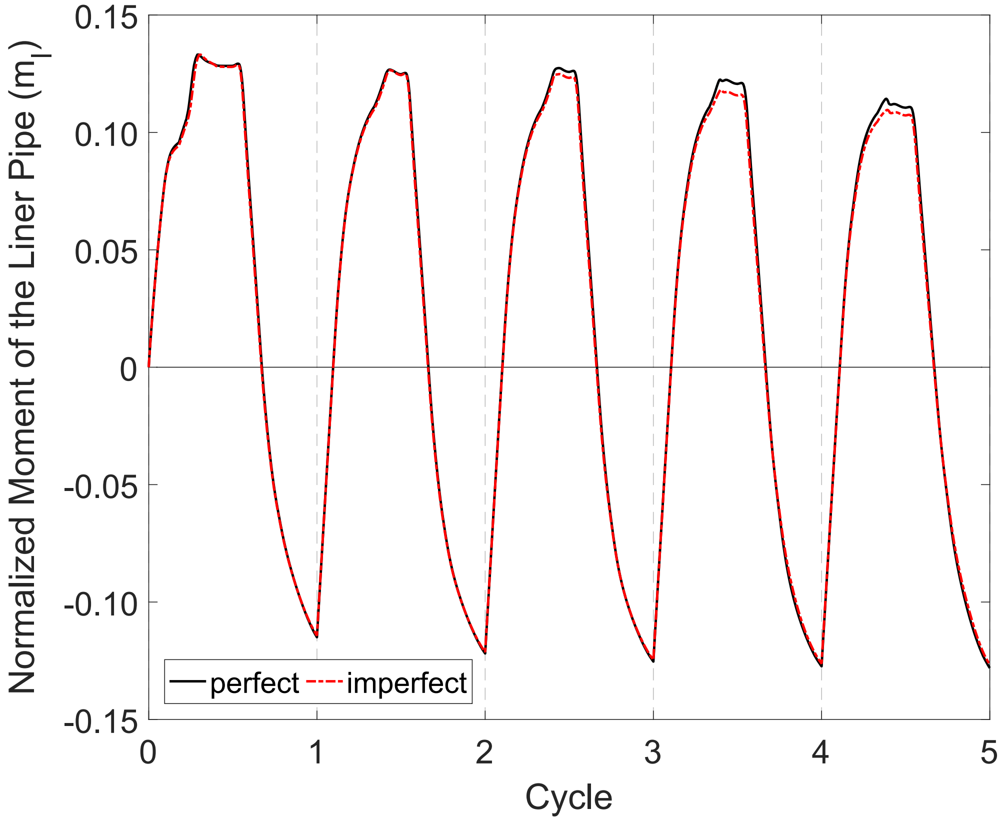

Figure 6.28 Normalised bending moment of the liner pipe (m_l) for perfect and imperfect liner, with respect to the number of cycles, for Reeling Case II.

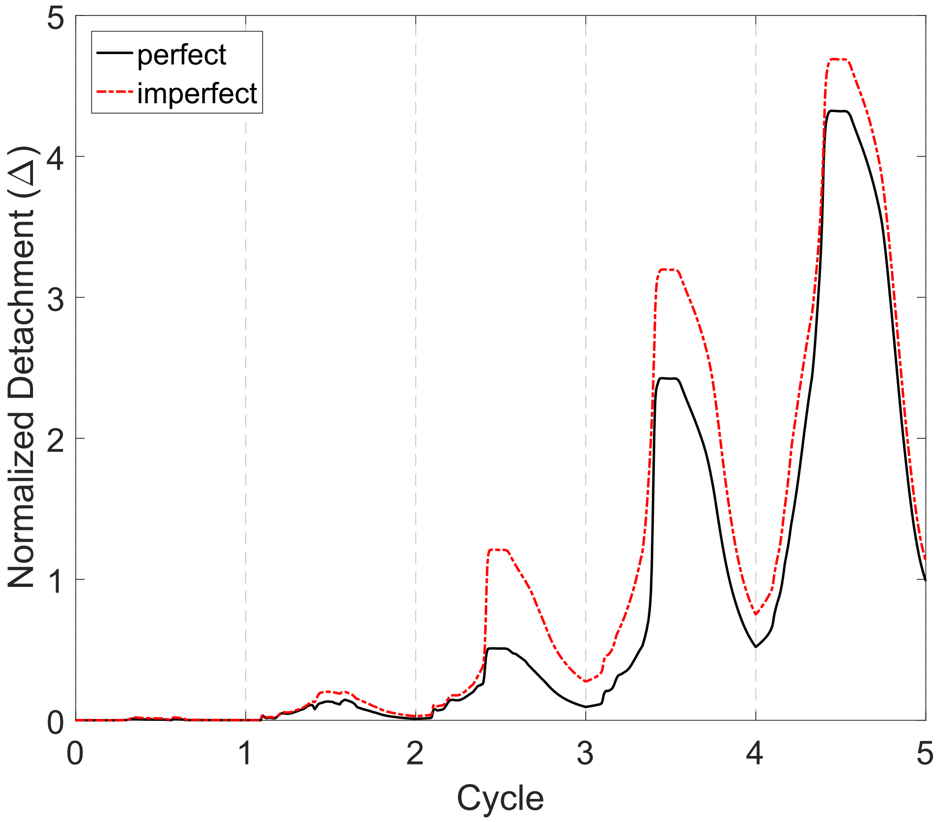

Figure 6.29 Liner detachment (Δ) at 6 o'clock location with respect to the number of cycles, for perfect and imperfect liner, for Reeling Case II.

6.4.5 Liner pipe wall thickness

Numerical analyses considering different values of wall thickness of the liner pipe have been conducted, to investigate its influence on liner pipe response during reeling. As shown in Chapter 5 (section 5.4.4), increasing liner pipe wall thickness, the detachment of the liner from the outer pipe is delayed, while local buckling of the liner pipe may be avoided in several cases. In addition to the base case (described in section 6.2.1), with liner wall thickness equal to 2.8 *mm* (denoted as $t_{l,A}$), three additional thickness values are also examined, considering liner pipes with increased wall thickness by 25% ($t_{l,B} = 3.5$ *mm*), 50% ($t_{l,C} = 4.2$ *mm*) and 100% ($t_{l,D} = 5.6$ *mm*). In the present analyses, all liner pipes are considered imperfection-free. Furthermore, the internal pressure applied during the manufacturing process is properly adjusted, in order to achieve similar mechanical bonding conditions at the end of the process (i.e. hoop compression equal to the same percentage of the yield stress of the liner; $\sigma_\theta / \sigma_{y,l}$). The loading path applied in the present study is the one followed in Reeling Case II, with back tension is equal to 2% of T_p.

Figure 6.30 presents the bending moment of the liner pipe (m_l) for each liner wall thickness value, with respect to the loading cycles. For consistency, the bending moment of each liner thickness case, presented in Figure 6.30, is normalised by $M_o = \sigma_{y,o} D_{m,o}^2 t_o$, where $D_{m,o}$ is the mean diameter of the outer pipe. The results show an increase of liner bending moment as the liner wall thickness increases, as expected due to the decrease of the liner diameter over thickness ratio. In addition, Figure 6.31 presents the evolution of liner detachment for each value of liner thickness case at 6 o'clock location, over the loading cycles, normalised by the wall thickness of the base case ($t_{l,A}$). As described in section 6.4.1, the lined pipe with liner wall thickness equal to $t_{l,A}$ exhibits uniform wrinkling during the first three cycles and develops a local buckle at the fourth cycle (Figures 6.7 and 6.15), and this is also represented by the moment drop on the corresponding cycle. However, increasing the liner pipe wall thickness local buckling is prevented. For wall thickness values equal to $t_{l,B}$ and $t_{l,C}$, the liner pipe at the end of the fifth cycle exhibits uniform wrinkling of significantly smaller amplitude than the corresponding amplitude of thickness $t_{l,A}$, as shown in Figure 6.32. The liner moment for $t_{l,B}$ and $t_{l,C}$ thickness is slightly reduced per cycle, due to wrinkling and the small amount of liner detachment. In the case of wall thickness equal to $t_{l,D}$, the liner pipe has a very good structural performance, with a negligible detachment from the outer pipe at the end of the fifth cycle (Figure 6.32).

Finally, during spooling on the fifth cycle, the liner detachment for thickness values equal to $t_{l,B}$, $t_{l,C}$ and $t_{l,D}$ is smaller by 152%, 186% and 192% respectively, than the detachment observed in the base case ($t_{l,A}$). In all the cases, local buckling of the liner is prevented. The main conclusion from the above results is that the use of liner pipe slightly thicker than the one of the base case, the lined pipe is capable of undergoing five winding-unwinding cycles with minor and negligible wrinkling.

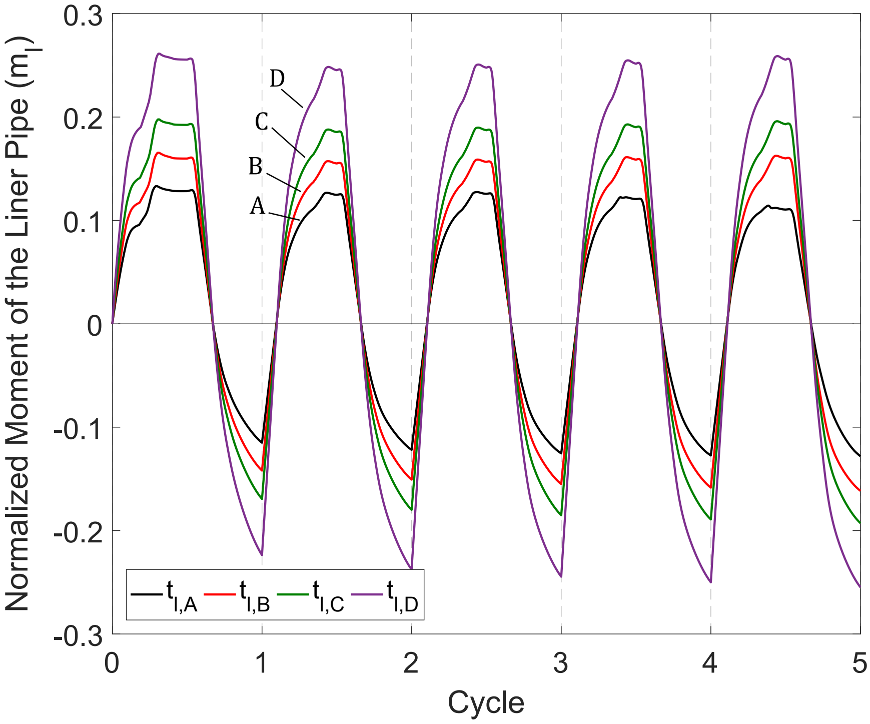

Figure 6.30 Normalised bending moment of the liner pipe (m_l) for different liner wall thickness values, with respect to the number of cycles, for Reeling Case II.

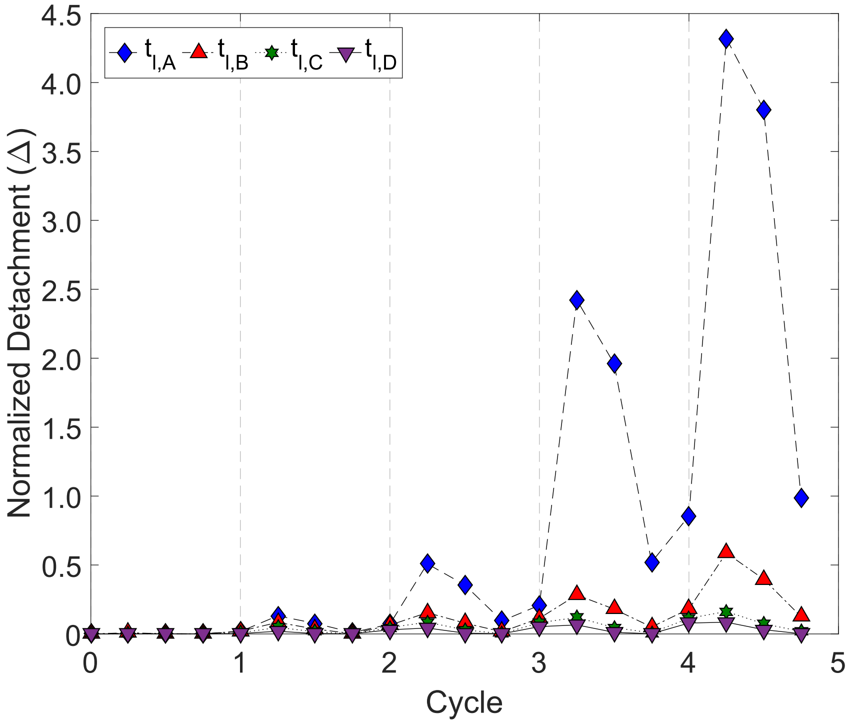

Figure 6.31 Liner normalised detachment (Δ) for different liner wall thickness values of liners, with respect to the number of cycles, for Reeling Case II.

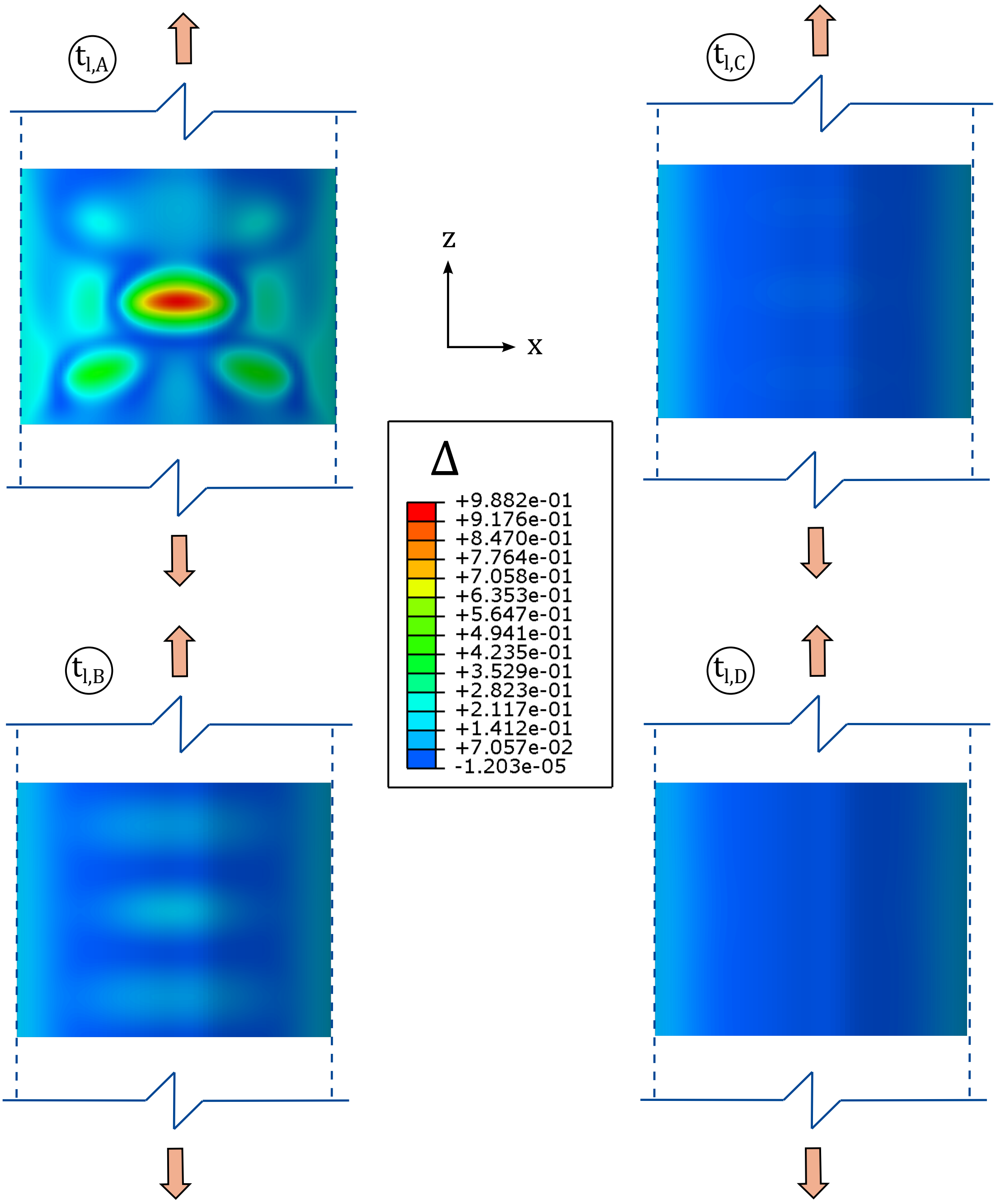

Figure 6.32 Sequence of liner pipe deformation and normalised detachment (Δ), presenting the buckling configuration at the end of fifth cycle at 6 o'clock location, for different liner wall thickness values, for loading Reeling Case II.

6.4.6 Reeling of internally pressurized lined pipe

Previous studies have demonstrated that internal pressure improves bending deformation capacity and may delay buckling of shells under bending (Houliara and Karamanos, 2006; Limam *et al.*, 2010; Mathon and Limam, 2006). In the case of double-walled pipes, the cyclic response of lined pipes under high levels of internal pressure has been examined in previous publications (Gouveia *et al.*, 2015; Sriskandarajah *et al.*, 2013*b*; Toguyeni and Banse, 2012), through full-scale experiments. Nevertheless, the beneficial effect of moderate levels of internal pressure on monotonic bending response of lined pipes was investigated extensively previously in sections 3.4.2 and 4.5.2. Subsequently, in Chapter 5 (section 5.4.5), the very good structural performance of lined pipes in the presence of moderate level of internal pressure, under cyclic loading, was presented.

The present section examines the effect of similar pressure level on the reeling response of lined pipe. The lined pipe is geometrically perfect, and has been fabricated using the fully heated thermo-mechanical manufacturing process. During cyclic loading (Reeling Case II) internal pressure 0.5 *MPa* is applied, which is equal to 10% of the plastic pressure of the liner pipe ($P_{y,l} = 2\sigma_{y,l}t_l/D_{m,l}$, where $D_{m,l}$ is the mean diameter of the liner pipe). During pressurization of the lined pipe, a tensile force (F_p) is also applied at the free end of the pipeline (as shown in Figure 6.1), equal to the product of the internal pressure and the internal cross-section of the liner ($F_p = P_{in}\pi(D_l - 2t_l)^2/4$) representing the force at the two capped ends due to the internal pressure. During reeling, the total force (due to pressurization and back tension) applied at the free end of the pipeline is equal to 2% of the yield tension of the outer pipe (T_p).

Figure 6.33 shows the normalised bending moment carried by the liner pipe (m_l), under pressurized and non-pressurized conditions, with respect to the loading cycles. In non-pressurized lined pipe, the liner detaches and uniform wrinkling develops during the first three cycles. Subsequently, local buckling occurs during the last two cycles (Figures 6.7 and 6.15) characterized by a moment drop, as shown in Figure 6.13, which is also explained in more detail in section 6.4.1. On the other hand, under a low level of internal pressure, the liner pipe does not detach from the outer pipe during the entire loading history (five loading cycles) and local buckling is prevented.

In an attempt to reduce the cost of the lined pipe, the combined effect of internal pressure and liner wall thickness on reeling response is examined, considering internal pressure equal to 0.5 *MPa* and a thinner liner pipe, with wall thickness value 15% smaller than the base case $t_{l,A}$ ($t_{l,E} = 2.38$ *mm*). Fully-heated thermo-mechanical manufacturing process is taken into account, adjusting the fabrication pressure in order to obtain an equivalent mechanical bonding in terms of the $\sigma_\theta/\sigma_{y,l}$ ratio at the end of the process. Following the simulation of the fabrication process, internal pressure (0.5 *MPa*) is applied, which is kept constant throughout the subsequent application of five reeling cycles. Bending loading follows the Reeling Case II pattern, under a $2\%T_p$ back tension. Figure 6.33 presents the normalised bending moment of each liner pipe. In the case of the thinner liner ($t_{l,E} = 2.38$), no liner pipe detachment is detected throughout the analysis, verifying the beneficial effect of moderate levels of internal pressure on liner detachment and local buckling formation.

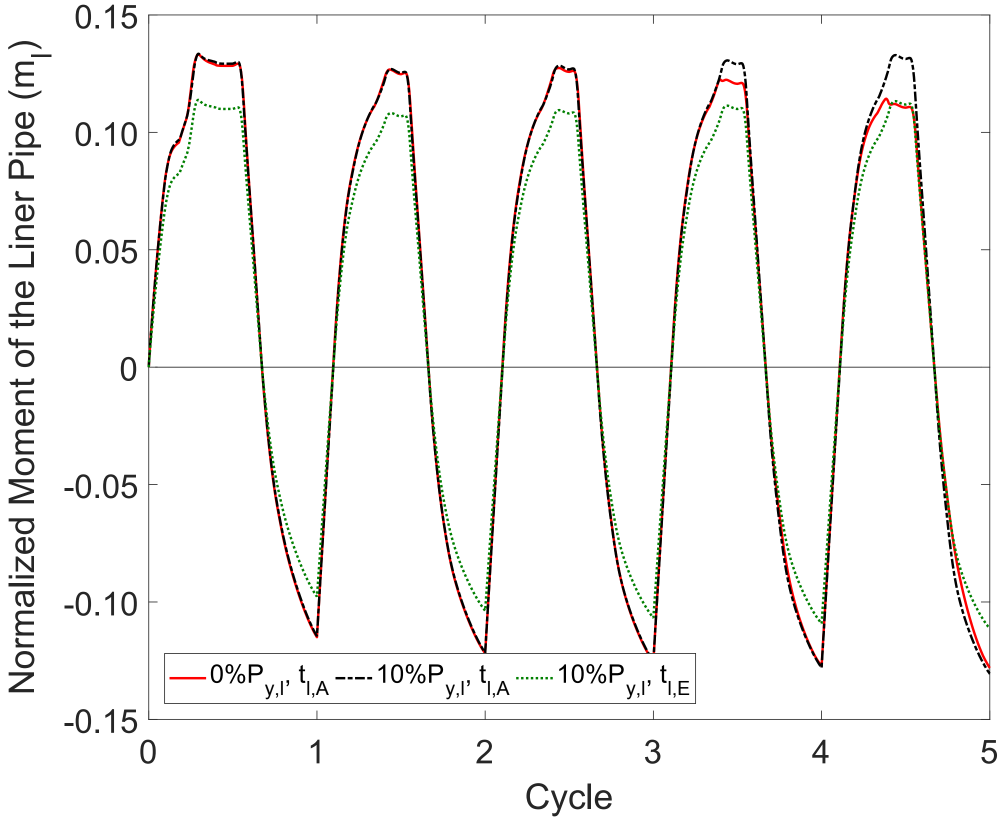

Figure 6.33 Normalised bending moment of the liner pipe (m_l) for different values of pressure and wall thickness, with respect to the number of cycles (Reeling Case II and pressure equal to 0.5 *MPa*).

6.5 Summary of results

In the present chapter, a large-scale numerical model is developed for investigating the structural response of mechanically bonded lined pipes during reeling installation process. In the first stage of the model, the fully heated thermo-mechanical manufacturing process of a lined pipe is simulated, while, in its second stage, a winding-unwinding cyclic loading is applied, under back tension, investigating its structural response. Five loading cycles are considered, representing offshore reeling installation that includes a failure-repair scenario.

The cyclic loading pattern is performed accounting for pipeline straightening at the end of the second and fifth cycle. Compared with reeling cyclic loading without straightening, it is found that liner buckling occurs at an early stage, immediately after the end of pipeline straightening and leads to significantly higher liner detachment at the 6 o'clock position, which is in contact with the reel. The influence of different reel diameters on liner response is also investigated, showing a significant effect on liner buckling. Considering a 10-meter reel radius ($\varepsilon_b = 1.59\%$), the liner pipe develops uniform wrinkling during the first three cycles and exhibits local buckling in the fourth cycle. Moreover, for a 12.79-meter reel radius ($\varepsilon_b = 1.25\%$), the liner pipe exhibits low amplitude wrinkling at the end of the fifth cycle avoiding local buckling, while in the case of a 8.23-meter radius ($\varepsilon_b = 1.93\%$), the liner pipe buckles at an early stage of loading on the third cycle. Different levels of back tension on liner buckling are examined, affecting the residual ovalization and local curvature of the pipeline. Applying tension up to 4% of outer pipe yield tension (T_p), the residual local curvature at the end of unwinding decreases, increasing the curvature range that the lined pipe is cyclically loaded, resulting in earlier detachment and local buckling of the liner pipe. On the other hand, further increase of back tension from 4% to 10% of T_p, the liner detachment rate decreases and liner buckling is delayed. The numerical results also show that increasing the back tension, the longitudinal compressive strain during spooling decreases, leading to lower rate of plastic strain accumulation in the liner pipe and delay of local buckling.

Moreover, imperfection sensitivity is examined, considering liners with initial geometric imperfection in the form of uniform wrinkling. The presence of initial imperfections results in higher liner detachment rate and earlier local buckling. Furthermore, several lined pipes are considered with increased liner pipe wall thickness, up to twice the thickness of the base case. In all those cases, no local buckling of the liner pipe occurs. For the thicker liner, very low amplitude uniform wrinkling at the 6 o'clock position is detected at the end of the entire loading history, which may be negligible for practical purposes. Finally, winding-unwinding of lined pipes, under relatively low level of internal pressure, is simulated, verifying the beneficial effect of internal pressure; no liner detachment or local buckles are detected at the end of the fifth cycle, even for liners with very small wall thickness.

Chapter 7

Summary, conclusions and recommendations

7.1 Summary of doctoral work

The main objective of the present doctoral work is the investigation of the mechanical behaviour of steel bi-metallic pipes, in terms of their structural response under different loading conditions. The present work has been motivated by practical engineering applications, in an attempt for better understanding and more accurate predictions of bifurcation and post-buckling response of steel double-walled pipes. The investigation is computational using advanced finite element tools, through the employment of a general-purpose finite element software. For the numerical analysis of each chapter, a proper numerical model is developed with non-linear finite elements accounting for geometric non-linearities and inelastic material behaviour. The numerical models of the present work are based on the findings and conclusions from previous publications. Nevertheless, further changes and developments are considered in the current research, towards improving the simulation capability of the numerical models and providing better understanding of the bi-metallic pipes buckling. Three main novel issues are examined in detail, which have not been considered in the existing literature:

- The main issue refers to cyclic loading of these bi-metallic pipes. This constitutes the main problem under reeling conditions and is tackled in a systematic form in Chapters 5 and 6.
- The second novel issue refers to the effect of manufacturing process on the structural response of bi-metallic pipes (Chapter 4).

- Finally, the in-depth investigation of internal pressure effects on structural response is an important novel aspect of the present study. It is described in detail in Chapter 3, as well as in special sections in every subsequent chapter.

Chapter 3 focuses on the structural response of lined pipes under monotonic bending. Two types of bi-metallic pipes are considered, “snug-fit” pipe (SFP) and “tight-fit” pipe (TFP), which account for the hoop compression of the liner pipe by the outer pipe due to manufacturing process. In the case of TF Pipes, the mechanical bonding between the outer and the liner pipe is simulated by an initial pre-stressing. Initially, the bending response of both types of lined pipes is simulated in the absence of internal pressure, verifying the numerical simulations reported in previous publications. In the following, the structural performance of lined pipes under low and moderate levels of internal pressure is examined. An ovalisation analysis is conducted on the examining the effect of different levels of internal pressure on cross-sectional ovality, while a three-dimensional analysis investigates the liner wrinkling and post-buckling behaviour of pressurized lined pipes, compared with non-pressurized ones. Furthermore, the effect of initial wrinkling of the liner pipe on buckling response is conducted for both types of pipes (non-pressurized and pressurized).

Chapter 4 presents a more rigorous finite element model, which incorporates the simulation of the manufacturing process of mechanically bonded lined pipes (at the first stage), while, at the second stage, the model proceeds to the analysis of monotonic bending response. Two types of lined pipe fabrication are analysed. The first is purely mechanical and consists of hydraulic expansion of both pipes up to elastic or plastic deformation in the outer pipe, while the second involves a thermo-hydraulic process (tight-fit pipe or TFP). The present analysis offers an integrated approach that employs a single finite element model, which includes simulation of both the manufacturing process and the structural bending response in subsequent stages. Special emphasis is given on the material model of the liner and the outer pipe. The materials of both pipes are described using advanced plasticity models obeying non-linear kinematic hardening, capable of accounting for reverse plastic loading effects, and are calibrated with available experimental data. Parametric analyses are also conducted, considering the effect of initial radial gap of both pipes, different heating temperatures during the thermo-hydraulic expansion, geometric imperfections and the presence of internal pressure during bending. The effect of different temperature levels, accounting for either temperature-dependent or temperature-independent material of the liner pipe, is also investigated during the thermo-hydraulic expansion.

The following chapter (Chapter 5) investigates the structural behaviour of lined pipes, subjected to cyclic loading conditions, representing loading conditions imposed by the reeling installation process. Those loading conditions are associated with maximum curvature values lower than the “critical” curvature determined by monotonic loading. The present model is unique and it uses a single numerical model that simulates the manufacturing process of a mechanically bonded lined pipe in its first stage and proceeds to its cyclic loading under five bending cycles, which represents a failure/repair scenario, in the second stage of the analysis. The model takes into account the entire plastic loading history of both pipes, including possible reverse plastic loading during the fabrication process. The results show that severe cyclic loading results in localized buckling of the liner pipe. Several analyses are conducted, considering different bending curvature ranges, as an attempt to quantify the influence of different reel and aligner radii. The effect of reverse bending during cyclic loading, the influence of geometric imperfections of the liner pipe, the effect of different values of liner wall thickness, the presence of low levels of internal pressure during cyclic bending, and the effect of different manufacturing parameters are also examined in detail in the present chapter.

Finally, in Chapter 6, the structural response of lined pipes under cyclic loading (spooling-unspooling and straightening) is investigated, representing more accurately the loading conditions during the reeling installation process with maximum curvature lower than the “critical” curvature that causes liner buckling under monotonic loading. A single numerical model is adopted that simulates the manufacturing process of a mechanically bonded lined pipe in its first stage and proceeds to its reeling performance in the second stage of the analysis, taking into account the entire plastic deformation in the liner pipe during the fabrication process, including possible reverse plastic loading. The analyses are aimed at simulating the mechanical performance of a mechanically bonded lined pipe subjected to five spooling-unspooling loading cycles, including a failure-repair scenario, and the effect of straightening. The results pinpoint the severe effect of cyclic loading on localized buckling of the liner pipe. Several analyses are conducted, considering different reel diameter values, which control the maximum imposed curvature. The effect of straightener during reeling loading, the structural response of the liner under different back tension values, the influence of geometric imperfections of the liner pipe, the effect of different values of liner wall thickness, and the presence of low levels of internal pressure during reeling are also investigated.

7.2 Novelty and key findings

This doctoral research investigated the structural response of lined pipes under monotonic and cyclic bending, using advanced finite element tools. The scope of this study was to simulate rigorously the structural performance of the liner pipe under different loading scenarios, and identify the influence of the principal geometric, material and loading parameters on liner buckling. The novelty of the present work refers to

- the systematic investigation of cyclic loading of bi-metallic pipes,
- the effect of manufacturing process on the structural response of mechanically bonded lined pipes, and the
- influence of relatively low levels of internal pressure on liner pipe buckling response.

The key findings of the research are summarised in the following.

- The results show a significant delay on liner detachment initiation from the outer pipe in the presence of relatively low levels of internal pressure, while the liner buckles locally in higher curvature values than the non-pressurized case.
- The pressure level considered in the present analyses is approximately six times lower than the one used in the industry. Therefore, the current industry practice should be readjusted, applying lower pressure levels during reeling, ensuring also the structural integrity of the liner pipe.
- In elastically expanded lined pipes, there is a residual radial gap at the end of the fabrication process. It is found that the residual gap value is smaller by one order of magnitude, compared with the initial radial gap value.
- In plastically expanded lined pipes, the liner pipe results in low hoop compression at the end of fabrication. The excessive plastic deformation in the liner pipe during manufacturing process, combined with low mechanical bonding between the two pipes, leads to a significant decrease of the buckling curvature of the liner pipe.
- The thermo-mechanical fabrication method results in higher mechanical bonding between the two pipes than the purely mechanical manufacturing process. This is attributed to higher recoverable hoop strain of the outer pipe at the end of manufacturing process. During depressurization and cooling, the outer pipe recovers the mechanical elastic strain and thermal strain, resulting in higher liner hoop compression, compared to the hydraulically expanded pipes. Therefore, the higher bonding between both pipes leads to higher buckling curvature values of the liner under bending because of biaxial compression.

- Different maximum temperature levels of the liner pipe during the thermo-mechanical manufacturing process, indicated an increase of the mechanical bonding between both pipes and the corresponding buckling curvature of the liner pipe, when the maximum temperature is reduced. Furthermore, the results show that considering temperature-independent material for both pipes leads to reasonable results.

- Applying negative (opposite sign) curvature values during cyclic bending, which represents the straightener during reeling, a significant influence on the liner detachment and local buckling is observed, compared with non-negative curvature values. This is observed in both models of Chapters 5 and 6.

- Considering slightly thicker liners than the ones proposed by DNV-OS-F101 (2013), and applying five bending cycles with global bending strain ε_b equal to 1.59% (reel diameter of 10 meters), which is a typical value in practical cases, local buckling of the liner pipe is avoided. This result is observed using both the pure bending model and the full-scale reeling model.

- The beneficial effect of moderate levels of internal pressure is also observed in case of cyclic bending. For internal pressure level equal to 5% of the plastic pressure of the liner pipe ($P_{y,l}$), a negligible liner detachment is observed for five bending cycles with global bending strain ε_b equal to 1.59%. Application of 10% of $P_{y,l}$ and considering thinner liners than the ones proposed by DNV-OS-F101 (2013), no detachment is observed, verifying the significant influence of relatively low internal pressure on liner buckling.

- Increasing back tension, the cross-sectional ovalisation of the outer pipe increases, which ovalises further the liner pipe, due to confinement, reducing its bending stiffness. This results in higher detachment values during reeling.

- Increasing further the back tension level, the compression at 6 o'clock location decreases during spooling. Therefore, the rate of plastic strain accumulation in the liner pipe decreases, delaying liner detachment and local buckling formation.

7.3 Recommendations for further study

This doctoral work has investigated in detail several aspects on the structural behaviour of pressurized and non-pressurized mechanically bonded pipes under monotonic and cyclic loading, representing reeling loading conditions. However, there is still room for further investigation, considering that several open issues exist within the topic of mechanical behaviour of lined (bi-metallic) pipes, worth of investigation.

The present model can be employed to develop design rules for bi-metallic pipelines, in terms of their structural behaviour and installation process. Therefore, it constitutes a very useful tool for code drafting committees related to pipeline engineering.

In the present work, local buckling of the liner pipe, which is considered as a performance criterion, is investigated in depth under monotonic and cyclic loading. However, the present work could be extended investigating fatigue phenomena at the welds, which are related due to severe plastic deformation during reeling installation, and constitute another important performance criterion. Plastic strain accumulation at the welds may lead to crack initiation, therefore fatigue and fracture analysis is an open issue and of high interest of investigation.

In addition, the present model constitutes a useful tool to simulate the complete loading history of lined pipes during manufacturing process and reeling, determining the exact state of stress and strain at the end of installation process. As a next step of the analysis, the present model could be used as a basis to investigate the structural response of HT/HP (high temperature; high pressure) pipelines. High temperature and pressure liquids may lead to lateral buckling of the pipeline on the seabed, therefore a more reliable analysis could be performed considering the exact state of stress and strain after reeling. Finally, the application of “Residual Curvature Method” in reeled pipes could be analysed, which is an effective method of controlling lateral buckling of HT/HP pipelines Zhang and Kyriakides (2021), considering proper adjustment of the present model.

References

Ades, C.S. (1957). Bending strength of tubing in the plastic range. *Journal of the aeronautical sciences*, **24**(8): pp. 605–610.

Alain, R., Violan, P., and Mendez, J. (1997). Low cycle fatigue behavior in vacuum of a 316L type austenitic stainless steel between 20 and 600 C Part I: fatigue resistance and cyclic behavior. *Materials Science and Engineering: A*, **229**(1-2): pp. 87–94.

API RP 1111 (1999). *Design,Construction,Operation and Maintenance of Offshore Hydrocarbon Pipelines (Limit State Design).*

Armstrong, P.J. and Frederick, C. (1966). A mathematical representation of the multiaxial bauschinger effect. *CEGB Report No. RD/B/N 731.*

Atlas Specialty Metals (18 February 2004). *Stainless Steel - Grade 316L - Properties, Fabrication and Applications (UNS S31603).* AZO MATERIALS, https://www.azom.com/article.aspx?ArticleID=2382.

Axelrad, E. (1961). Flexure of thin-walled beams under large elastic displacements. *Izvestiya Akademii Nauk SSSR, Otdelenie Tekhnicheskikh Nauk, Mekhanika i Mashinostroenie*, **3**: pp. 124–132.

Axelrad, E. (1962). Flexure and instability of thin-walled pressurized tubes. *Izvestiya Akademii Nauk SSSR, Otdelenie Tekhnicheskikh Nauk, Mekhanika i Mashinostroenie*, **1**: pp. 98–114.

Axelrad, E. (1965). Refinement of buckling-load analysis for tube flexure by way of considering precritical deformation. *Izvestiya Akademii Nauk SSSR, Otdelenie Tekhnicheskikh Nauk, Mekhanika i Mashinostroenie*, **4**: pp. 133–139.

Backhaus, G. (1968). Zur fließgrenze bei allgemeiner verfestigung. *Zeitschrift für Angewandte Mathematik und Mechanik*, **48**(2): pp. 99–108.

Bari, S. and Hassan, T. (2002). An advancement in cyclic plasticity modeling for multiaxial ratcheting simulation. *International Journal of Plasticity*, **18**(7): pp. 873–894.

Bauschinger, J. (1881). Ueber die Veraenderung der Elasticitaetgenze und des Elasticitaetmodulus Verschiedener Metalle. *Civilingeneur*, **27**: pp. 289–348.

Brazier, L. (1927). On the flexure of thin cylindrical shells and other "thin" sections. *Proceedings of the Royal society of London, Series A*, **116**(773): pp. 104–114.

Brown, G., Tkaczyk, T., and Howard, B. (2004). Reliability based assessment of minimum reelable wall thickness for reeling. In: *2004 International Pipeline Conference, Calgary, Alberta, Canada*, American Society of Mechanical Engineers Digital Collection, IPC2004-0733, pp. 1951–1960.

Brush, D. and Almroth, B. (1975). *Buckling of Bars, Plates, and Shells*. McGraw-Hill, New York.

BS 8010-2:2004 (2004). *Code of practice for pipelines: Part 2–subsea pipelines*. British Standards Institution, London, UK.

Callister, W.D. and Rethwisch, D.G. (2018). *Materials Science and Engineering: An Introduction*. 10th edition, Wiley, New York.

Campbell, B.R., Jewett, J.B., Gunnion, N.S., and Burton, C.C. (2006). K2 Flowlines and Risers: From Design to Precommissioning. In: *Offshore Technology Conference, Houston, Texas, USA*, Offshore Technology Conference, OTC-18304-MS.

Chaboche, J.L. (1986). Time-independent constitutive theories for cyclic plasticity. *International Journal of Plasticity*, **2**(2): pp. 149–188.

Chaboche, J.L. (2008). A review of some plasticity and viscoplasticity constitutive theories. *International Journal of Plasticity*, **24**(10): pp. 1642–1693.

Chaboche, J.L. and Nouailhas, D. (1989*a*). Constitutive Modeling of Ratchetting Effects—Part I: Experimental Facts and Properties of the Classical Models. *Journal of Engineering Materials and Technology*, **111**(4): pp. 384–392.

Chaboche, J.L. and Nouailhas, D. (1989*b*). Constitutive Modeling of Ratchetting Effects—Part II: Possibilities of Some Additional Kinematic Rules. *Journal of Engineering Materials and Technology*, **111**(4): pp. 409–416.

Chaboche, J.L. and Rousselier, G. (1983*a*). On the Plastic and Viscoplastic Constitutive Equations–Part I: Rules Developed With Internal Variable Concept. *Journal of Pressure Vessel Technology*, **105**(2): pp. 153–158.

Chaboche, J.L. and Rousselier, G. (1983*b*). On the Plastic and Viscoplastic Constitutive Equations–Part II: Application of Internal Variable Concepts to the 316 Stainless Steel. *Journal of Pressure Vessel Technology*, **105**(2): pp. 159–164.

Chaboche, J.L., Van, K.D., and Cordier, G. (1979). Modelization of the strain memory effect on the cyclic hardening of 316 stainless steel. *SMiRT 5 - Berlin, Germany*.

Chai, H.F. and Laird, C. (1987). Mechanisms of cyclic softening and cyclic creep in low carbon steel. *Materials Science and Engineering*, **93**: pp. 159–174.

Chakravarti, B. (2004). Method of manufacturing same for production of clad piping and tubing. US Patent 6,691,397.

Chang, K.H. and Pan, W.F. (2009). Buckling life estimation of circular tubes under cyclic bending. *International Journal of Solids and Structures*, **46**(2): pp. 254–270.

Chatzopoulou, G. (2014). *Finite element simulation of UOE pipe manufacturing process and its effect on offshore pipeline mechanical behavior*. Master's thesis, Department of Mechanical Engineering, University of Thessaly.

Chatzopoulou, G., Karamanos, S.A., and Varelis, G.E. (2016*a*). Finite element analysis of cyclically-loaded steel pipes during deep water reeling installation. *Ocean Engineering*, **124**: pp. 113–124.

Chatzopoulou, G., Karamanos, S.A., and Varelis, G.E. (2016*b*). Finite element analysis of UOE manufacturing process and its effect on mechanical behavior of offshore pipes. *International Journal of Solids and Structures*, **83**: pp. 13–27.

Chatzopoulou, G., Sarvanis, G.C., Karamanos, S.A., Mecozzi, E., and Hilgert, O. (2019). The effect of spiral cold-bending manufacturing process on pipeline mechanical behavior. *International Journal of Solids and Structures*, **166**: pp. 167–182.

Chen, W.C. and Petersen, C.W. (1991). Corrosion performance of welded CRA-lined pipes for flowlines. In: *Offshore Technology Conference, Houston, Texas, USA*, Offshore Technology Conference, OTC 6693.

Chen, W.F. and Han, D.J. (1988). *Plasticity for structural engineers*. Springer, Berlin.

Corona, E. and Kyriakides, S. (1988). On the collapse of inelastic tubes under combined bending and pressure. *International Journal of Solids and Structures*, **24**(5): pp. 505–535.

Corona, E. and Kyriakides, S. (1991). An experimental investigation of the degradation and buckling of circular tubes under cyclic bending and external pressure. *Thin-Walled Structures*, **12**(3): pp. 229–263.

Corona, E., Lee, L.H., and Kyriakides, S. (2006). Yield anisotropy effects on buckling of circular tubes under bending. *International Journal of Solids and Structures*, **43**(22-23): pp. 7099–7118.

Cottrell, A.H. and Bilby, B.A. (1949). Dislocation theory of yielding and strain ageing of iron. *Proceedings of the Physical Society. Section A*, **62**(1): p. 49.

Dafalias, Y.F. (1981). A novel bounding surface constitutive law for the monotonic and cyclic hardening response of metals. In: *6th International Conference on Structural Mechanics in Reactor Technology, Paris, France*.

Dama, E., Karamanos, S.A., and Gresnigt, A.M. (2007). Failure of locally buckled pipelines. *ASME, Journal of Pressure Vessel Technology*, **129**(2): pp. 272–279.

De Koning, A., Nakasugi, H., and Li, P. (2004). TFP and TFT back in town (Tight fit CRA lined pipe and tubing). *Stainless Steel World*: pp. 53–61.

de Souza Neto, E.A., Peric, D., and Owen, D.R.J. (2011). *Computational methods for plasticity: theory and applications*. John Wiley & Sons.

Dezhi, Z., Kuanhai, D., Taihe, S., Yuanhua, L., Hongjun, Z., Tianlei, L., and Yongxing, S. (2014). Theoretical and experimental study of bimetal-pipe hydroforming. *ASME, Journal of pressure vessel technology*, **136**(6): p. 061402.

DNV-OS-F101 (2013). *Submarine pipeline systems*. Det Norske Veritas.

Dyau, J.Y. and Kyriakides, S. (1992). On the response of elastic-plastic tubes under combined bending and tension. *Journal of Offshore Mechanics and Arctic Engineering*, **114**(1): pp. 50–62.

Elchalakani, M., Zhao, X.L., and Grzebieta, R. (2004). Cyclic bending tests to determine fully ductile section slenderness limits for cold-formed circular hollow sections. *Journal of Structural Engineering*, **130**(7): pp. 1001–1010.

EN-1993-1-2 (2005). *Eurocode 3: Design of steel structures - Part 1-2: General rules - Structural fire design.*

Endal, G., Levold, E., and Ilstad, H. (2012). Method for laying a pipeline having an inner corrosion proof cladding. US Patent 8,226,327.

Estefen, S. (1999). Collapse behaviour of intact and damaged deepwater pipelines and the influence of the reeling method of installation. *Journal of Constructional Steel Research*, **50**(2): pp. 99–114.

Fabian, O. (1977). Collapse of cylindrical, elastic tubes under combined bending, pressure and axial loads. *International Journal of Solids and Structures*, **13**(12): pp. 1257–1270.

Fajuyitan, O.K. and Sadowski, A.J. (2018). Imperfection sensitivity in cylindrical shells under uniform bending. *Advances in Structural Engineering*, **21**(16): pp. 2433–2453.

Focke, E., Gresnigt, A., and Meek, J. (2006). Small Scale Reeling Tests. In: *The Sixteenth International Offshore and Polar Engineering Conference, San Francisco, California, USA*, International Society of Offshore and Polar Engineers, ISOPE-I-06-009.

Focke, E.S. (2007). *Reeling of tight fit pipe*. Ph.D. thesis, Faculty of Civil Engineering, Delft University of Technology.

Focke, E.S., Gresnigt, A.M., Meek, J., and Nakasugi, H. (2004). The 2-dimensional modelling of the manufacturing process of tight fit pipe (TFP). In: *The Fourteenth International Offshore and Polar Engineering Conference*, International Society of Offshore and Polar Engineers.

Gellin, S. (1980). The plastic buckling of long cylindrical shells under pure bending. *International Journal of Solids and Structures*, **16**(5): pp. 397–407.

Gouveia, J., Sriskandarajah, T., Karunakaran, D., Manso, D., Chiodo, M., Zhou, D., Cao, L., Rao, V., Vargas, T., and Escudero, C. (2015). Steel Catenary Risers (SCRs): from Design to Installation of the First Reeled CRA Lined Pipes. Part I-Risers Design. In: *Offshore Technology Conference, Houston, Texas, USA*, Offshore Technology Conference, OTC-25839.

Gray, F., Howard, B., Pieton, A., and Gallart, R. (2009). The qualification and continued evolution of reeled steel catenary risers. In: *ASME 28th International Conference on Ocean, Offshore and Arctic Engineering, Honolulu, Hawaii, USA*, American Society of Mechanical Engineers Digital Collection, OMAE2009-79176, pp. 97–110.

Gross, N. (1953). Experiments on short-radius pipe-bends. *Proceedings of the Institution of Mechanical Engineers*, **167**(1b): pp. 465–479.

Gross, N. and Ford, H. (1953). The flexibility of short-radius pipe-bends. *Proceedings of the Institution of Mechanical Engineers*, **167**(1b): pp. 480–509.

Guo, T., Ozturk, F., Jarrar, F., and Sheikh-Ahmad, J.Y. (2017). Analysis of contact pressure of mechanically lined corrosion resistant alloy pipe by hydraulic expansion process. *ASME, Journal of Pressure Vessel Technology*, **139**(2): p. 021212.

Hall, E.O. (1970). *Yield point phenomena in metals and alloys*. Plenum Press, New York.

Hallai, J.F. and Kyriakides, S. (2011*a*). On the effect of Lüders bands on the bending of steel tubes. Part I: Experiments. *International Journal of Solids and Structures*, **48**(24): pp. 3275–3284.

Hallai, J.F. and Kyriakides, S. (2011*b*). On the effect of Lüders bands on the bending of steel tubes. Part II: Analysis. *International Journal of Solids and Structures*, **48**(24): pp. 3285–3298.

Harrison, B., Yuan, L., and Kyriakides, S. (2016). Measurement of lined pipe liner imperfections and the effect on wrinkling and collapse under bending. In: *ASME 35th International Conference on Ocean, Offshore and Arctic Engineering, Busan, South Korea*, American Society of Mechanical Engineers Digital Collection, OMAE2016-54539.

Hartmann, S. and Haupt, P. (1993). Stress computation and consistent tangent operator using non-linear kinematic hardening models. *International Journal for Numerical Methods in Engineering*, **36**(22): pp. 3801–3814.

Hassan, T. (1994). *Ratcheting in cyclic plasticity of metals: Experiments and modeling*. Ph.D. thesis, Department of Engineering Mechanics, The University of Texas at Austin.

Hassan, T., Corona, E., and Kyriakides, S. (1992). Ratcheting in cyclic plasticity, part II: Multiaxial behavior. *International Journal of Plasticity*, **8**(2): pp. 117–146.

Hassan, T. and Kyriakides, S. (1992). Ratcheting in cyclic plasticity, part I: Uniaxial behavior. *International Journal of Plasticity*, **8**(1): pp. 91–116.

Herynk, M.D., Kyriakides, S., Onoufriou, A., and Yun, H.D. (2007). Effects of the UOE/UOC pipe manufacturing processes on pipe collapse pressure. *International Journal of Mechanical Sciences*, **49**(5): pp. 533–553.

Hibbitt, H., Karlsson, B., and Sorensen, P. (2016). Abaqus analysis user's manual version 2016. *Dassault Systèmes Simulia Corp, Providence, RI.*

Hilberink, A. (2011). *Mechanical behaviour of lined pipe*. Ph.D. thesis, Faculty of Civil Engineering, Delft University of Technology.

Hilberink, A., Gresnigt, A., and Sluys, L. (2010*a*). A finite element method approach on liner wrinkling of snug fit lined pipe. In: *The Twentieth International Offshore and Polar Engineering Conference, Beijing, China*, International Society of Offshore and Polar Engineers.

Hilberink, A., Gresnigt, A., and Sluys, L. (2010*b*). Liner wrinkling of lined pipe under compression: a numerical and experimental investigation. In: *ASME 29th International Conference on Ocean, Offshore and Arctic Engineering, Shanghai, China*, American Society of Mechanical Engineers, OMAE2010-20285.

Hilberink, A., Gresnigt, A., and Sluys, L. (2011). Mechanical behaviour of lined pipe during bending: numerical and experimental results compared. In: *ASME 30th International Conference on Ocean, Offshore and Arctic Engineering, Rotterdam, The Netherlands*, American Society of Mechanical Engineers, OMAE2011-49434.

Hong, S.G., Yoon, S., and Lee, S.B. (2003). The effect of temperature on low-cycle fatigue behavior of prior cold worked 316L stainless steel. *International Journal of Fatigue*, **25**(9-11): pp. 1293–1300.

Houliara, S. and Karamanos, S. (2006). Buckling and post-buckling of long pressurized elastic thin-walled tubes under in-plane bending. *International Journal of Non-Linear Mechanics*, **41**(4): pp. 491–511.

Houliara, S. and Karamanos, S.A. (2010). Stability of long transversely-isotropic elastic cylindrical shells under bending. *International Journal of Solids and Structures*, **47**(1): pp. 10–24.

Howard, B. and Hoss, J.L. (2016). Method of spooling a bi-metallic pipe. US Patent App. 15/070,664.

Hu, F., Shi, G., and Shi, Y. (2016). Constitutive model for full-range elasto-plastic behavior of structural steels with yield plateau: Calibration and Validation. *Engineering Structures*, **118**: pp. 210–227.

Hu, F., Shi, G., and Shi, Y. (2018). Constitutive model for full-range elasto-plastic behavior of structural steels with yield plateau: Formulation and Implementation. *Engineering Structures*, **171**: pp. 1059–1070.

Ishlinskii, I.U. (1954). General theory of plasticity with linear strain hardening. *Ukr. Mat. Zh*, **6**: p. 314.

ISO 13623 (2000). *Petroleum and Natural Gas Industries Pipeline Transportation Systems*. International Standard.

Jiao, R. and Kyriakides, S. (2009). Ratcheting, wrinkling and collapse of tubes under axial cycling. *International Journal of Solids and Structures*, **46**(14-15): pp. 2856–2870.

Jiao, R. and Kyriakides, S. (2010). Wrinkling of tubes by axial cycling. *Journal of Applied Mechanics*, **77**(3).

Jiao, R. and Kyriakides, S. (2011*a*). Ratcheting and wrinkling of tubes due to axial cycling under internal pressure: Part I experiments. *International Journal of Solids and Structures*, **48**(20): pp. 2814–2826.

Jiao, R. and Kyriakides, S. (2011*b*). Ratcheting and wrinkling of tubes due to axial cycling under internal pressure: Part II analysis. *International Journal of Solids and Structures*, **48**(20): pp. 2827–2836.

Ju, G.T. and Kyriakides, S. (1991). Bifurcation buckling versus limit load instabilities of elastic-plastic tubes under bending and external pressure. *Journal of Offshore Mechanics and Arctic Engineering*, **113**(1): pp. 43–52.

Ju, G.T. and Kyriakides, S. (1992). Bifurcation and localization instabilities in cylindrical shells under bending–II. Predictions. *International Journal of Solids and Structures*, **29**(9): pp. 1143–1171.

Kane, R.D., Wilheim, S.M., Yoshida, T., Matsui, S., and Iwase, T. (1991). Analysis of bimetallic pipe for sour service. *SPE Production Engineering*, **6**(03): pp. 291–296.

Kang, G. and Gao, Q. (2005). Uniaxial ratcheting of SS316L stainless steel at high temperature: experiments and simulations. In: *Proceedings of 18th International Conference on Structural Mechanics in Reactor Technology, Beijing, China*.

Karamanos, S.A. (2002). Bending instabilities of elastic tubes. *International Journal of Solids and Structures*, **39**(8): pp. 2059–2085.

Karamanos, S.A. (2016). Mechanical behavior of steel pipe bends: an overview. *Journal of Pressure Vessel Technology*, **138**(4): p. 041203.

Karamanos, S.A. and Tassoulas, J.L. (1991). Stability of inelastic tubes under external pressure and bending. *Journal of Engineering Mechanics*, **117**(12): pp. 2845–2861.

Karamanos, S.A. and Tassoulas, J.L. (1996*a*). Tubular members. i: Stability analysis and preliminary results. *Journal of Engineering Mechanics*, **122**(1): pp. 64–71.

Karamanos, S.A. and Tassoulas, J.L. (1996*b*). Tubular members. II: Local buckling and experimental verification. *Journal of Engineering Mechanics*, **122**(1): pp. 72–78.

Karjadi, E., Boyd, H., Demmink, H., and Thibaux, P. (2015). Reeling Pipeline Material Characterization: Testing, Material Modeling and Offshore Measurement Validation. In: *ASME 34th International Conference on Ocean, Offshore and Arctic Engineering, St. John's, Newfoundland, Canada*, American Society of Mechanical Engineers, OMAE2015-41919.

Kavanagh, W.K., Harte, G., Farnsworth, K.R., Griffin, P.G., Hsu, T.M., Jefferies, A., and Desalos, A.P. (2004). Matterhorn steel catenary risers: critical issues and lessons learned for reel-layed SCRs to a TLP. In: *Offshore Technology Conference, Houston, Texas, USA*, Offshore Technology Conference, OTC-16612-MS.

Khan, A.S. and Huang, S. (1995). *Continuum theory of plasticity*. John Wiley & Sons.

Kopp, F., Light, B.D., Preli, T.A., Rao, V.S., and Stingl, K.H. (2004). Design and installation of the Na Kika export pipelines, flowlines and risers. In: *Offshore Technology Conference, Houston, Texas, USA*, Offshore Technology Conference, OTC-16703-MS.

Kyriakides, S. (2017). Effects of Reeling on Pipe Structural Performance—Part I: Experiments. *Journal of Offshore Mechanics and Arctic Engineering*, **139**(5): p. 051706.

Kyriakides, S. (2018). Personal communication.

Kyriakides, S. and Corona, E. (2007). *Mechanics of offshore pipelines: volume 1 buckling and collapse*, volume 1. Elsevier.

Kyriakides, S., Corona, E., Madhavan, R., and Babcock, C.D. (1989). Pipe collapse under combined pressure, bending, and tension loads. In: *Offshore Technology Conference, Houston, Texas, USA*, Offshore Technology Conference, OTC-6104-MS.

Kyriakides, S., Dyau, J.Y., and Corona, E. (1994). Pipe collapse under bending, tension and external pressure (BEPTICO). Computer Program Manual. *University of Texas, Engineering Mechanics Research Laboratory Report No. 94/4*.

Kyriakides, S. and Ju, G.T. (1992). Bifurcation and localization instabilities in cylindrical shells under bending–I. Experiments. *International Journal of Solids and Structures*, **29**(9): pp. 1117–1142.

Kyriakides, S. and Shaw, P.K. (1982). Response and stability of elastoplastic circular pipes under combined bending and external pressure. *International Journal of Solids and Structures*, **18**(11): pp. 957–973.

Landgraf, R.W. (1970). The resistance of metals to cyclic deformation. *ASTM STP*, **467**: pp. 3–36.

Lebey, J. and Roche, R. (1979). Tests on mechanical behaviour of 304 L stainless steel under constant stress associated with cyclic strain. *Fatigue & Fracture of Engineering Materials & Structures*, **1**(3): pp. 307–318.

Lecomte, H., Hogben, S., Smith, J., Bednar, J., Day, J., and Palmer, M. (2002). BP Marlin: first flexible pipelay with newbuild deepwater pipelay vessel. In: *Offshore Technology Conference, Houston, Texas, USA*, Offshore Technology Conference, OTC-14185-MS.

Lee, M.G., Kim, D., Kim, C., Wenner, M.L., Wagoner, R.H., and Chung, K. (2007). A practical two-surface plasticity model and its application to spring-back prediction. *International Journal of Plasticity*, **23**(7): pp. 1189–1212.

Lehmann, T. (1972). Einige bemerkungen zu einer allgemeinen klasse von stoffgesetzen für große elasto-plastische formänderungen. *Ingenieur-Archiv*, **41**(4): pp. 297–310.

Lemaitre, J. and Chaboche, J.L. (1994). *Mechanics of solid materials*. Cambridge University Press, Cambridge, UK.

Limam, A., Lee, L.H., Corona, E., and Kyriakides, S. (2010). Inelastic wrinkling and collapse of tubes under combined bending and internal pressure. *International Journal of Mechanical Sciences*, **52**(5): pp. 637–647.

Liu, F., Zheng, J., Xu, P., Xu, M., and Zhu, G. (2004). Forming mechanism of double-layered tubes by internal hydraulic expansion. *International Journal of Pressure Vessels and Piping*, **81**(7): pp. 625–633.

Liu, Y. and Kyriakides, S. (2016). Effect of Reeling on Pipeline Structural Performance. In: *ASME 35th International Conference on Ocean, Offshore and Arctic Engineering, Busan, South Korea*, American Society of Mechanical Engineers Digital Collection, OMAE2016-54866.

Liu, Y. and Kyriakides, S. (2017). Effect of geometric and material discontinuities on the reeling of pipelines. *Applied Ocean Research*, **65**: pp. 238–250.

Liu, Y., Kyriakides, S., and Dyau, J.Y. (2017). Effects of Reeling on Pipe Structural Performance—Part II: Analysis. *Journal of Offshore Mechanics and Arctic Engineering*, **139**(5): p. 051707.

Liu, Y., Kyriakides, S., and Hallai, J.F. (2015). Reeling of pipe with Lüders bands. *International Journal of Solids and Structures*, **72**: pp. 11–25.

Lubliner, J. (2008). *Plasticity theory*. Dover Publications, New York.

Mahin, S.A., Popov, E.P., and Zayas, V.A. (1980). Seismic behavior of tubular steel offshore platforms. In: *Offshore Technology Conference, Houston, Texas, USA*, Offshore Technology Conference, OTC-3821-MS.

Mair, J. (2012). Reelable mechanically lined pipe suited for ultra-deepwater sour service: Qualifications widened to higher pressures, larger diameters. *Offshore (Conroe, Tex.)*, **72**(9).

Mair, J., Schuller, T., Holler, G., Henneicke, F., and Banse, J. (2013). Reeling and unreeling and internally clad pipeline. *US Patent Application Publication, US*, **34390**: p. A1.

Manouchehri, S. (2012). A discussion of practical aspects of reeled flowline installation. In: *ASME 31st International Conference on Ocean, Offshore and Arctic Engineering, Rio de Janeiro, Brazil*, American Society of Mechanical Engineers, OMAE2012-83649, pp. 531–542.

Manouchehri, S., Howard, B., and Denniel, S. (2008). A discussion of the effect of the reeled installation process on pipeline limit states. In: *The Eighteenth International Offshore and Polar Engineering Conference, Vancouver, Canada*, International Society of Offshore and Polar Engineers, ISOPE-I-08-395.

Marines-Garcia, I., Aldana-Díaz, J.A., Darcis, P.P., and Quintanilla, H.M. (2016). Seamless Linepipe Response Under Small and Full Scale Reeling Simulation. In: *ASME 35th International Conference on Ocean, Offshore and Arctic Engineering, Busan, South Korea*, American Society of Mechanical Engineers Digital Collection, OMAE2016-54031.

Martinez, M. and Brown, G. (2005). Evolution of pipe properties during reel-lay process: experimental characterisation and finite element modelling. In: *ASME 24th International Conference on Offshore Mechanics and Arctic Engineering, Halkidiki, Greece*, American Society of Mechanical Engineers Digital Collection, OMAE2005-67074, pp. 419–429.

Mathon, C. and Limam, A. (2006). Experimental collapse of thin cylindrical shells submitted to internal pressure and pure bending. *Thin-Walled Structures*, **44**(1): pp. 39–50.

Meiwes, K.C., Erdelen-Peppler, M., and Brauer, H. (2014*a*). Impact of Small-Scale reeling Simulation on Mechanical Properties on Line Pipe Steel. In: *The 10th International Pipeline Conference, Calgary, Alberta, Canada*, American Society of Mechanical Engineers Digital Collection, IPC2014-33161.

Meiwes, K.C., Höhler, S., Erdelen-Peppler, M., and Brauer, H. (2014*b*). Full-Scale Reeling Tests of HFI Welded Line Pipe for Offshore Reel-Laying Installation. In: *The 10th International Pipeline Conference, Calgary, Alberta, Canada*, American Society of Mechanical Engineers Digital Collection, IPC2014-33163.

Melan, E. (1938). Zur plastizität des räumlichen kontinuums. *Ingenieur-Archiv*, **9**(2): pp. 116–126.

Menier, P. (2003). Devils Tower Export Lines: 160 Miles of 18 OD Reeled Rigid Pipe. In: *Offshore Technology Conference, Houston, Texas, USA*, Offshore Technology Conference, OTC-15338-MS.

Montague, P., Walker, A., and Wilmot, D. (2010). Test on cra lined pipe for use in high temperature flowlines. In: *Offshore Pipeline Technology Conference, Amsterdam, Netherlands*.

Morrow, J. (1965). Cyclic plastic strain energy and fatigue of metals. *ASTM STP*, **378**: pp. 45–87.

Murphey, C. and Langner, C. (1985). Ultimate pipe strength under bending, collapse and fatigue. In: *Proceedings of the 4th International Conference on Offshore Mechanics and Arctic Engineering*, volume 1, pp. 467–477.

Naderi, G., Torshizi, S.E.M., and Dibajian, S.H. (2021). Experimental-numerical study of residual stress in tight fit pipe. *International Journal of Pressure Vessels and Piping*, **190**: p. 104286.

Nagata, Y. and Tsuru, E. (2016). Geometry and Collapse Pressure of HF-ERW Line Pipe Reel-laid in Deepwater. In: *The 26th International Ocean and Polar Engineering Conference, Rhodes, Greece*, International Society of Offshore and Polar Engineers, ISOPE-I-16-668.

Netto, T. and Estefen, S. (1994). Ultimate strength behaviour of submarine pipelines under external pressure and bending. *Journal of Constructional Steel Research*, **28**(2): pp. 137–151.

Netto, T.A., Botto, A., and Lourenço, M. (2008*a*). Fatigue performance of pre-strained pipes with girth weld defects: Local deformation mechanisms under bending. *International Journal of Fatigue*, **30**(6): pp. 1080–1091.

Netto, T.A., Lourenco, M., and Botto, A. (2008*b*). Fatigue performance of pre-strained pipes with girth weld defects: Full-scale experiments and analyses. *International Journal of Fatigue*, **30**(5): pp. 767–778.

Ohno, N. and Wang, J.D. (1993*a*). Kinematic hardening rules with critical state of dynamic recovery, part I: formulation and basic features for ratchetting behavior. *International Journal of Plasticity*, **9**(3): pp. 375–390.

Ohno, N. and Wang, J.D. (1993*b*). Kinematic hardening rules with critical state of dynamic recovery, part II: Application to experiments of ratchetting behavior. *International Journal of Plasticity*, **9**(3): pp. 391–403.

Osborn, D. and Worringer, J. (1999). Clad tubular product and method of manufacturing same. US Patent 5,988,484.

Pan, W.F., Wang, T.R., and Hsu, C.M. (1998). A curvature-ovalization measurement apparatus for circular tubes under cyclic bending. *Experimental Mechanics*, **38**(2): pp. 99–102.

Papadaki, C.I., Chatzopoulou, G., Sarvanis, G.C., and Karamanos, S.A. (2018). Buckling of internally-pressurized spiral-welded steel pipes under bending. *International Journal of Pressure Vessels and Piping*, **165**: pp. 270–285.

Pardue, T. and Vigness, I. (1951). Properties of thin-walled curved tubes of short-bend radius. *Transactions of the ASME*, **73**: pp. 77–87.

Pasqualino, I.P. and Neves, H.G. (2010). Collapse Pressure of Reeled Rigid Pipes. *Mecánica Computacional*, **29**(80): pp. 7913–7925.

Pasqualino, I.P., Silva, S.L., and Estefen, S.F. (2004). The effect of the reeling laying method on the collapse pressure of steel pipes for deepwater. In: *ASME 23rd International Conference on Offshore Mechanics and Arctic Engineering, Vancouver, British Columbia, Canada*, American Society of Mechanical Engineers Digital Collection, OMAE2004-51513, pp. 247–254.

Peckner, D. and Bernstein, I.M. (1977). *Handbook of stainless steels*. McGraw-Hill, New York.

Pépin, A., Tkaczyk, T., O'Dowd, N., and Nikbin, K. (2017). Low cycle fatigue of subsea mechanically lined pipeline with liner imperfections. In: *ASME 36th International Conference on Ocean, Offshore and Arctic Engineering, Trondheim, Norway*, American Society of Mechanical Engineers Digital Collection, OMAE2017-62487.

Pilo, D., Reik, W., Mayr, P., and Macherauch, E. (1979). Cyclic induced creep of a plain carbon steel at room temperature. *Fatigue & Fracture of Engineering Materials & Structures*, **1**(3): pp. 287–295.

Prager, W. (1955). The theory of plasticity: a survey of recent achievements. *Proceedings of the Institution of Mechanical Engineers*, **169**(1): pp. 41–57.

Prager, W. (1956). A new methods of analyzing stresses and strains in work hardening plastic solids. *Journal of Applied Mechanics*, **23**: pp. 493–496.

Ramberg, W. and Osgood, W.R. (1943). Description of stress-strain curves by three parameters. *Technical Note No. 902, National Advisory Committee For Aeronautics, Washington DC.*

Ravikiran, A., Dubey, P.N., Agrawal, M.K., Reddy, G.R., Singh, R.K., and Vaze, K.K. (2015). Experimental and numerical studies of ratcheting in a pressurized piping system under seismic load. *Journal of Pressure Vessel Technology*, **137**(3).

Reissner, E. (1959). On finite bending of pressurized tubes. *Journal of Applied Mechanics*, **26**(3): pp. 386–392.

Reissner, E. (1961). On finite pure bending of cylindrical tubes. *Oesteer. Ingenieur Archives*, **15**: pp. 165–172.

Rotter, J.M., Sadowski, A.J., and Chen, L. (2014). Nonlinear stability of thin elastic cylinders of different length under global bending. *International Journal of Solids and Structures*, **51**(15-16): pp. 2826–2839.

Runesson, K. and Mroz, Z. (1989). A note on nonassociated plastic flow rules. *International Journal of Plasticity*, **5**(6): pp. 639–658.

Sadowski, A.J. and Rotter, J.M. (2013). Solid or shell finite elements to model thick cylindrical tubes and shells under global bending. *International Journal of Mechanical Sciences*, **74**: pp. 143–153.

Sadowski, A.J., Rotter, J.M., Reinke, T., and Ummenhofer, T. (2015). Statistical analysis of the material properties of selected structural carbon steels. *Structural Safety*, **53**: pp. 26–35.

Sadowski, A.J., Rotter, J.M., Stafford, P.J., Reinke, T., and Ummenhofer, T. (2017). On the gradient of the yield plateau in structural carbon steels. *Journal of Constructional Steel Research*, **130**: pp. 120–130.

Sadowski, A.J., Wong, W.J., Li, S.C.S., Málaga-Chuquitaype, C., and Pachakis, D. (2020). Critical buckling strains in thick cold-formed circular-hollow sections under cyclic loading. *Journal of Structural Engineering*, **146**(9): p. 04020179.

Satoh, A., Okamoto, H., Fukui, K., Uchida, J.i., Ogawa, K., Taka, T., Furugen, M., and Kimoto, M. (1996). Process for manufacturing clad pipe. US Patent 5,584,428.

Schulz, W., Worringer, J., and Osborn, D. (1999). Process for the manufacture of cladded metal pipes. US Patent 5,940,951.

Seide, P. and Weingarten, V.I. (1961). On the buckling of circular cylindrical shells under pure bending. *Journal of Applied Mechanics*, **28**: pp. 112–116.

Shaw, P. and Kyriakides, S. (1985). Inelastic analysis of thin-walled tubes under cyclic bending. *International Journal of Solids and Structures*, **21**(11): pp. 1073–1100.

Shitamoto, H. and Hisamune, N. (2013). Effect of Full-and Small-Scale Reeling Simulation on Mechanical Properties of Weldable 13Cr Seamless Line Pipe. In: *ASME 32nd International Conference on Ocean, Offshore and Arctic Engineering, Nantes, France*, American Society of Mechanical Engineers Digital Collection, OMAE2013-10681.

Shitamoto, H., Sagara, M., Amaya, H., Hisamune, N., Motoya, D., and Watatani, Y. (2014). Effect of Reeling Simulation on the Mechanical Properties of New Duplex Stainless Steel for Line Pipe. In: *ASME 33rd International Conference on Ocean, Offshore and Arctic Engineering, San Francisco, California, USA*, American Society of Mechanical Engineers Digital Collection, OMAE2014-23694.

Simo, J.C. (1987). A J2-flow theory exhibiting a corner-like effect and suitable for large-scale computation. *Computer Methods in Applied Mechanics and Engineering*, **62**(2): pp. 169–194.

Sriskandarajah, T., Rao, V., and Ragupathy, P. (2013*a*). Seal weld fatigue assessment for CRA lined pipe for HP/HT applications. In: *The Twenty-third International Offshore and Polar Engineering Conference*, International Society of Offshore and Polar Engineers.

Sriskandarajah, T., Roberts, G., and Rao, V. (2013*b*). Fatigue Aspects of CRA Lined Pipe for HP/HT Flowlines. In: *Offshore Technology Conference, Houston, Texas, USA*, Offshore Technology Conference, OTC 23932.

Stephens, W.B., Starnes Jr., J.H., and Almroth, B.O. (1975). Collapse of long cylindrical shells under combined bending and pressure loads. *AIAA Journal*, **13**(1): pp. 20–25.

Thodla, R., Gordon, R., and Gui, F. (2015*a*). Effect of Reeling on Fatigue Crack Growth Behavior of Welded API5LX65 Line Pipe. In: *ASME 34th International Conference on Ocean, Offshore and Arctic Engineering, St. John?s, Newfoundland, Canada*, American Society of Mechanical Engineers Digital Collection, OMAE2015-42412.

Thodla, R., Gordon, R., and Gui, F. (2015*b*). Effect of Reeling on Sulfide Stress Corrosion Cracking of Welded API5LX65 Line Pipe. In: *ASME 34th International Conference on Ocean, Offshore and Arctic Engineering, St. John?s, Newfoundland, Canada*, American Society of Mechanical Engineers Digital Collection, OMAE2015-42414.

Timoshenko, S.P. and Gere, J.M. (1961). *Theory of elastic stability*. New York: McGraw-Hill.

Tkaczyk, T. and Pepin, A. (2014). Methods of reel-laying a mechanically lined pipe. US Patent 8,864,417.

Tkaczyk, T., Pepin, A., and Denniel, S. (2011). Integrity of Mechanically Lined Pipes Subjected to Multi-Cycle Plastic Bending. In: *ASME 30th International Conference on Ocean, Offshore and Arctic Engineering, Rotterdam, The Netherlands*, American Society of Mechanical Engineers, OMAE2011-49270.

Tkaczyk, T., Vasilikis, D., and Pepin, A. (2020). Effect of pre-strain on bending strain capacity of mechanically lined pipe. In: *ASME 39th International Conference on Ocean, Offshore and Arctic Engineering, Virtual, Online*, American Society of Mechanical Engineers, OMAE2020-18450.

Toguyeni, G.A. and Banse, J. (2012). Mechanically Lined Pipe: Installation by Reel-Lay. In: *Offshore Technology Conference, Houston, Texas, USA*, Offshore Technology Conference, OTC 23096.

Toguyeni, G.A., Pepe, N., Barritte, G., Banse, J., Schmidt, T., Jones, R.L., and Mair, J.A. (2013). High strength carbon steel and CRA lined pipe for reel-lay installation. In: *Offshore Technology Conference, Houston, Texas, USA*, Offshore Technology Conference, OTC-24053-MS.

Tseng, N. and Lee, G. (1983). Simple plasticity model of two-surface type. *Journal of Engineering Mechanics*, **109**(3): pp. 795–810.

Tsuru, E., Shitamoto, H., Ozaki, M., Tomioka, K., and Muraki, T. (2016). Mechanical Properties and Performance Prediction for HF-ERW Line Pipes Reel-laid. In: *The 26th International Ocean and Polar Engineering Conference, Rhodes, Greece*, International Society of Offshore and Polar Engineers, ISOPE-I-16-666.

Tvergaard, V. (1983). Plastic buckling of axially compressed circular cylindrical shells. *Thin-Walled Structures*, **1**(2): pp. 139–163.

Ucak, A. and Tsopelas, P. (2011). Constitutive model for cyclic response of structural steels with yield plateau. *Journal of Structural Engineering*, **137**(2): pp. 195–206.

Ucak, A. and Tsopelas, P. (2012). Accurate modeling of the cyclic response of structural components constructed of steel with yield plateau. *Engineering Structures*, **35**: pp. 272–280.

van Es, S.H.J., Gresnigt, A.M., Vasilikis, D., and Karamanos, S.A. (2016). Ultimate bending capacity of spiral-welded steel tubes–Part I: Experiments. *Thin-Walled Structures*, **102**: pp. 286–304.

Varelis, G.E. and Karamanos, S.A. (2014). Buckling of high-strength steel cylinders under cyclic bending in the inelastic range. *Journal of Pressure Vessel Technology*, **136**(2): p. 021207.

Vasilikis, D. (2012). *Structural behavior and stability of cylindrical steel shells with lateral confinement*. Ph.D. thesis, Department of Mechanical Engineering, University of Thessaly.

Vasilikis, D. (2018). Personal communication.

Vasilikis, D. and Karamanos, S.A. (2012). Mechanical behavior and wrinkling of lined pipes. *International Journal of Solids and Structures*, **49**(23-24): pp. 3432–3446.

Vasilikis, D. and Karamanos, S.A. (2013). Wrinkling of lined steel pipes under bending. In: *ASME 32nd International Conference on Ocean, Offshore and Arctic Engineering, Nantes, France*, American Society of Mechanical Engineers, OMAE2013-11122.

Vasilikis, D., Karamanos, S.A., van Es, S.H.J., and Gresnigt, A.M. (2016). Ultimate bending capacity of spiral-welded steel tubes–Part II: Predictions. *Thin-Walled Structures*, **102**: pp. 305–319.

von Karman, T. (1911). Uber die formanderung dunnwandiger rohre. *Zeitschrift Des Vereines Deuticher Ingenieure*, **55**: pp. 1889–1895.

von Mises, R. (1928). Mechanik der plastischen Formänderung von Kristallen. *Zeitschrift für Angewandte Mathematik und Mechanik*, **8**(3): pp. 161–185.

Voyiadjis, G.Z. and Foroozesh, M. (1990). Anisotropic distortional yield model. *Journal of Applied Mechanics*, **57**(3): pp. 537–547.

Voyiadjis, G.Z. and Yaghoobi, M. (2019). Chapter 2 - Nonlocal continuum plasticity. In: *Size Effects in Plasticity*, (eds.) G.Z. Voyiadjis and M. Yaghoobi, Academic Press, pp. 81–190.

Wang, J., Sadowski, A.J., and Rotter, J.M. (2018). Influence of ovalisation on the plastic collapse of thick cylindrical tubes under uniform bending. *International Journal of Pressure Vessels and Piping*, **168**: pp. 94–99.

Wang, X., Li, P., and Wang, R. (2005). Study on hydro-forming technology of manufacturing bimetallic CRA-lined pipe. *International Journal of Machine Tools and Manufacture*, **45**(4-5): pp. 373–378.

Wilmot, D. and Montague, P. (2011). The suitability of cra lined pipes for flowlines susceptible to lateral buckling. In: *SUT Global pipeline buckling symposium, Perth, Australia*, pp. 23–24.

Xu, Z., Gardner, L., and Sadowski, A.J. (2017). Nonlinear stability of elastic elliptical cylindrical shells under uniform bending. *International Journal of Mechanical Sciences*, **128**: pp. 593–606.

Xuesheng, W., Peining, L., and Ruzhu, W. (2004). Estimation of residual contact pressure in hydraulically expanded CRA-lined pipe. *Chinese Journal of Mechanical Engineering-English Edition-*, **17**(4): pp. 598–601.

Yoshida, T., Mann, T., Matsuda, S., Matsui, S., Atsuta, T., Toma, S., and Itoga, K. (1981). The development of corrosion-resistant tubing. In: *Offshore Technology Conference, Houston, Texas, USA*, Offshore Technology Conference, OTC 4153.

Yuan, L. (2015). *On the liner wrinkling and collapse of bi-material pipe under bending and axial compression*. Ph.D. thesis, Department of Engineering Mechanics, The University of Texas at Austin.

Yuan, L. and Kyriakides, S. (2014*a*). Liner wrinkling and collapse of bi-material pipe under bending. *International Journal of Solids and Structures*, **51**(3-4): pp. 599–611.

Yuan, L. and Kyriakides, S. (2014*b*). Plastic bifurcation buckling of lined pipe under bending. *European Journal of Mechanics-A/Solids*, **47**: pp. 288–297.

Yuan, L. and Kyriakides, S. (2015). Liner wrinkling and collapse of girth-welded bi-material pipe under bending. *Applied Ocean Research*, **50**: pp. 209–216.

Yuan, L. and Kyriakides, S. (2020). Liner buckling during reeling of lined pipe. *International Journal of Solids and Structures*, **185-186**: pp. 1–13.

Yun, H.D., Peek, R.R., Paslay, P.R., and Kopp, F.F. (2004). Loading history effects for deep-water s-lay of pipelines. *Journal of Offshore Mechanics and Arctic Engineering*, **126**(2): pp. 156–163.

Zeinoddini, M., Mo'tamedi, M., Asil Gharebaghi, S., and Parke, G.A.R. (2016). On the ratcheting response of circular steel pipes subject to cyclic inelastic bending: A closed-form analytical solution. *International Journal of Mechanical Sciences*, **117**: pp. 243–257.

Zeng, D., Deng, K., Lin, Y., Shi, T., Shi, D., and Zhou, L. (2014). Theoretical and experimental study of the thermal strength of anticorrosive lined steel pipes. *Petroleum Science*, **11**(3): pp. 417–423.

Zhang, W. and Kyriakides, S. (2021). Controlled pipeline lateral buckling by reeling induced curvature imperfections. *Marine Structures*, **77**: p. 102905.

Ziegler, H. (1959). A modification of Prager's hardening rule. *Quarterly of Applied mathematics*, **17**(1): pp. 55–65.